University of Cyprus

UNIVERSITY OF CYPRUS

Department of Electrical and Computer Engineering

Photonic Techniques for mm-wave and THz Generation & Transmission

G.K.M.Hasanuzzaman

A Dissertation Submitted to the University of Cyprus in Partial Fulfillment of the Requirements for the Degree of Doctor of Philosophy

May, 2019

Validation Page

Doctoral Candidate: G.K.M. Hasanuzzaman

Doctoral Dissertation Title: Photonic Techniques for mm-wave and THz Generation & Transmission.

The present Doctoral Dissertation was submitted in partial fulfillment of the requirements for the Degree of Doctor of Philosophy at the ***Department of Electrical and Computer Engineering*** *and was approved on May 6, 2019 by the members of the* ***Examination Committee***.

Examination Committee:

Research Supervisor: _____

Prof. Stavros Iezekiel

Committee Member: _____

Prof. Guillermo Carpintero

Universidad Carlos III de Madrid, Spain

Committee Chair: _____

Prof. Georgios Ellinas

Committee Member: _____

Prof. Andreas Othonos

Committee Member: _____

Prof. Constantinos Pitris

Declaration

The present doctoral dissertation was submitted in partial fulfillment of the requirements for the degree of Doctor of Philosophy of the University of Cyprus. It is a product of original work of my own, unless otherwise mentioned through references, notes, or any other statements.

G.K.M.Hasanuzzaman

Abstract

High spectral purity microwave sources are key components for several important applications in telecommunications, navigation, and radar. In particular, low phase noise performance is critical for emerging applications in high-speed fibre-wireless links in the mm-wave and THz bands where high spectral efficiency modulation formats (e.g. 16 QAM, 64 QAM, and 256 QAM) are used to increase the throughput.

The use of photonic techniques for the generation of mm-wave and THz carriers is attractive from the point of view of providing both superior phase noise performance (as compared to conventional microwave sources based on electron devices) and also allowing distribution over low loss and high bandwidth optical fibres. This thesis therefore focuses on new approaches to photonic generation and transmission of mm-wave and THz signals.

For low loss THz guided transmission, polymer based hollow core nested anti-resonant node-less fibre (HC-NANF) has been designed for 1 THz with record low loss of 0.05 dB/m, 0.4 THz wide low loss transmission window and near zero group velocity dispersion. In a modified design, single mode guidance and bending loss are also investigated.

To generate mm-wave and THz signals by photonic-assisted approaches, the two most important photonic based methods - the optoelectronic oscillator (OEO) and optical frequency comb generator (OFCG) - are combined both in self-oscillating and separately driven structures. These combine the low-phase noise advantage of the OEO together with the potential of the OFCG to generate signals into the THz range. For the self-oscillating optical frequency comb generator (SOFCG), we report on both theoretical and experimental results; a mm-wave signal at 94.8 GHz is generated and then applied in a radio over fibre link where 23 optical comb lines (with a spacing of 11.84 GHz) are generated. An LTE Advanced signal of 20 MHz bandwidth modulated with 64 QAM is transmitted with an EVM of 2.23% over

a 1.3 m wireless distance.

In addition, a tunable OEO (6.58 -18.36 GHz) where the tunability is obtained by a phase modulator based microwave photonic (MWP) filter is used to drive an OFCG. Signals at 101.5 GHz and 242.6 GHz are generated for OEO drive signals of 16.92 GHz and 17.33 GHz respectively. This set-up is then used to implement a RoF link at 242.6 GHz with a 6 Gbaud 16 QAM data modulation which results in 24 Gbps wireless transmission over a 30 cm distance with a bit error rate (BER) less than the forward error correction (FEC) limit.

Finally, the thesis concludes with a roadmap for future work including a W-band OEO to generate low phase noise mm-wave signals without up-conversion, a multi-core fibre (MCF) based mm-wave generation, radio over fibre link and power over fibre link to realise electrical connection free remote antenna units with the help of a zero-biased uni travelling carrier photodiode (UTC-PD), and an integrated SOFCG to reduce size,weight and power consumption (SWaP).

Περίληψη

Η υψηλή φασματική καθαρότητα σε μικροκυματικές πηγές είναι βασικό συστατικό σε πολλαπλές σημαντικές εφαρμογές, όπως σε συστήματα τηλεπικοινωνιών, πλοήγησης, και ραντάρ. Πιο συγκεκριμένα, για τις αναδυόμενες εφαρμογές υψηλού ρυθμού μετάδοσης σε οπτικά και ασύρματα δίκτυα, η λειτουργία αυτών των συστημάτων με χαμηλό θόρυβο φάσης είναι αποφασιστικής σημασίας. Επίσης, είναι καθοριστικής σημασίας και σε συστήματα που λειτουργούν με χιλιοστομετρικά κύματα καθώς και σε συστήματα που λειτουργούν στις συχνότητες THz, όπου χρησιμοποιούνται διάφορες τεχνικές διαμόρφωσης υψηλής φασματικής απόδοσης (π.χ. 16 QAM, 64 QAM, και 256 QAM) για την αύξηση της δυνατότητας διεκπεραίωσης δεδομένων.

Η χρήση φωτονικών τεχνικών για την παραγωγή χιλιοστομετρικών κυμάτων καθώς και φορέων στις συχνότητες THz είναι ελκυστική για την λειτουργία συστημάτων με χαμηλό θόρυβο φάσης σε σύγκριση με τις συμβατικές μικροκυματικές πηγές. Επίσης, η χρήση αυτών των τεχνικών επιτρέπει τη μετάδοση σημάτων μέσω οπτικών ινών με χαμηλό θόρυβο και υψηλό εύρος ζώνης. Επομένως, η συγκεκριμένη διατριβή εστιάζεται σε νέες τεχνικές φωτονικής για την παραγωγή και μετάδοση χιλιοστομετρικών κυμάτων καθώς και σημάτων στις συχνότητες THz.

Για την μετάδοση σημάτων στις συχνότητες THz με χαμηλές απώλειες, σχεδιάστηκαν οπτικές ίνες βασισμένες σε πολυμερή με κενό πυρήνα για λειτουργία στη συχνότητα 1 THz, προσφέροντας χαμηλές απώλειες μετάδοσης σε ένα φασματικό εύρος 0.4 THz, και σχεδόν μηδενική διασπορά ομαδικής ταχύτητας. Επίσης σχεδιάστηκε βελτιωμένη οπτική ίνα, για μονότροπη μετάδοση σήματος με χαμηλή απώλεια κάμψης.

Για την παραγωγή χιλιοστομετρικών κυμάτων καθώς και σημάτων στις συχνότητες THz, οι δύο πιο σημαντικές μέθοδοι βασισμένες στη φωτονική – ο οπτοηλεκτρονικός

ταλαντωτής (ΟΗΤ) και η οπτική γεννήτρια κτένα συχνότητας (ΟΓΚΣ) – χρησιμοποιούνται μαζί. Αυτό συνδυάζει το πλεονέκτημα χαμηλού θορύβου φάσης των ΟΗΤ μαζί με την προοπτική των ΟΓΚΣ για την παραγωγή σημάτων σε THz εύρος. Θεωρητικά και πειραματικά αποτελέσματα αναδεικνύουν την εγκυρότητα αυτής της προσέγγισης, συμπεριλαμβανομένων πειραμάτων μετάδοσης σήματος σε δίκτυα ραδιοεπικοινωνίας-μέσω-ινών με χαμηλό δυαδικό ρυθμό σφάλματος.

Τέλος, η διατριβή ολοκληρώνεται με σχέδιο δράσης για μελλοντική εργασία, συμπεριλαμβανομένων καινούργιων τεχνικών για τη παραγωγή χιλιοστομετρικών κυμάτων χαμηλού θορύβου χωρίς πάνω-μετατροπή, πολύκλωνων ινών βασισμένων σε παραγωγή χιλιοστομετρικών κυμάτων, δικτύων ραδιοεπικοινωνίας-μέσω-ινών και δικτύων ισχύς-μέσω-ινών για τη δημιουργία ηλεκτρονικών συνδέσεων χωρίς κινούμενη μονάδα αντένας, καθώς και τεχνικών για την υλοποίηση αυτό-ΟΓΚΣ με ολοκληρωμένα φωτονικά κυκλώματα.

Acknowledgements

Firstly, I would like to thank my supervisor Professor Stavros Iezekiel for his guidance and encouragement throughout the last three and a half years.

My sincere thanks also goes to Dr. Atsushi Kanno and Dr. Pham Tien Dat of the National Institute of Information and Communications Technology, Japan (NICT) who provided me an opportunity to join their team as an intern, and who gave access to their laboratory and research facilities. In addition, I also thank the team at DTU (Professor Idelfonso Tafur Monroy) who hosted me for a secondment from February to May 2017 to work on their MCF experiments and the team at UCL (Professor John Mitchell) who hosted me from March to July 2018.

Finally, I acknowledge financial support from the FiWiN5G project under the framework of the European Union's Horizon 2020 Research and Innovation Programme under the Marie Skłodowska-Curie grant agreement No. 642355.

Contents

List of Figures

List of Tables

List of Acronyms

Acronym	Description
ADC	Analogue to digital converter
AR	Anti-resonant
ASE	Amplified spontenous emission
AWG	Arbitrary waveform generator
BER	Bit error rate
BPD	Balanced photodetector
CNR	Carrier power to noise power density ratio
C-RAN	Centralized radio access network
DDMZM	Dual drive Mach-Zehnder modulator
DFB	Distributed feedback
DSB	Double side band
DSF	Dispersion shifted fibre
DWFL	Dual wavelength fibre laser
EBPF	Electrical bandpass filter
EDFA	Erbium doped fibre amplifier
EOM	Electro-optic modulator
ESA	Electrical spectrum analyser
EVM	Error vector magnitude
FBG	Fibre Bragg grating
FDD	Frequency division duplexing
FE	Finite element
FEC	Forward error correction
FIR	Finite impulse response

Acronym	Description
FL	Fibre laser
FQM	Filter quality multiplier
FSR	Free spectral range
FWHM	Full wave half-maximum
FWM	Four wave mixing
HC-AR	Hollowcore anti-resonant
HCF	Hollowcore fibre
HC-NANF	Hollowcore anti-resonant nodeless fibre
HDPE	High-density polyethylene
HOM	Higher order mode
HOMER	Higher order mode extinction ratio
IIR	Infinite impulse response
IMPATT	Impact ionization avalanche transit time
IMWP	Integrated microwave photonics
ITU	International Telecommunication Union
LNA	Low noise amplifier
LO	Local oscillator
LSB	Lower side band
LTE	Long-Term Evolution
MCF	Multi-core fibre
MIMO	Multiple input multiple output
MLL	Mode locked laser
MMIC	Monolithic microwave integrated circuit
mm-wave	Milimetre wave
MTI	Moving target indicator
MWP	Microwave photonics
MZM	Mach-Zehnder modulator
OCS	Optical carrier suppression
OEO	Optoelectronic oscillator
OFC	Optical frequency comb

Acronym	Description
OFCG	Optical frequency comb generator
OFDM	Orthogonal frequency division multiplexing
OSA	Optical spectrum analyser
PA	Power amplifier
PBG	Photonic bandgap
PCF	Photonic crystal fibre
PD	Photo-detector
PML	Perfectly matched layer
PMMA	Polymethyl-methacrylate
PPM	Parts per million
PSD	Power spectral density
QAM	Quadrature amplitude modulation
QCL	Quantum cascade laser
QM	Quality Multiplier
QPSK	Quadrature phase shift keying
RAU	Remote antenna unit
RIN	Relative intensity noise
RoF	Radio over Fibre
ROM	Reciprocating optical modulator
RTO	Real time oscilloscope
SBS	Stimulated Brillouin scattering
SC-SMF	Singe core single mode fibre
SDM	Space division multiplexing
SHM	Sub-harmonic mixer
SISO	Single input single output
SMF	Single mode fibre
SOFCG	Self-oscillating optical frequency comb generator
SOA	Semiconductor optical amplifier
SSB	Single side band
SWaP	Size weight and power

Acronym	Description
TIR	Total internal reflection
TOBF	Tunable optical bandpass filter
USB	Upper side band
UTC-PD	Uni-travelling carrier photo-diode
WGMR	Whispering gallery mode resonator
WSS	Wavelength selective switch

List of Symbols

Symbol	Description
c	Speed of light in vacuo
d	Cladding tube diameter of HC-AR fibre
D	Core-diameter of HC-AR fibre
d_f	Fraunhofer distance
E	Electric field
f	Frequency
n	Refractive index
t	HC-AR fibre tube thickness
f_c	Resonant frequency of HC-AR fibre
f_d	Doppler frequency shift
J_m	m-th order Bessel function
R_b	Bending radius
R_b^{cr}	Critical bending radius of HC-AR
Q	Quality factor
β_2	Waveguide dispersion
ε_0	Permittivity in free-space
λ	Wavelength
μ_0	Permeability in free-space
v	Velocity of moving target
τ	Delay time
ϕ	Phase
ω	Angular frequency
$\delta\nu$	Laser linewidth
$\Re$	Responsivity

CHAPTER 1

Introduction

1.1 Introduction

Microwave photonics is an interdisciplinary field which brings together radio frequency engineering and optoelectronics, and studies the interaction between microwave and optical signals. Its primary applications are generation, distribution, control, processing and analysis of microwave signals by the means of photonics [1, 2]. These functions are listed in Table 1.1 along with indicative examples, of which radio-over-fibre has been one of the most important.

Table 1.1: Major microwave photonics functions and their applications.

Microwave photonics function	Example
Generation	Optoelectronic oscillator [3], arbitrary waveform generation [4], optical heterodyning
Distribution	Radio over fibre link [5]
Control	Optical phase locked loop [6]
Processing	Microwave photonic filtering, analogue to digital conversion [7], and optical delay lines [8]
Analysis of microwave signals	Instantaneous frequency measurement [9]

Radio-over-fibre (RoF) enables seamless media conversion between radio and optical signals in a fibre-wireless link and plays a key role in reducing the offset between wireline and wireless data rates. Consequently, RoF with high capacity fibre-wireless links operating in the millimetre wave (mm-wave) band is being considered for mobile backhauling and fronthauling in the future 5G era and beyond [10, 11]. Other applications (as shown in Fig. 1.1) include the enhancement of network resilience against disasters [12], the last mile access network where deployment of the optical network is difficult or not economical, and non-telecom applications, such as linear cell radar systems in airports and railways as illustrated in Fig. 1.2 [13]. Both mobile and fixed wireline communications continue to see impres-

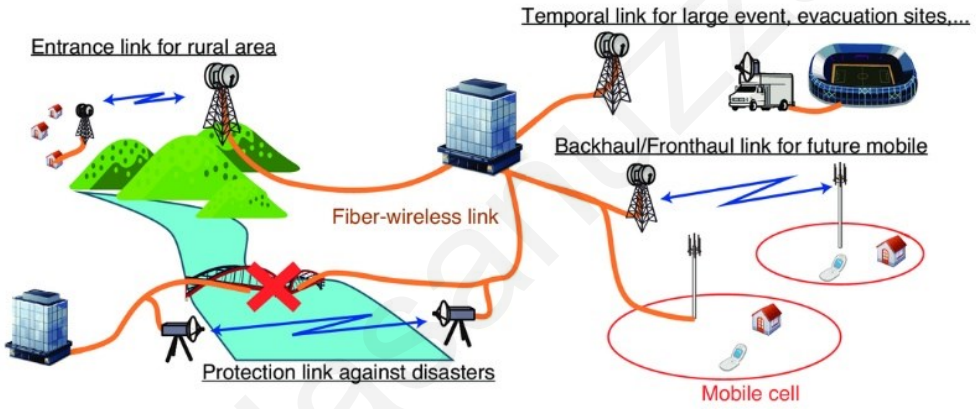

Fig. 1.1. Telecom application scenarios of RoF based fibre wire-less link. Courtesy: A. Kanno, NICT, Japan.

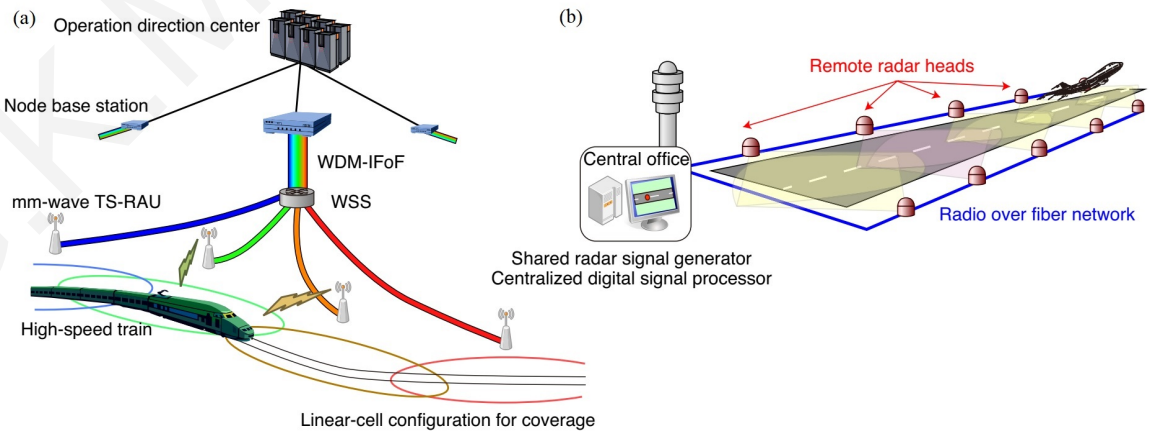

Fig. 1.2. Non-telecom application scenarios of RoF based fibre wireless link (a) a linear cell based radio communication system between train and track-side (b) radio over fibre based foreign debris detection system for surveillance of airport runway. After [14].

sive growth in demand for parameters such as bit rate, and this trend is forecast to continue for the foreseeable future [15]. Consequently communication systems such as optical fibre and wireless have evolved through several generations; in the case of wireless communications, we are in the era of intensive 5G research and development, with a number of trials now underway [16]. 5G is significantly different from previous generations with respect to various parameters as illustrated in Fig. 1.3, and in particular with the need for multi-Gbps data rates (e.g. for high definition video streaming), for massive machine communications (as in the Internet of Things) and ultra-low latency (e.g. for autonomous vehicles and remote surgery). To meet high data rate demands (e.g. 1 Gbps in indoor download links) two approaches have been considered in 5G; (i) moving towards the mm-wave band and (ii) high spectral efficiency modulation formats such as 64 QAM and 256 QAM. In the latest release

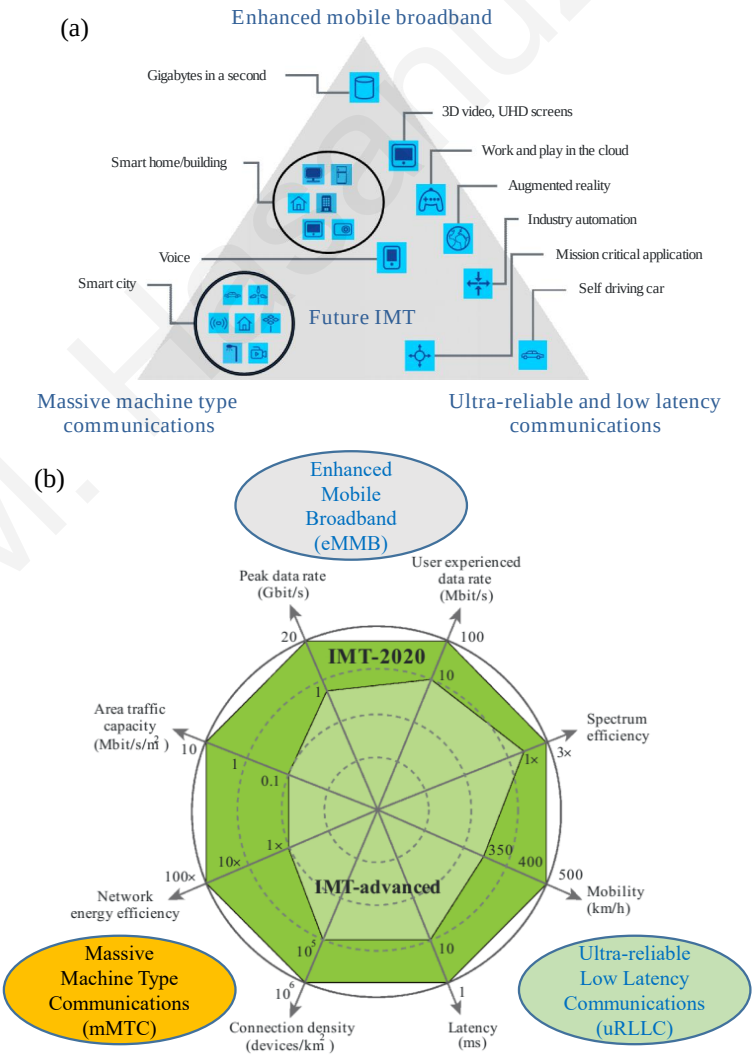

Fig. 1.3. (a) 5G application scenarios (b) key performance indicators. After [16].

of 3GPP, two frequency bands have been allocated for 5G deployment; one is in the sub-6 GHz range (450 MHz - 6 GHz) while the other is above 24 GHz (24.25-56.4 GHz) [17].

Apart from 5G, there is increasing interest in the mm-wave and terahertz (THz) parts of the spectrum for other applications, including medical diagnostics, testing of pharmaceutical drugs, spectroscopy, imaging, sensing, biotechnology, security, and radioastronomy [18, 19]. Implementing wireless links in the mm-wave band with highly spectrally efficient modulation formats requires good quality carrier signals (i.e. with low phase noise) to meet the error vector (EVM) magnitude requirements. The effect of phase noise on various application scenarios is discussed in chapter 2.

This thesis has three main themes which will be elaborated in the following sections of this chapter, and then described in detail in the following chapters. These all revolve around the existing needs (as defined by 5G amongst other applications) and projected requirements *inter alia* of future mm-wave and THz systems, for the low-phase noise generation of mm-wave and THz signals using photonics, and the subsequent distribution over low-loss optical fibre. Specifically, we consider: (i) development of low-loss THz fibres; (ii) W-band self-oscillating optical frequency combs derived from the optoelectronic oscillator topology; and (iii) optoelectronic-oscillator driven optical frequency combs for frequency-tunable operation at frequencies in excess of 200 GHz. Before considering these aspects, we briefly review conventional, all-electronics approaches to sinusoidal signal generation in the next section, followed by photonics-based methods for oscillators and frequency combs.

1.2 Electronic techniques for mm-wave and THz signal generation

As shown in Fig. 1.4 the mm-wave band (30 GHz to 300 GHz) and the THz band (0.1 to 10 THz) are located between the microwave and infrared. Therefore, two enabling technologies exist for mm-wave and THz signal generation, namely electronics and photonics. In this section, electronic techniques for mm-wave and THz signal generation are briefly discussed while in the next section the details of photonic techniques are presented.

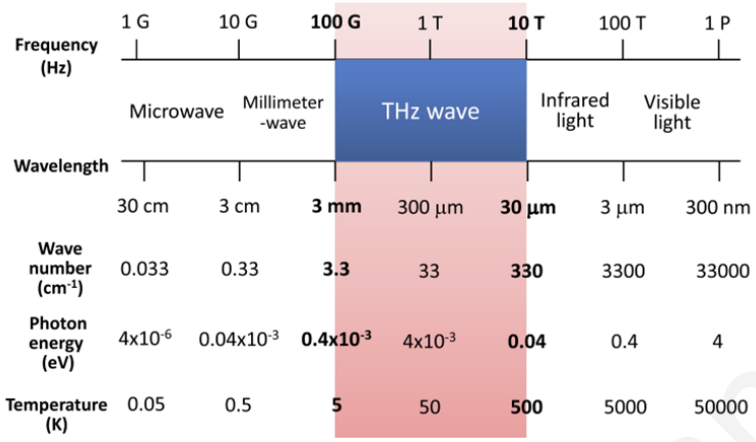

Fig. 1.4. The electromagnetic spectrum. After [19].

- **Electrical multiplication:** The first electronic approach to be considered is the multiplication method where mm-wave signals can be generated from low-frequency oscillators by frequency multiplication. However, the phase noise of the output signal increases according to the relationship $20 \times \log_{10} N$, where N is the multiplication factor. Consequently there is a 6 dB increase of phase noise with every doubling in the frequency which in turn makes this method unsuitable for generating low phase noise mm-waves. This implementation is also complicated and can be costly.

- Other electronics approaches for generation of THz signals are Gunn diode oscillators, impact ionization avalanche transit-time (IMPATT) diode oscillators, backward wave oscillators, quantum cascade lasers (QCL), and resonant tunneling diodes. IMPATT diode oscillators can generate high-power tones at frequencies greater than 300 GHz; however, because of the avalanche breakdown process required for signal generation the phase noise is very poor [20]. Transferred electron oscillators, such as Gunn diode oscillators, can generate frequencies in excess of 100 GHz. Although they display better phase noise than IMPATT diode oscillators, their noise performance is not as good as that of photonically-generated signals. Additionally, due to the high loss associated with electrical distribution lines such as coaxial cable, distribution of mm-wave signals in the electrical domain is not practical.

In contrast, photonically-assisted approaches not only allow the generation of mm-waves and THz waves with high purity but also allow distribution to a remote site with low transmission loss via standard single mode fibre (SMF). This is possible due to the inherent broadband

and low loss property of optical fibre.

1.3 Generation of mm-wave and THz waves: Photonic assisted approaches

One of the most useful attributes of microwave photonics technology is the availability of high bandwidth photodetection, which consequently enables the generation of microwave, mm-wave and THz signals through a variety of topologies and devices [2, 21]. This ranges from the use of discrete devices as in mode-locked lasers [22], gain-switched lasers [23], external modulation [24, 25], and nonlinear optics [26] to generate optical combs, through to more complex topologies such as optoelectronic oscillators (OEOs) [27] and recirculating optical loops [12]. In all cases the motivation is the feasibility of producing a signal directly in the optical domain, allowing it to be distributed and processed photonically. Various photonic based techniques for mm-wave and THz signal generation are described below.

1.3.1 Optical heterodyning

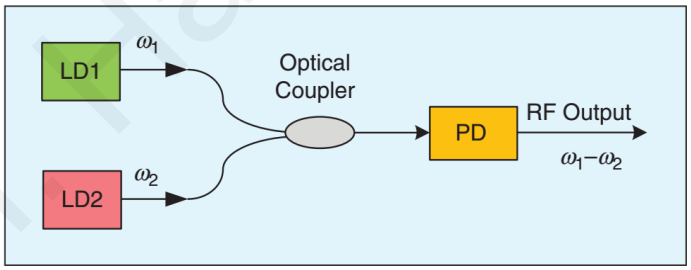

Fig. 1.5. Beating of two optical waves at a PD for the generation of a microwave signal

The simplest and most flexible method for generating THz signals by photonic means is optical heterodyning where a beat signal is generated by two free-running optical sources with fixed frequency separation as shown in Fig. 1.5. The output RF signal frequency is equal to the frequency separation between the optical sources. Assuming we have two optical waves given by

$$E_1(t) = E_{01}\cos(\omega_1 t) + \phi_1$$

and

$$E_2(t) = E_{02}\cos(\omega_2 t) + \phi_2$$

where E_{01}, E_{02} are the amplitude terms and ϕ_1,ϕ_2 are the phase terms of the two optical waves, then the signal at the output of the photo-detector (PD) is given by:

$$I(t) = \Re|E(t)|^2 = \Re|E_1(t) + E_2(t)|^2 = \Re P_1 + \Re P_2 + 2\Re\sqrt{P_1 P_2}\cos[(\omega_1 - \omega_2)t + (\phi_1 - \phi_2)] \tag{1.1}$$

where $\Re$ is the responsivity of the photodetector, and P_1 and P_2 are the optical powers associated with E_1 and E_2. Considering the limited bandwidth of the photodetector, the current at the output of the photodetector is given by:

$$I_{RF}(t) = 2\Re\sqrt{P_1 P_2}\cos[(\omega_1 - \omega_2)t + (\phi_1 - \phi_2)]. \tag{1.2}$$

Although this technique is capable of generating electrical signals up to the THz band, limitations include its wavelength stability and corresponding frequency and phase fluctuation. The optical phase fluctuation is converted to phase noise in the electrical domain. The stability of the generated signal may fail to meet the fluctuation tolerance of the ITU regulation [28–30]. According to the ITU regulation, the required tolerance of the centre frequency should be less than $\pm$ 150 ppm at a radio frequency of 30-275 GHz. For a multi-gigabit system in the 60-GHz band, the tolerance should be less than $\pm$ 20 ppm.

1.3.2 Dual wavelength DFB source

The phase fluctuation between the two wavelengths due to path length difference may be eliminated by introducing a dual wavelength source where two DFB lasers are monolithically integrated onto a quantum dash material and combined with a Y coupler [31]. Figure 1.6(a) shows a monolithically integrated dual wavelength DFB laser source which is used to generate a 146 GHz carrier frequency by optical heterodyning; the lasers are grown on InGaAsP and the two laser wavelengths are separated by about 20 μm. The wavelength separation of the reported dual wavelength DFB laser determines the frequency of the generated signal which can be tuned through the DC bias currents I_{DFB1} and I_{DFB2} as shown in Fig. 1.6(b). It is also possible to realise the dual wavelength concept with a fibre ring laser as shown in Fig. 1.6(c) where two wavelengths are generated from the same cavity [2].

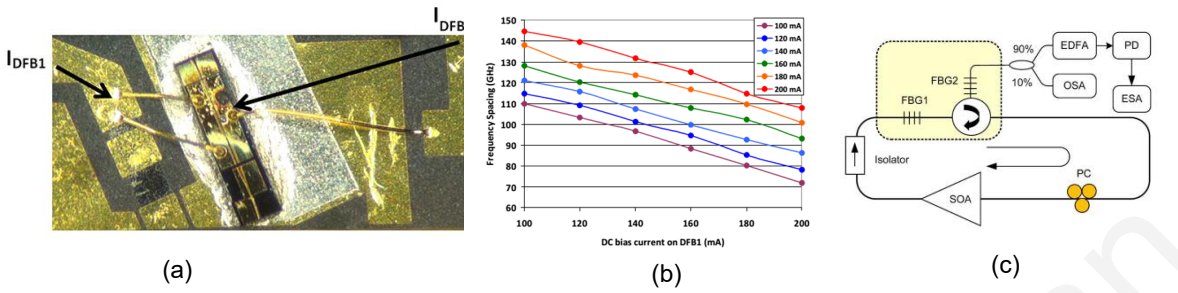

(a) (b) (c)

Fig. 1.6. (a) Photograph of a dual wavelength source, composed of two DFB lasers (DFB_1 and DFB_2) combined through a Y-coupler. (b) Dependence of the frequency spacing between DFB_1 and DFB_2 wavelengths as the DFB_1 current is varied at various fixed values of DFB_2 current. After [31]. (c) A dual wavelength single-longitudinal-mode fibre ring laser for mm-wave generation. After [2].

1.3.3 Dual-wavelength fibre laser

The spectral purity of mm-wave and THz wave signals generated by a dual-mode laser or two separate lasers is poor due to the low coherency of the two longitudinal modes. On the other hand, a dual wavelength fibre laser (DWFL) is a promising concept because the fibre laser provides optical output with high coherency. In [32], a DWFL was used to generate a 60 GHz signal where a photonic crystal fibre (PCF) was included inside the laser cavity to select two lasing modes. In the laser ring cavity, the PCF helps to stabilize the dual-wavelength and functions as a wavelength selective switch due to its wavelength dependent characteristics. A typical experimental set up of a DWFL is shown in Fig. 1.7.

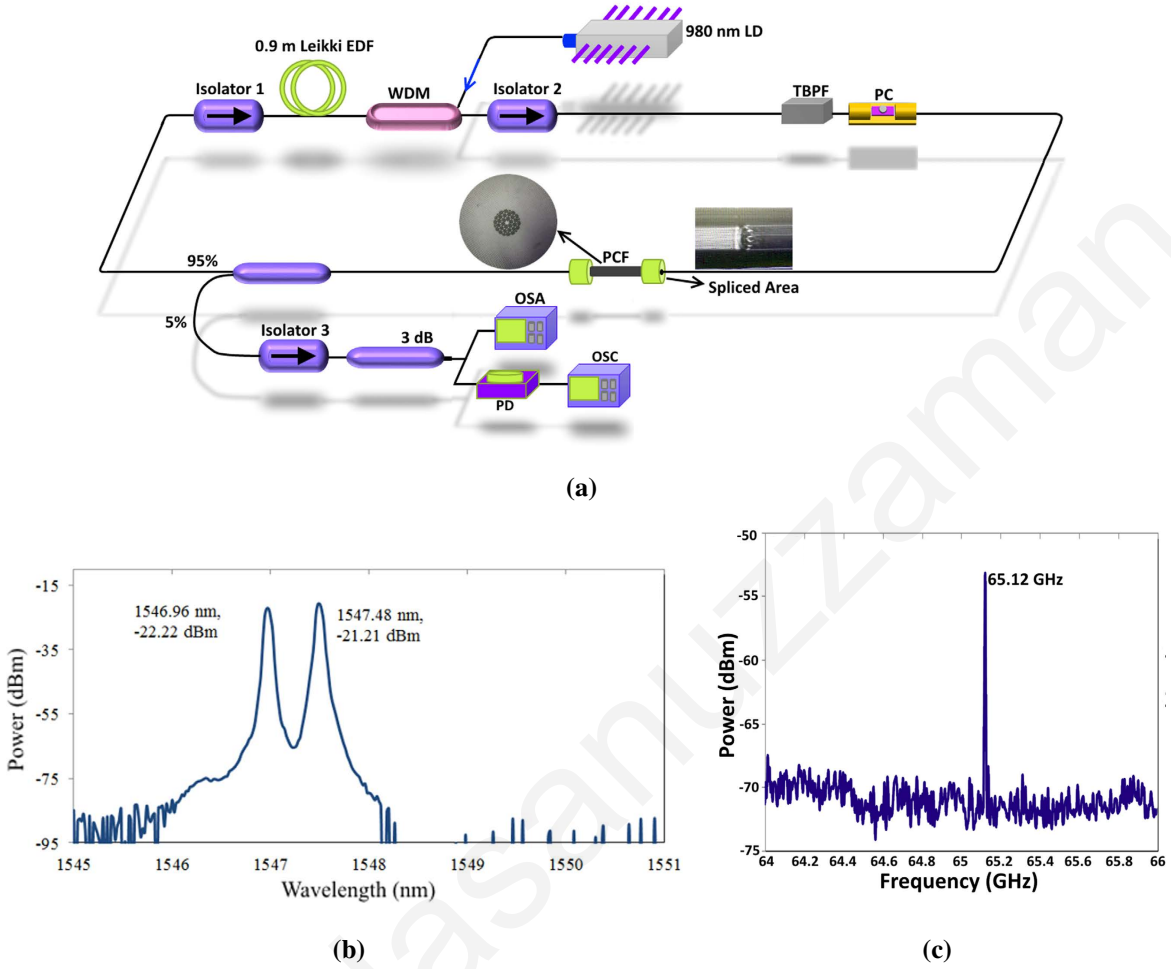

Fig. 1.7. (a) Experimental setup to generate stable dual-wavelength fibre laser. (b) Optical spectrum of DWFL lasing at wavelengths 1546.96 nm and 1547.48 nm, and (c) The beating frequency of 65.12 GHz in the ESA. After [32].

1.3.4 External modulation

In the external modulation technique, a microwave signal modulates an optical carrier via an electro optic modulator such as the Mach-Zehnder modulator (MZM). A Mach-Zehnder modulator acts as the optical equivalent of an amplitude modulator (i.e. an intensity modulator), generating stable upper sideband (USB) and lower sideband (LSB) components. In particular, the dual drive Mach-Zehnder modulator (DDMZM) is widely used in radio-over-fibre systems to generate millimeter wave and terahertz signals. Figure 1.8 shows the schematic of a DDMZM and the static light-voltage characteristic of an MZM (which in its simplest form is a modulator in which a phase shift is only applied to one of the arms of the Mach-Zehnder interferometer). For an optical carrier frequency of ω_c that is represented by an electric field wave with amplitude E_0, the output of the DD-MZM is given by:

$$E_{out} = \frac{1}{\sqrt{2}} E_0 (e^{j\Delta\phi_1(t)} + e^{j\Delta\phi_2(t)}) e^{j\omega_c t} \tag{1.3}$$

with $\Delta\phi_1(t)$ and $\Delta\phi_2(t)$ being the phase changes in arm "1" and "2" respectively, due to the Pockels effect originating from the electric fields applied to the electrodes. These phase changes are given by:

$$\Delta\phi_1(t) = \frac{\pi}{V_\pi} V_{DC_1} + \frac{\pi}{V_\pi} V_1 \sin(\omega_m t) \tag{1.4}$$

$$\Delta\phi_2(t) = \frac{\pi}{V_\pi} V_{DC_2} + \frac{\pi}{V_\pi} V_2 \sin(\omega_m t) \tag{1.5}$$

where V_{DC_1} and V_{DC_2} are the applied DC voltages for arm 1 and 2, respectively, while V_1 and V_2 are the corresponding amplitudes of the RF voltage components. We can define $m_i = \frac{\pi}{V_\pi} V_i$

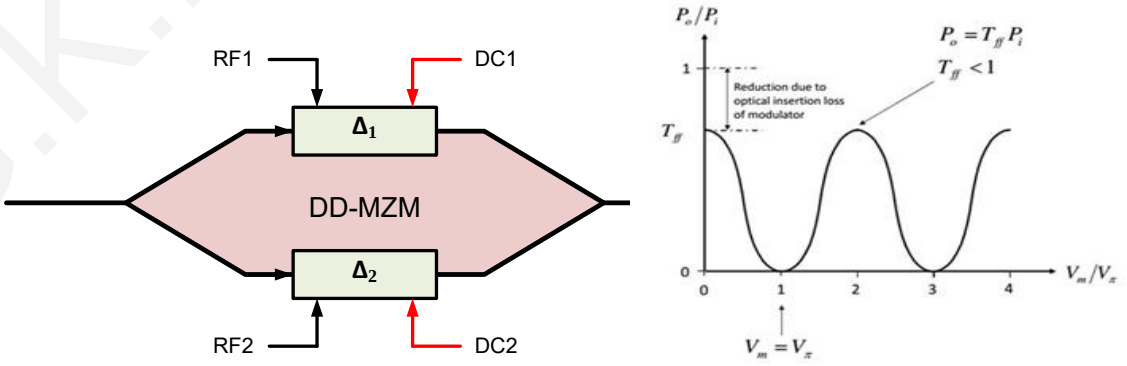

Fig. 1.8. (a) Schematic of a dual drive Mach-Zehnder modulator (b) DC characteristic curve of the MZM.

as the modulation index. Analysis then shows that E_{out} is a Bessel function of the first kind and the output of the MZM is the sum of the carrier frequency and sideband components determined by the modulation frequency. Previous work shows that by properly choosing the modulation index m, applied DC voltages and phase of the applied RF signal, double side band, double side band with suppressed carrier and single side band spectra can be generated.

The MZM is biased at the minimum transmission point to suppress the even order components. If we set the bias to a minimum transmission point, and we neglect the higher order components above the second order, double- side band suppressed carrier optical modulation can be achieved. In this case the output contains the first order LSB and USB and by beating the first order sidebands at a PD, a frequency doubled microwave signal is generated as shown in Fig.1.9(a). In contrast, when the bias of the MZM is at the maximum transmission point, the odd order sideband components are suppressed [21, 25]. Thus the output comprises the optical carrier and two second-order sidebands. By using a notch filter to remove the optical carrier, and then beating the two sidebands at the PD, a frequency quadrupled microwave signal is generated as shown in Fig.1.9(b).

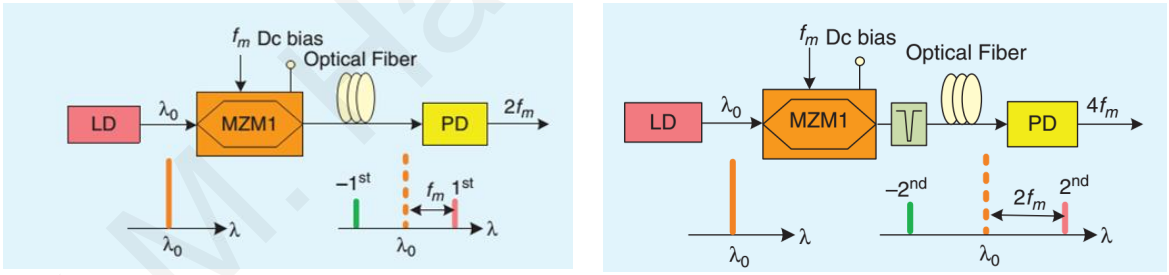

(a) **(b)**

Fig. 1.9. (a) Frequency doubling by biasing the MZM at the minimum transmission point. (b) Frequency quadrupling by biasing the MZM at the maximum transmission point. The optical carrier is removed by an optical notch filter. After [21].

1.3.5 Reciprocating optical modulator

A reciprocating optical modulator (ROM), consists of a pair of optical filters and optical phase modulator as shown in Fig.1.10(a). A ROM can generate high order-sideband components effectively where one of the optical filters is placed at the optical input port and the

other is at the output port [25]. The operating principle of the reciprocating optical modulator

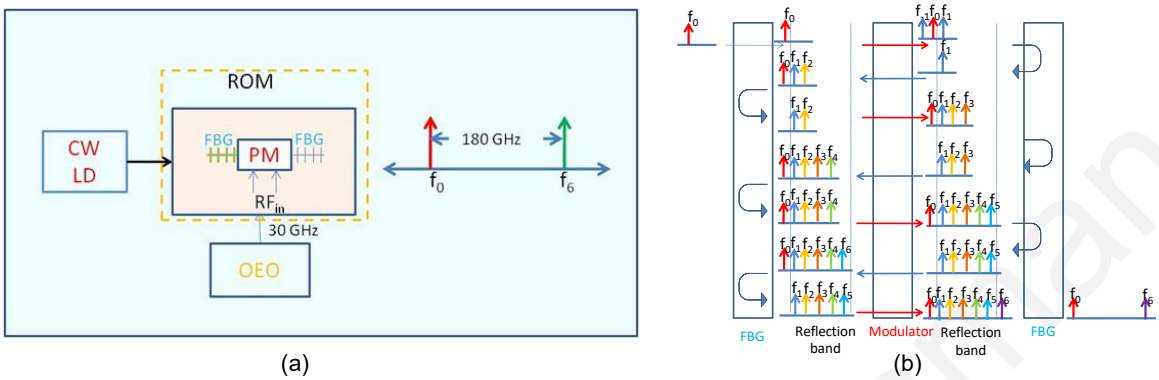

Fig. 1.10. (a) Schematic of reciprocating optical modulator (b) Operating principle of reciprocating optical modulator.

can be described using Fig. 1.10(b). As mentioned earlier, a reciprocating optical modulator consists of two optical filters and an optical modulator mounted between them. A lightwave is inserted into the modulator through one of the filters (input filter), and comes out from the other filter (output filter). The input filter transmits an unmodulated input lightwave from a light source, but reflects lightwaves in a specific optical frequency range. The output filter also reflects light waves in a specific optical frequency range, but transmits the spectral components which we aim to generate.

Consider an unmodulated light wave from a laser source, whose frequency is f_0, and is fed to the input filter. Since the input light wave frequency lies outside the reflection band of the input filter it is modulated by the phase modulator. The output of an optical phase modulator can be expressed by

$$\sum_{n=-\infty}^{\infty} J(\Delta\phi)\exp^{i2\pi f_n} f_n = f_0 + nf_m \tag{1.6}$$

where f_m is the frequency of the sinusoidal RF signal applied to the electrical ports of the optical modulator, $\Delta\phi$ denotes the amplitude of the induced phase shift of the light wave at the modulator and J_n is the n-th order Bessel function of the first kind. A block diagram of sixth-order order harmonic generation is shown in Fig.1.10. Suppose that the two filters reflect the spectral components f_{+1}, f_{+2}, f_{+3}, f_{+4}, and f_{+5}. For simplicity, consider that the modulator creates only first order side bands denoted by f_{+1} and f_{-1}. The output filter reflects f_{+1} and passes the others. The f_{+1} component is again modulated by the modulator and produces f_{+2} and f_0 sideband components. Similarly f_{+3}, f_{+4}, f_{+5} and f_{+6} components

are generated based on the above mechanism as shown in Fig. 1.10(b). Since the filter rejection-band covers the frequencies from f_{+1} to f_{+5}, the f_{+0} and f_{+6} components are available at the output of the ROM. Heterodyning in a high speed photodiode results in an electrical signal corresponding to the frequency difference between f_{+0} and f_{+6}.

1.3.6 Optoelectronic oscillator

Of the photonics-based approaches to microwave and mm-wave signal generation, the optoelectronic oscillator (OEO) is particularly attractive because it can generate low phase noise oscillation without any reference RF signal [3]; indeed, a state-of-the-art X-band OEO has demonstrated phase noise as low as -163 dBc/Hz at an offset frequency of 6 kHz when it oscillates at 10 GHz [33] , thus making it extremely competitive with regards to this parameter when compared with electronics-based microwave oscillators. The generic OEO topology consists of a hybrid optoelectronic loop where the self-sustained oscillation is obtained (under a small-signal approximation) from the Barkhausen criteria. Since the OEO forms one of the main themes of the thesis, it will be described in greater detail in Chapter 3.

1.3.7 Optical frequency comb generation with optical heterodyne

The optical frequency comb generator (OFCG) is a very convenient way to generate a number of phase-correlated optical carriers with accurate frequency spacing. It is a useful tool for various applications in microwave and millimeter wave photonic technologies including optical and microwave waveform generation, optical signal processing, and fibre optic communication [26]. Optical frequency combs are especially useful for the latest generation of optical multicarrier communication systems, where information is encoded onto so-called super channels [34]. Several approaches have been demonstrated theoretically and experimentally for the generation of optical combs. Conventionally, mode-locked lasers, fibre nonlinearities and external modulation are the principal methods for OFC generation. As with the OEO, the OFCG is one of the main themes of this thesis, hence a more detailed description is also provided in Chapter 3.

Fig. 1.11 shows the arrangement for generating mm-wave and THz signals with the combination of an OFCG and the optical heterodyne technique. Two optical tones with the desired frequency spacing are selected by a wavelength selective switch (WSS) and then beat in a

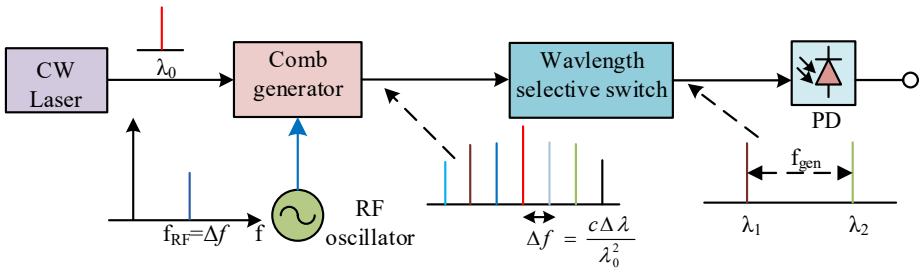

Fig. 1.11. Conceptual diagram of optical frequency comb with optical heterodyning based mm-wave generation.

high speed photo-detector (PD) to generated the electrical signal at the required frequency. Specifically, if the wavelength spacing of the tones is $\Delta\lambda$, then the corresponding frequency that is generated at the PD is given by:

$$\Delta f = \frac{c\Delta\lambda}{\lambda_1\lambda_2} \tag{1.7}$$

where Δf is the frequency of generated signal through heterodyning, c is the speed of light in vacuo, and λ_1 and λ_2 are the wavelengths of the selected two tones.

1.4 Scope and novel contributions of the thesis

The remaining chapters outline the work conducted towards the realization of photonically-enabled mm-wave and THz signal generation, modulation and transmission.

- The second chapter covers the state-of-the-art of THz links and subsystems, with an extensive literature review in which the various reported systems are compared and contrasted with respect to transmitter and receiver technology, modulation format, fibre and wireless path lengths, use of single-carrier or multi-carrier transmission and implementation of SISO (single input single output) or MIMO (multiple input multiple output).
- Chapter 3 deals with the detailed description of two of the most important microwave photonic techniques for mm-wave and THz signal generation, namely the optoelectronic oscillator (OEO) and the optical frequency comb generator (OFCG). The operating principle of the OEO, side mode suppression techniques (both in the optical and electrical domain), sources of phase noise, and tunability are discussed along with a consideration of OFCG theory and operation.

The next three chapters, viz. Chapters 4, 5 and 6, describe the novel contributions of the thesis in the areas of low loss THz fibres, self-oscillating optical frequency comb generators, and frequency tunable OEO driven OFCGs operating above 200 GHz. These contributions are outlined below, described in detail in the corresponding chapters, and are then revisited and re-evaluated in the conclusions in Chapter 7.

- The numerical design (using the finite element package COMSOL) of two new polymer based hollow core anti-resonant (HC-AR) fibres is presented in Chapter 4 for low loss THz guided transmission. The first design (Design-I) is based on hollow core nested anti-resonant node-less (HC-NANF) structures while the second design (Design-II) is based on a classical HC-AR structure. Design-I basically focuses on the low loss transmission by incorporating additional anti-resonant elements called nested tubes. In particular, a six-element based HC-NANF design is predicted to provide low loss THz guidance (with a transmission loss of 0.05 dB/m at 1 THz, a 0.4 THz wide low-loss transmission window and a 0.6 THz flat dispersion window). This proposed design is the first demonstration of a HC-NANF fibre in the THz band and it provides the lowest material absorption loss amongst the state-of-the-art fibres operating at 1 THz (as compared in Table 4.2). Therefore, the HC-NANF is a strong potential candidate for long-haul THz guided transmission and due to its relatively simple cross-section (as compared to other THz fibres), is expected to be relatively easy to fabricate. However, examination of the higher-order mode extinction ratio indicates that Design-1 cannot guarantee single mode guidance. Hence the key target of Design-II is to obtain single mode guidance by selecting suitable geometrical and material parameters. A regular HC-AR fibre is able to support single mode guidance by maintaining the shape factor d/D of the fibre, where d is the inner diameter of the anti-resonant tubes and D is the core diameter. At $d/D = 0.69$, the core guided higher order modes are phase matched with the anti-resonant tube guided modes. Consequently, the higher order modes exhibit higher transmission loss than the fundamental mode and the fibre effectively operates under single mode guidance. Although the HC-AR fibre provides relatively higher transmission loss than the HC-NANF fibre, it maintains a greater higher-order mode extinction ratio. As with the HC-NANF, the HC-AR fibre also has a relatively simple cross-section, requiring only seven capillaries.

- Chapter 5 describes the simulation and experimental work carried out on self-oscillating optical frequency comb generators (SOFCG) based on a dual-loop OEO topology. This includes a W-band radio over fibre link based on a SOFCG that was implemented at NICT in Tokyo. In comparing the OEO with the OFCG, one sees that the former does not require an external microwave synthesizer and offers low phase noise performance, but the latter is capable (through wavelength selective filtering) of providing signals at sub-THz frequencies. Hence the SOFCG combines the advantages of both the OEO and the OFCG, namely generation of low phase noise mm-wave and sub-THz signals without requiring an external microwave source. This is achieved via a modification of the dual loop OEO topology, in which the Mach-Zehnder intensity modulator is substituted with a dual-drive Mach-Zehnder modulator. Whereas in the OEO, the optical part of the loop supports a double-sideband optical spectrum which upon photodetection results in a microwave output, in the SOFCG the optical spectrum is that of a comb. Photodetection of the comb spacing then results in the RF signal that both drives the dual-drive Mach-Zehnder modulator and can be used as a direct output. Experimental validation of the SOFCG concept resulted in the generation of twenty-three optical comb lines with a frequency spacing of 11.84 GHz (defined by an electrical band pass filter in the optoelectronic loop). By filtering two comb lines and heterodyning in a photo-diode, a mm-wave signal at 94.8 GHz was experimentally generated and indeed signals up to 260 GHz could be generated with a suitably high bandwidth photo-diode. In addition, the SOFCG reported here outperforms a conventional OFCG (driven by an external microwave source), providing a single sideband phase noise that is 27 dB better at an offset of 10 kHz. This highlights the potential of our contribution to its use in demanding applications such as those in mm-wave phase modulated RoF systems. The SOFCG was subsequently employed in a W-band radio-over-fibre link in which a 64 QAM LTE-Advanced signal transmitted over a 1.3 m wireless distance, with an error vector magnitude (EVM) less the EVM limit. This is the first experimental demonstration of an SOFCG for a RoF link at W-band (specifically 94 GHz), which is of interest in front hauling in 5G systems.
- In Chapter 6, a novel photonic technique for mm-wave and THz signal generation is demonstrated with an OFCG that is driven by a frequency tunable OEO. This work

was motivated by the fact that while the SOFCG described in Chapter 5 offers excellent phase noise performance and the capability of generating mm-wave signals, it does not offer frequency tunability. Frequency tunability would be a useful attribute for multi-carrier systems. This limitation can be obviated by reverting to a conventional OFCG topology, but then driving this with a tunable OEO instead of a conventional microwave synthesizer. By using a separate OEO, one can then employ a phase modulator instead of an intensity modulator, with the advantage that when combined with a tunable optical band pass filter, this acts both as a modulator and a tunable microwave photonic filter. Using this novel approach, signals at 101.5 GHz and 242.6 GHz are generated by selecting two comb lines originating from the comb generator and further beating in a high speed photodiode. This tunable THz generation technique is an attractive alternative to other techniques in that it is implemented with commercial off-the-shelf telecommunications industry components.

A radio over fibre link at 242.6 GHz is also implemented with a 16-QAM 6 Gbaud/s modulating signal resulting in a throughput of 24 Gbps. The obtained bit error rate was below the forward error correction (FEC) limit. The latter part of Chapter 6 then focuses on the modified version of an OEO where the key novelty is the addition of an optoelectronic infinite impulse response (IIR) filter inside the OEO loop to further enhance the Q factor of the filter section with a view to obtaining spur free RF oscillation. Cascading of these two microwave photonic filters enhances the OEO loop Q factor and thus helps to suppress the side modes by an additional 12 dB, subsequently reducing the close to carrier phase noise by an additional 20 dB in the generated microwave signal. The experimental work described in Chapter 6 was carried out at University College London (UCL) during a secondment.

- Finally, Chapter 7 summarises the findings and overall conclusions of the thesis, and suggestions for future work are outlined. Specifically, three new areas of research are proposed: (i) multicore fibre based mm-wave generation, radio-over- fibre, and power-over-fibre (ii) W-band optoelectronic oscillators and (iii) an integrated microwave photonics implementation of a self-oscillating comb generator.

1.5 List of published papers

The following papers were published during the course of the research carried out for this thesis, and relate to the material in Chapters 4,5 and 6 in addition to Appendix A.

Journal papers:

[1] **G. K. M. Hasanuzzaman**, A. Kanno, P. T. Dat and S. Iezekiel, "Self-Oscillating Optical Frequency Comb: Application to Low Phase Noise Millimeter Wave Generation and Radio-Over-Fiber Link," in Journal of Lightwave Technology, vol. 36, no. 19, pp. 4535-4542, Oct.1, 2018.

[2] **G. K. M Hasanuzzaman**, S. Iezekiel, C. Markos and M. Habib, "Hollow-core fiber with nested anti-resonant tubes for low-loss THz guidance", Optics Communications, vol. 426, pp. 477-482, 2018.

[3] G. Charalambous, **G. K. M. Hasanuzzaman**, A. Perentos, and S. Iezekiel, "High-Q wavelength division multiplexed optoelectronic oscillator based on a cascaded multi-loop topology," Optics Communications, vol. 387, pp. 361–365, 2017.

Conference papers:

[1] **G. K. M. Hasanuzzaman**, Haymen Shams, Cyril C. Renaud, John Mitchell and Stavros Iezekiel “Photonic THz Generation Using Optoelectronic Oscillator driven Optical Frequency Comb Generator” 2018 International Topical Meeting on Microwave Photonics (MWP), 22-25, Oct., 2018, Toulouse, France.

[2] **G. K. M. Hasanuzzaman** and S. Iezekiel, “Multi-core Fiber Based Mm-Wave Generation, Radio-over- Fiber, and Power-over-Fiber”, 11th International Symposium on Communication Systems, Networks, and Digital Signal Processing, CSNDSP 2018, 18-20, July, 2018, Budapest.

[3] Atsushi Kanno, **G. K. M. Hasanuzzaman**, Naokatsu Yamamoto, Stavros Iezekiel, "Optical frequency comb applied optoelectronic oscillator for millimeter-wave signal generation and its application," Proc. SPIE 10634, Passive and Active Millimeter-Wave Imaging XXI, 106340E,8 May,2018,2018, Orlando, Florida, United States.

[4] **G. K. M. Hasanuzzaman**, A. Kanno, P. T. Dat, and S. Iezekiel, "W-band Radio-over-fiber Link Based on Self-oscillating Optical Frequency Comb Generator," in Optical Fiber Communication Conference, OSA Technical Digest, Optical Society of America, paper no. W1F.6, Mar., 2018, San Diego, California, USA.

[5] **G.K.M. Hasanuzzaman**, S. Spolitis, T. Salgals, J. Braunfelds, A. Morales, L.E. Gonzalez, S. Rommel, R. Puerta, P. Asensio, V. Bobrovs, S. Iezekiel and I. Tafur Monroy" Performance Enhancement of Multi-Core Fiber Transmission Using Real-Time FPGA Based Pre-Emphasis" in OSA Asia Communications and Photonics Conference, paper M2H.1, 10–13 Nov. 2017, Guangzhou, China.

[6] G. Charalambous, **G.K.M. Hasanuzzaman**, A. Perentos and S. Iezekiel, "Optoelectronic Recirculating Delay Line Implementation of a High-Q Optoelectronic Oscillator" in International Tropical meeting on Microwave Photonics 2017, 23-26 Oct. 2017, Beijing China.

[7] **G. K. M. Hasanuzzaman** and S. Iezekiel, "Self-oscillating optical comb generator based on optoelectronic oscillator," in SPIE 10103, Terahertz, RF, Millimeter, and Submillimeter-Wave Technology and Applications X, Vol. 10103, p. 1010320, 24 February 2017, San Francisco, California, USA.

[8] G. Charalambous, **G. K. M. Hasanuzzaman**, A. Perentos, and S. Iezekiel, "Ultra-high-Q Optoelectronic Oscillator based on Bilaterally Coupled Loops," in 2016 IEEE International Topical Meeting on Microwave Photonics (MWP), 31 Oct.-3 Nov. 2016, Long Beach, CA, USA.

[9] G. Charalambous, **G. K. M. Hasanuzzaman**, A. Perentos, and S. Iezekiel, "Optoelectronic oscillator based on class AB photonic link," in 2016 18th International Conference on Transparent Optical Networks (ICTON), 10-14 July 2016, Trento, Italy.

CHAPTER 2

State-of-the-Art of Fibre Wireless Links

2.1 Introduction

This chapter covers the state-of-the-art of fibre wireless links operating at or above 100 GHz. In addition to considerations of modulation and signal processing techniques, and transmitter and receiver architectures, the free space channel is also studied, with an emphasis on the contributions to path loss arising from precipitation. A brief introduction to phase noise and its effect on phase modulated systems is also discussed.

2.2 State-of-the-art of THz links and sub systems

To deal with the high data rates required by modern wireless smart devices, the use of terahertz waves has been considered. However, compared with fibre-optic communication or radio communications (<40 GHz carrier frequency), THz communications is still in its infancy. A number of studies have been reported on THz signal generation (both electronic and photonic approaches), detection (coherent and incoherent), processing and transmission using both SISO and MIMO techniques. In addition, several photonic wireless/ wireless transmission systems in the THz band have been demonstrated and some of the most notable of these are summarized in Table 2.1.

The transmission window between 200 and 300 GHz has attracted strong interest due to low atmospheric transmission losses. It has been shown that multichannel THz links with

moderately higher spectral efficiency such as QPSK, 8 QAM, and 16 QAM increase the overall transmission capacity and reduce the bandwidth requirement for electronic devices. Data rates of up to 100 Gbps have been achieved in a multi-channel THz system at 237.5 GHz by using different modulation formats for each channel and a monolithic microwave integrated circuit (MMIC) receiver [22] at the Karlsruhe Institute of Technology. A mode locked laser based comb generator was used with a programmable optical filter and a UTC-PD to generate a multicarrier signal, with the reported SISO system consisting of three channels operated at Ch1=225 GHz, Ch2=237.5 GHz, and Ch3=250 GHz. The system provides an aggregate 100 Gbps wireless transmission over 20 m distance where Ch2 and Ch3 each carry an 8 Gbaud 8 QAM signal and Ch1 carries a 13 Gbaud 16 QAM signal. Multi-channel THz links have also been demonstrated at UCL; in 2014, Shams *et al.* [23] reported a three channel THz link at 200 GHz where each channel was modulated with 12.5 Gbd QPSK giving a total speed of 75 Gbps over 40 km fibre and 2 cm wireless transmission. The optical carriers were generated using a single MZM with an optical carrier suppression (OCS) technique. A 100 Gbps THz link operating at 200 GHz has also been demonstrated by the same group [34]. In this case four optical subcarriers were used where each carrier was modulated with a 12.5 Gbaud QPSK signal; a gain switched laser source was used to generate the optical sub-carriers.

Multiband transmission schemes where channels are operated in different frequency bands is an interesting approach for improving data rates without increasing the bandwidth requirement for drive electronics and electro-optic devices. The generation and transmission of multiband signals have been demonstrated at 60 GHz and in the 75-110 GHz band. Recently a five band radio over fibre link at 200 GHz to 280 GHz (200 GHz, 235 GHz, 250 GHz, 265 GHz and 280 GHz) was demonstrated in [35]. The reported link provides 100 Gbps (20 Gbps in each band) data rates using a 10 Gbaud QPSK modulation format with Nyquist bandwidth. An optical frequency comb generator based on an MZM was employed to generate optical phase related tones spaced by 15 GHz. A multiband system at 90 GHz and 300 GHz has been demonstrated by Kanno *et al.* [11], while a capacity record of 400 Gbps was demonstrated using multiband transmission at 37.5 GHz and 100 GHz with polarization division multiplexing and a MIMO system [36].

Table 2.1: Summary of wireless communication ≥ 100 GHz. UTC-PD: Uni-travelling carrier photodiode, PDM: polarization division multiplexing, QPSK: Quadrature phase shift keying, MIMO: Multiple input multiple output, SISO: Single input single output, QAM: Quadrature amplitude modulation, SHM: sub-harmonic mixing, DSP: digital signal processing, MZM: Mach-Zehnder modulator, WSS: wavelength selective switch, MMIC: Monolithic microwave integrated circuit.

Frequency (GHz) (Year),Affiliation	Technology		Modulation format	Data rate and BER	Fibre length	Wireless length	Single carrier /Multi-carrier	FEC/(SISO/ MIMO)	Ref.
	Tx	Rx							
100 (2012) FUS (China)	PD+heterodyne(ECL)+ horn antenna(25dBi)	Horn antenna(25dBi)+ SHM+offline DSP	PDM+QPSK	108 Gbps BER=3.8×10^{-3}	80 km	1 m	Single	2×2 MIMO	[37]
100 (2013) HUC (China)	Polarization sensitive heterodyne	Coherent	PDM+OFDM	30.67 Gbps	40 km	5 m	Single	2×2 MIMO	[38]
100, and 37.5 GHz (2013),FUS (China)	Optical heterodyne	SHM+offline DSP	PMD 16QAM (37.5 GHz)	400 Gbps	80 km	1.5 m at 37.5 GHz	Four channel (Two channel in each band)	2×2 MIMO	[36]
			PDM QPSK (100 GHz)			0.7 m at 100 GHz			
120 (2012) NTT Japan	UTC-PD	Envelope detector using Schottky barrier diodes(SBD)	ASK	10 Gbps	-	1 km	Single	SISO	[39]
146 (2012) UCL (UK)	Dual DFB +UTC-PD	SHM (Schottky)	OOK	1 Gbps	-	2.5 cm	Single	SISO	[31]
200 (2015) UCL (UK)	Gain switched comb+ WSS+UTC-PD+ Horn antenna(20dBi)	Horn antenna (20dBi)+SHM+ offline processing	QPSK (12.5 Gbuad)	100 Gbps	40km	2cm	Four subcarriers	SISO	[23]
200 (2014) UCL (UK)	MZM Comb+ WSS+UTC-PD+ horn antenna(20dBi)	Horn antenna (20dBi)+SHM+ offline DSP	QPSK (12.5 Gbuad)	75 Gbps	40km	2cm	Three subcarriers	SISO	[34]
220-280 (2015) UCL (UK)	MZM Comb+optical heterodyne receiver + horn antenna(20dBi)	Horn antenna(20dBi)+ SHM+offline DSP	Each channel 10 Gbaud QPSK	100 Gbps (20 Gbps in each band),BER>10^{-3}	10km	-	5band,(220,235, 250,265,280GHz)	SISO	[35]
237.5 (2013) KIT (Germany)	MLL comb+WS+ UTC-PD+Canonical horn antenna(22.1dBi)+lens	Canonical horn antenna+MMIC+sub harmonic mixer	Ch1=16QAM,(52Gbps) Ch2=8QAM,(24Gbps) Ch2=8QAM,(24Gbps)	100 Gbps BER=3×10^{-3} At PRx=-30dBm	-	20m	Three subcarriers	7%, SISO	[22]

2.3 Phase noise

Although both oscillators and frequency combs are specified with respect to several parameters (e.g. output power, tuning range, thermal stability), in modern communications and radar applications, phase noise performance is critical. Phase noise is commonly used to measure the frequency stability of an oscillator. It is the result of small random fluctuations of the phase of an electrical signal. An ideal oscillator will deliver a signal

$$v(t) = V_0 \cos(\omega_0 t + \phi), \tag{2.1}$$

where V_0 is the peak amplitude, $\omega_0 = 2\pi f_0$ is the angular frequency and ϕ is the constant phase. However, a real life oscillator signal fluctuates in amplitude and phase which can be represented by:

$$v(t) = V_0[1 + \alpha(t)]\cos(\omega_0 t + \phi(t)), \tag{2.2}$$

where $\alpha(t)$ is the amplitude fluctuation and $\phi(t)$ is the phase fluctuation. In early work [40], phase noise was defined using the following equation:

$$L(f) = \frac{\text{Single sideband noise power in 1 Hz bandwidth}}{\text{carrier power}}. \tag{2.3}$$

However, this definition has been abandoned because it cannot differentiate between amplitude noise (AM) and phase-modulated (PM) noise [41]. The current definition of phase noise is instead represented by:

$$\begin{aligned} L(f) &= \frac{1}{2} S_\phi(f) \\ &= 10 \times \log_{10}[S_\phi(f) - 3\text{dB}] \quad [\text{in dBc/Hz}] \end{aligned} \tag{2.4}$$

where $S_\phi(f)$ is defined as the one-sided power spectral density of random phase fluctuation $\phi(t)$. The unit of phase noise dBc/Hz in Eq. 2.4 means "dB below the carrier in a 1 Hz bandwidth".

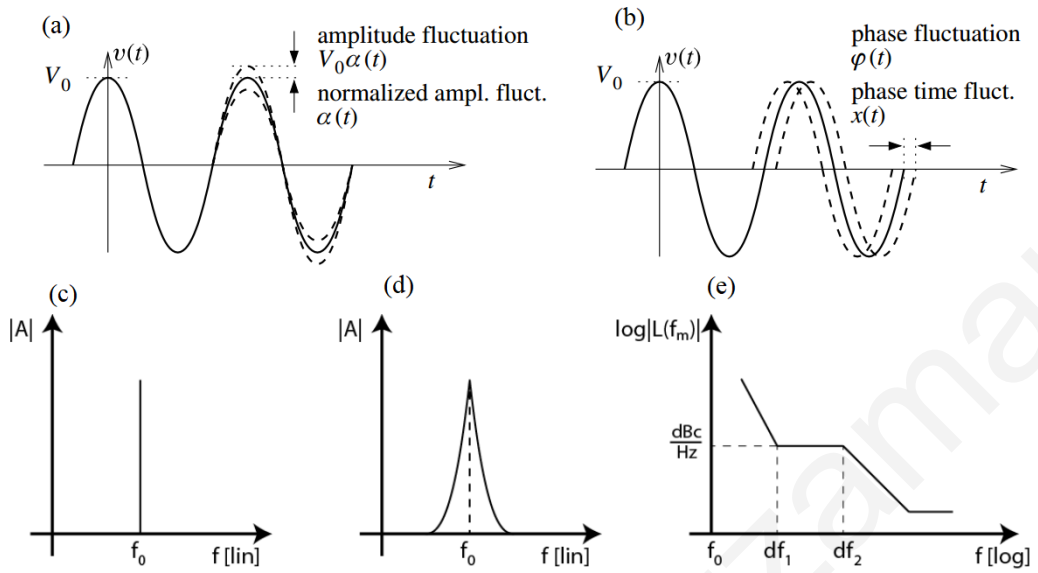

Fig. 2.1. (a) Amplitude noise (b) Phase noise (c) Oscillator without phase noise (d) Oscillator with phase noise (e) Typical phase noise profile.

2.3.1 Effect of oscillator phase noise on system performance

The RF oscillator phase noise plays a key role in the performance of different microwave and microwave photonic sub-systems. In this section, the effect of oscillator phase noise on the performance of several sub-systems is discussed.

A. Radar

The noise of the carrier plays an important role in the performance of radar. In a moving target indicator (MTI) Doppler radar, the velocity of the target is determined by mixing the transmitted carrier with the received reflected signal and monitoring the small shifted frequency beat (Doppler shift) as shown in Fig. 2.2. The Doppler shift (f_d) can be calculated from the following relationship

$$f_d = \frac{2}{c} f_0 \upsilon \tag{2.5}$$

where f_0 is the frequency of operation, and υ is the velocity of a moving target. The Doppler frequency shift of a MTI radar operating at 10 GHz (X-band) for various target speeds is listed in Table 2.2. For slow moving objects, the offset between the transmitted and received signals is very small. Since the phase noise of the transmitted signal close to the carrier is high, the target may end up being hidden by the phase noise of the carrier. Therefore, the probability of detection could be challenging.

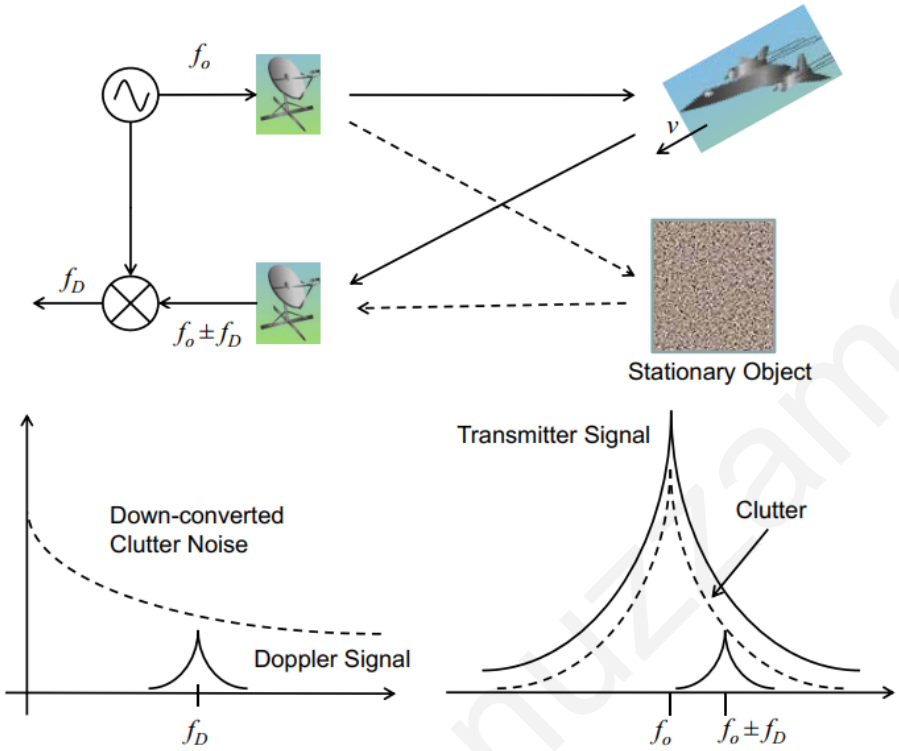

Fig. 2.2. A simplified Doppler shift radar system demonstrating the effects of phase noise on the down converted Doppler shift. The reflected signal will be extremely low power and can be buried under unwanted signal, clutter,or phase noise due to either the transmitter power amplifier or the receiver local oscillator. After [42].

By way of example, Fig. 2.3 shows the effect of phase noise on detection probability. For a 90% detection probability of a coherent radar operating at 10 GHz, the phase noise

Table 2.2: Doppler frequency shift (Hz) versus target speed (mph) at 10 GHz

Speed (mph)	Reflected frequency (Hz)
1	30
10	298
20	596
30	894
50	1490
100	2980
300	8940

requirement is -130 dBc/Hz for a 10 MHz oscillator to detect a target moving at 4 km/h. The probability of detection drops to 45% when the phase noise is degraded by 5 dB.

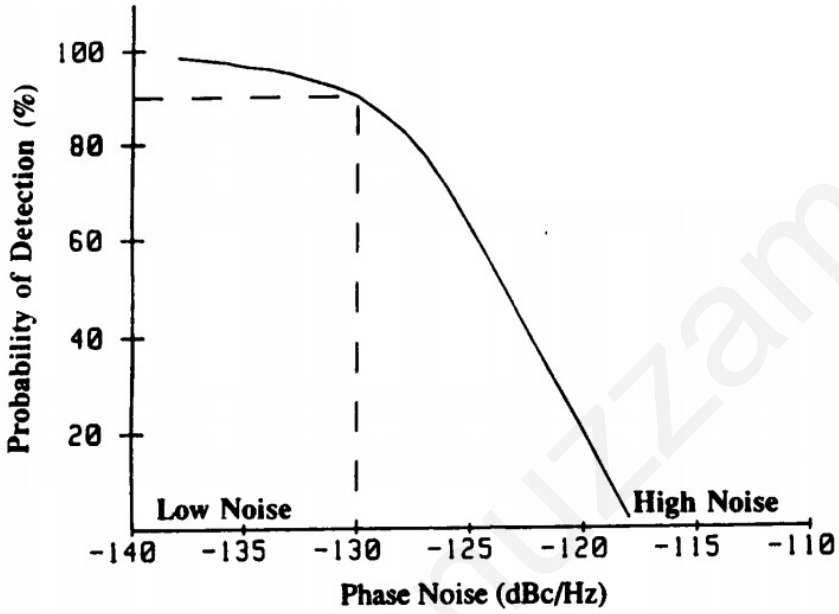

Fig. 2.3. Coherent radar probability of detection as a function of reference oscillator phase noise. After [43].

B. Phase modulated systems

In a phase modulated system such as quadrature phase shift keying (QPSK) or m-quadrature amplitude modulation (m-QAM), the IQ position of the demodulated signal on the constellation diagram depends on the amplitude and phase information. The amplitude noise affects the distance from the origin while the phase noise has an impact on the angular position of the constellation point as shown in Fig. 2.4. As a result, the bit error rate (BER) or the error vector magnitude (EVM) depends on the local oscillator phase noise. The relationship between the LO phase error and EVM can be evaluated by the following equation [44] and is illustrated in Fig. 2.5:

$$EVM = \sqrt{\frac{1}{SNR} + 2 - 2e^{-\frac{\phi_{rms}^2}{2}}} \tag{2.6}$$

where ϕ_{rms} is the LO rms phase error. The EVM increases with the increment of the phase error.

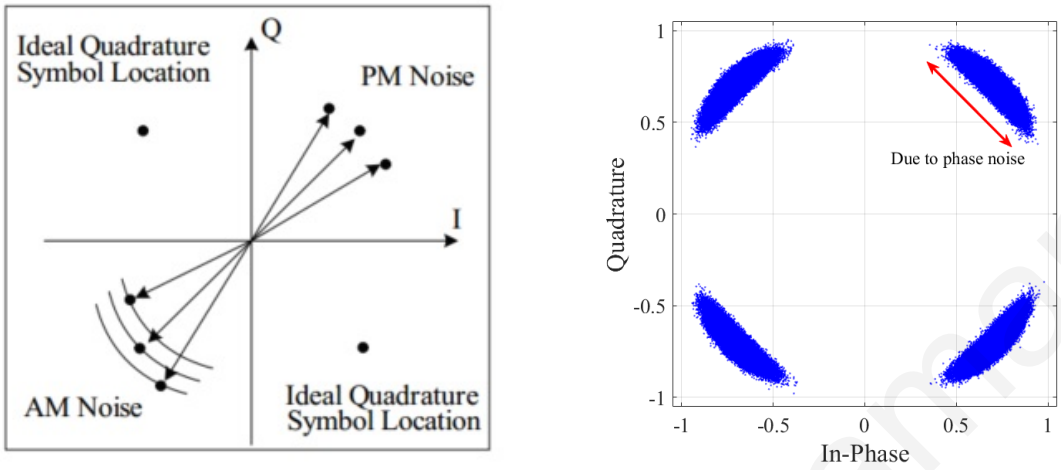

(a) **(b)**

Fig. 2.4. The effect of phase noise on EVM. After [42].

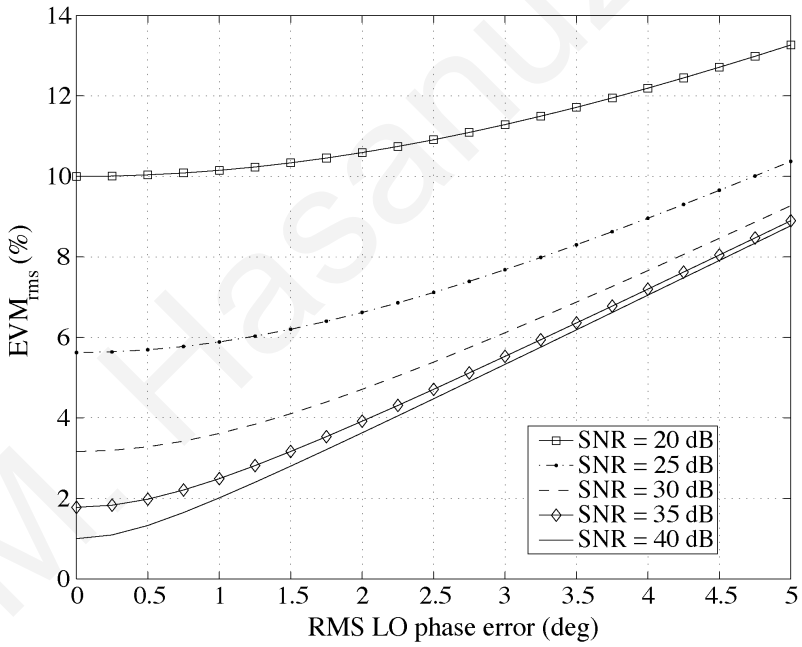

Fig. 2.5. EVM variation with LO phase error. After [44].

2.3.2 When is the phase noise important?

In the above mentioned applications, phase noise is important. However, at what offset frequency from the carrier it is significant varies from one application to another. To illustrate this point, twelve phase noise profiles in four groups have been considered as listed in Table 2.3 and depicted in Fig. 2.6. Within each group, the phase noise of a specific offset frequency is changed while keeping the remaining part of the profile the same. The phase error of each

Table 2.3: Different phase noise profiles to illustrate the effect of phase noise on phase error.

Profile	Phase noise (at an offset frequency in Hz)								Phase
name	100	1 k	10 k	100 k	1 M	10 M	100 M	1 G	error
A1	-40	-80	-100	-110	-115	-120	-125	-125	4.922
A2	-50	-80	-100	-110	-115	-120	-125	-125	2.366
A3	-60	-80	-100	-110	-115	-120	-125	-125	1.713
B1	-50	-80	-100	-110	-115	-120	-125	-125	2.366
B2	-50	-85	-100	-110	-115	-120	-125	-125	2.22
B3	-50	-90	-100	-110	-115	-120	-125	-125	2.11
C1	-50	-80	-95	-110	-115	-120	-125	-125	2.375
C2	-50	-80	-100	-110	-115	-120	-125	-125	2.366
C3	-50	-80	-105	-110	-115	-120	-125	-125	2.361
D1	-50	-80	-100	-105	-115	-120	-125	-125	2.375
D2	-50	-80	-100	-110	-115	-120	-125	-125	2.366
D3	-50	-80	-100	-115	-115	-120	-125	-125	2.362

profile has been calculated with the method described in [45].

From Table 2.3 it is seen that the close to carrier phase noise (up to 1 kHz offset) has the most significant effect on phase error and hence the EVM as illustrated in Fig. 2.5. Finally, Fig. 2.7 shows some typical ranges of offset frequencies where phase noise is important for different applications [40].

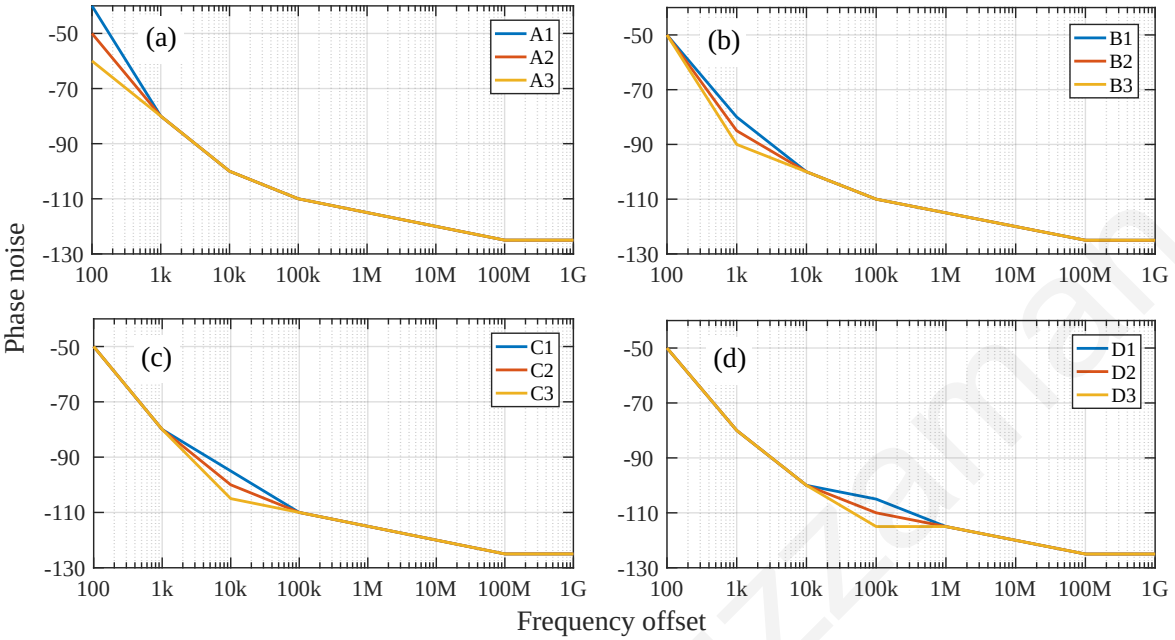

Fig. 2.6. Phase noise profile listed in Table 2.3 (a) Group A (b) Group B (c) Group C (d) Group D.

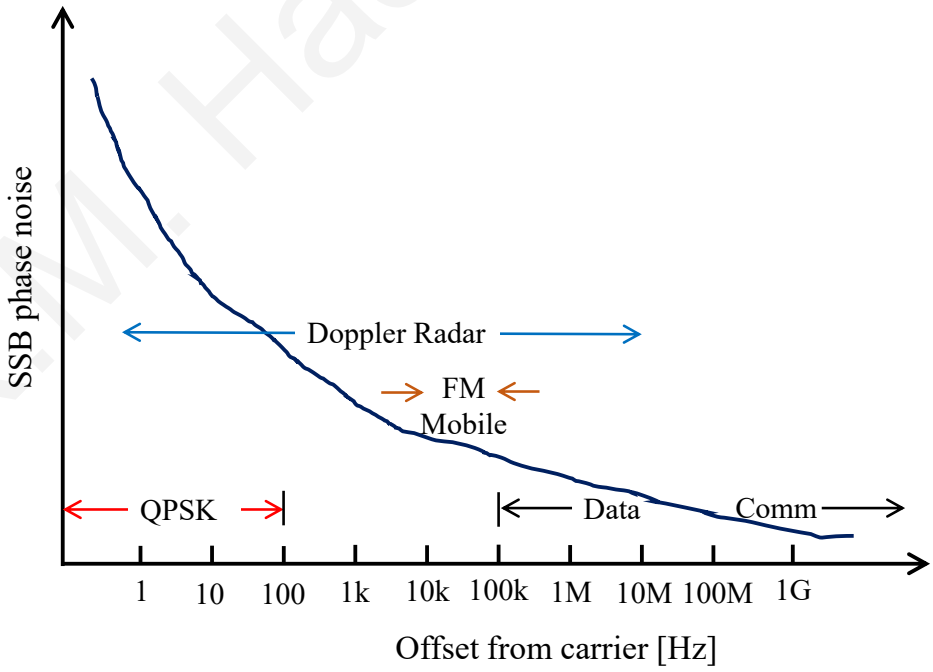

Fig. 2.7. Typical ranges of offset frequencies where phase noise is important for different applications. The figure is reproduced from [40].

2.4 Guiding of mm-waves and THz waves in free space

THz waves are attractive for wireless communication because they offer huge bandwidth which is essential for increasing data capacity. However, this comes at a disadvantage: large signal loss. The attenuation in the atmosphere at frequencies above 100 GHz is much higher than that in the microwave frequency band and the large attenuation not only limits service coverage but also degrades the signal to noise ratio of the system which influences data capacity as well. The performance of any wireless system is affected by the physical characteristics of the transmission media (the channel) itself. Three main contributors can be identified for computing the total path loss: the free-space path loss, the atmospheric gaseous attenuation and attenuation induced by rain fall. Fog and cloud also contribute to the path loss. The THz band is very frequency selective and we therefore have to indentify suitable transmission windows [46].

2.4.1 Free space path loss

Even without any additional attenuation in the wireless transmission path of the wave, the received power is much lower than the transmitted power. The difference between transmitted power and received power in wireless transmission is termed the free space path loss or spreading loss. The spreading loss accounts for the attenuation due to the expansion of the wave as it propagates through the medium. In a wireless link with fixed antenna effective area, as the transmission distance increases the power is transmitted in a wide area which increases quadratically with the distance. The free-space path loss can be estimated from the Friis formula [47]:

$$L_{FSdB/Km} = 32.4 + 20\log_{10}(f) + 20\log_{10}(d) - G_{TxdBi} - G_{RxdBi} \tag{2.7}$$

where, f is the frequency in MHz, d is distance between transmitter and receiver in km and G_{Tx} and G_{Rx} are the gains for the transmitter and receiver antenna in dBi. The Friis transmission equation is only applicable for distances exceeding the Fraunhofer distance which can be calculated from:

$$d_f = \frac{2D^2}{\lambda} \tag{2.8}$$

where D is the largest dimension of the antenna and λ is the wavelength of the radio signal. Equation 2.7 shows that the received power is not only quadratically dependent on the dis-

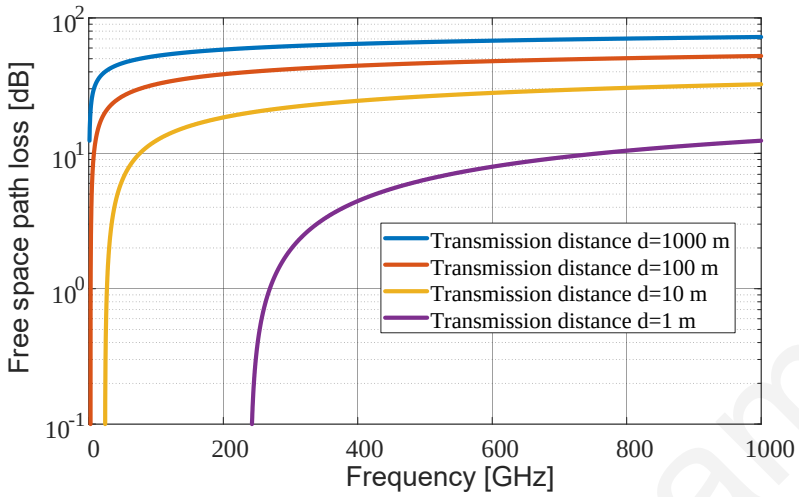

Fig. 2.8. Free space path loss as a function of frequency in four different transmission distances with antenna gain of 40 dBi for the transmitting and receiving antenna.

tance but also on the frequency. The quadratic-dependency of the free space path loss is due to the reduction of the effective area of the antenna with rising frequency.

2.4.2 Attenuation due to rain

For THz waves the size of the rain droplets falls within the range of a wavelength and this will lead to Mie scattering of the electromagnetic waves. The specific attenuation due to rain not only depends on the amount of rainfall but also on the size of rain drops [48]. An important performance criterion for outdoor wireless communication is reliability of the link under varying weather conditions. An estimation of the rain attenuation is given by:

$$\gamma_R = kR^{\alpha} \tag{2.9}$$

where γ_R (dB/km) is the specific rain attenuation and R (mm/hour) is the rain rate parameter for determining the intensity of the rainfall. The coefficients k and α are frequency dependent; a set of values of k and α is given in the ITU Recommendation P.838-3 [48]. Rain types are separated as 'drizzle: 0.25 mm/hour' 'light rain: 2.5 mm/hour', 'heavy rain: 0.25 mm/hour' and 'tropical rain: 100 mm/hour' [48]. An analytical result of the attenuation due to rain based on the ITU Recommendation P.838-3 is shown Fig. 2.9, where it is seen that tropical rain has a very serious impact compared to drizzle and light rain.

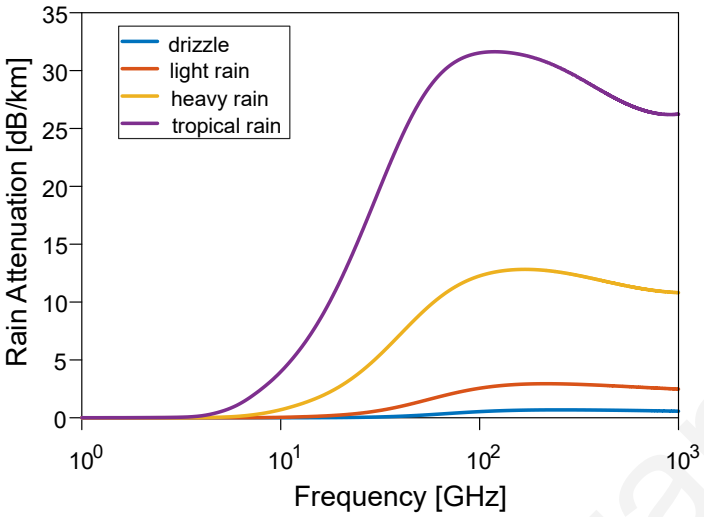

Fig. 2.9. Rainfall attenuation as a function of frequency.

2.4.3 Attenuation due to fog

For clouds or fog consisting of small droplets with diameters less than 0.01 cm electromagnetic waves in the THz band can be scattered by the small fog droplets which leads to attenuation. A mathematical model based on Rayleigh scattering has been developed by the ITU and published as Recommendation ITU-R P.840-6 [49]. Frequency dependence of attenuation for medium fog which is equivalent to water vapour density of $0.05\text{g}/\text{m}^3$ and thick fog which is equivalent to water vapour density of $0.5\text{g}/\text{m}^3$ is shown in Fig. 2.10.

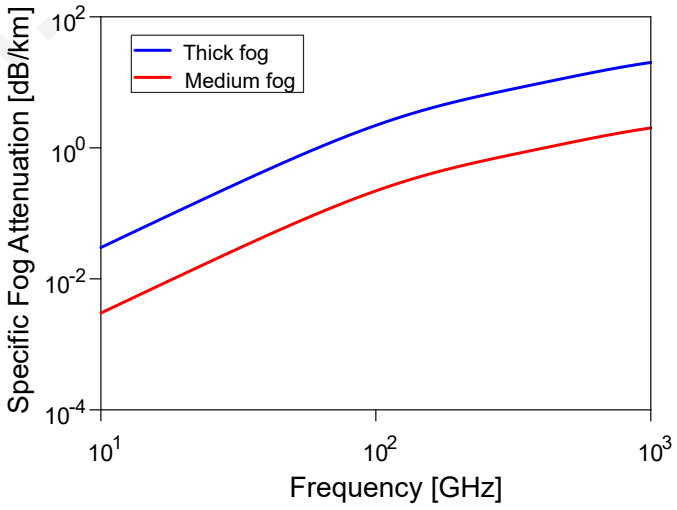

Fig. 2.10. Attenuation of electromagnetic waves by medium fog (water vapour density of $0.05\text{g}/\text{m}^3$) and thick fog (water vapour density of $0.5\text{g}/\text{m}^3$) at a temperature of 15^0C.

2.4.4 Attenuation due to the atmosphere

While propagating through the atmosphere, an electromagnetic wave is attenuated by molecular absorption. The amount of attenuation depends on the frequency difference between the electromagnetic wave and the resonance of the molecules. If the frequency of the wave coincides with the resonance frequency, the attenuation becomes a relative maximum [47, 50]. However, higher harmonics, sum or difference frequencies can also lead to an increase of attenuation. Figure 2.11 shows the dependency of atmospheric attenuation on frequency for an air pressure of 1013 hPa, a temperature of 15^0C and a water vapour density of 7.5 g/m^3). Figure 2.11 has been developed on the basis of ITU Recommendation ITU-R P.676-10 [51]. The atmospheric attenuation is strongly affected at specific frequencies such as 60 GHz, 120 GHz, 183 GHz, 335 GHz, 375 GHz, 443 GHz, 557GHz, and 752 GHz [47]. Table 2.4 shows the possible transmission windows available below 1 THz for fixed wireless links. In Chapter 5 we describe development of radio-over-fibre systems operating in Window I, while in Chapter 6 we consider a radio-over-fibre system demonstration for Window III.

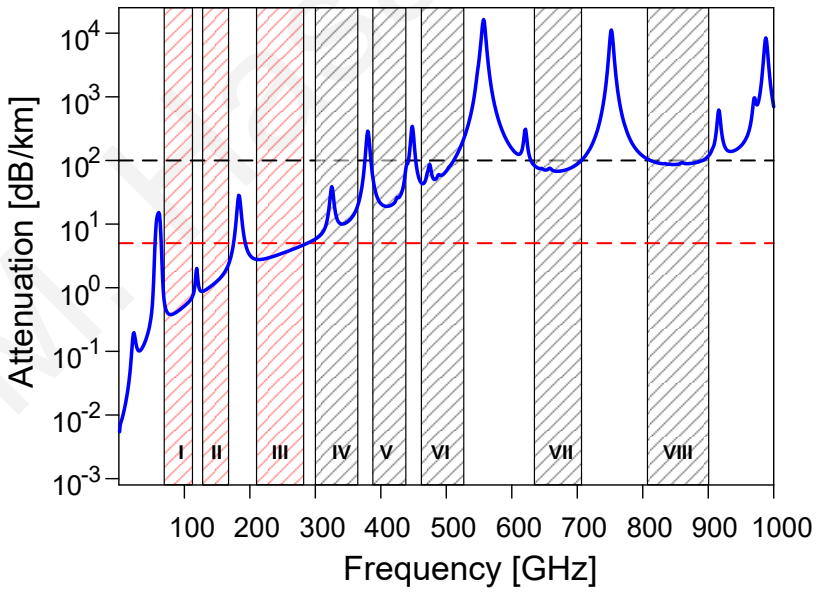

Fig. 2.11. Specific attenuation of the Earth's atmosphere at sea level in the frequency range 1 GHz to 1000 GHz for an air pressure of 1013 hPa, a temperature of 15^0C and a water vapour density of 7.5 g/m^3. The shaded regions describe the possible windows available.

Table 2.4: Possible transmission windows in mm-wave and THz band for the application of fixed wireless links.

	Window No.	Bandwidth [GHz]	Centre frequency [GHz]
Below 300 GHz	I	35	95
	II	30	150
	III	60	250
Above 300 GHz	IV	76	338
	V	58	414
	VI	62	484
	VII	85	669
	VIII	94	855

2.5 Conclusion

Various reported THz fibre wireless links have been compared and contrasted with respect to transmitter and receiver technology, modulation format, fibre and wireless distance, and the employment of single or multi-carrier transmission. In this respect, the following combination proves attractive: (i) the use of optical frequency combs for the generation of THz signals (with either a single or multiple carriers in a single transmission band or with multi-band transmission), (ii) higher spectral efficiency modulation formats such as 16 QAM, and (iii) the MIMO technique. These themes will be examined in detail in chapters 5 and chapter 6, in which we demonstrate how optoelectronic oscillators can be combined with optical frequency comb generators to provide low phase noise mm-wave and THz signals without any reference RF signal. In the next chapter, the operating principles of both the OEO and OFCG are discussed.

CHAPTER 3

Optoelectronic Oscillator and Optical Frequency Comb Generation

3.1 Introduction

In the first chapter, photonic-assisted methods for mm-wave and THz signal generation were described. In this chapter, two of the most useful techniques, namely the optoelectronic oscillator (OEO) and optical frequency comb generator (OFCG) are presented in more detail. The first part of this chapter covers the OEO including its principle of operation, side mode suppression techniques, and sources of noise and tunability, while different OFCG implementations are discussed in the latter part. Finally, the effect of dispersion induced power fading in microwave photonic links is discussed.

3.2 Optoelectronic oscillator

The OEO has attracted significant research interest in microwave photonics since its first implementation in 1996 due to its promising features, including highly pure oscillation, dual output capability (i.e. both microwave and microwave-modulated optical), tunability, and high-frequency operation [3]. These distinct features make an OEO attractive for many applications including low phase noise microwave and millimeter wave (mm-wave) generation [53], modern instrumentation [54], sensing [55], radar systems, and frequency down conversion [56]. A generic OEO consists of a hybrid optoelectronic loop as shown in Fig.

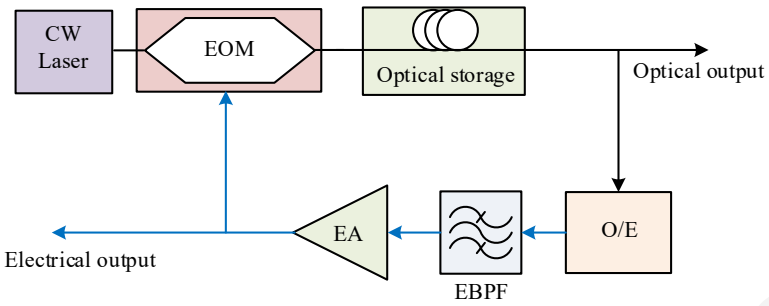

Fig. 3.1. Basic structure of single-loop OEO. The black lines represent the optical path while the blue lines represent the electrical path.

3.1 where self-sustained oscillation is obtained (under a small-signal approximation) from the Barkhausen criteria as shown in Fig. 3.2. The optical path includes a continuous wave (CW) light source, a modulator (phase or intensity), a photodetector, and an optical energy storage element, while the electrical path consists of a high Q bandpass filter and RF amplifier. Usage of high Q optical storage elements such as long lengths of optical fibre and the

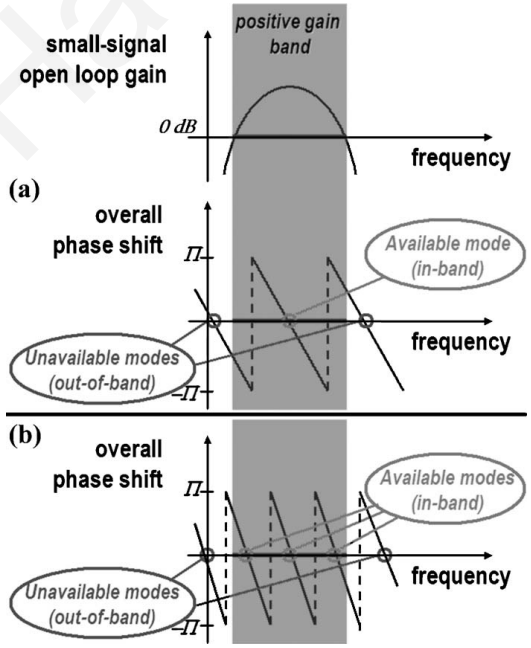

Fig. 3.2. Satisfaction of both amplitude and phase conditions for OEOs with (a) short delay length where only one mode satisfies the oscillation condition (b) long fibre length where multiple modes satisfy the oscillation condition. After [52].

recently introduced whispering gallery mode resonator (WGMR) [3,57] results in high spectral purity. In an OEO, the phase noise is independent of the oscillation frequency, whereas the Q factor of the optoelectronic loop determines the close to the carrier phase noise. The noise floor is determined by the shot noise of the photodetector [58].

3.2.1 Side mode suppression

The quality factor of an OEO depends on the time delay induced by the storage element (either a long single-mode optical fibre or resonator) in the optical part of the loop. The loaded quality factor of the oscillator can be calculated as follows:

$$Q = \frac{f_o}{\Delta f} = \frac{2\pi f_o \tau^2}{\delta} \tag{3.1}$$

where δ represents the signal-to-noise ratio measured after photodetection, τ is the total open-loop time delay of the oscillating loop, and Δf is measured at full width at half-maximum (FWHM). Examining the above formula, one sees that to obtain a high Q-factor, one may increase the length of the storage element (e.g.optical fibre). On the other hand, an OEO is inherently a multi-mode device where the mode spacing or free spectral range (FSR) is determined by the length of the cavity (L) with the relationship:

$$FSR = \frac{c}{nL}, \tag{3.2}$$

where n is the refractive index of the cavity. Using a long cavity results in enhancement of the Q factor, but makes the FSR too narrow and consequently it is difficult to suppress side modes. For example, a 1 km long fibre results in an FSR of approximately 200 kHz. In a classical OEO as shown in Fig. 3.1, an electrical bandpass filter (EBPF) is normally used to define the oscillation frequency. An EBPF is unable to select a single oscillating mode since its passband is much wider than the FSR of a long-cavity OEO. Therefore, the oscillation consists of several side modes as illustrated in Fig. 3.3. However, in several applications, it is desirable to suppress the side modes and this may be achieved either through photonic or electronics based approaches. The main theme of all side mode suppression techniques is to increase the Q factor of the mode selector (filter).

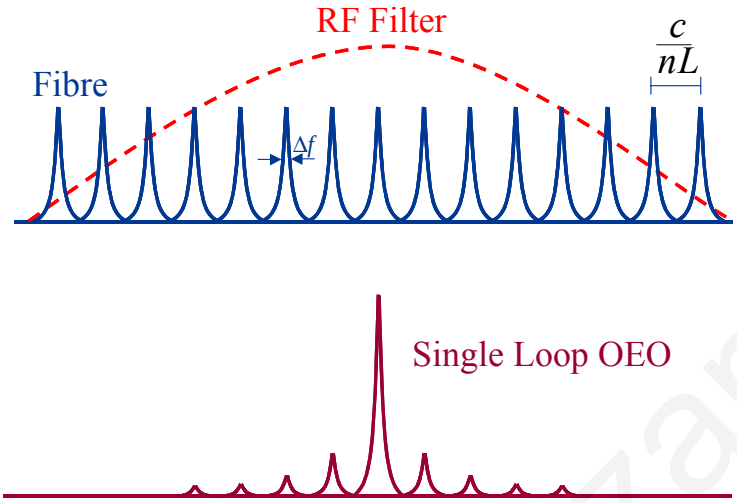

Fig. 3.3. Illustration of the mode selection and spurious level in a single loop OEO. The RF modes due to the long loop (top solid curve) are shown with the RF filter's frequency response (dashed curve) leading to the OEO oscillating spectrum at the bottom. After [59].

3.2.2 Photonics based approaches for side mode suppression

Two of the key photonics based methods for side mode suppression are the use of multi-loop topologies and high Q cavity optical filters. In the former, two or more loops of optical fibres of different lengths are employed, while in the latter a Fabry-Perot cavity or whispering gallery mode resonator (WGMR) is used to realise an optical filter. These techniques are described in more detail below, along with more recent methods based on the use of microwave photonic filters.

A. Multi-loop OEO configuration

The multi-loop configuration is the first and most widely used of the photonic techniques for side mode suppression, in which a single loop OEO topology is modified with the addition of one or more additional optical paths. A dual-loop OEO is shown in Fig. 3.4. Due to the filter-like behaviour of the multi-loop configuration, the amplitudes of the spurious modes are reduced [52]. In addition to the side mode suppression, the dual-loop configuration provides an additional advantage; reduction of the oscillation threshold condition by 6 dB which in turn reduces the gain requirement for oscillation [60]. In the dual loop OEO the mode spacing (FSR) is determined by the short loop and the phase noise is determined by

the long loop. However, the resultant Q of the combined loop is lower than that of the long loop.

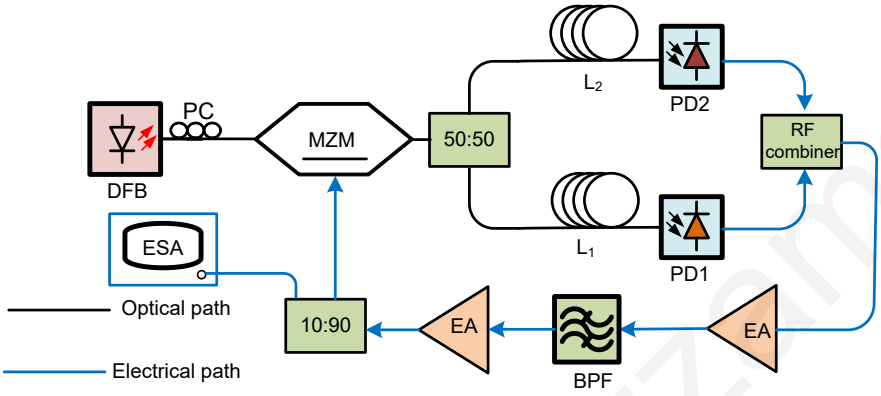

Fig. 3.4. Basic structure of dual-loop OEO.

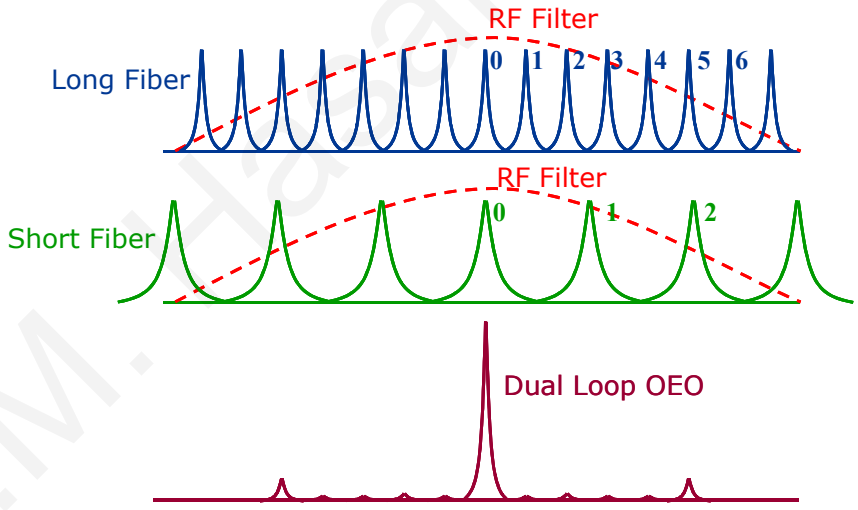

Fig. 3.5. Illustration of the mode selection and spurious level in a dual loop OEO. The RF modes due to the long fibre loop are shown with the filter magnitude transfer function (dashed curve) and the short fibre loop RF spectra. This leads to the OEO oscillating spectrum shown at the bottom. After [59].

B. High Q- optical filter

Although a multi-loop configuration is effective in reducing the level of unwanted side modes, it also reduces the overall Q factor. Generally, a dual-loop configuration provides

60-80 dB suppression of the first neighbouring side modes which is not enough for certain applications. To suppress the side modes without sacrificing the Q factor, a Fabry-Perot (FP) etalon with ultra-high finesse has been used as a mode selector instead of the conventioal RF filter. Fig. 3.6 shows the schematic structure and operating principle of a conventional RF filter based OEO and FP-etalon based OEO. Due to the higher Q factor and ultra low temperature dependency of the Fabry-Perot etalon, it provides less phase noise and higher stability as compared to the RF filter based OEO [61].

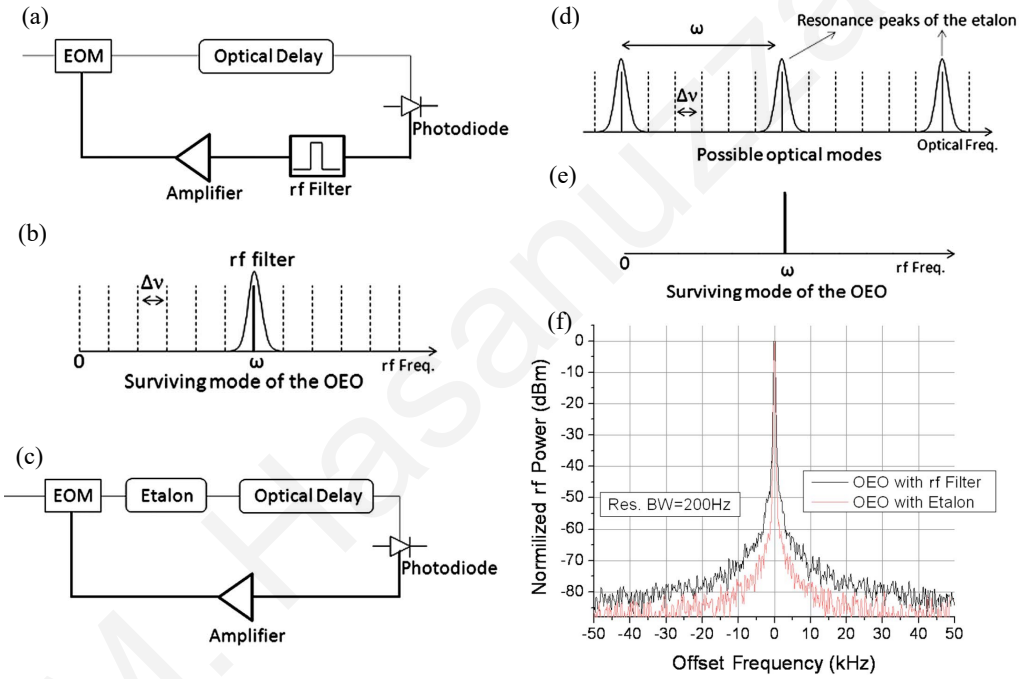

Fig. 3.6. (a) Block diagram of a standard OEO with RF filter, (b) Filtering of one of the RF modes ($\Delta\nu$ is the beat tone of the adjacent optical modes) by using an RF filter, (c) Fabry–Perot etalon based OEO scheme (d) Filtering of the optical modes with the etalon transmission function, (e) Beat tone of the optical modes that are separated by ω or the free spectral range (FSR) of the etalon, (f) Comparison of phase noise of the OEO with RF filter and with etalon (normalized power). After [61].

C. Cascaded microwave and microwave photonic filter

One promising approach to achieve both high selectivity and a high Q factor is to cascade a single passband RF filter with a periodic spectral response microwave photonic (MWP) filter. A MWP filter is a photonic sub-system that, when inserted between an RF modulator

and a photodetector, functions as an electrical filter. Cascading a single passband RF filter and an optoelectronic infinite impulse response (IIR) filter section has been used to suppress the side modes of an OEO by reducing the passband of the filter. The single passband section determines the centre frequency of oscillation and the IIR section provides the high Q filtering for side mode suppression. Such a topology was used in [62] with an electrical bandpass filter and an optoelectronic IIR section as shown in Fig. 3.7, yielding an OEO which exhibited a side mode suppression of 93 dB at an oscillation frequency of 29 GHz.

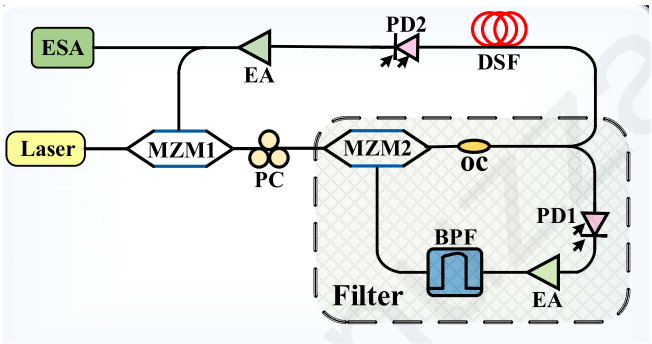

Fig. 3.7. Schematic diagram of an OEO employing an optoelectronic hybrid band-pass filter with ultra-high Q value at 29 GHz. MZM: Mach-Zehnder modulator. PC: polarization controller. DSF: dispersion shifted fibre. EA: electrical amplifier. BPF: band-pass filter. PD: photodetector. ESA: electrical spectrum analyzer. After [62].

D. Cascaded MWP filters

A side mode suppressed OEO may also be realised by using a cascade of two MWP filters, in which the first has a single passband while the second is based on an IIR transfer function. This approach permits frequency tunability since the centre frequency of the single-passband MWP filter can be tuned relatively easily. In [63] a tunable OEO incorporating a stimulated Brillouin scattering (SBS) based tunable single-passband MWP filter and an active recirculating delay lined based IIR filter was reported, and is shown in Fig. 3.8. The reported OEO provides a side mode suppression of 95 dB and a tuning range of DC to 40 GHz.

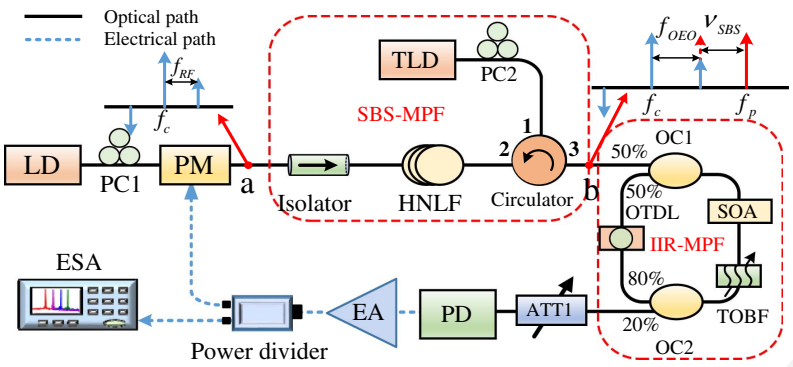

(a)

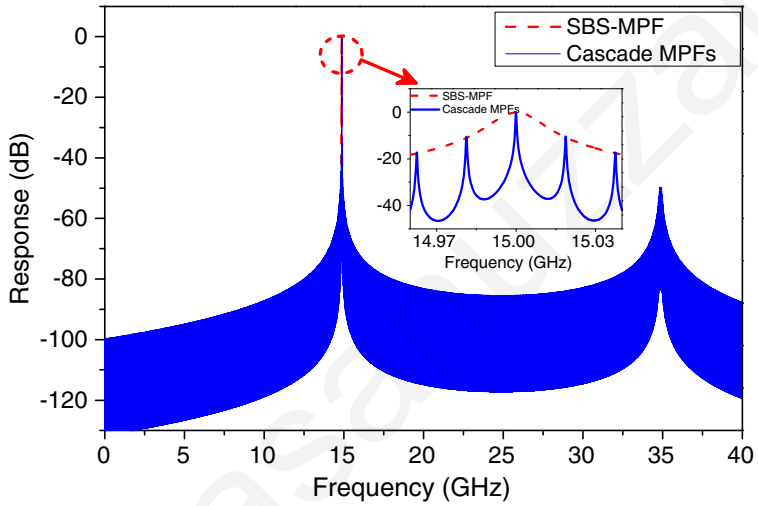

(b)

Fig. 3.8. (a) Cascaded MWP filter based OEO where the first stage is based on SBS while the second stage is based on all-optical IIR implementation. LD: laser diode; PC: polarization controller; PM: phase modulator; HNLF: highly nonlinear fibre; TLD: tunable laser diode; OC: optical coupler; SOA: semiconductor optical amplifier; TOBF: tunable optical bandpass filter; OTDL: optical tunable delay line; ATT: attenuator; PD: photodetector; EA: electrical amplifier; ESA: electrical spectrum analyzer. (b) Frequency response of the cascaded MWP filters. After [63].

3.2.3 Electronics based techniques for side mode suppression

A. Quality multiplier:

A quality multiplier (QM) is a positive feedback microwave loop that increases the selectivity and gain of the the related circuit. If a QM is combined with a broadband electrical filter, the bandwidth and the insertion loss of the filter decreases. Hence if an electrical filter with a QM is used in an OEO loop, the loop Q-factor will increase and the spurious modes will be suppressed [64]. A schematic diagram of a filter quality multiplier (FQM) and the effect of the QM on filter bandwidth are shown in Fig. 3.9a and Fig. 3.9b respectively. In [64], a single loop OEO with 15 km fibre length was demonstrated with a FQM at a 3 GHz operating frequency resulting in 120 dB side mode suppression, and -119 dBc/Hz single side band phase noise at 10 kHz offset.

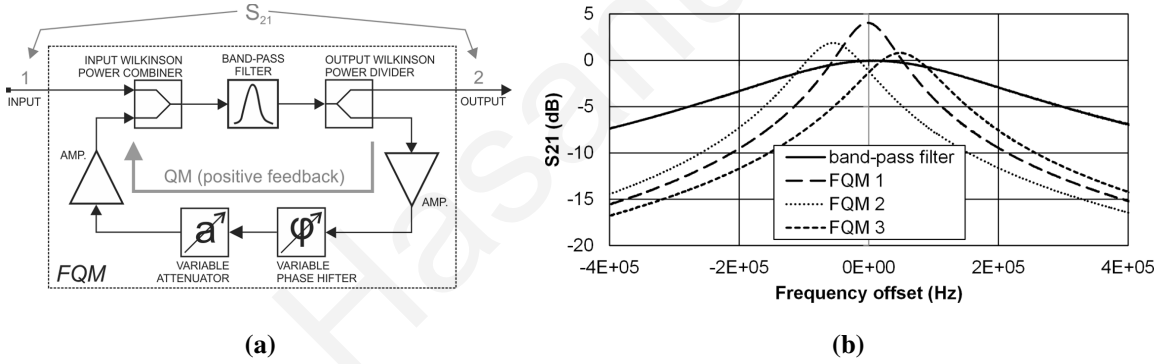

(a) **(b)**

Fig. 3.9. (a) Schematic diagram of a FQM. Two microwave amplifiers, a variable phase shifter and a variable attenuator represent the QM and the positive feedback to a bandpass filter. (b) Comparison of the bandpass filter's bandwidth with the FQM bandwidth (FQM 1). The bandwidth of the FQM is nine times narrower (40 kHz instead of 360 kHz). After [64].

B. Dual injection locked OEO

A dual optical loop OEO can add an additional 30 dB side-mode suppression as compared to a single loop OEO. However, the dual loop configuration sacrifices the high Q produced by the long fibre; the overall Q is averaged between the high Q and low Q provided by the long and short fibre length, respectively. An injection locked dual OEO has been reported [65,66] as shown in Fig. 3.10 to solve the problem of maintaining a high Q while eliminating side modes. In this configuration, a slave OEO (with short fibre length) is used to filter out the

multi-mode spurs of the high-Q master OEO. The RF output generated from a master OEO (single loop with long fibre length) was injected into a slave OEO (single loop with short fibre length) via an RF coupler. As a result of injection locking, the frequency and phase of the slave OEO was locked to the master OEO. The fibre length of the slave was selected in such a way that the first spurious mode falls outside the RF filter bandwidth resulting in single mode operation of the slave OEO. As a result, spurious free oscillation has been obtained as shown in Fig. 3.11 [65].

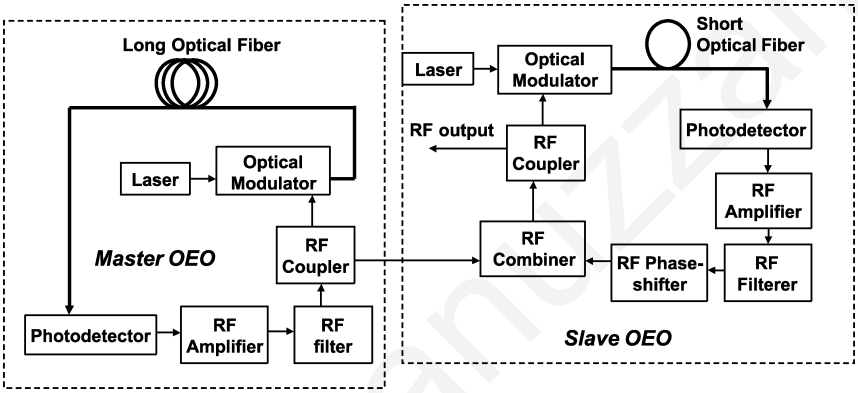

Fig. 3.10. Block diagram of an injection-locked dual OEO. After [65].

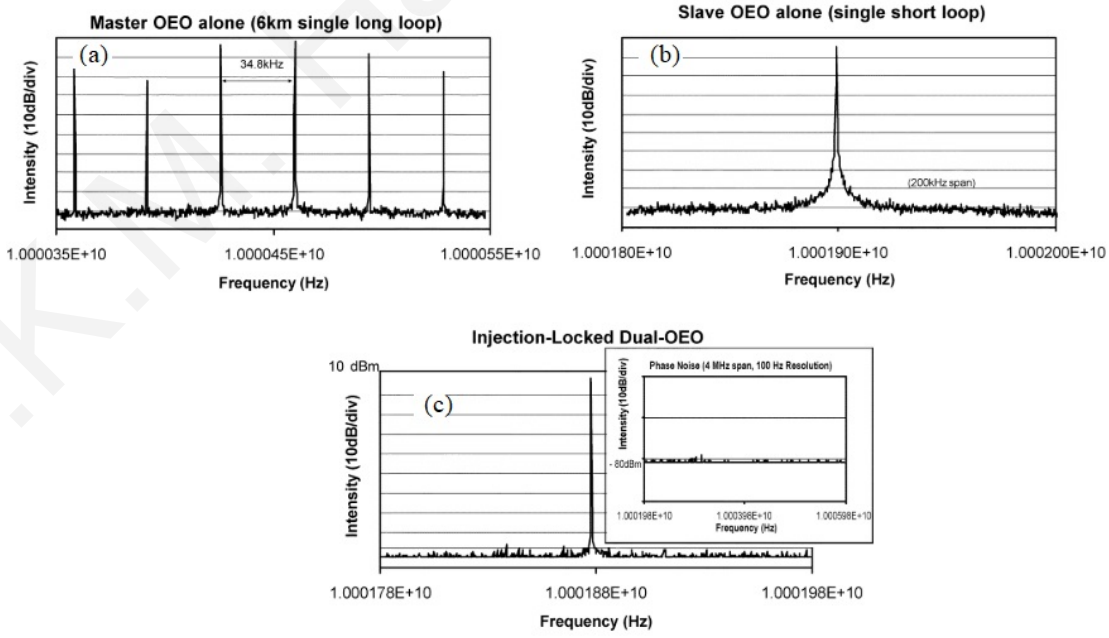

Fig. 3.11. RF spectrum for the: (a) master OEO alone, (b) slave OEO alone, and (c) injection-locked OEO. (Spectra (a)–(c) are taken with the same span, resolution, and reference level.) After [65].

C. Injection locking with low frequency

The dual injection locked technique described in the previous subsection requires two complete OEO loops oscillating at the same frequency which increases the cost of the whole system because two sets of optical and electrical components in the same band are required. Moreover, the stability of the system depends on both oscillating loops. In [67], an injection locking technique was reported where a low frequency external RF source is used to lock a high frequency OEO oscillation through higher order side-mode generation in a Fabry-Perot laser diode. The configuration consists of two subsections; the higher order mode generation unit and the OEO as shown in Fig. 3.12. A 20 GHz RF signal was generated with 65 dB side mode suppression as shown in Fig. 3.13; for injection locking, a 20^{th}-order harmonic was generated from a 1 GHz reference signal.

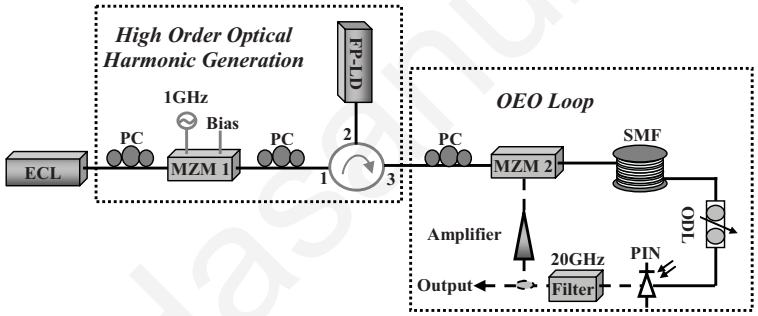

Fig. 3.12. Configuration of an injection-locked OEO where the injection signal is lower than the OEO oscillation frequency. After [67].

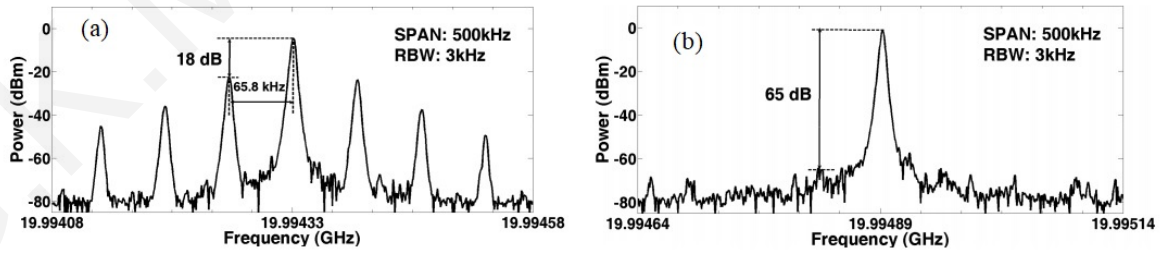

Fig. 3.13. RF spectra. (a) Free-running OEO. (b) Injection-locked OEO. After [67].

Finally, Table 3.1 shows a comparison of the OEOs discussed in this section for side mode suppression.

Table 3.1: Comparison of OEO topologies for side-mode suppression. HNLF: Highly nonlinear fibre, DSF: Dispersion shifted fibre.

OEO topology	Frequency	Number of fibre loops	Fibre length	SSB phase noise @ 10 kHz	Side mode suppression
Dual-loop OEO [68]	12 GHz	Dual	10 km/ 5.5 km	-109 dBc/Hz	60 dB
OEO with FP Etalon [69]	10.5 GHz	Single	2 km	-105 dBc/Hz	105 dB
OEO with cascaded RF and MWP filter [62]	29.99 GHz	Single	3 km DSF	-113 dBc/Hz	83 dB
OEO with cascaded MWP filters [63]	32.02 GHz	Single	1 km HNLF	-106 dBc/Hz	95 dB
OEO with FQM [64]	3 GHz	Single	15 km	-140 dBc/Hz	120 dB
Dual injection locked OEO [65]	10 GHz	Single	6 km/ 50 m	-150 dBc/Hz	140 dB
Injection locked OEO with low frequency RF signal [67]	20 GHz	Single	3 km	-110 dBc/Hz	65 dB

3.3 Sources of phase noise and mitigation techniques

OEOs have noise sources that originate in both the optical and electrical segments as shown in Fig. 3.14. The key noise sources that contribute to the overall phase noise include laser frequency and relative intensity noise (RIN), photodiode shot noise, thermal noise and flicker noise from the RF amplifier, and Rayleigh-scattering-induced amplitude noise in the optical storage element. Some noise sources (thermal, flicker, shot and laser frequency noise) contribute directly to the phase noise while others such as RIN and Rayleigh scattering are converted to phase noise through amplitude-to-phase noise conversion in the nonlinear devices in the OEO loop (e.g. the photodetector and RF amplifier). The dominant noise source at any frequency differs from system to system since it depends on the exact specifications of the various components present in the loop. The various types of noise sources and their mitigation techniques are described below.

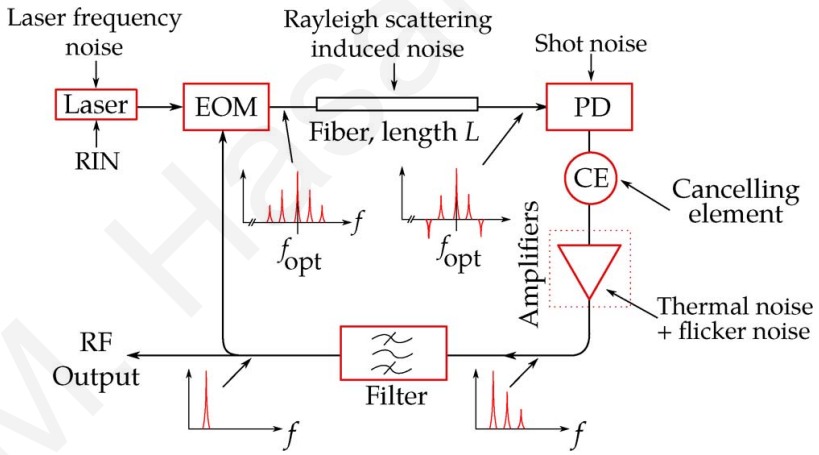

Fig. 3.14. Illustration of sources of noise in an OEO. After [70].

- Laser frequency noise: The laser frequency fluctuation is converted into microwave phase noise in an optoelectronic loop through the chromatic dispersion phenomenon [71], according to:

$$\delta\psi = 2\pi f_0 \lambda_0^2 D_\lambda \frac{L}{c} \delta\nu \tag{3.3}$$

where $\delta\psi$ is the phase fluctuation, f_0 is the microwave frequency (i.e. OEO oscillation frequency), λ_0 is the optical source wavelength, D_λ is the dispersion of fibre at λ_0, c is the velocity of the light, L is the fibre length, and $\delta\nu$ is the laser linewidth. The

corresponding phase noise power spectral density is given by:

$$S_{\phi,fopt}(f) = \chi^2 S_v(f) \tag{3.4}$$

where $S_v(f)$ is the power spectral density (PSD) of the laser frequency noise and

$$\chi = 2\pi f_0 \lambda_0^2 D_\lambda \frac{L}{c}. \tag{3.5}$$

Fig. 3.15 shows the phase noise of an OEO considering two different types of fibre; standard single mode fibre (SMF) and dispersion shifted fibre. The use of dispersion shifted fibre enables a 10 dB reduction of phase noise compared to the SMF when all other components remain unchanged. So significant improvement in phase noise can be obtained by using a more frequency stable laser, using (near) zero dispersion shifted fibre at the operating wavelength or operating the laser at the zero dispersion wavelength (near 1300 nm for standard fibre).

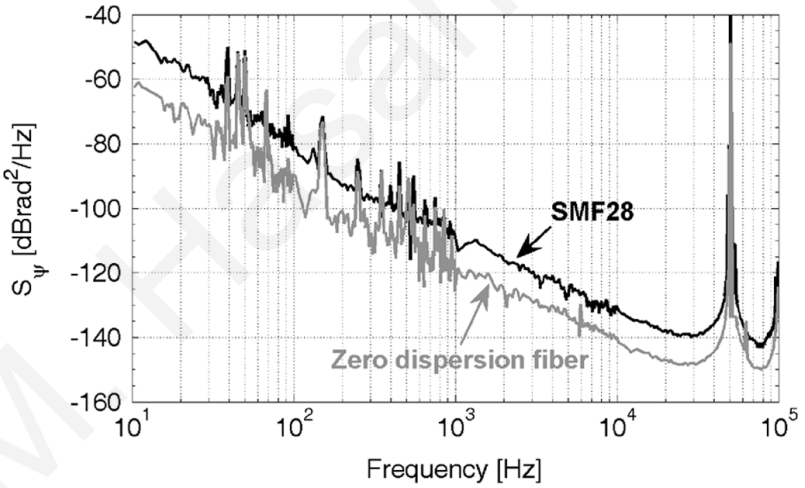

Fig. 3.15. Illustration of the effect of laser frequency noise on OEO phase noise. The laser frequency noise is converted to the OEO phase noise through the fibre dispersion. After [72].

- Fibre length dependent noise: According to the theoretical model of Yao and Maleki [3], the close to carrier phase noise of a fibre-based OEO decreases quadratically with the fibre length [3]. However, in practice, it does not follow exactly the model as illustrated in Fig. 3.16 [73]. For example the phase noise of the 6 km fibre is higher than the expected value which indicates that there should be one or more sources of noise induced by the fibre. Rayleigh scattering and stimulated Brillouin scattering are the two fibre length dependent sources of noise in a microwave photonic link and also

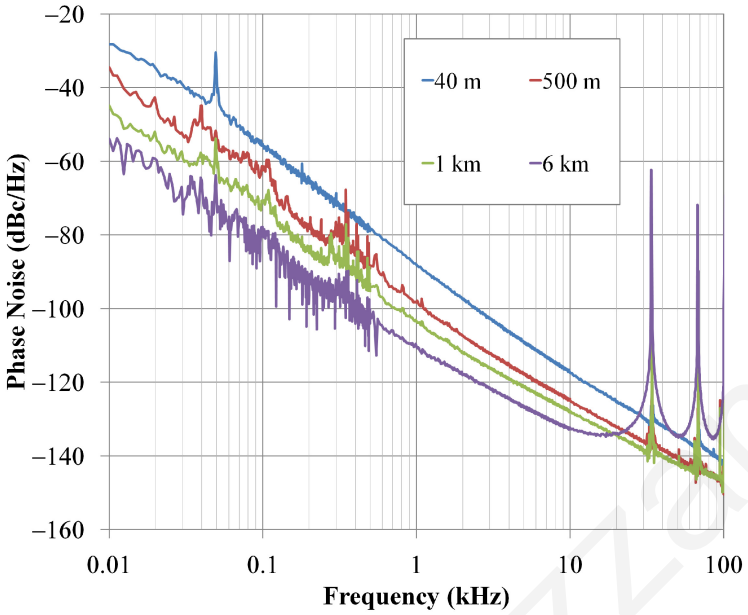

Fig. 3.16. Contribution of fibre length to phase noise plots of 10 GHz single-loop OEO. After [73].

in an OEO. Rayleigh scattering occurs due to the variation of refractive index along the fibre length introduced by wavelength-order random density fluctuations during the manufacturing process. Stimulated Brillouin scattering (SBS) is a nonlinear effect introduced due to the interaction of light with phonons which creates a counter propagating Stokes wave with a frequency shift of approximately 11 GHz relative to the optical carrier while the light due to Rayleigh scattering propagates both in the forward and the backward direction. The gain-bandwidth of SBS and Rayleigh scattering is 10 MHz and 10 kHz respectively. Both phenomena introduce amplitude noise in the optical domain and appear as phase noise in the electrical domain after photo-detection in a microwave photonic link and OEO. In order to suppress the noise induced by the two types of scattering in an OEO loop or a microwave photonic link, the continuous wave light is either frequency or amplitude modulated as shown in Fig. 3.17.

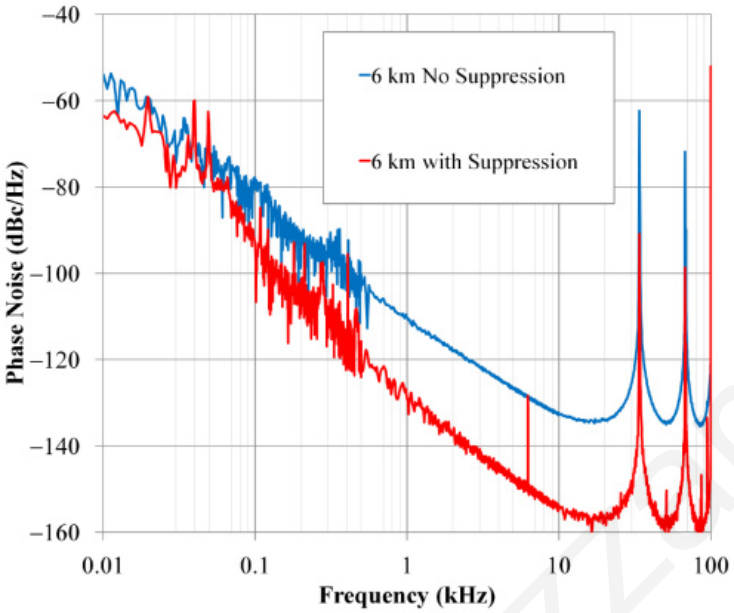

Fig. 3.17. Phase noise plots of 10 GHz single-loop OEOs with and without frequency modulation to suppress the effect of Rayleigh scattering. After [73].

3.4 Tunable OEO

Several applications such as radar, modern instrumentation, phase-locked loops, clock recovery circuits, wireless transceivers, and frequency synthesizers [74–76] require a tunable RF source with low phase noise performance and in many cases a frequency tunable OEO (TOEO) could be a potential candidate in place of an all-electronic approach. A tunable band-pass filter section (either in electrical or optical form) is generally inserted in the OEO loop to achieve the frequency tuning operation. Table 3.2 lists a number of TOEOs, comparing and contrasting them in terms of tuning range, phase noise, and tuning method.

In [53], a tunable OEO based on stimulated Brillouin scattering (SBS) was proposed to achieve a carrier with a tunable frequency from DC - 60 GHz, while in [77] a tunable OEO (3 - 28 GHz) was implemented in which two optical phase modulators (PMs) were cascaded with a phase shifted fibre Bragg grating (PS-FBG). A relatively simple technique was also reported in [78] to achieve a tunable frequency range from 4.74 GHz - 38.8 GHz based on using an optical PM and a tunable optical bandpass filter (TOBF), where the tunability was realized by changing the optical bandwidth of a TOBF. Later, a modified version of [78] was reported for a tuning range up to 57.7 GHz [79].

No.	Tuning range	Phase noise	No. of loops	Method of tunability	Realized by	Comment	Ref. No.
1	4.74 to 38.38 GHz	<-120 dBc /Hz @ 10 KHz offset whole tunable range	Single	Tunable microwave photonic filter	PM + tunable OBPF	Tunable range could be extended to hundreds of GHz by replacing the PM with one having a larger frequency response	[78]
2	3.39 to 57.5 GHz	< -120 dBc/Hz @10 kHz offset whole tunable range	Dual	Tunable microwave photonic filter	PM+ tunable OBPF	Extended version of [78]	[79]
3	DC to 40 GHz	-100 dBc/Hz @10 kHz offset	Dual	Tunable microwave photonic filter	MZM+ HNLF+ SBS effect	Frequency tuning is obtained by tuning the wavelength of pump laser	[80]
4	DC to 60 GHz	-100 dBc/Hz @10 kHz offset	Dual	Tunable microwave photonic filter	MZM+ HNLF+ SBS effect	Extended version of [81]	[53]
5	Up to 40 GHz	Below 100 dBc/Hz @100 kHz offset	Single	Tunable microwave photonic filter	PM+ HLNM +SBS effect	Chip based OEO, chalcogenide glass works as SBS medium, frequency tuning obtained by, tuning pump laser frequency	[82]

Continued on next page

Table 3.2 – *Continued from previous page*

No.	Tuning range	Phase noise	No. of loops	Method of Tunability	Realized by	Comment	Ref. No.
6	28 GHz- 41 GHz	Below -106dBc/Hz @10 kHz offset whole tunable range	Single	Microwave photonic filter	Amplified feedback laser (AFL)	Tuning the bias current (I_A)	[75]
7	8.5 GHz- 9.5 GHz	-103dBc/Hz @10 KHz offset at oscillation frequency 10 GHz	Single	Injection locking	A tunable synthesizer	Does not contain narrow band electronic filter	[83]
8	5.8 to 11 GHz	-107.4 dBc/Hz at an offset frequency of 10 kHz	Dual	Chirp effect on MZM	A tunable microwave attenuator, chirped fibre Bragg grating.	No electrical microwave filter, frequency tuning is realized by adjusting the attenuator	[84]
9	0 to 40 GHz	-113 dBc/Hz @ 10 kHz offset at 8.18 oscillation frequency	Single	Tuning the SBS pump wavelength	Cascaded microwave photonic filter. (a single passband MPF and an IIR filter)	The IIR filter is based on an active recirculating fibre delay loop	[63]

Continued on next page

Table 3.2 – *Continued from previous page*

No.	Tuning range	Phase noise	No. of loops	Method of Tunability	Realized by	Comment	Ref. No.
10	4.078 to 13.05 GHz	-96.9 dBc/Hz @ 10 kHz offset at 6 GHz oscillation frequency	Dual	Dispersion induced microwave photonic filter	Dual output MZM+ unbalanced fibre path+ linearly chirped fibre Bragg grating	Tunability is obtained by changing the fibre length after the output of 1×2 MZM	[85]
11	6 to 60 GHz	-105 dBc/Hz @ 10 kHz offset at 51 GHz oscillation frequency	Single	Fabry-Perot filter	Fabry-Perot filter+ tunable optical delay line	Tunability is obtained by aligning the cavity modes with etalon resonance and higher order harmonic of the free spectral range (FSR).	[69]

Table 3.2: Comparison of TOEO with different tuning methods

3.5 Optical frequency comb generation

An optical frequency comb (OFC) can generate evenly spaced discrete optical multi-tones that can replace several single mode laser diodes. Not all multi-wavelength sources are considered to be optical frequency combs; only those that (i) maintain high spectral coherency across the whole bandwidth and (ii) those for which the spacing can be tuned independently with accuracy [86] are categorised as OFCs. Several techniques have been identified to generate OFCs including mode-locked lasers, nonlinear optics, electro-optic modulation, and optical re-circulating loops. A brief introduction to these individual techniques will be discussed in subsequent sub-sections. The key figures of merit for OFC generators (OFCGs) are high coherence, high stability, low noise, high efficiency, low cost, simplicity and good spectral flatness (i.e. each optical frequency component should ideally have the same intensity) [24].

3.5.1 Mode locked laser

Mode locked lasers (MLL) are widely used in OFC generation [87]. In a MLL, the longitudinal cavity modes are phase matched to generate ultra-short repetitive pulses in the time domain. A regularly spaced pulse train in the time domain corresponds to an OFC in the frequency domain. Mode locking can be obtained actively or passively; the former technique uses a modulator inside the laser cavity which is driven by an external RF source while the latter technique uses a nonlinear saturable absorber. The mode locking concept is illustrated in Fig. 3.18 and the time domain to frequency domain relationship in a MLL is depicted in Fig. 3.19

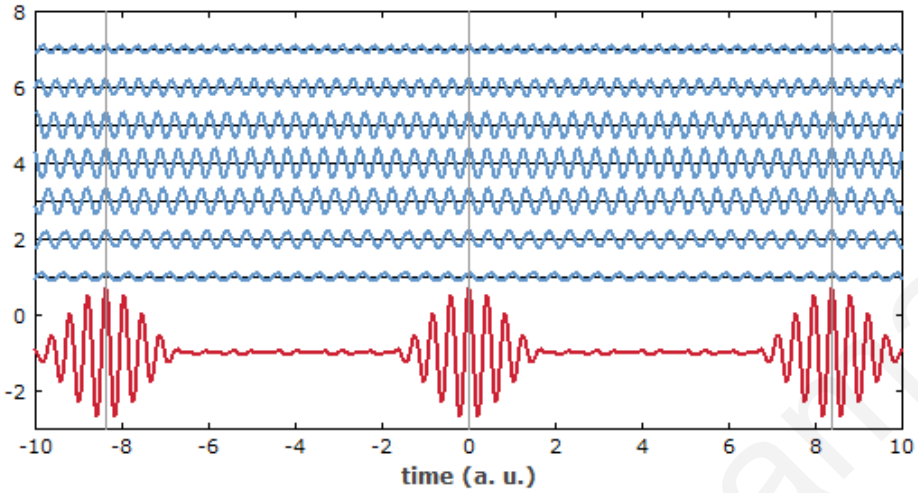

Fig. 3.18. Operating principle of a mode locking technique. A periodic pulse train (red curve) is synthesized by adding seven oscillations with slightly different frequencies and varying amplitudes (blue curves). The points in time where all the oscillations add up in phase are indicated by the black vertical lines. After [88].

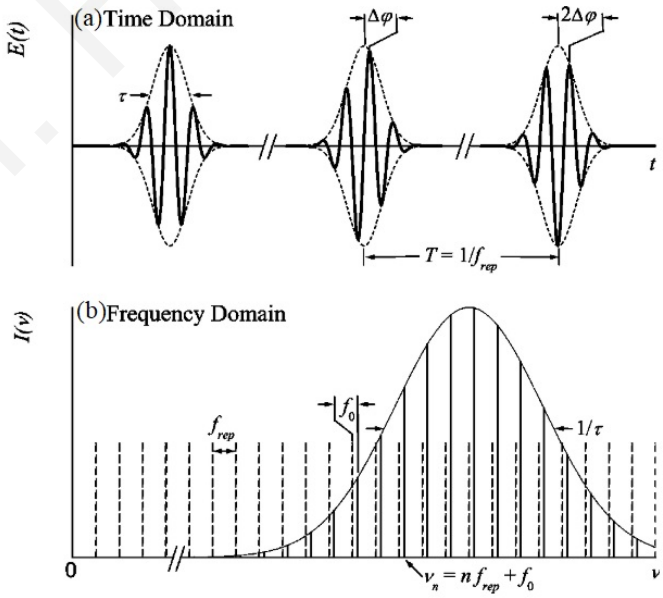

Fig. 3.19. Relationship between time domain and frequency domain in a MLL. After [87].

3.5.2 Gain switching

A MLL can generate optical multi-tones over a wide bandwidth, but cavity complexity is one of the limiting issues [89]. Additionally, it does not offer frequency tunability due to the fixed cavity length which determines the comb spacing. As with the MLL, short optical pulses and therefore an OFC can be generated using gain switching of a laser. In a gain switched laser, short pulses are obtained by modulating the gain of the laser cavity. In [89–91], gain switching techniques were used to generate an OFC; Fig.3.20(a) shows the experimental set up of an externally injected gain switched laser for OFC generation. In this set-up, a FP-LD (slave laser, I_{th}=8 mA) is operated in single mode (through injection locking of an external cavity master laser). The slave laser is then gain-switched with the aid of a 24 dBm RF (10 GHz) sinusoidal signal and 40 mA ($5I_{th}$) DC bias current (applied via a bias tee). The spectrum obtained by the gain-switching is broadened by a phase modulator and the broadened spectrum is shown in Fig. 3.20(b)

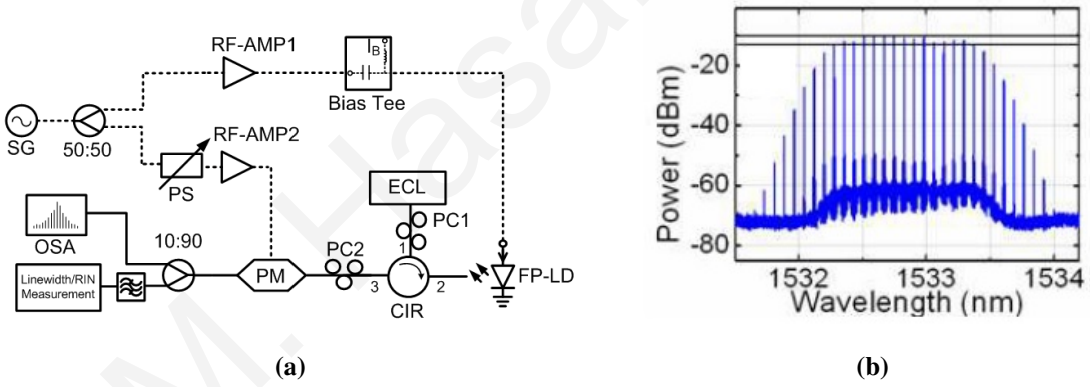

(a) **(b)**

Fig. 3.20. (a) Schematic diagram of a gain-switched FP-LD based OFCG. Optical paths are represented by continious lines while electrical paths are represented by dashed lines (b) Optical spectrum of the generated combs with the arrangement of Fig. 3.20(a). After [89].

3.5.3 Four wave mixing

An OFC may also be generated via four wave mixing (FWM) [92]. In the scheme of Fig. 3.21(a), the FWM technique is used to broaden the side modes generated by an EOM which is modulated by an external RF signal. The output of the EOM is then amplified by an EDFA to a high optical power in order to generate FWM inside the dispersion shifted fibre (DSF). The generated spectrum is shown in Fig. 3.21(b).

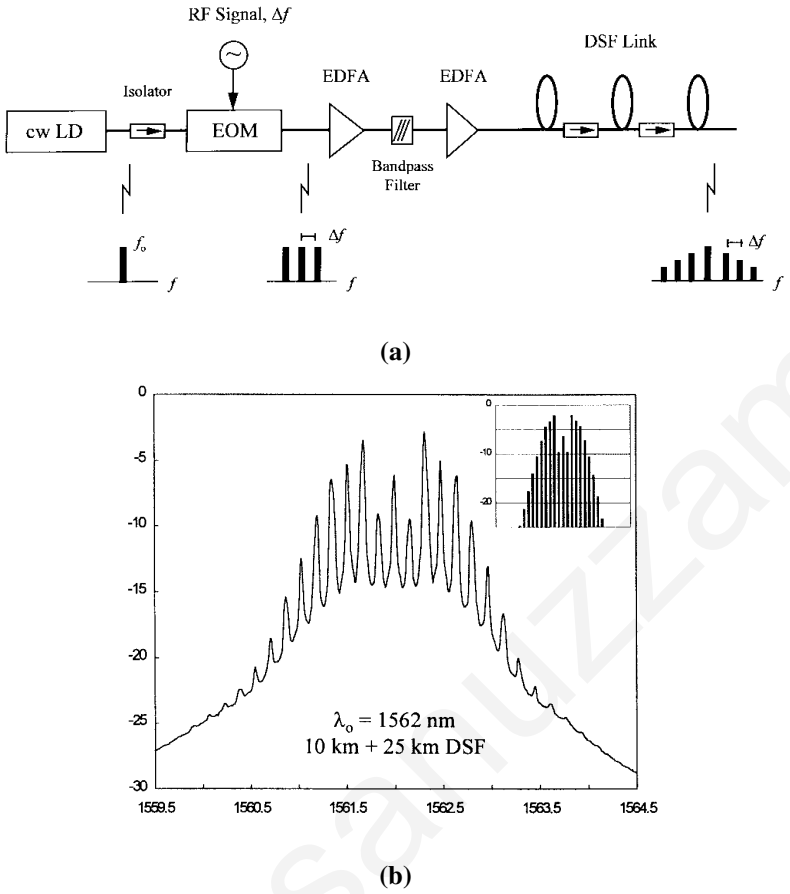

Fig. 3.21. (a) Operational block diagram of a FWM based OFCG where FWM is used to expand the side modes generated by the electro-optic modulator (EOM). (b) optical spectrum generated from the arrangement of Fig. 3.21. After [92].

3.5.4 Electro-optic modulation

In an external modulation based OFC generator, a RF signal of a certain frequency is fed to the RF port of an electro-optic modulator (EOM) (either phase or intensity) while the modulator is connected to a single tone continuous wave (CW) light source. The number of generated comb lines and spectral flatness depends on the driving signal amplitude and modulator characteristics (such as V_π, and bandwidth). In [93], a seven-line OFC was generated by employing a dual-parallel Mach-Zehnder modulator (DPMZM) as shown in Fig. 3.22. In this scheme, the sub-modulator of one arm of the DPMZM is biased at the minimum transmission point while the other sub-modulator is biased at the maximum transmission point. As a result, odd harmonics are generated in one arm (minimum transmission point biased) and even harmonics are generated in the other arm (maximum transmission point biased) as

shown in Fig. 3.22(a). The experimentally generated spectrum is shown in Fig. 3.22(b).

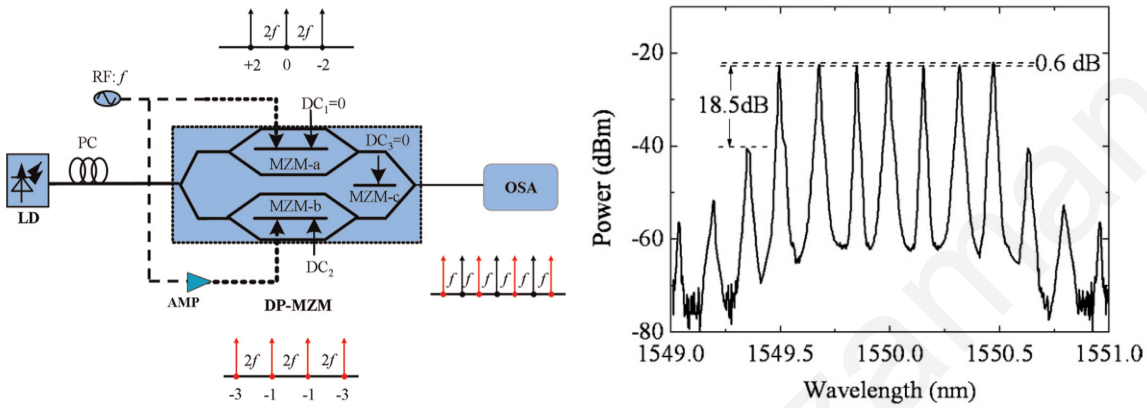

(a) **(b)**

Fig. 3.22. (a) Schematic diagram of a parallel Mach–Zehnder modulator based OFC generator. LD: laser diode. IM: intensity modulator. RF: radio frequency. DC: DC power supply. OSA: optical spectrum analyzer. MZM-a is biased at its maximum transmission point, MZM-b is biased at its minimum transmission point, and MZM-c is biased at zero. (b) Optical spectrum with seven comb lines. After [93].

Generally, a single modulator based OFC is unable to provide a large number of comb lines. To broaden the comb lines, a well-known alternative approach is to place several EOMs (intensity and phase) in tandem as shown in Fig. 3.23.

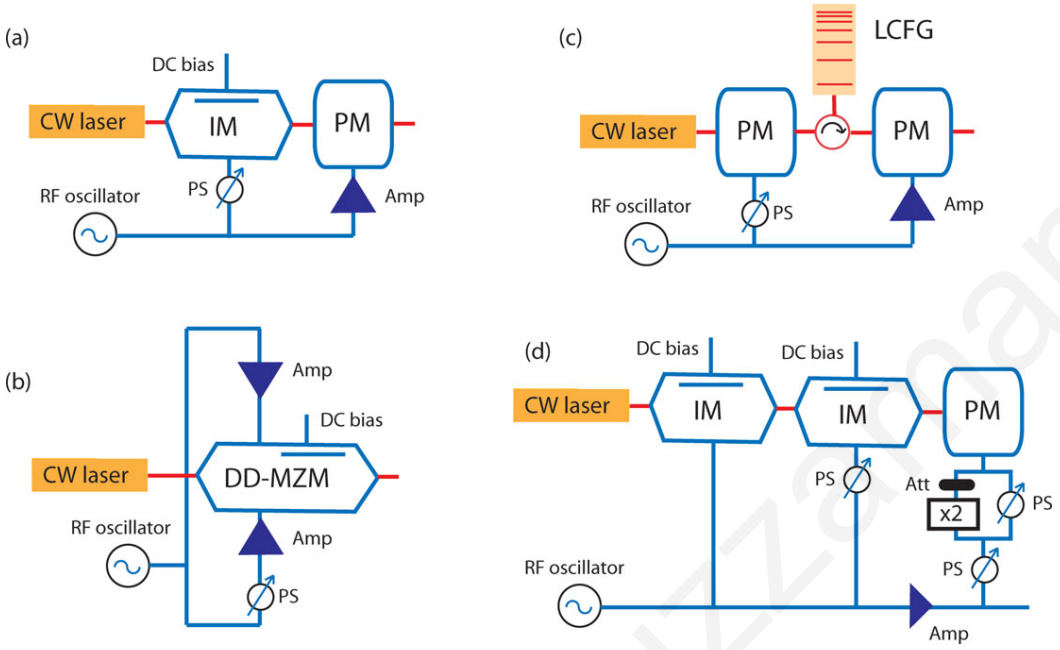

Fig. 3.23. Layout of common electro-optic modulation based OFCGs that can provide a spectrally flat envelope by an adequate optimization of the bias condition and phase shift. IM: intensity modulator; PM: phase modulator; DD-MZM: dual-drive Mach-Zehnder modulator; Amp: RF amplifier; PS: electrical phase shifter; LCFG: linearly chirped fibre Bragg grating; Att: attenuator. After [86].

3.5.5 Optical re-circulating loop

Due to the limited RF bandwidth of optical modulators and the driving signal amplitude restriction, the OFC signal bandwidth is typically less than 1 THz in an external modulation based OFC generator [94]. An optical frequency comb using single side-band carrier modulation in an amplified optical fibre loop can eliminate the aforementioned modulator driving issues. The topology is illustrated in Fig. 3.24(a) where one input port of an optical coupler is used to input the single optical tone while one output port is used to monitor the optical output of the comb generator. The remaining input and output ports are used to complete the loop. A single side band (SSB) modulator and an optical amplifier to compensate the optical losses make up the active parts of the recirculating loop [95]. The output of the comb generator is illustrated in Fig. 3.24(b). In [94], one simple modification was introduced; a single side band suppressed carrier (SSB-SC) modulator was used instead of an SSB modulator as shown in Fig. 3.25.

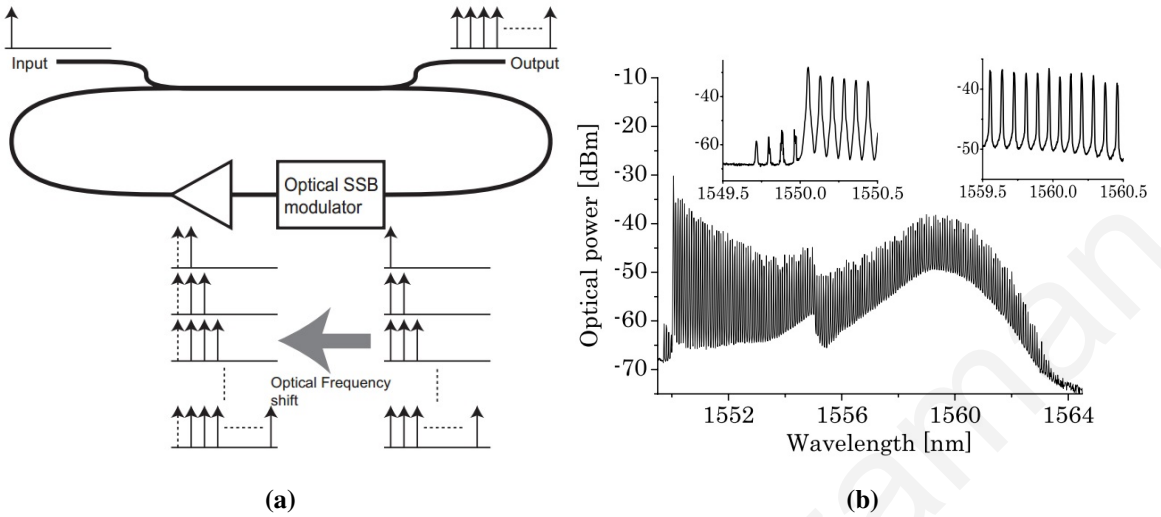

Fig. 3.24. Optical comb generator using an optical SSB modulator. After [95].

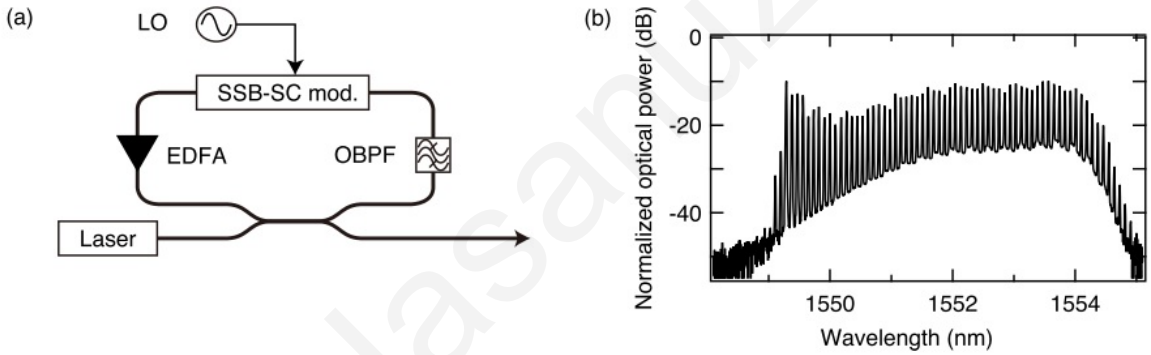

Fig. 3.25. (a) Block diagram of a recirculating frequency shifter, and (b) its generated optical frequency comb signal. After [10].

3.6 Dispersion induced power fading

In conventional intensity modulated microwave and mm-wave photonic links, modulation results in a double sideband (DSB) signal where two side bands are located either side of the optical carrier. After passing through a dispersive element (e.g. optical fibre), the two side bands experience different amounts of phase shift relative to the optical carrier. Generally a photodetector is used to generate the microwave signal by beating the optical tones. In DSB modulation two beat signals of identical frequency are generated by beating the two side bands with the carrier and the resultant signal is the sum of two beat notes. As the two side band signals experience different phase shifts during transmission through the dispersive element, the photodetected microwave signals produce phase shifts relative to one another.

If the phase shift is π then complete cancellation occurs. Therefore, the intensity of the generated microwave signal depends on the relative phase difference between the two tones. The power variation depends on the fibre dispersion parameter (D), transmission distance (L) and operating frequency (f_{RF}) as expressed by the following equation [2, 96]:

$$P_{RF} \propto \cos^2\left(\frac{\pi L D}{c}\lambda_c^2 f_{RF}^2\right) \tag{3.6}$$

where λ_c is the wavelength of the optical carrier and c is the velocity of light in vacuum. The

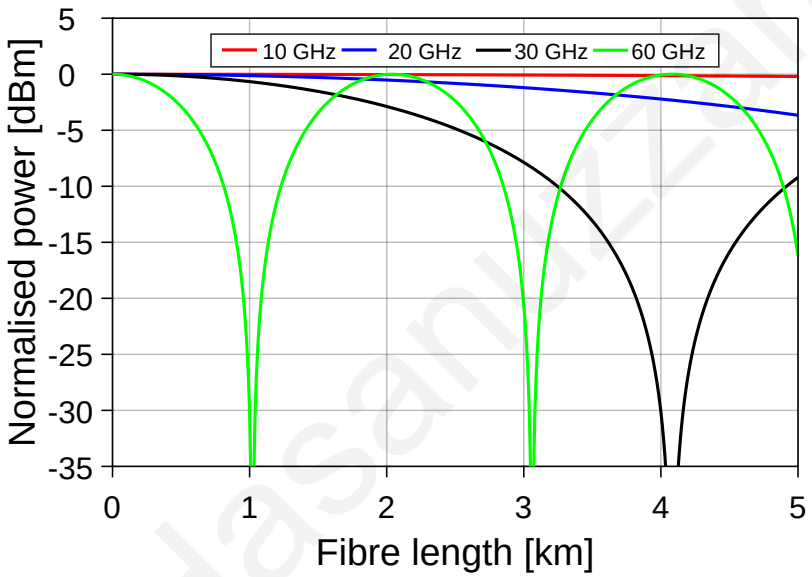

Fig. 3.26. Dispersion-induced power fading for standard single mode fibre at 1550 nm as a function of fibre length for four different frequencies.

dispersion-induced power fading as a function of fibre length (L) and operating frequency (f_{RF}) is shown in Fig. 3.26 and Fig. 3.27 respectively. The periodic power fading is more pronounced at relatively higher frequencies and longer link lengths.

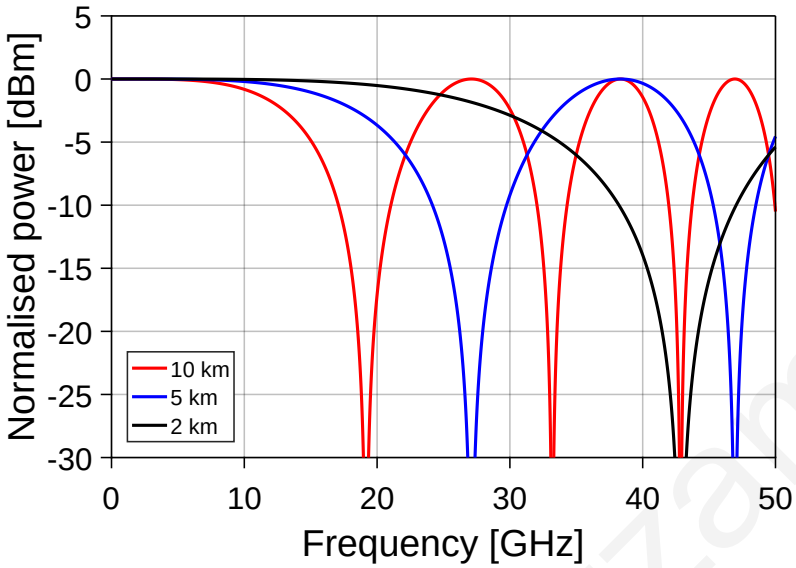

Fig. 3.27. Dispersion-induced power fading for standard single mode fibre at 1550 nm as a function of frequency for three different fibre lengths.

3.7 Conclusion

Two of the most widely used methods for the photonic synthesis of microwave and mm-wave signals have been considered in this chapter, namely the optoelectronic oscillator (OEO) and the optical frequency comb (OFC) generator. The operating principles, design and performance considerations (such as phase noise and frequency tunability) and topologies for various OEO and OFC generators have been described, compared and contrasted. Finally, we considered the impact of optical fibre dispersion-induced power fading, since this can potentially impact on loop oscillation conditions.

We revisit the themes of the OEO and OFCG in chapters 5 and 6 respectively. In Chapter 5 a self-oscillating optical frequency comb generator, which is based on an OEO topology, is presented for W-band frequency generation and subsequent use in a W-band radio-over-fibre link. In Chapter 6, a tunable OEO is implemented and used to drive an OFC generator for 242.6 GHz signal generation and demonstration of radio-over-fibre at this frequency. This last result represents an important step in the exploitation of the THz frequency range for wireless communications. However, there is also developing interest in guided transmission of THz signals, and this is the theme of the next chapter.

CHAPTER 4

Low-loss Hollow-core Anti-resonant Fibre for THz Waveguiding

4.1 Introduction

In recent years, the terahertz (THz) band (ranging from 0.1-10 THz) has attained great research interest due to its promising and potential applications in the field of security, sensing, astronomy, and communications [18, 97]. Although dry air offers the lowest attenuation and dispersion to the THz band, free space THz systems introduce additional unavoidable losses during the coupling, transporting and management of the THz beam [18]. Moreover, waveguides are indispensable in certain cases; when the application point is inaccessible, or it is required to interact with the sample strongly and to confine or focus to a smaller spot size with high power delivery [98]. In contrast to the other two key parts (sources and detectors) of THz systems, waveguides are not only useful for distributing THz beams but also as functional devices [99].

One of the main challenges is to design a low loss waveguide in the THz regime. Two effective approaches have been considered recently to realise a low-loss waveguide structure in the THz band with additional properties such as low bending loss and low dispersion. The first approach uses relatively low loss polymer based waveguides such as poly(methylmethacrylate) (PMMA) [100], Teflon [101] , high-density polyethylene (HDPE) [102], and Topas [103] instead of hollow metallic and glass waveguides. Among the aforementioned

polymers, Topas provides the lowest absorption and its bulk material loss is 100 times lower than PMMA [103]. The second and most effective approach is to confine a high fraction of power in air and simultaneously maintain tight confinement [99, 103] since as mentioned before dry air provides the lowest attenuation in the THz band. Combining these two approaches, different wave guiding structures have been considered including subwavelength fibre [104], porous-core fibres [97, 105, 106], and hollow-core fibres [102, 107].
Hollow-core fibre (HCF) can guide light in low index materials such as vacuum, gas or liquid and exhibits attractive properties such as low transmission loss, low nonlinearity, and low dispersion [108]. The most exciting aspect of HCF is that its refractive index may be tuned by changing the low index material's (air, gas or liquid) composition and pressure. HCFs can be categorized according to their guiding mechanism. The first type, the photonic bandgap (PBG) fibre, is more common and guides light in the air-core based on the photonic bandgap [109]. The second type guides light via inhibited coupling (IC) between the core modes and cladding modes [110]. Hollow core anti-resonant (HC-AR) fibre is one kind of IC guiding fibre where a single layer of anti-resonant tube surrounds the hollow air-core. Due to the relatively simple design and low loss guidance, HC-AR fibres have recently gained much attention in the fibre community both in the infrared and THz band [111]. One of the remarkable and unique properties of HC-AR fibre is that 99.99% of light can be guided in the air-core which can drastically reduce the material absorption loss in the THz band.

In this chapter, two hollow core anti resonant (HC-AR) fibre designs will be presented for the transmission of THz waves. The first design is mainly focused on low loss transmission with a nested HC-AR architecture while the second one with a non-nested HC-AR structure is designed to maintain low loss guidance and single mode operation simultaneously. We used the state-of-the-art finite element (FE) based COMSOL software to perform the numerical simulations. Detailed transmission characteristics of both designs are discussed in the subsequent sections.

4.2 State-of-the-art of THz fibre

One of the keys to the continued growth of terahertz (THz) technology is the development of low loss waveguides, and in particular hollow-core (HC) fibres in which most of the power is guided in the air which has low absorption in the THz spectral range [18, 99] while main-

taining strong confinement. In the operating frequency region of 1 THz, relatively low loss waveguides based on polymers such as PMMA [100], Teflon [107], HDPE [112], Zeonex [113] and Topas [99] have been investigated. Using these materials, various groups have reported different terahertz waveguiding structures, including subwavelength fibre [104], porous-core fibres [97, 101, 114], dielectric tube waveguide [115] and HC fibres [107, 112] to guide THz waves. In porous core (PC) fibres both the core and cladding consist of air-hole microstructures; these fibres have been investigated for low-loss THz waveguiding with high birefringence and low waveguide dispersion [114]. Guiding can be based either on total internal reflection (TIR) or a photonic band gap (PBG) depending on the air density in the air-hole micro-structured core [116]. Porous core PBG fibres provide lower effective material loss than PC-TIR fibres [99]. However, limited transmission bandwidth, strong overlap of the core modes with the surrounding cladding and relatively high group velocity dispersion (especially at the band-gap edges) are major limitations of PC-PBG fibres [116, 117].

HC fibres can be categorized into two types. The first one is a HC photonic band gap fibre (HC-PBG) which guides light via the photonic band gap effect. As with PC-PBG fibres, the HC-PBG fibre suffers from limited transmission bandwidth. The second type is an anti-resonant HC fibre also known as an inhibited coupling HC fibre in which the light guiding mechanism is based on the combination of an anti-resonant effect and inhibited coupling between the core modes with the cladding modes [118, 119].

4.3 Principle of operation: HC-AR fibre

A convential HC-AR fibre consists of a single layer of cladding tubes as illustrated in Fig. 4.1(a). In HC-AR fibre, the light guiding mechanism is based on the combination of an anti-resonant effect and inhibited coupling between the core modes and the cladding modes [118, 119]. This type of fibre offers much broader transmission bandwidth and low light-dielectric overlap [120]. One of the key properties of the HC-AR fibre is that it exhibits a sequence of narrow-bandwidth high-loss “resonant” regions and wide-bandwidth low-loss “anti-resonant” regions. In the resonant regions, core modes become phase matched with the cladding modes causing high transmission losses while in the anti-resonant regions modes are tightly confined in the air core. The spectral position and bandwidth of “resonant” and “anti-resonant” regions depend significantly on the anti-resonant unit tube thickness

(t) [121]. The frequency of the first order resonance is given by [118]:

$$f_c \approx \frac{c}{2t\sqrt{n^2-1}} \tag{4.1}$$

where n is the refractive index of the thin tube material, and c denotes the speed of light in vacuum.

More recently, HC-AR fibres with nested anti-resonant elements have been introduced [119]. These fibre designs are a modified form of HC-AR fibre as shown in Fig. 4.1(b) where smaller tubes are nested inside the tubes defining the core, further enhancing the spatial overlap between the fundamental core mode and the cladding mode thus resulting in a tighter confinement. Moreover, it has been shown that a node-free arrangement in which the cladding tubes are non-touching reduces the confinement loss [118, 122, 123].

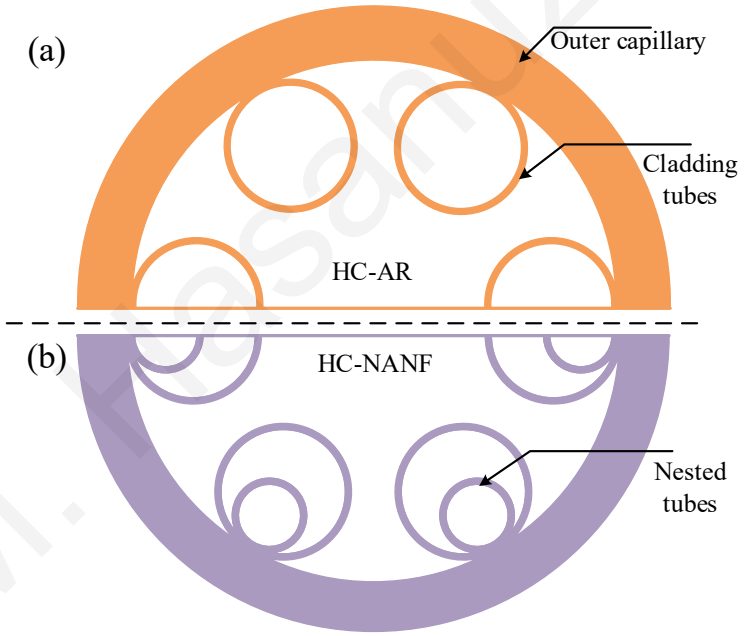

Fig. 4.1. Cross section view of (a) HC-AR fibre (b) HC-NANF

4.4 Nested HC-AR fibre: Design-I

In this section, a hollow-core nested anti-resonant node-free fibre (HC-NANF) is investigated in the THz regime (specifically 0.5 THz – 1.5 THz). Numerical results show that the proposed HC-NANF offers record low effective material loss, broad low loss transmission bandwidth centred at 1 THz, near-zero waveguide dispersion and effectively single mode operation while the fibre design relies upon experimentally feasible and realistic fabrication

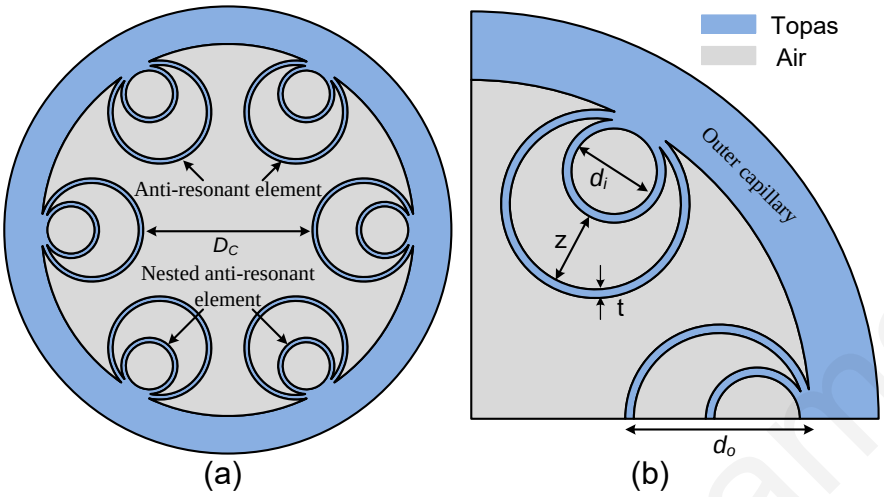

Fig. 4.2. Geometry of HC-NANF. The fibre has a core diameter $D_C = 3$ mm, outer capillary diameter, $d_o = 2.6$ mm, tube separation $z = 1$ mm and wall thickness, $t = 0.09$ mm.

parameters. Optimizing the design parameters, we predict: an effective material loss of 0.05 dB/m; a confinement loss of 3.4×10^{-4} dB/m at 1 THz; a bending loss of 10^{-2} dB/m at 45 cm bending radius; a low loss transmission band from 0.8 THz to 1.2 THz, for which the total transmission loss is below 0.095 dB/m; and a 0.6 THz flat dispersion band where the dispersion parameter β_2 is less than 0.115993251 ps/THz/cm.

4.4.1 Design of HC-NANF geometry

The geometry of the HC-NANF is shown in Fig. 4.2. The cladding consists of six circular anti-resonant (AR) tubes in a node-less configuration; each AR tube contains a single circular nested tube. It has been shown that a six-element HC-NANF offers better confinement loss performance than eight or ten elements [118]. In our simulations, we found that a core diameter (D_C) of 3 mm and an outer capillary diameter (d_o) of 2.6 mm gives confinement loss of the order 10^{-4}dB/m, which is low enough to consider for THz guidance. Other design parameters (wall thickness t and tube separation z) were chosen to ensure the anti-resonant first transmission window has a loss minimum around 1 THz. The dimension of the inner capillary diameter d_i is determined from the following relation,

$$d_i = d_o - z - 2t. \tag{4.2}$$

Topas was selected as the fibre material due to its promising property in the THz band, including lower bulk material loss than PMMA and Teflon, and a constant refractive index

of n = 1.5258 in the 0.1 THz - 1.5 THz range [103]. The bulk material loss of Topas (α_{mat}) is linearly proportional to frequency in the range of 0.2-1.6 THz and it can be estimated by $\alpha_{mat} = 0.36(f - 0.4) + 0.06$ where f is in THz and α_{mat} is in dB/cm [18]. The numerical simulations were performed using *COMSOL* software. To calculate the confinement loss of the proposed fibre, a circular perfectly matched layer (PML) was imposed in the outermost part of the structure. In order to obtain accurate results both the mesh size and perfectly-matched layer parameters were set according to [118].

4.4.2 Optimization of the total loss of the HC-NANF

In THz fibre, the dominant type of loss is material absorption loss (also known as effective material loss) which is then added to the confinement loss to estimate the total transmission loss. Effective material loss (α_{EML}) and confinement loss (α_{CL}) are the two major sources of losses. The fraction of power (η) confined in different regions such as air or fibre material is used to quantify the light-material overlap. We calculated α_{EML}, α_{CL} and η according to [18, 116];

$$\alpha_{EML} = \frac{(\varepsilon_0/\mu_0)^{1/2} \int_{A_{\text{mat}}} n\alpha_{\text{mat}} |E|^2 dA}{2\int_{\text{All}} S_z dA} = \alpha_{\text{mat}}\eta_m \tag{4.3}$$

$$\alpha_{CL} = 8.686 \left(\frac{2\pi f}{c}\right) \text{Im}(n_{\text{eff}}) \quad \text{dB/m} \tag{4.4}$$

$$\text{Fraction of Power } \eta = \frac{\int_x S_z dA}{\int_{\text{all}} S_z dA}. \tag{4.5}$$

In the above equations ε_0 and μ_0 are the permittivity and the permeability of vacuum, respectively, f is the frequency of the light, c is the speed of light in vacuum and Im(n_{eff}) is the imaginary part of the effective refractive index of the guided mode. Integration of the numerator in Eq. 4.3 is performed over the solid material region of Topas because air is transparent in the THz frequency band while integration of the denominator is done over all regions (material and air-holes). The Poynting vector in the direction of propagation is denoted as $S_z = Re(\vec{E} \times \vec{H}^*)\hat{z}$, where $\vec{E}$ is the electric field component and $\vec{H}$ is the magnetic field component. The parameter α_{EML} is the product of bulk material loss (α_{mat}) and the fraction of power in the background material (η_m) which is then added to α_{CL} to obtain the total transmission loss. To optimize the design parameter, we investigated the effect of core diameter (D_C) and outer capillary external diameter (d_o) on losses as shown in Fig. 4.3(a) and 4.3(b) respectively. As observed from Fig. 4.3 (a) a relatively larger core diameter (D_C)

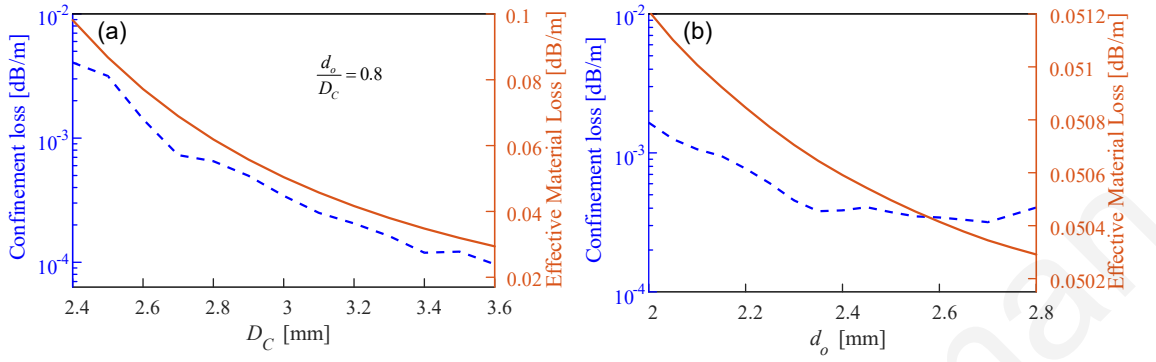

Fig. 4.3. Confinement loss and effective material loss as a function of (a) Core diameter (D_C) (b) Outer capillary external diameter (d_o).

results in reduced losses. However, a larger core diameter also increases the critical bend radius and overall fibre diameter. Furthermore, the fibre's overall diameter also plays an important role in fibre flexibility. In order to be flexible and compact, the fibre should be as thin as possible. Taking these factors into consideration, from here on we set D_C = 3 mm and d_o= 2.6 mm where the confinement loss is 3.4307×10^{-4} dB/m, the effective material loss is 0.05 dB/m and the overall fibre diameter is 8.5 mm. The fibre diameter is comparable with the fibre in [27].

As discussed earlier, the guiding mechanism of HC-NANF is based on the anti-resonant effect where the anti-resonant tube thickness t determines the position of the high loss resonant windows. The first order resonance frequencies calculated using Eq. 4.1 are listed in Table 4.1 for different tube thickness. The calculated resonance frequencies shown in Ta-

Table 4.1: First order resonance frequencies for different tube thickness (t).

Tube thickness (t) in mm	Resonance frequency (f_c) in THz
0.08	1.62
0.09	1.44
0.10	1.30
0.11	1.18
0.15	0.87
0.20	0.65

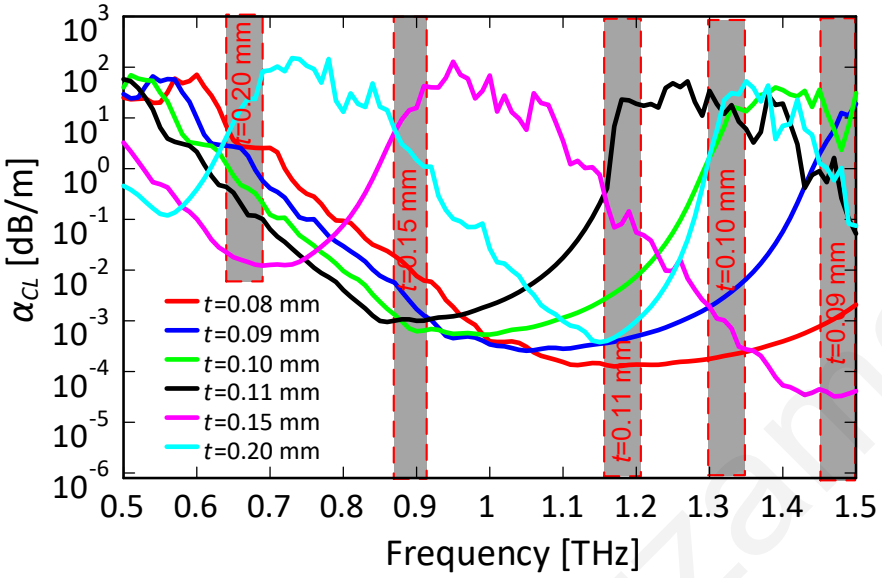

Fig. 4.4. Confinement loss as a function of frequency for different tube thickness t with $D_C = 3$ mm, $d_o = 2.6$ mm and $z = 1$ mm. The grey shaded regions represent the beginning of the resonant bands for the corresponding tube thickness.

ble 4.1 are in good agreement with the simulated results of Fig. 4.4 where confinement loss is plotted against frequency for different t. The peak in the confinement loss (for t = 0.10 mm) occurs at around 1.3 THz (Fig. 4.4), which agrees with the analytical results obtained by using (4.1).

First, we investigated the effect of the wall thickness t on the loss of the proposed fibre while keeping $D_C = 3$ mm, $d_o = 2.6$ mm and $z = 1$ mm. Confinement loss, effective material loss and total loss of the proposed THz fibre as a function of frequency for different values of wall thickness are shown in Fig. 4.4. In the anti-resonant band, the effective material loss dominates the total loss but at the edges of the anti-resonant band confinement loss dominates the total loss. Figure 4.4 shows that for the higher values of t (e.g. 0.15 mm and 0.20 mm) the resonant band falls around 1 THz resulting in higher transmission losses. The anti-resonant band falls around 1 THz for the relatively lower values of t (e.g. 0.08 mm and 0.09 mm). At 1 THz the confinement loss is lowest for t = 0.09 mm while the effective material loss is lowest for t = 0.08 mm as shown in Fig. 4.5. Although the total loss is lowest for t = 0.08 mm we chose t = 0.09 mm as the preferred value since it provides a wide band low loss characteristic centred at 1 THz as shown in Fig. 4.6.

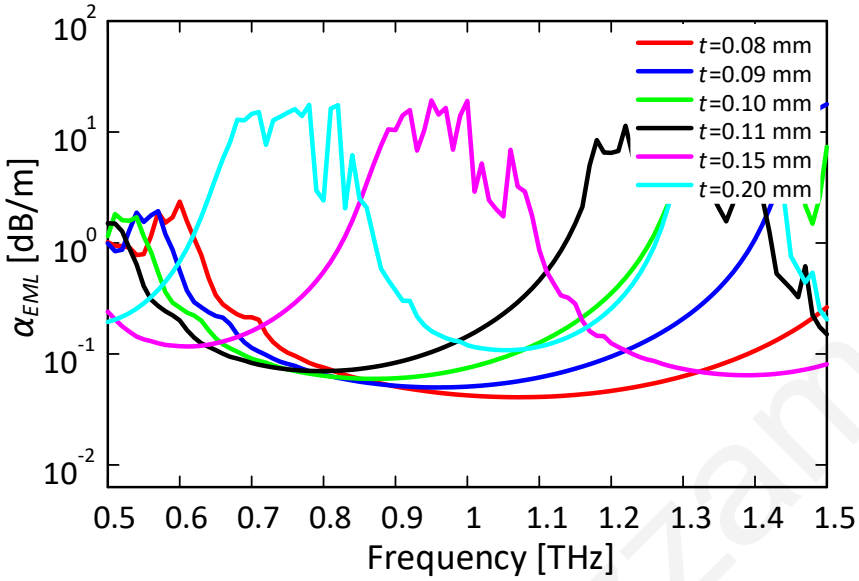

Fig. 4.5. Effective material loss as a function of frequency for different tube thickness t with $D_C = 3$ mm, $d_o = 2.6$ mm and $z = 1$ mm.

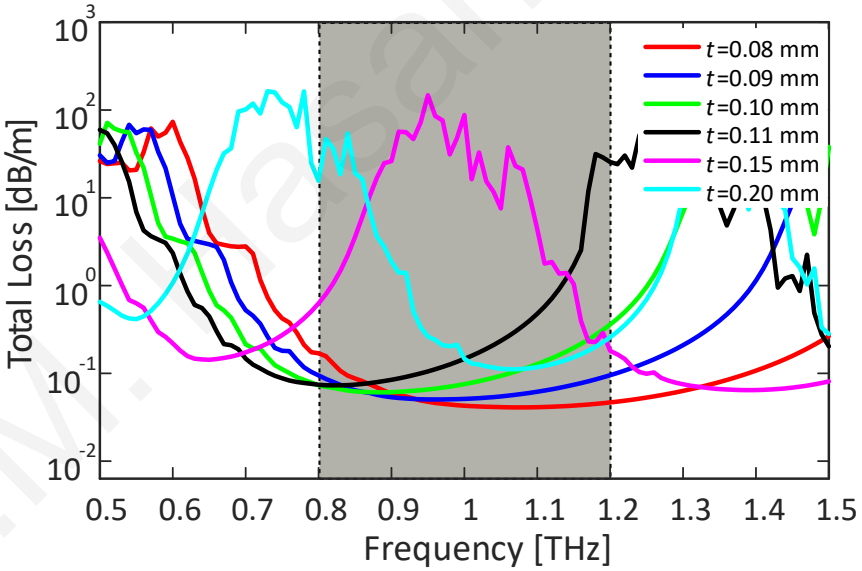

Fig. 4.6. Total loss as a function of frequency for different values of tube thickness t with $D_C = 3$ mm, $d_o = 2.6$ mm and $z = 1$ mm. The grey shaded region is our band of interest where total loss is minimum for $t = 0.09$ mm (blue line) with low loss characteristics centred at 1 THz.

4.4.3 Scaling the tube separation

The effect of tube separation z on the loss properties was also investigated. Figure 4.7 shows the loss properties of the fibre as a function of tube separation z at a frequency of 1 THz. The confinement loss is high for both high and low values of z, with minimum confinement loss

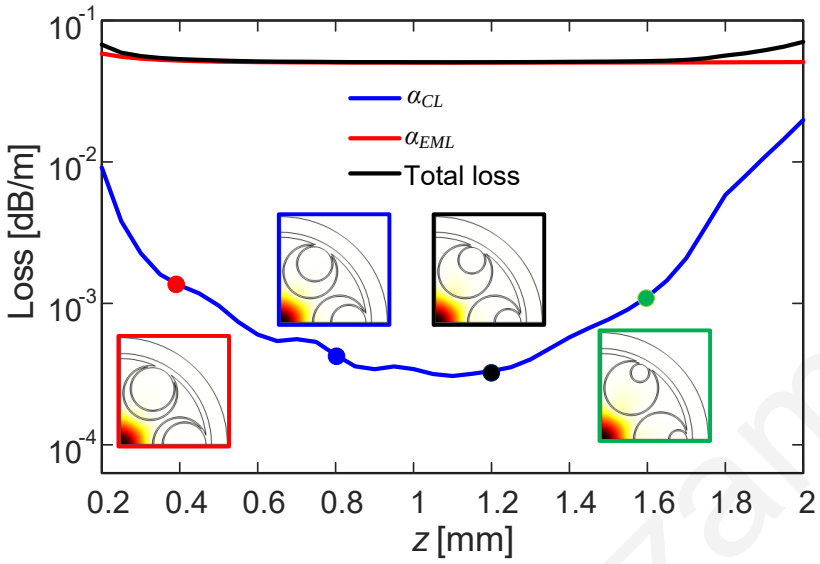

Fig. 4.7. Effect of changing tube separation z on loss properties with fixed $D_C = 3$ mm, $d_o = 2.6$ mm, $t = 0.09$ mm and f =1 THz. The colour of the frame corresponds to the colour of the dot points in the plot.

at around 1 mm. However, there is no significant effect of z on effective material loss.

4.4.4 Comparison between nested and non-nested structure

Figure 4.8 compares the loss performance between the nested HC-AR fibre (with the inner capillary of diameter d_i) and non-nested HC-AR fibre (without the inner capillary of diameter d_i). The non-nested structure provides $\sim 10^2$ times higher confinement loss than the nested structure and thus results in higher total loss. As shown in the contour plot of Fig.4.8(c) and 4.8(d), the light is confined strongly for the nested structure. We find that the total loss of the nested HC-AR fibre is 0.05 dB/m whereas the non-nested HC-AR fibre has a loss of 0.1 dB/m at 1 THz for $D_C = 3$ mm, $d_o = 2.6$ mm and $t = 0.09$ mm.

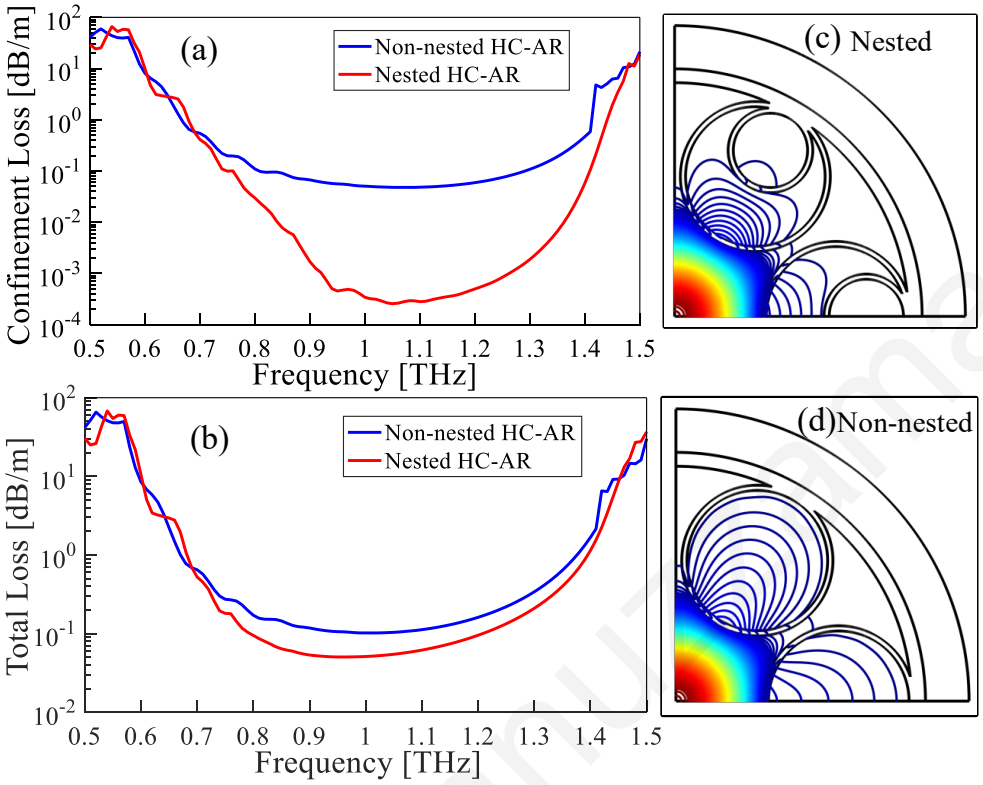

Fig. 4.8. (a) Confinement loss as a function of frequency (b) Total loss as a function of frequency. Contour plot of electric field pattern of (c) Nested structure (d) Non-nested structure at 1 THz for $D_C = 3$ mm, $d_o = 2.6$ mm and $t = 0.09$ mm.

4.4.5 Effectively single mode guidance

The higher-order- mode extinction ratio (HOMER), defined as the ratio of the higher order mode with lowest loss to the fundamental mode, is used to investigate the single-mode property of the fibre. The variation of total loss, effective refractive index of the first three core guided modes (LP_{01}, LP_{11} and LP_{21}) and HOMER as a function of frequency is shown in Fig.4.9. It can be seen from Fig.4.9 that at a frequency around 1.34 THz the calculated HOMER is 23. This indicates that the losses of higher order modes are at least 23 times higher than the fundamental guided mode which makes the fibre guidance effectively single-mode at the expense of total loss.

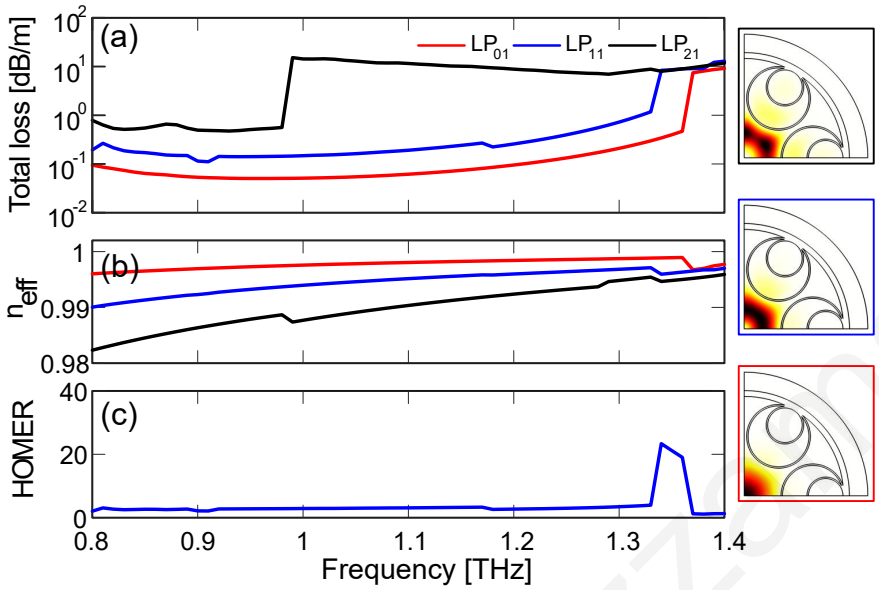

Fig. 4.9. Single mode performance of the proposed fibre as a function of frequency with $D_C = 3$ mm, $d_o = 2.6$ mm, $t = 0.09$ mm and $z = 1$mm. (a) Total loss (b) Mode index curve (c) HOMER. The colour of the frame corresponds to the colour of the lines in plot (a) and (b).

4.4.6 Dispersion

As stated earlier, the refractive index of Topas is constant between 0.1 THz and 1.5 THz. Therefore, the material dispersion contribution to the chromatic dispersion can be neglected and we need to calculate only the waveguide dispersion to illustrate the chromatic dispersion profile of the proposed fibre. The group velocity β_2 can be estimated from Eq. 4.6 in [116]:

$$\beta_2 = \frac{2}{c}\frac{dn_{\text{eff}}}{d\omega} + \frac{\omega}{c}\frac{d^2 n_{\text{eff}}}{d\omega^2}. \tag{4.6}$$

Figure 4.10 shows that the proposed fibre offers near zero flat dispersion from 0.8 THz to 1.4 THz, where β_2 <0.1159 ps/THz/cm. The variation of β_2 in the flat band is 0.0983 $\pm$ 0.01766 ps/THz/cm. It is noted that the low loss transmission band shown in Fig. 4.4(c) corresponds with the flat dispersion band shown in Fig.4.10.

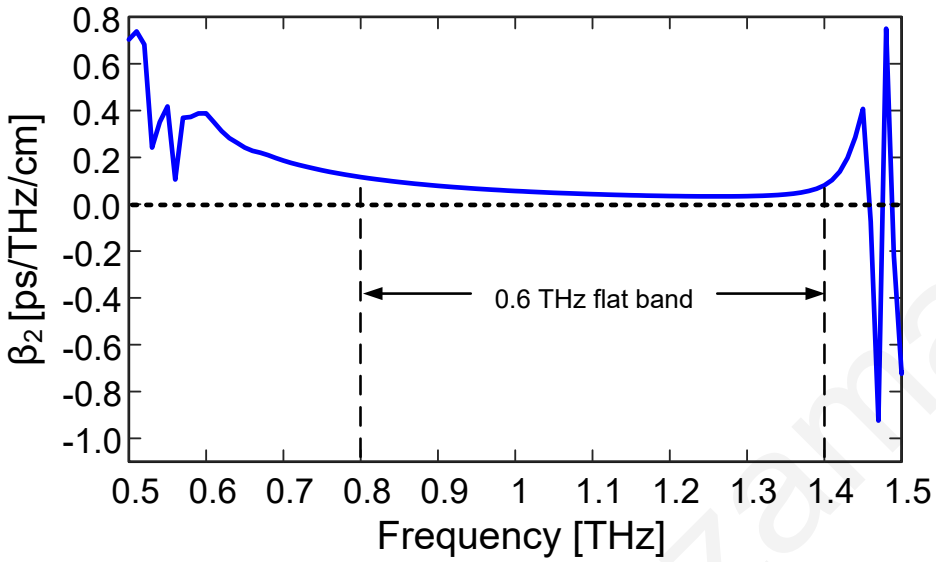

Fig. 4.10. Dispersion parameter as function of frequency with $D_C = 3$ mm, $d_o = 2.6$ mm, $t = 0.09$ mm and $z = 1$mm. The dispersion flattened region coincides with the low loss band shown in Fig. 4.4(c).

4.4.7 Bending loss

To calculate the bending loss, we used the conformal transformation method to estimate the refractive index profile. We calculated the effective refractive index after bending using the method in [119] which is based on:

$$n'(x,y) = n(x,y)\exp(x/R_b) \tag{4.7}$$

where R_b is the bending radius, x is the transverse distance from the centre of the fibre, $n(x,y)$ is the refractive index profile of the straight fibre and $n'(x,y)$ is the equivalent refractive index after bending. Bending loss dependency on frequency and normalized bending radius with the optimum design parameters are illustrated in Fig.4.11 and Fig.4.12 respectively considering the bending direction towards the x direction. The coupling effect of this type of fibre is sensitive to structural parameters [124] and we observe a peak in bending loss after the first minima as shown in Fig.4.11 and Fig. 4.12. The peak in the bending loss profile can be predicted analytically from the structural parameters using the following equation for critical bending radius [124]:

$$R_b^{cr} = 1.71\frac{D_C^3}{\lambda^2}\frac{(d_i/D_C)^2}{1-(d_i/D_C)}\cos\theta \tag{4.8}$$

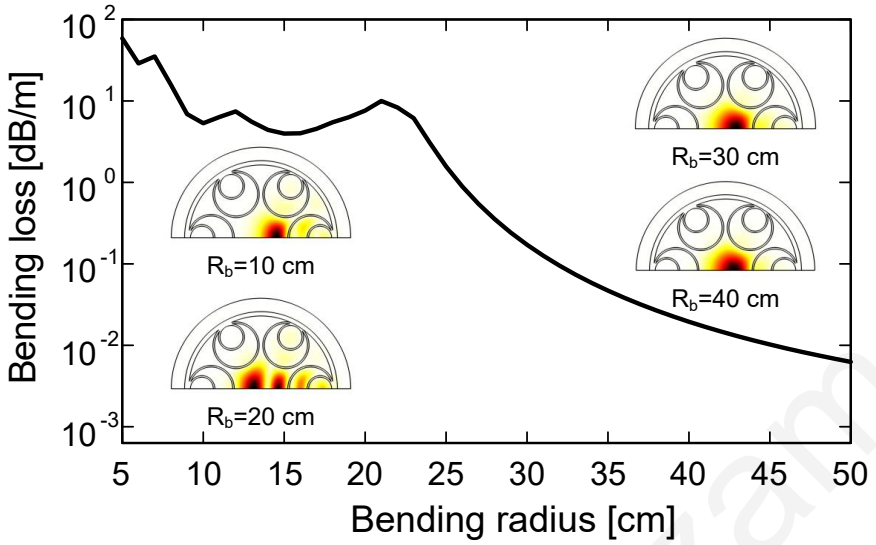

Fig. 4.11. Calculated bending loss as a function of bending radius at 1 THz with $D_C = 3$ mm, $d_o = 2.6$ mm, $t = 0.09$ mm and $z = 1$ mm. A peak in bending loss is observed at $R_b \backsim 21$ cm.

where λ is the operating wavelength and θ is the angle between the bending plane (x-axis) and the capillaries. For our design parameters, we obtain a critical bending radius of 17 cm by using Eq. 4.8. The difference between the analytically and the numerically calculated critical bending radius is due to the approximations used in deriving Eq. 4.8 [124]. A bending loss of less than 10^{-2} dB/m is obtained when the bend radius is more than 45 cm.

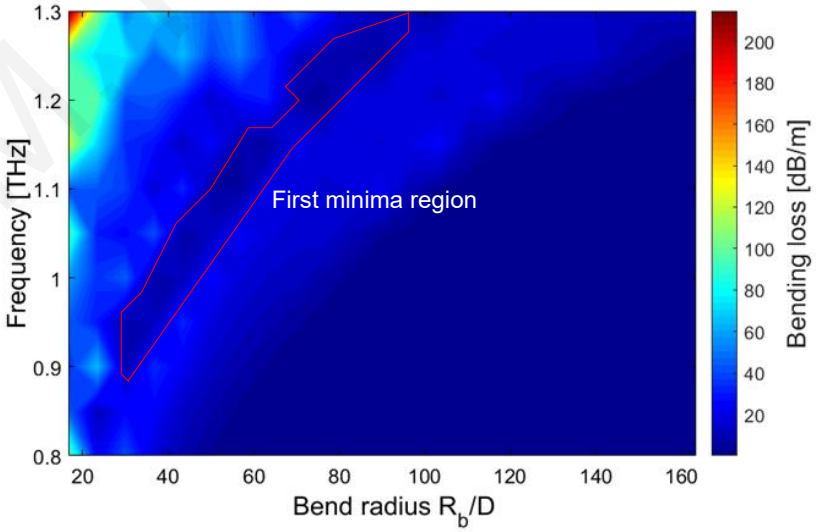

Fig. 4.12. Calculated bending loss as a function of frequency and normalized bending radius with $D_C = 3$ mm, $d_o = 2.6$ mm, $t = 0.09$ mm and $z = 1$mm.

4.5 Single mode non-nested HC-AR fibre: Design-II

In the previous section, a HC-NANF was demonstrated with low transmission loss. However, the proposed design does not guarantee effectively single-mode operation, mainly due to the high confinement factor and low interaction of light with dielectric material, which reduces the higher-order modes (HOMs) loss. Therefore, it is still a challenge to launch a pure fundamental mode (LP_{01}-mode) without HOM contamination in the THz regime. In [125], a silica-based HC-AR fibre in the infrared band was experimentally and numerically demonstrated in which single mode guidance can be obtained by maintaining the shape factor (*d/D* = 0.68), where *d* is the inner diameter of the anti-resonant tubes and *D* is the core diameter as defined in Fig. 4.13. At this condition, the core guided higher order modes (HOMs) are phase matched (being resonant) with the anti-resonant tubes guided modes. As a result, the HOMs exhibit relatively higher transmission loss compared to the fundamental mode which in turn ensures effectively single mode operation.

In this section, we examine the feasibility of applying the concept of a silica-based HC-AR fibre to the polymer-based fibre in the THz regime where the total transmission loss depends both on the material absorption loss and confinement loss, whereas in silica-based fibre the total transmission loss in the infrared band depends only on the confinement loss because the material absorption loss of silica is negligible [126]. We present a simple six-tube HC-AR fibre which simultaneously shows low transmission loss and effectively single-mode operation at 1 THz. We found that single-mode operation is obtained when the *d/D* ratio becomes 0.69. The highest higher-order-mode-extinction ratio (HOMER) is approximately 17. The total transmission loss at this condition is 0.12 dB/m. We also investigate the bending loss of the proposed fibre. The proposed fibre can be potentially applied to emerging THz applications for which low loss single-mode guidance is essential.

4.5.1 Design of HC-AR geometry

Fig. 4.13 shows the geometry of the proposed HC-AR fibre. The fibre cladding consists of six evenly-spaced circular non-touching anti-resonant tubes. In Fig. 4.13, *D* denotes the core diameter (the minimum distance between two diametrically opposite anti-resonant elements) while *d* denotes the inner diameter of the anti-resonant elements. The thickness of

the anti-resonant tubes is represented by t. In this study, we aimed to design a THz fibre at 1 THz. In our previous work in [127], we found that when t = 0.09 mm and D = 3 mm the transmission profile provides symmetric characteristics centred at 1 THz. In this design, we considered the same design parameters as in [127] except for the value of d; here we varied the fibre shape factor (d/D ratio) to find a suitable value of d to obtain single mode guidance. We consider Topas (a cyclic olefin copolymer) for the fibre material due to its lower bulk material absorption loss compared to other polymers such as Teflon and PMMA. Other key attributes of Topas include constant refractive index over a broad frequency range [128] and inertness to water vapour [97]; at 1 THz, the refractive index of Topas is 1.5258.

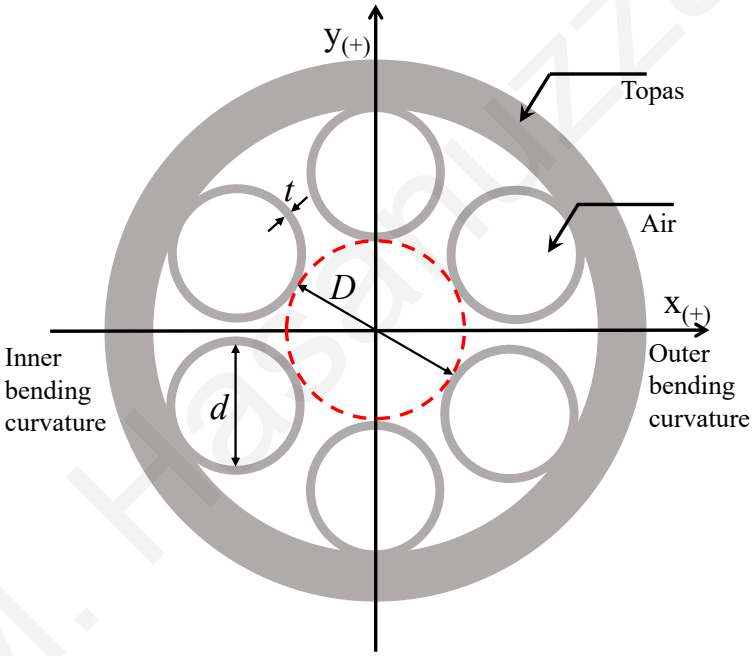

Fig. 4.13. Cross-section of the proposed single circular ring, six anti-resonant elements based HC-AR fibre with the key design parameters indicated.

4.5.2 Results and discussion

A. Transmission loss

The refractive index of the core and cladding guided modes can be approximated by the Marcatili and Schmeltzer equation [129]:

$$n_{nm} = \sqrt{1 - \left(\frac{u_{nm}}{\pi}\right)^2 \left(\frac{\lambda}{d_i}\right)^2} \tag{4.9}$$

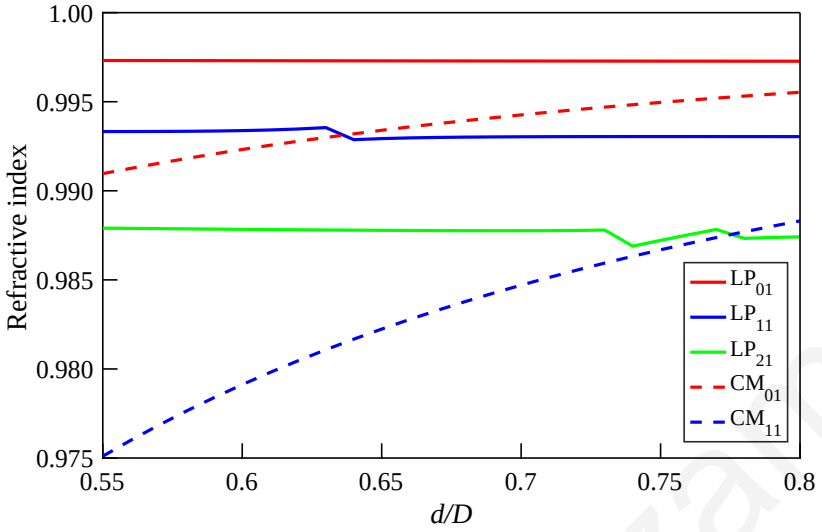

Fig. 4.14. Modal index of LP_{01}, LP_{11}, and LP_{21} modes as a function of *d/D* ratio

where u_{mn} is the m-th zero of the Bessel function J_m, λ is the wavelength, and d_i is the inner diameter of the capillary $\{d_i = D$ for the core and $d_i = d$ for the cladding capillaries$\}$. Fig. 4.14 shows the modal indices of the first three core guided modes (LP_{01}, LP_{11}, and LP_{21}) and two anti-resonant capillary guided modes, referred in the following as cladding modes (CM_{01}, and CM_{11}) calculated by using finite element modelling as a function of the *d/D* ratio. From Fig. 4.14, it is seen that when *d/D* is 0.63, the LP_{11} mode refractive index becomes equal to that of the CM_{01} mode and when *d/D* is 0.73 the LP_{21} mode's refractive index becomes equal to that of the CM_{11} mode. In this condition, the core guided modes (being resonant) become phase matched with the cladding modes. The simple expressions for *d/D* at which the LP_{11} mode couples with CM_{01} and the LP_{21} mode couples with CM_{11} can be derived from Eq. 4.9 as follows:

$$\frac{d}{D}\Big|_{LP_{01}\ mode\ coupled\ with\ CM_{01}} = \frac{u_{01}}{u_{11}} \approx 0.63 \tag{4.10}$$

and

$$\frac{d}{D}\Big|_{LP_{21}\ mode\ coupled\ with\ CM_{11}} = \frac{u_{11}}{u_{21}} \approx 0.75. \tag{4.11}$$

The numerically computed results are in excellent agreement with the analytical results. At these particular *d/D* values, due to resonant effects both the confinement loss and the total transmission loss of the HOMs become higher than the fundamental mode as shown in Fig. 4.15 and Fig. 4.16 respectively. Both the confinement loss and the total transmission

loss increase with the increment of the *d/D* ratio. Phase matching phenomena can also be envisaged from the electric field patterns shown in Fig. 4.17. At *d/D*=0.63, the LP_{11} mode couples with the CM_{01} mode resulting in higher confinement and total transmission loss. However, the LP_{01} mode is strongly confined at higher *d/D* values. Alternatively, the LP_{21} mode is phase matched with the CM_{11} mode at *d/D*=0.75, causing higher confinement and transmission loss.

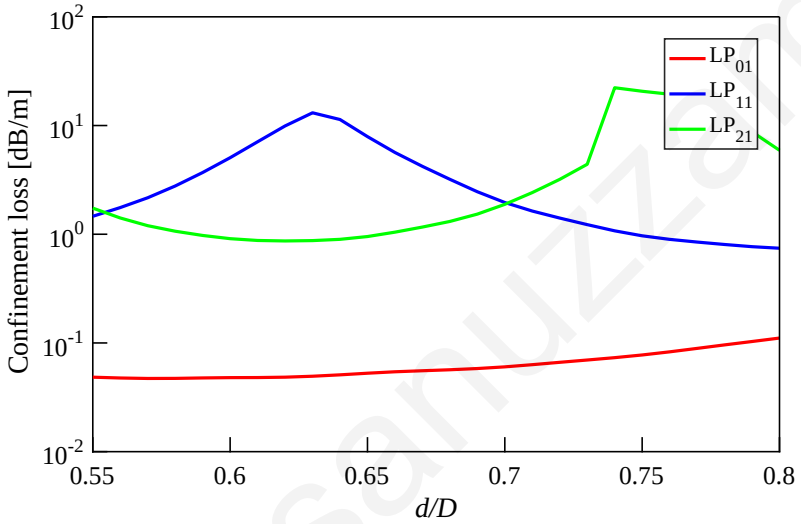

Fig. 4.15. Confinement loss of LP_{01}, LP_{11}, and LP_{21} modes as a function of *d/D* ratio.

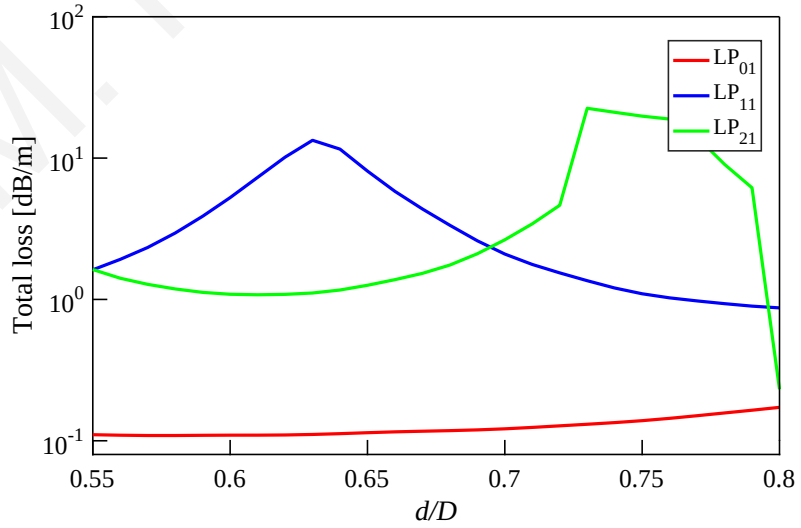

Fig. 4.16. Total loss of LP_{01}, LP_{11}, and LP_{21} modes as a function of *d/D* ratio.

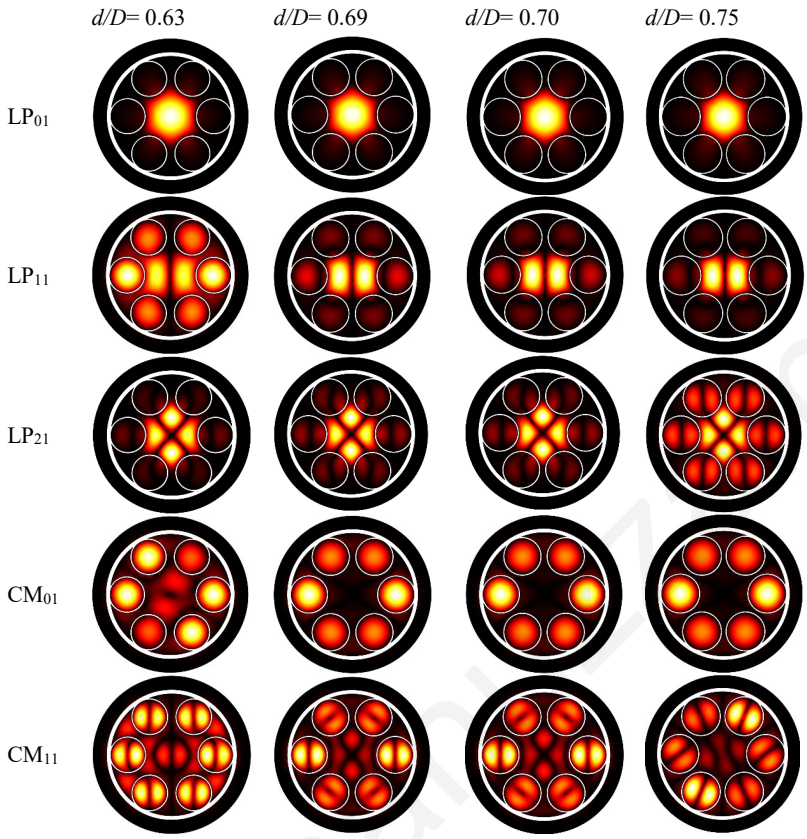

Fig. 4.17. Electric field patterns of the three core guided modes (LP_{01}, LP_{11}, and LP_{21}) and two cladding guided modes (CM_{01} and CM_{11}) at different values of *d/D*. The fundamental LP_{01} mode is confined tightly inside the core. The LP_{11} mode is resonant with the CM_{01} mode at *d/D*=0.63 while LP_{21} is in resonance with the CM_{11} mode at *d/D*=0.75. The maximum higher order mode suppression occurs at *d/D*=0.69.

B. Single-mode operation

The term higher order mode extinction ratio (HOMER) as defined in section 4.4.5 is generally used to quantify the HOM suppression. Fig. 4.18 shows the HOMER as a function of the ratio *d/D*. The maximum value of HOMER is approximately 17 when *d/D* is equal to 0.69. At *d/D* values lower than 0.69, the transmission loss of the LP_{21} mode is lower than that of the LP_{11} mode, while at *d/D* values higher than 0.69 the transmission loss of LP_{11} is lower than that of the LP_{21} mode as shown in Fig. 4.16. The obtained HOMER of the THz fibre considered here is less than the corresponding fibre considered in the infrared region [130]. The material absorption loss (of the silica based fibre) in the infra-red band does not have a significant influence on total transmission loss and it is not generally considered during total

loss calculation. In contrast, in the THz band (for polymer based fibre) both the confinement loss and the material absorption loss contribute significantly to the total transmission loss, where the material absorption loss is proportional to the light-dielectric overlap. As stated earlier, HC-AR fibre offers low dielectric overlap for the fundamental mode and the HOM as well.

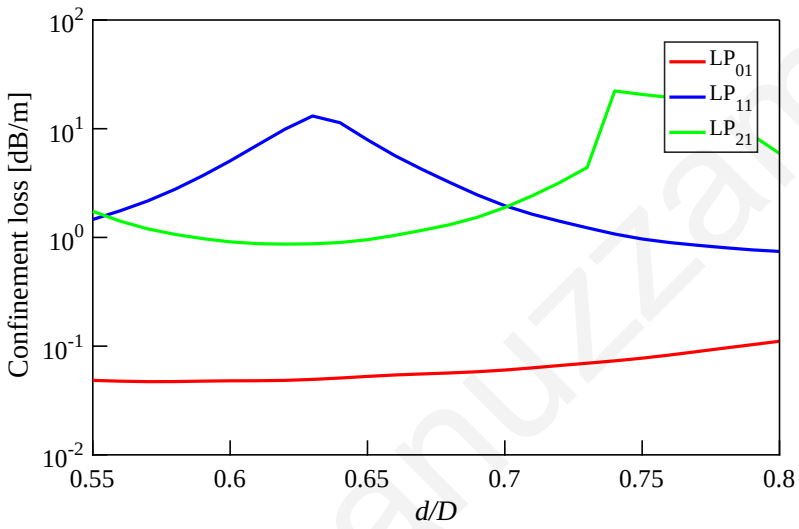

Fig. 4.18. HOMER as a function of *d/D* ratio of HC-AR.

C. Bending loss

We also investigated the bending loss of the proposed HC-AR fibre. We used the standard conformal transformation method to modify the refractive index of the equivalent straight fibre. The bending loss as a function of bend-radius is shown in Fig. 4.19. We found peaks in the bending loss profile for a bending radius around 29 cm and 63 cm for $d/D = 0.69$. The reason for such peaks in bending loss is due to the strong coupling between the core mode and the cladding mode. The first peak is due to coupling with cladding capillaries located at an angle of 60^0 relative to the bending direction (Fig. 4.20(b)) while the second peak is for the capillary located at $\theta = 0^0$ (Fig. 4.20(e)). At these specific bending radii (i.e. critical bending radii), the refractive index of the core guided mode matches with the capillary modes and increases the leakage loss. The critical bending radius can be explicitly calculated from Eq. 4.8. Substituting the values of our design parameters into Eq. 4.8, we obtain a critical bend radius of 78 cm for $\theta = 0^0$ and 34 cm for $\theta = 60^0$. The offset between the FE based computed result and the analytical result is due to approximations considered

in deriving Eq. 4.8 as explained in [124]. The bending radius loss is less than 1 dB/m when the bending radius is above 75 cm.

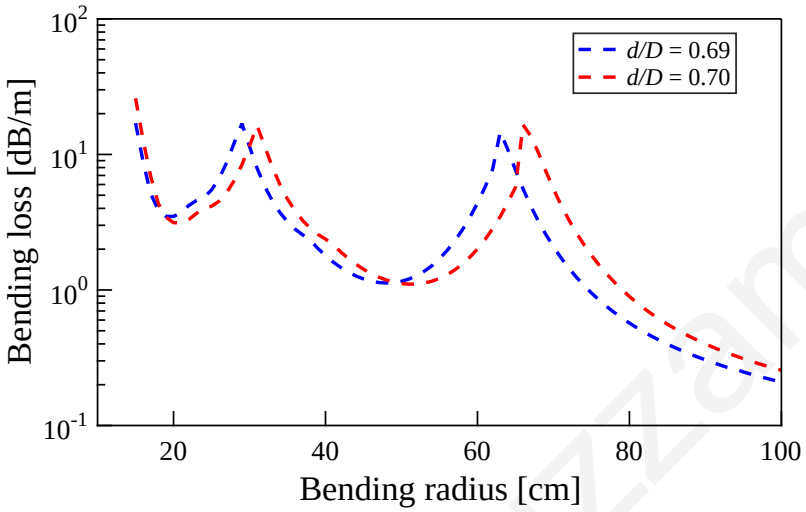

Fig. 4.19. Bending loss as a function of bending radius of the HC-AR fibre.

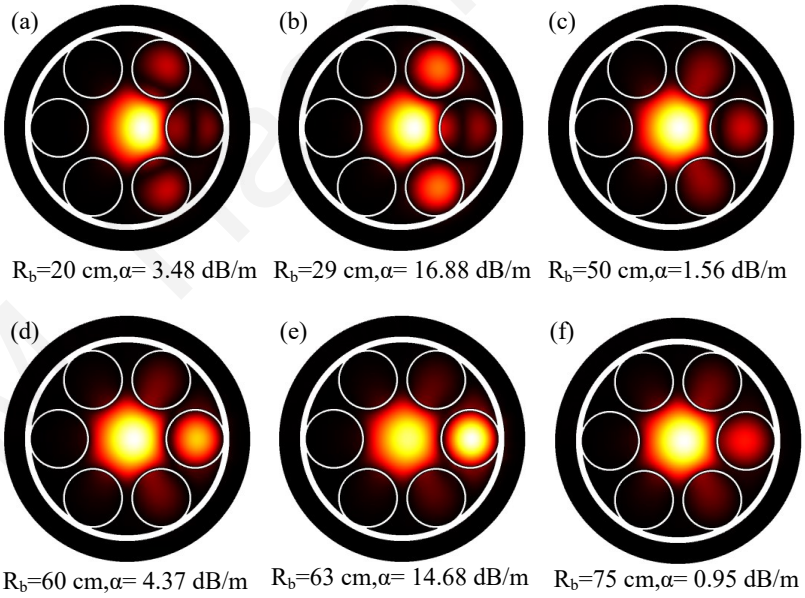

Fig. 4.20. Numerically calculated electric field distribution with loss of the proposed fibre with D=3 mm, d/D=0.69, and t=0.09 mm at an operating frequency of 1 THz.

4.6 Conclusion

Two anti-resonant fibre structures for low loss THz guidance with other additional properties such as dispersion, single-mode guidance and bending loss have been considered. We inves-

Table 4.2: Recently reported THz fibres operating around 1 THz (PC-TIR: Porous core total internal reflection, PC-PBG: Porous core photonic band gap, HC-PBG: Hollow core photonic band gap, HC-IC: Hollow core inhibited coupling, EML: Effective material loss).

THz fibres	Structure Core-cladding	Operating frequency	Guiding mechanism	Fibre material	EML	
					In cm-1	In dB/m
Ref [97]	Octagonal -Octagonal	1 THz	PC-TIR	Topas	0.076	33.0068
Ref [101]	Hexagonal- Hexagonal	1 THz	PC-TIR	Teflon	0.12	52.116
Ref [106]	Circular-Octagonal	1 THz	PC-TIR	Topas	0.056	24.3208
Ref [105]	Hexagonal- Kagome	1 THz	PC-IC	Topas	0.035	15.2005
Ref [99]	Hexagonal-Honeycomb	1.05 THz	PC-PBG	Topas	0.046	20
Ref [116]	Hexagonal- Hexagonal	1 THz	PC-PBG	Topas	0.099	43.2
Ref [107]	HC -Triangular lattice	1 THz	HC-IC	Teflon	0.01	4.343
Ref [112]	HC-Triangular lattice	0.95 THz	HC-PBG	HDPE	0.0015	0.66
Ref [100]	HC -Kagome	1 THz	HC-IC	PMMA	0.4	173.72
Proposed Design-I	HC -Nested tube lattice	1 THz	HC-IC	Topas	0.00011	0.05
Proposed Design-II	HC - tube lattice	1 THz	HC-IC	Topas	0.00013	0.06

tigated the effect of nested anti-resonant elements on losses and the modal properties of a hollow-core for THz applications for the first time. By engineering the design parameters in such a way as to maintain the experimental feasibility of the design, we obtain low effective material loss of 0.05 dB/m at f =1 THz, a 0.4 THz wide low transmission loss window and 0.6 THz wide dispersion flattened band.

Additionally, the proposed HC-NANF requires stacking of only 12 capillaries compared for example to HC-PBG fibres (the fibre in [112] requires 60 hexagonally-shaped air holes in the cladding alone) or porous core fibres ([97] requires 49 air holes in the core alone). Table 4.2 summarizes and directly compares recently reported THz fibres operating around 1 THz (including the proposed HC-NANF structure in this work) in terms of structural parameters, guiding mechanisms and effective material loss. Based on previous reports it is evident that the proposed HC-NANF is the best potential candidate for ultra-low loss, broadband THz wave guiding with high power delivery.

CHAPTER 5

Self-oscillating Optical Frequency Comb Generator based on Optoelectronic Oscillator

5.1 Introduction

Among the photonic assisted methods discribed in section 1.3 for mm-wave and THz signal generation, the optoelectronic oscillator (OEO) and the optical frequency comb generator (OFCG) are amongst the most widely used. The former (OEO) provides very high spectral purity signals as both microwave and modulated optical outputs [3], while the latter (OFCG) is a convenient way to generate phase correlated and accurately spaced optical tones with many applications, including millimeter-wave and THz signal generation, generation of optical multi-carriers, optical signal processing and optical coherence tomography [26, 131]. Typically, an external modulation-based OFCG relies on an external microwave oscillator to provide the seed tone, but in recent work this has been replaced with OEOs, resulting in self-oscillating optical frequency comb generators (SOFCG) [27, 131].

The conceptual block diagrams of the OEO, OFCG and SOFCG shown in Fig.5.1 are compared and contrasted as follows. A SOFCG is essentially an OFCG with optoelectronic feedback: the optical comb is photodetected, producing a microwave output whose fundamental frequency corresponds to the comb spacing, and this fundamental tone is then used to drive the OFCG, thus completing the loop. Hence the resulting SOFCG shares many of the attributes of the OEO (loop oscillation and generation of a microwave output), but whereas the

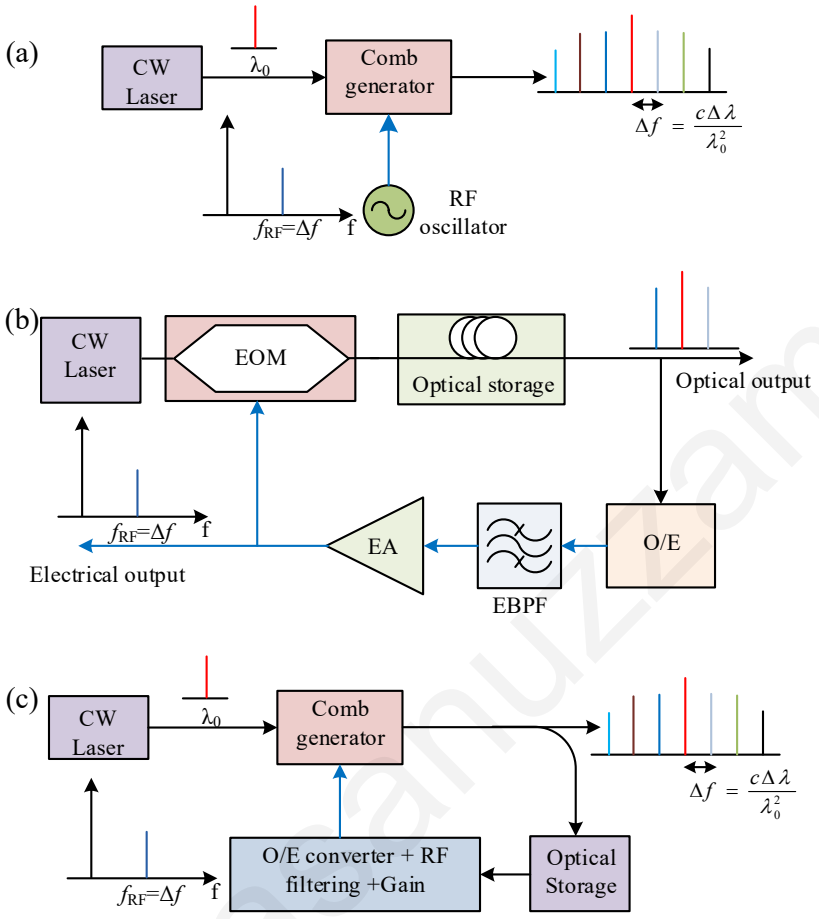

Fig. 5.1. Conceptual block diagram of (a) an external modulation based optical frequency comb; (b) optoelectronic oscillator; and (c) a self-oscillating optical frequency comb. The optical and electrical paths are represented by black lines and blue lines respectively. CW: continuous wave, EOM: electro-optic modulator, EA: electrical amplifier, EBPF: electrical band pass filter.

optical portion of the OEO supports only a single wavelength modulated by the microwave oscillation, the SOFCG supports an optical comb. The SOFCG therefore has the advantage of dispensing with an external microwave source, whilst retaining the low-phase noise attributes of the OEO and the comb generation aspect of the OFCG. Although a conventional OEO could be used to drive a comb generator separately (by connecting the electrical output of the OEO of Fig. 5.1(b) to the RF port of the comb generator of Fig. 5.1(a)), this would result in the need for an additional modulator and associated bias circuitry as compared to Fig.5.1(c), which will add to the system cost and footprint.

In this chapter, the simulation and experimental work on a self-oscillating frequency comb is discussed. Initially, a proof of concept SOFCG model is analyzed using a commercially

available simulation package (VPItransmissionMaker^{TM}) [132]. Then the system is experimentally implemented with commercially available off-the-shelf (COTS) components. The SOFCG is based on a dual-loop topology employing a dual-drive Mach-Zehnder modulator and balanced photodetection [133]. We also applied the SOFCG to implement a RoF link operating at W-band (94.8 GHz), in which two wavelengths are extracted by a programmable wavelength selective switch (WSS), with modulation being subsequently applied to one wavelength prior to heterodyne photo-detection as shown in the conceptual diagram of Fig. 5.2 [134]. We finally indicate an alternative SOFCG topology in which the WSS is integral to the loop, thus avoiding having to photodetect all the tones of the optical comb [135].

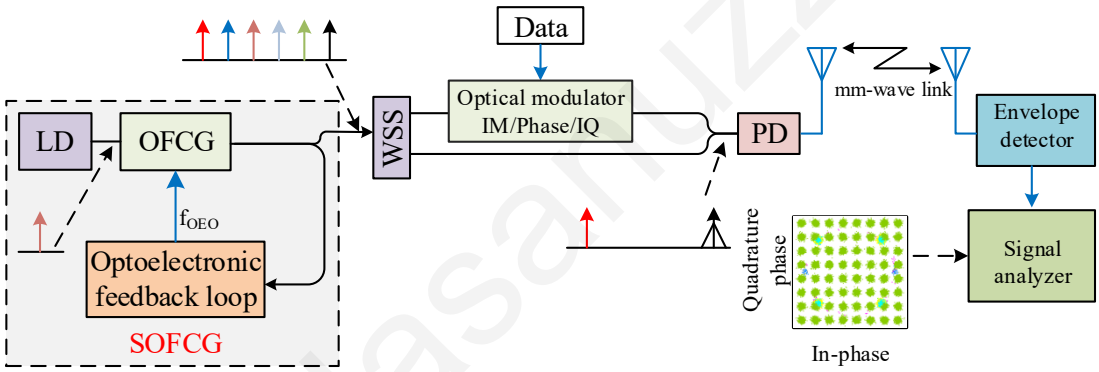

Fig. 5.2. Block diagram of a SOFCG based radio over fibre link. LD - Laser diode, WSS - Wavelength selective switch, IM - Intensity modulation, PD - Photodetector

5.2 Self-oscillating frequency comb generation

Self-oscillating optical frequency comb generation is a promising concept which combines two emerging techniques in microwave photonics, namely optical frequency comb generation and optoelectronic oscillators as described in the earlier section. Several schemes have been reported to generate self-oscillating optical frequency combs. In [136], Sakamoto *et al.* proposed a self-oscillating optical frequency comb based on an OEO loop employing a lithium niobate phase modulator and fibre Bragg grating (FBG) filter. The reported SOFCG in [136] provides a bandwidth of 120 GHz with a frequency spacing of 9.95 GHz. Tunable optical frequency comb generation based on an optoelectronic oscillator was reported in [131]. A wideband (larger than 40 nm) comb with a frequency spacing of 25 GHz and

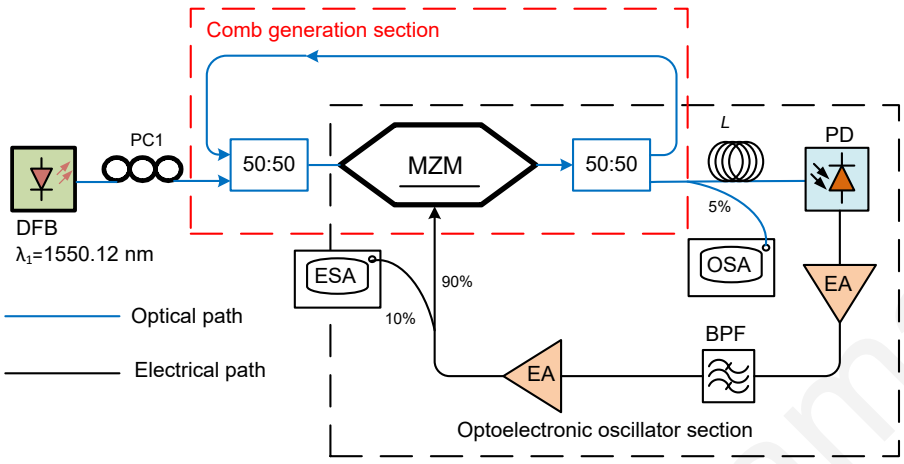

Fig. 5.3. Basic operation principle of the proposed self-oscillating optical frequency comb generator.

single side band phase noise (SSB) of -122 dBc/Hz at 10 kHz offset by incorporating a commercially available integrated OFCG (OptoComb Inc.) in the OEO loop was reported in [131]. In [27], an ultra-flat OFCG based on an OEO loop employing an intensity modulator and a phase modulator in cascade was demonstrated experimentally. The reported SOFCG exhibited 11 flat top lines whose spectral flatness was within 0.82 dB and 0.93 dB when the comb spacing was 10 GHz and 12 GHz respectively.

5.3 Simulation work on SOFCG

In this section, simulation results of an OEO-based optical frequency comb generator (without using an external microwave frequency synthesizer) are presented. A frequency comb generator section (based on an optical feedback loop) is inserted in an OEO loop to realize the SOFCG as shown in Fig. 5.3. The OEO is used to generate a reference microwave source which determines the frequency spacing of the generated comb lines. Thus, a wideband optical frequency comb and low phase noise microwave signal can be generated simultaneously during the OEO's oscillation. To validate the concept, a SOFCG model is analyzed using the commercially available VPItransmissionMaker^{TM} simulation package. The model predicts seven comb lines covering a band width of 30 GHz with a power variation of 20 dB and comb spacing of 5 GHz.

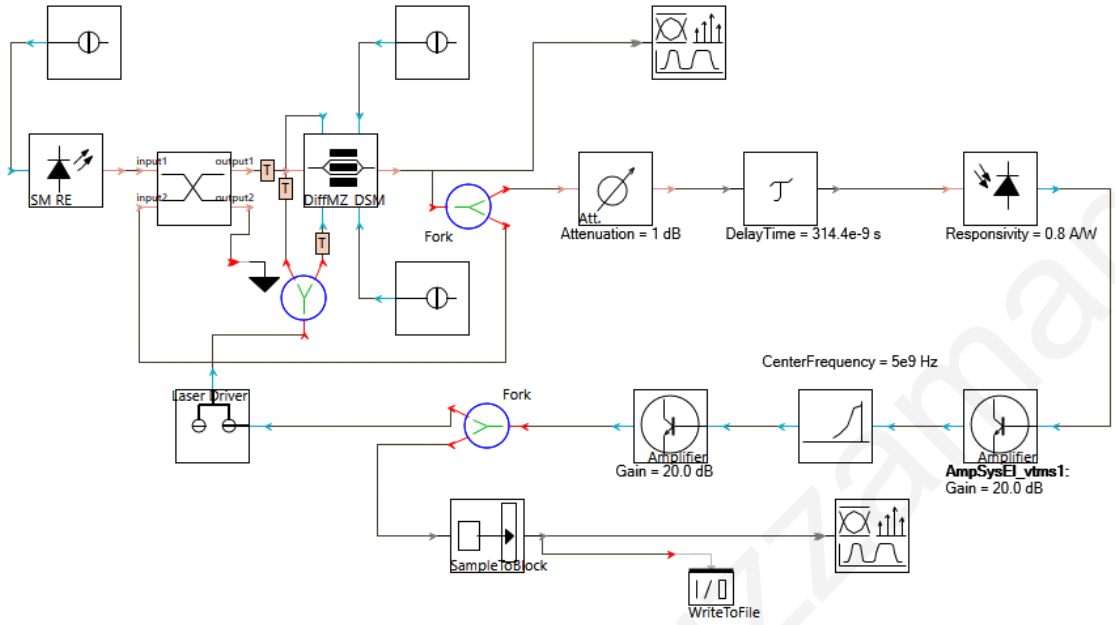

Fig. 5.4. Schematic of SOFCG using the VPItransmissionMakerTM software.

5.3.1 Simulation set-up

The proposed concept has been simulated with VPItransmissionMaker^{TM} software. The schematic layout of the model with realistic parameter values is depicted in Fig. 5.4 for the self-oscillating optical comb as described above. The DFB laser (of Fig. 5.3) is modelled by a single-mode rate-equation based semiconductor laser (SM-RE), with optical output power of 17 mW at a wavelength of 1550 nm. The output optical signal is fed to a 3 dB four-port directional coupler which is modelled by a cross coupler with coupling coefficient 0.5. Another input of the cross coupler is provided from the output of a fork module which is placed after a quadrature-biased dual drive MZM with V_π = 5 V, optical insertion loss 5 dB, and extinction ratio 35 dB. A delay signal unit is used to realize the single mode fibre (SMF) section of Fig. 5.3; the delay time is fixed to $\tau = 314.4$ ns which is equivalent to a fibre length of 65 m. An attenuator is used to characterize the loss of the optical fibre and device to fibre coupling loss. A PIN photodiode (PD) model is used as an optical to electrical converter with responsivity 0.8 A/W, and thermal noise, dark current and shot noise parameters are enabled during simulation to represent the noise characteristics of the PD. A band-pass filter (BPF) is represented by a fourth order Butterworth filter with a centre frequency of 5 GHz and 3-dB bandwidth of 12 MHz. The centre frequency of the BPF determines the gain bandwidth of the

OEO loop and hence determines the oscillation frequency and comb spacing. The low noise amplifier (LNA) and power amplifier (PA) section of Fig. 5.3 are realized with an electrical amplifier module, and two electrical amplifier stages are used during the simulation, each with 20 dB gain.

The simulation model is executed with a periodic boundary condition with a default time window equal to 32786/bit rate, where the bit rate default = 5 Gb/s. In VPItransmissionMaker^{TM}, periodic boundary conditions allow parallel simulation of the RF and optical elements [137]. The time window determines the frequency resolution of the signal analyser and the frequency resolution is inversely proportional to the time window.

5.3.2 Simulation results and discussion

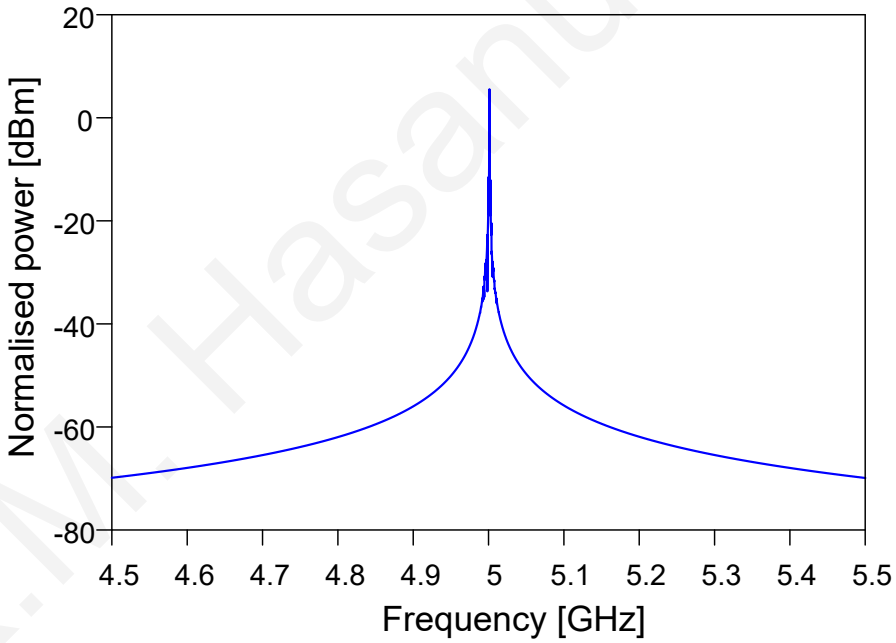

Fig. 5.5. Electrical spectrum of the generated oscillation at 5 GHz.

In this section, we present the simulation results of our proposed system which was obtained using the VPItransmissionMaker^{TM} commercial software. We set the parameters of the different electrical and optical components as described in the simulation setup section. Initially we set the electrical amplifier gain to a relatively low value and we observed that there was no oscillation due to insufficient gain in the OEO loop. Then, we set the electrical amplifier gain to a relatively high value and we observed that there were many modes in the oscillation spectrum due to the broad gain bandwidth available. Finally, we set the amplifier gain to

a value for which only one mode oscillates. We set the centre frequency of the electrical band-pass filter to 5 GHz with a 3 dB bandwidth of 12 MHz. Figure 5.5 shows the electrical spectrum of the generated oscillation signal at 5 GHz with a span of 1 GHz. The normalized power of the 5 GHz oscillation signal is 7 dBm. The optical spectrum of the generated optical frequency comb is shown in Fig. 5.6. The comb spacing is 5 GHz, which is equal to the oscillation frequency of the single loop OEO section. The SOFCG provides seven comb lines covering a bandwidth of 30 GHz and the flatness of the comb lines is within 20 dB.

Carrier power to noise power density ratio (CNR) is an important parameter which should be as large as possible for reliable transmission of information. The CNR is defined as the ratio of the carrier power P_C and the noise power density N_0 at the position of the carrier:

$$CNR\,[\text{dBHz}] = 10 \times \log_{10}\left(\frac{P_C}{N_0 \Delta f}\right) \tag{5.1}$$

Here, the noise power density N_0 is normalized to a bandwidth of $\Delta f = 1$ Hz. As seen in Fig. 5.6 the CNR of the spectrum is larger than 75 dBHz at a reference bandwidth of 1 Hz, thus proving the potential usefulness of the proposed comb for communications.

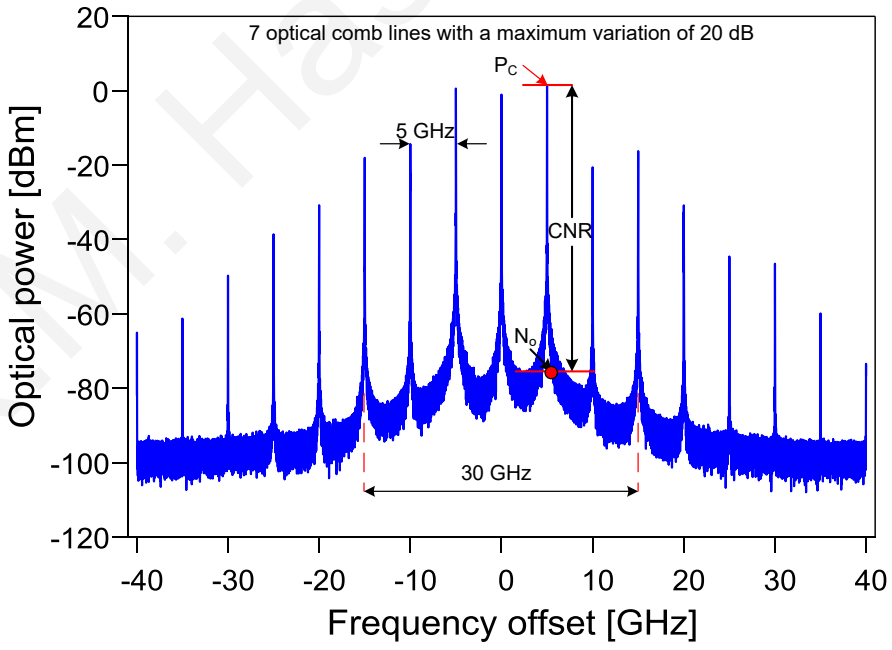

Fig. 5.6. Spectrum of the optical comb.

5.4 Experimental work on SOFCG

A self-oscillating optical frequency comb generator (SOFCG) based on a dual loop opto-electronic oscillator with balanced detection scheme in the optoelectronic feedback section has been experimentally demonstrated. The SOFCG provides 23 comb lines with the frequency spacing equal to 11.84 GHz, the oscillation frequency of the OEO section. Using the SOFCG, a 94.8 GHz mm-wave signal is generated by selecting two tones and heterodyning in a high speed photo diode. The phase noise performance of the generated mm-wave signal is compared with an external synthesizer based mm-wave generation technique and we find the former is superior over the latter. A radio-over-fibre link was implemented with the self-oscillating frequency comb. An LTE Advanced OFDM FDD 64-QAM signal of 20 MHz bandwidth was transmitted over 1.3 m wireless distance with an EVM of 2.23%. The following sections describe this work in details.

5.4.1 SOFCG based mm-wave and THz signal generation

The self-oscillating optical frequency comb (SOFCG) topology that we use in this work is shown in Fig. 5.7(a). It is based on an OFCG that employs a dual-drive Mach-Zehnder modulator (MZM) as shown in Fig. 5.7(b); applying large-signal RF inputs of different amplitudes, a flat comb can be obtained as described in [138]. The optoelectronic feedback loop in Fig. 5.7(a) comprises a dual-loop balanced detection scheme in which a balanced photodetector is fed via a short (L_1) and long (L_2) fibre respectively, an electrical band pass filter (EBPF) for selection of the desired frequency and an electrical amplifier (EA) which along with an erbium-doped fibre amplifier (EDFA) is required to meet the loop gain condition. By using balanced photo-detection, the impact of RIN from the optical source is reduced, and it has also been shown that this approach reduces the phase noise of microwave photonic links through common mode noise suppression [139,140]. Moreover, the dual-loop configuration is a well-known technique in OEOs, designed to overcome the limitation of a small microwave free spectral range (FSR) that single-loop OEOs suffer from, by applying side-mode suppression [141]. Hence the combination of balanced photodetection and a dual-loop topology helps to minimize the SOFCG phase noise.

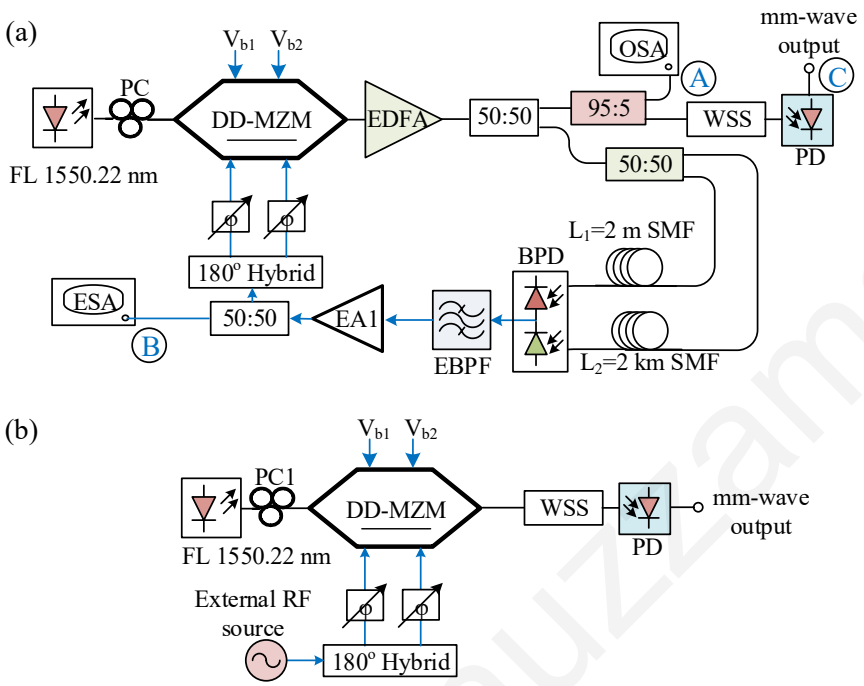

Fig. 5.7. Experimental set-up of: (a) SOFCG; (b) OFCG. The optical and electrical paths are represented by black and blue lines respectively. FL: fibre laser, DD-MZM: dual-drive Mach-Zehnder modulator, EDFA: erbium doped fibre amplifier, BPD: balanced photodetector, EBPF: electrical band pass filter, EA: Electrical amplifier, WSS: wavelength selective switch, ESA: electrical spectrum analyzer, OSA: optical spectrum analyzer, PC: polarization controller

5.4.2 Signal analysis based on DDMZM and balanced detection

For the signal analysis we considered the simplified open-loop version of the SOFCG from Fig. 5.7(a) as illustrated in Fig. 5.8. RF signals of different amplitudes (but identical frequency ω_m) are injected into the two arms of the DDMZM with push-push architecture [142]. The phase shifts induced by the applied RF signals are $S_1(t) = A_1\cos(\omega_m t)$ and $S_2(t) = A_2\cos(\omega_m t)$ respectively, and the output of the modulator can be expressed as [138]:

$$E_{\text{out}} = \frac{1}{2}E_{\text{in}}\left[e^{j\theta_1}e^{jA_1\cos\,\omega_m t} + e^{j\theta_2}e^{jA_2\cos\,\omega_m t}\right] \tag{5.2}$$

where $\theta_1 = \pi V_{b1}/V_{\pi 1}$ and $\theta_2 = \pi V_{b2}/V_{\pi 2}$ are the phase shifts induced by the DC bias of arms 1 and 2 respectively; $A_1 = \pi V_1/V_{\pi 1}$ and $A_2 = \pi V_2/V\pi_2$ are the modulation indices in which V_1 and V_2 are the amplitudes of the RF drive signals and $V_{\pi 1}$ and $V_{\pi 2}$ are the half-wave voltages of arms 1 and 2 respectively.

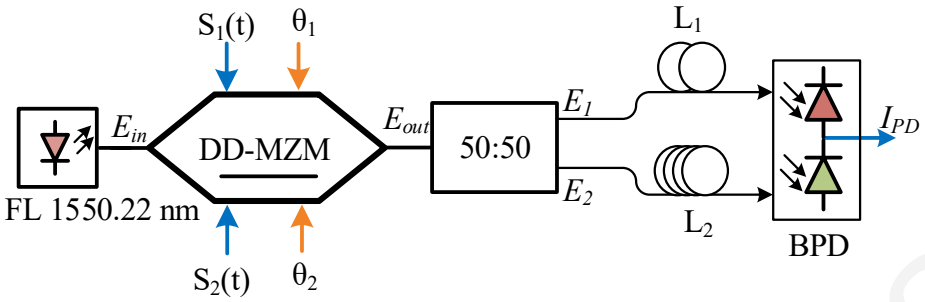

Fig. 5.8. Simplified open-loop version of Fig. 5.7 (a) for signal analysis. The optical and electrical paths are represented by black and blue lines respectively.

The electric fields at the two output ports (E_1 and E_2) of the directional coupler can be expressed by the following equations, considering a 90-degree phase difference between the two ports [143]:

$$E_1 = \frac{1}{2\sqrt{2}} E_{\text{in}} \left[e^{j\theta_1} e^{jA_1 \cos \omega_m t} + e^{j\theta_2} e^{jA_2 \cos \omega_m t} \right] \tag{5.3}$$

and

$$\begin{aligned} E_2 &= \frac{e^{i\frac{\pi}{2}}}{\sqrt{2}} E_{\text{out}} \\ &= -\frac{1}{2\sqrt{2}} E_{\text{in}} [e^{-j\theta_1} e^{jA_1 \cos \omega_m t} + e^{-j\theta_2} e^{jA_2 \cos \omega_m t}]. \end{aligned} \tag{5.4}$$

Assuming the two paths are perfectly balanced (through the use of variable optical attenuators and phase shifters), the corresponding photodetected currents are:

$$\begin{aligned} I_1 &= \Re E_1 E_1^* \\ &= \frac{1}{2\sqrt{2}} \Re |E_{\text{in}}|^2 [2 + e^{j(\theta_1 - \theta_2)} e^{j(A_1 - A_2) \cos \omega_m t} \\ &\quad + e^{-j(\theta_1 - \theta_2)} e^{-j(A_1 - A_2) \cos \omega_m t}] \end{aligned} \tag{5.5}$$

and

$$\begin{aligned} I_2 &= \Re E_2 E_2^* \\ &= \frac{1}{2\sqrt{2}} \Re |E_{\text{in}}|^2 [2 + e^{-j(\theta_1 - \theta_2)} e^{j(A_1 - A_2) \cos \omega_m t} \\ &\quad + e^{j(\theta_1 - \theta_2)} e^{-j(A_1 - A_2) \cos \omega_m t}]. \end{aligned} \tag{5.6}$$

where $\Re$ is the responsivity for each photodiode of the BPD (where it is assumed they are identical). Hence the resulting BPD photocurrent is given by:

$$\begin{aligned} I_{PD} &= I_1 - I_2 \\ &= j^2\sqrt{2}\Re|E_{\text{in}}|^2\left[\frac{e^{j(\theta_1-\theta_2)}-e^{-j(\theta_1-\theta_2)}}{2j}\right]\cdot \\ &\quad \left[\frac{e^{j(A_1-A_2)\cos\,\omega_m t}-e^{-j(A_1-A_2)\cos\,\omega_m t}}{2j}\right] \\ &= -\sqrt{2}\Re|E_{\text{in}}|^2[\sin(\theta_1-\theta_2)\sin((A_1-A_2)\cos\omega_m t]. \end{aligned} \tag{5.7}$$

Upon filtering by the bandpass filter, the first-order term in Eq. 5.7 is selected:

$$I_{PD} = -2\sqrt{2}\Re|E_{\text{in}}|^2\sin(2\Delta\theta)J_1(2\Delta A)\cos\omega_m t. \tag{5.8}$$

where $\Delta A = (A_1 - A_2)/2$ and $\Delta\theta = (\theta_1 - \theta_2)/2$. From Eq. 5.8, we find that I_{PD} is maximized when $\Delta\theta = \pi/4$ which is also the condition of maximum conversion efficiency for ultra-flat comb generation [138].

A. Experimental set-up

The SOFCG depicted in Fig. 5.7(a) was evaluated experimentally. A fibre laser (FL) of 15 Hz linewidth and 13 dBm output power at 1550.22 nm was used as a continuous-wave (CW) optical source for the DDMZM. The DDMZM functions both as the E/O converter for the optoelectronic loop and as a frequency comb generator as described in the previous section. The output of the DDMZM was then amplified by an erbium-doped fibre amplifier (EDFA) and split into two paths by a 50:50 coupler, with one being used to form the loop. The other was diverted (via a 95:5 coupler which was used to monitor the optical spectrum at point Ⓐ with a Yenista Optics OSA-20 optical spectrum analyzer) to the optical output of the SOFCG. Short and long fibre lengths of L_1 = 2 m and L_2= 2 km respectively were used to feed a balanced photodiode (Finisar BPDV2150R, with a 3−dB bandwidth of 43 GHz and responsivity of 0.45 A/W). A microwave band pass filter (EBPF) (Tamagawa SBF-203 BPF with a 3-dB bandwidth of 300 MHz) was used to select the desired RF signal, which was subsequently amplified by a low noise amplifier (SHF 806E with 26 dB gain) prior to a RF power splitter, one output of which was connected to the RF port of the DDMZM to close the SOFCG loop and the other to an electrical signal analyzer (Agilent N9030A PXA) at point

Ⓑ for monitoring the spectrum and measuring the phase noise performance. In addition, by selecting any two comb lines at the optical output of the SOFCG it is possible to generate (through heterodyning in a photodiode with sufficiently high bandwidth) mm-wave signals of integral multiples of the comb frequency spacing. By placing a programmable wavelength selective switch (Finisar WaveShaper 16000S) immediately after the optical output of the SOFCG, we selected two lines in order to generate the corresponding mm-wave signal at the output of a high speed photodiode (Finisar XPDV4120R) as indicated by point Ⓒ in Fig. 5.7 (a).

5.4.3 SOFCG results for RF signal generation

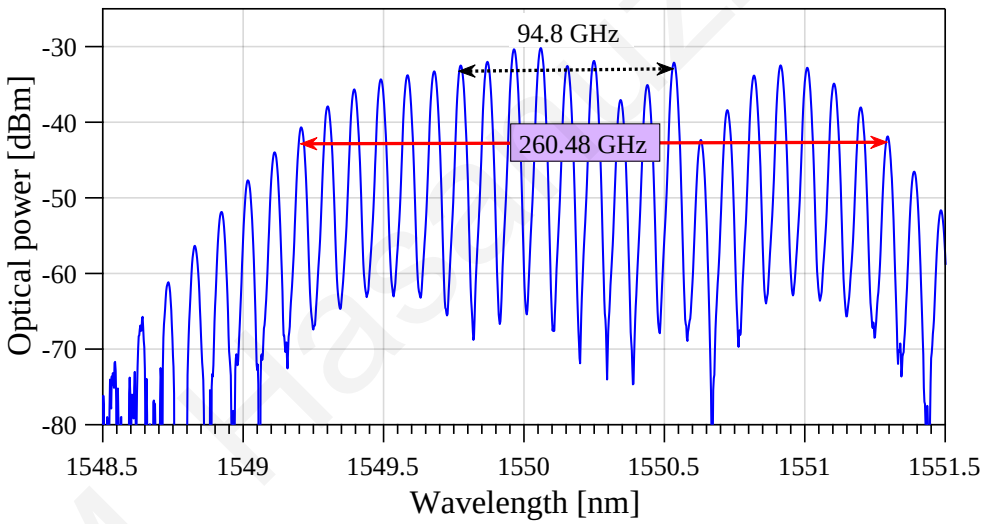

Fig. 5.9. Optical spectrum of the generated optical frequency comb with a frequency spacing of 11.84 GHz at the centre wavelength of 1550.22 nm (measured with an OSA at point Ⓐ in Fig. 5.7(a))

The optical spectrum of the generated comb lines from the SOFCG (as taken from point Ⓐ in Fig. 5.7(a) is shown in Fig. 5.9; the comb spacing is 11.84 GHz, with 23 comb lines being generated considering approximately 12 dB deviation from the peak. In this preliminary proof-of-concept work, comb flatness was not prioritized, given that the end application was mm-wave RoF (as will be described in subsection 5.4.5). The electrical spectrum of the corresponding 11.84 GHz signal (measured at point Ⓑ in Fig. 5.7(a)) is shown in Fig. 5.10. This frequency is determined by the dual-loop fibre topology of the SOFCG and the passband of the EBPF. A side mode suppression ratio of 60 dB was obtained with the balanced detection based dual-loop configuration, as shown in Fig. 5.10(c). In

addition, the single side band (SSB) phase noise of the generated RF oscillation at point Ⓑ was measured using the phase noise measurement functionality of the signal analyzer, and this is compared with a commercial microwave synthesizer set to an oscillation frequency of 11.84 GHz (HP 83620A) in Fig. 5.11. The phase noise of the SOFCG is lower than the HP synthesizer beyond the 1 kHz offset. The SSB phase noise of the 11.84 GHz signal at a 10 kHz offset is 22 dB lower for the SOFCG (-110 dBc/Hz) than for the HP 83620A (-88 dBc/Hz). Table 5.1 compares and contrasts some recently reported SOFCG in terms of optical bandwidth, number of comb lines, comb spacing and phase noise. As indicated in Table 5.1 our proposed system provides wider optical bandwidth with typical phase noise than the other recently reported articles. Additionally, [27] used two modulators (cascading of a DD-MZM with a PM) while our system requires only one modulator (DD-MZM)

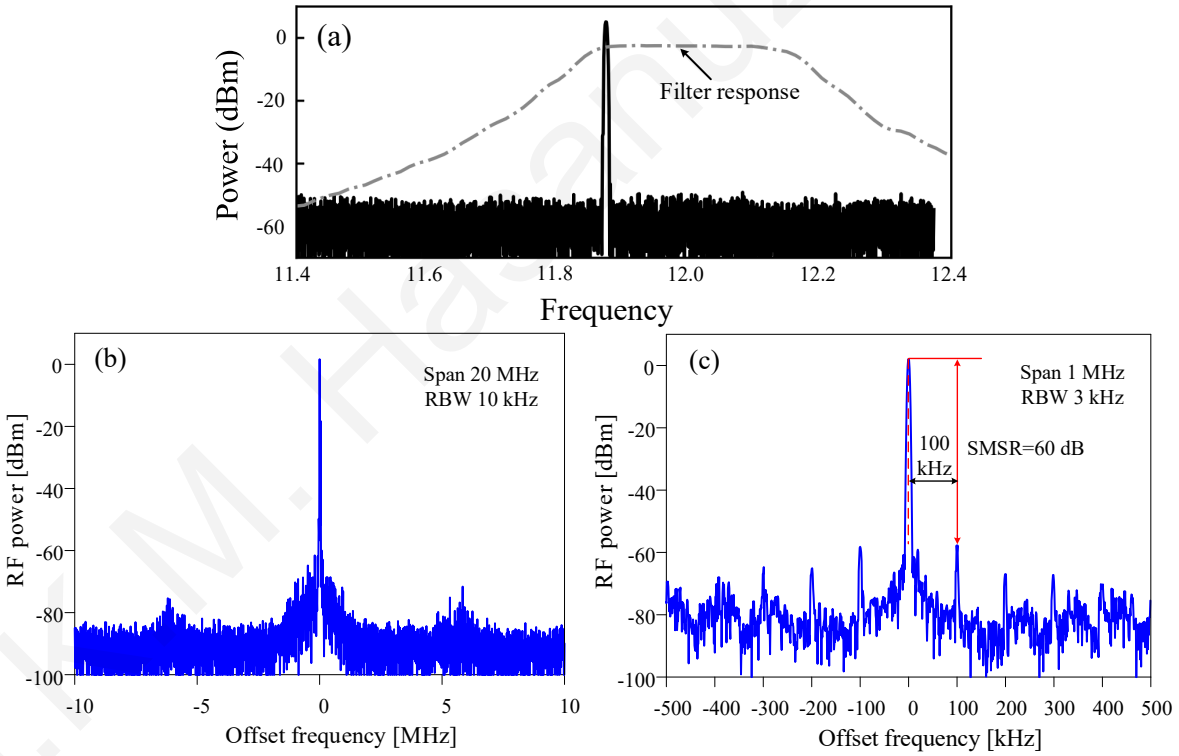

Fig. 5.10. Electrical spectrum of the 11.84 GHz signal. (a) Span 2 GHz (b) Span 20 MHz, RBW 10 kHz (c) Span 1 MHz, RBW 3 kHz. A side mode suppression ratio of 60 dB has been obtained.

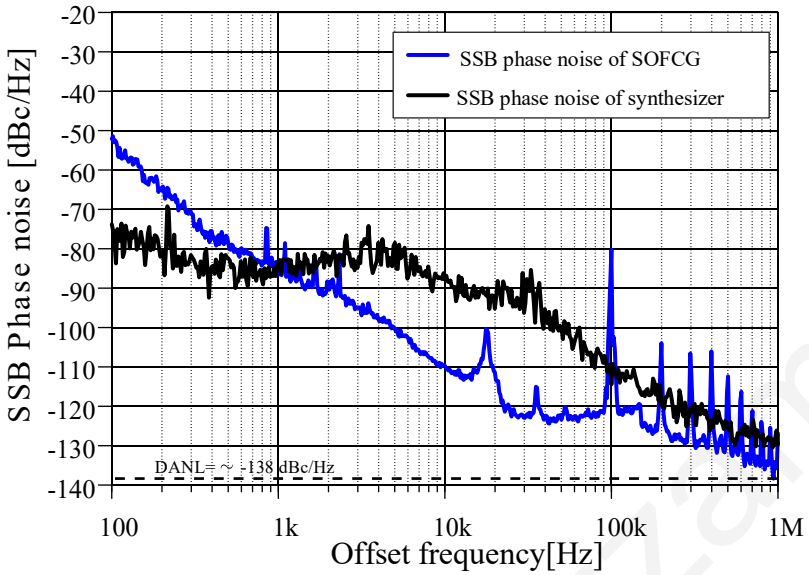

Fig. 5.11. SSB phase noise of the 11.84 GHz oscillation measured at point Ⓑ for the SOFCG (blue line) and of an HP 83620A synthesizer (black line).

Table 5.1: Comparison of recently reported SOFCG.

Ref.	Optical bandwidth	Comb lines	Comb spacing	Phase noise
[144]	120 GHz (10 dB)	13	9.95 GHz	-93 dBc/Hz @ 100 kHz
[27]	160 GHz (10 dB)	17	10 GHz	-122 dBc/Hz @ 10 kHz
	156 GHz (10 dB)	14	12 GHz	-115 dBc/Hz @ 10 kHz
[145]	144 GHz (10 dB)	13	12 GHz	Not available
	120 GHz (10 dB)	13	10 GHz	-101 dBc/Hz @ 10 kHz
[62]	86 GHz (10 dB)	9	10.89 GHz	-93 dBc/Hz @ 10 kHz
Our Work	260 GHz (12 dB)	23	11.84 GHz	-110 dBc/Hz @ 10 kHz

5.4.4 Low phase noise mm-wave generation using SOFCG and comparison with OFCG- and RF synthesizer based approaches

Using the wavelength selective switch for the SOFCG, we selected two lines spaced eight intervals apart (Fig. 5.12(a)) in order to generate a 94.8 GHz signal (Fig. 5.12(b)) at the output of the high speed photodiode (point Ⓒ in Fig. 5.7(a)) and then measured the SSB phase noise. We then proceeded to compare the phase noise performance of the SOFCG with that of the corresponding OFCG shown in Fig. 5.7, in order to verify the superiority of the former method. In this case the OFCG was driven by an HP 83620A synthesizer at 11.84 GHz, with the WSS again set to filter out two comb lines spaced eight intervals apart so as to generate a 94.8 GHz signal. In addition to direct generation of the 94.8 GHz signal through use of the WSS and heterodyning, it is also possible in principle to use electronic frequency multiplication of the SOFCG's RF oscillation frequency. With this approach, a frequency multiplier would be placed at point Ⓑ in Fig. 5.7(a), with a multiplication factor set to eight. However, when a reference microwave signal is multiplied by N, the phase noise is degraded by $20 \times \log_{10} N$, which for a factor of eight results in an additional 18 dB penalty. We therefore used this and the measured results from subsection 5.4.3 in order to estimate the phase noise performance of the SOFCG and HP 83620A synthesizer when electronic multiplication is used instead of comb line selection and heterodyning. The comparison between the SOFCG, the OFCG, and the RF synthesizer for the SSB phase noise performance at 94.8 GHz is shown in Fig.5.13 and also summarized in Table 5.2 for both the

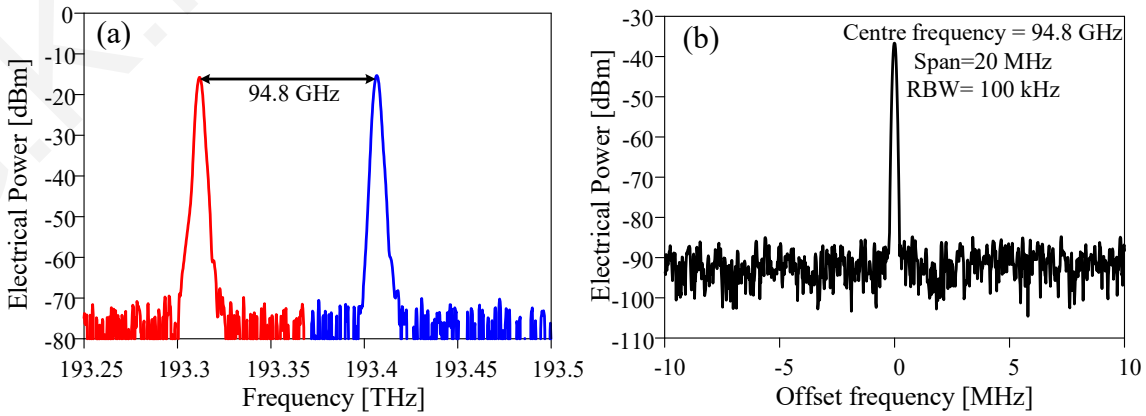

Fig. 5.12. (a) Optical spectrum of two tone signal with spacing of 94.8 GHz (b) The electrical spectrum of the generated 94.8 GHz oscillation

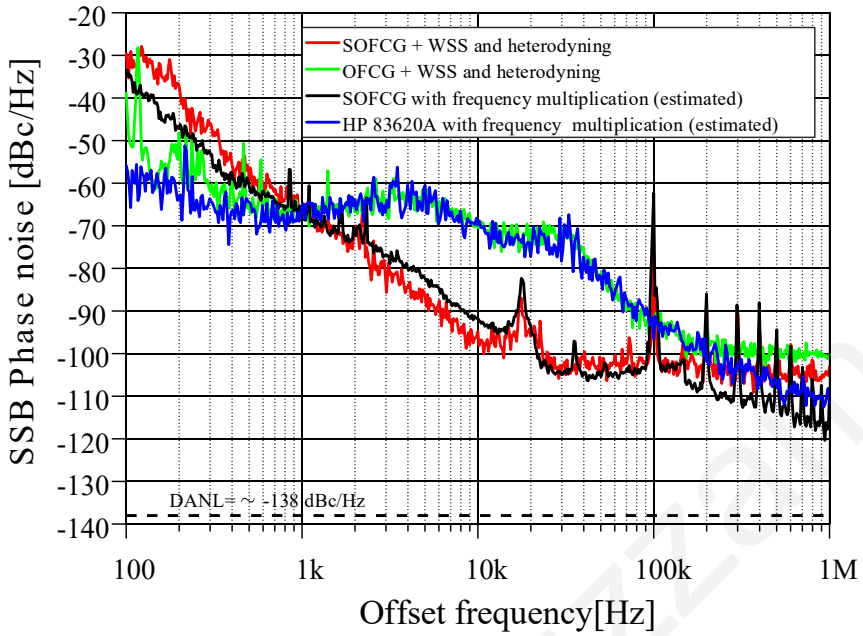

Fig. 5.13. Measured SSB phase noise of: 94.8 GHz signal generated using SOFCG (red line); 94.8 GHz signal generated using conventional OFCG (green line). Estimated SSB phase noise of the 94.8 GHz signal using SOFCG and multiplication (black line) and of the 94.8 GHz signal using a synthesizer and multiplication (blue line).

WSS-heterodyning approach and the electronic multiplication method. From Fig.5.13 and Table 5.2 it is seen that the SOFCG-based mm-wave generation using heterodyning of the comb lines performs better than the other approaches. The SSB phase noise of this method is 27 dB better than the conventional OFCG based approach at an offset frequency of 10 kHz. The improvement is intrinsically due to the SOFCG topology, which in a similar way to OEO topologies can provide optoelectronic oscillation of high spectral purity inside the loop.

Table 5.2: SSB phase noise (dBc/Hz) performance at 94.8 GHz for the SOFCG and OFCG using WSS and heterodyning (measured) and using electronic multiplication ($\times 8$) of the 11.84 GHz signal from the OFCG and RF synthesizer (estimated).

SSB Phase Noise (dBc/Hz)	Offset frequency			
	100 Hz	1 kHz	10 kHz	100 kHz
SOFCG + WSS and heterodyning	-32.01	-65.92	-96.99	-101.06
SOFCG with frequency multiplication (estimated)	-33.55	-66.04	-92.09	-101.46
OFCG + WSS and heterodyning	-45.87	-66.68	-69.66	-92.68
HP 83620A with frequency multiplication (estimated)	-58.92	-66.01	-70.50	-92.01

5.4.5 SOFCG- based radio-over-fibre link

A. Experimental set-up

We developed a 94.8 GHz RoF link based on the SOFCG arrangement of Fig. 5.7. The proof-of-concept experimental set-up is illustrated in Fig. 5.14. The two-tone optical signal required for heterodyning in order to generate the mm-wave carrier was obtained from the SOFCG (Fig.5.14(a)) using the techniques described in subsection 5.4.4. A Finisar WaveShaper 16000S was used to select two comb lines (separated by 94.8 GHz) and route them into two different output ports. One of these outputs was routed through a MZM for data modulation as shown in Fig. 5.14(b); we used an Agilent PSG vector signal generator (E8267D) to generate a LTE-A standard downlink signal centered at 1 GHz with a bandwidth of 20 MHz and modulation format 64 QAM. The modulated comb line was combined with the other comb line. The combined optical signal was then amplified by an EDFA; filtered by a 1 nm tunable optical band pass filter to remove the out-of-band amplified spontaneous emission (ASE); and adjusted by a variable optical attenuator (VOA) to control the input optical power before heterodyning in a high speed photodiode (Finisar XPDV4120R) as shown in Fig. 5.14(c). The output of the photodetector was amplified by a power amplifier (PA). The amplified signal was connected to a horn antenna with a gain of 23 dBi (at 95

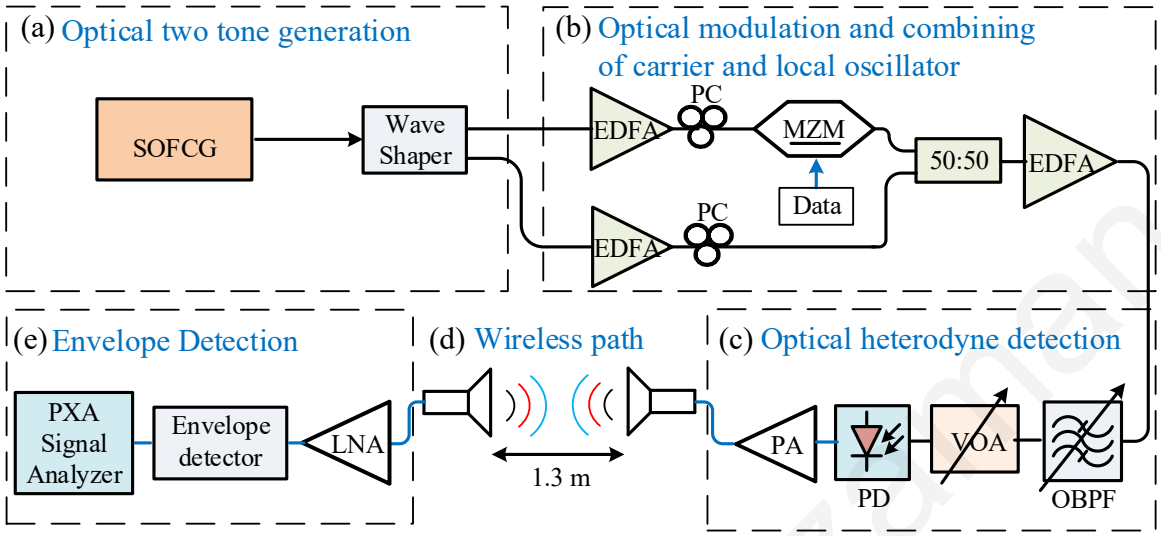

Fig. 5.14. Experimental setup of the SOFCG based radio over fibre link. (a) Optical two tone generation section (b) Optical modulation and combining of carrier and local oscillator (c) Optical heterodyning in high speed photodetector (d) Wireless section (e) Envelope detection section. The SOFCG block consists of the arrangement in Fig. 5.7.

GHz) and propagated over a 1.3 m wireless link. A second identical horn antenna placed in the same polarization was used to receive the radiated signal. The received W band signal was then amplified by a low noise amplifier (LNA), down converted by an envelope detector and analyzed by a vector signal analyzer (Agilent N9030A PXA). A Schottky barrier diode (SBD) was used as the envelope detector.

B. Experimental results and discussion

(i) Effect of modulating signal power: The effect of modulating signal power (P_{in}) on the error vector magnitude (EVM) under varying modulating signal power is depicted in Fig. 5.16(a) for a LTE-A 64 QAM signal transmitted over a 1.3 m wireless distance. The modulating signal power was varied from -4 dBm to 5 dBm and we found that the EVM is reduced for higher modulating signal powers. This is due to the fact that increasing modulating power enhances the SNR of the signal, resulting in a low EVM as shown in Fig. 5.16 (b)-(d).

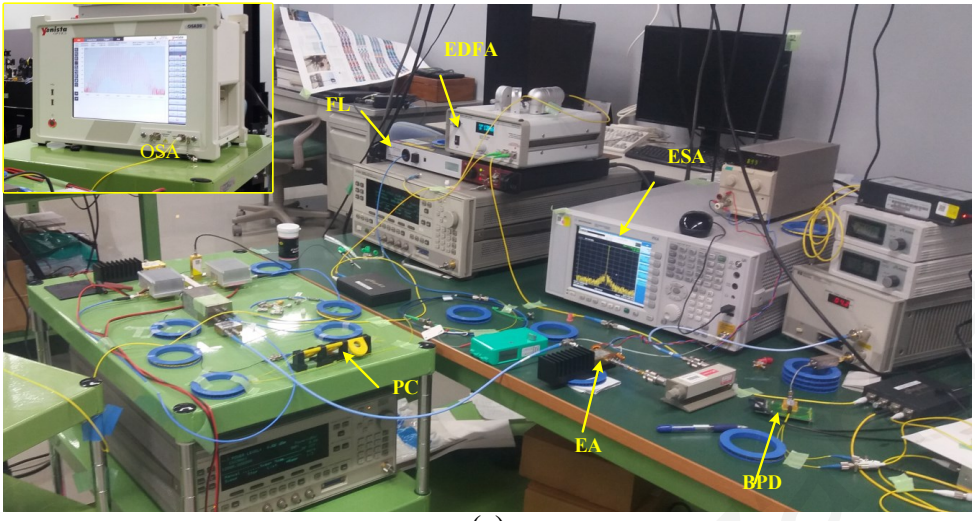

(a)

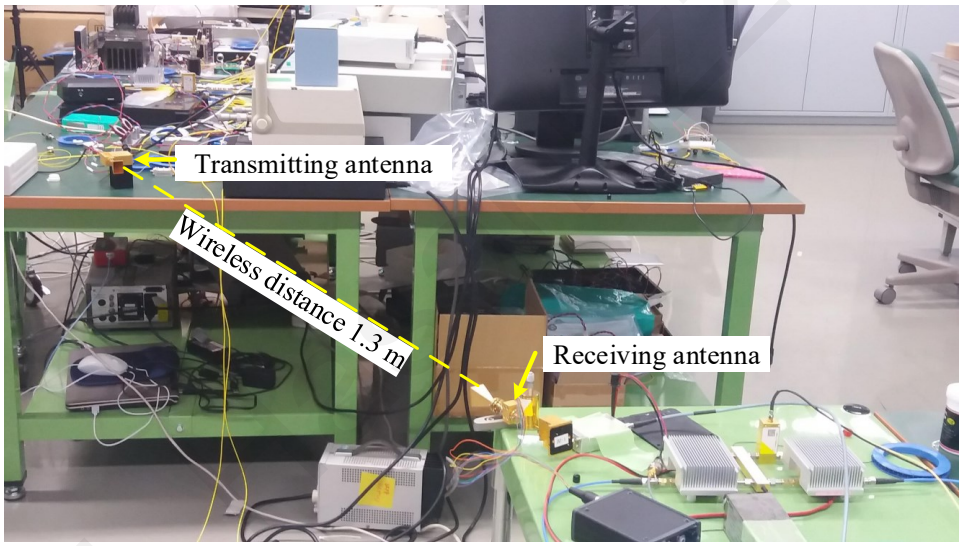

(b)

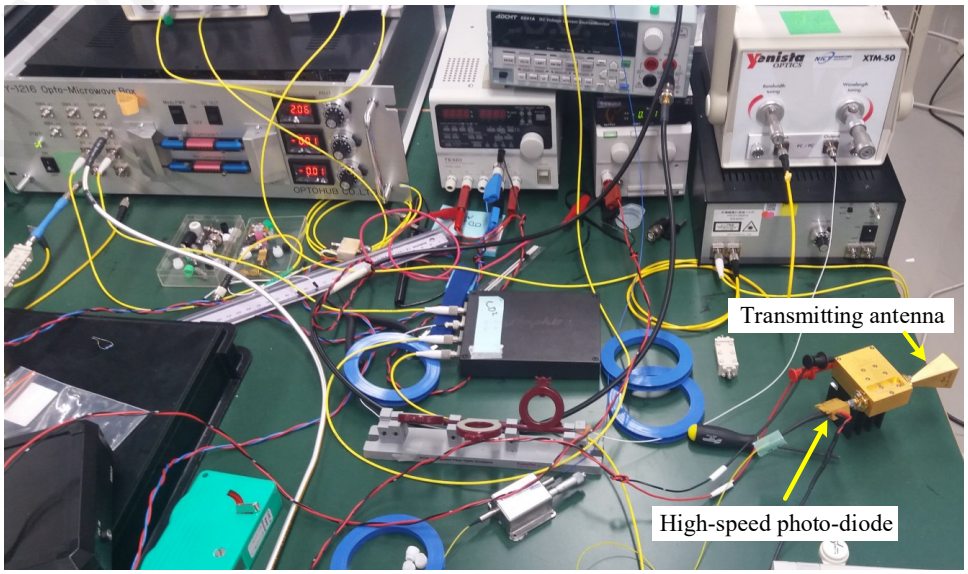

(c)

Fig. 5.15. Photographs of (a) SOFCG (b) Wireless section (c) Optical modulation and heterodyning section.

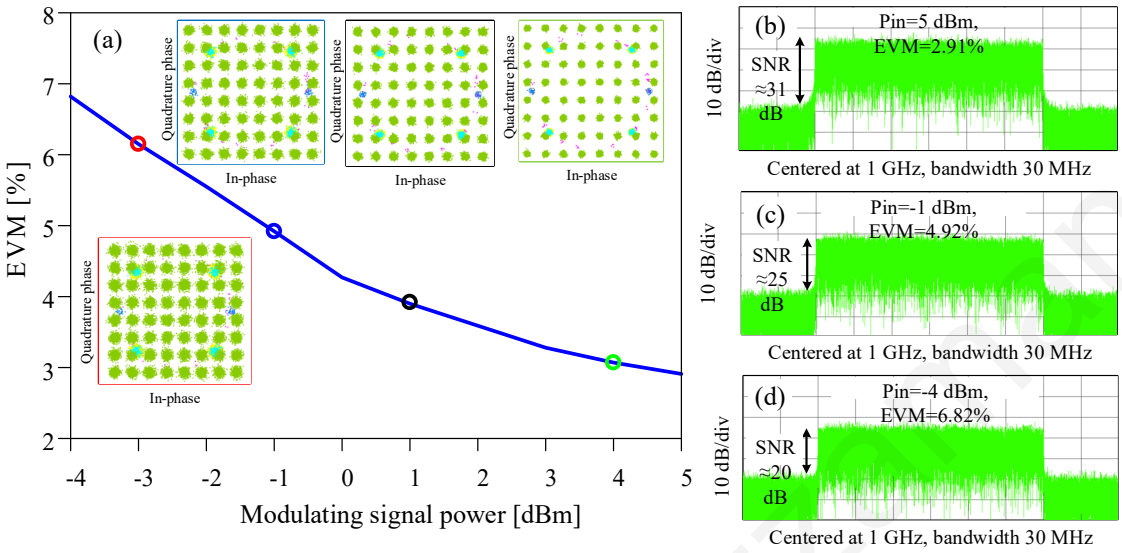

Fig. 5.16. (a)EVM vs modulating signal power. The colour of the frame corresponds to the colour of the dot points in the plot. (b)-(d) Electrical spectrum of the demodulated signal for different modulating power condition. EVM decreases with the increment of modulating power due to the increment of SNR (64 QAM OFDM signal, 1.3 m wireless transmission distance).

(ii) Effect of photocurrent:A variable optical attenuator in front of the photodiode was then used to adjust the incident optical power and hence the generated I_P. The measured EVM as a function of photocurrent (I_P) is illustrated in Fig. 5.17 for a LTE-A 64 QAM signal transmitted over a 1.3 m wireless distance. The lowest obtained EVM is 2.23% at I_p =2 mA. For values of I_P above 2 mA, the EVM increases due to the saturation effect in the amplifier stage at the receiver. The measured EVM is degraded by 45% for a 50% reduction of I_p. The insets show the corresponding constellation diagrams. The measured EVM is within the limit of 8% for 64 QAM [10, 146] for a photocurrent above I_P=0.6 mA.

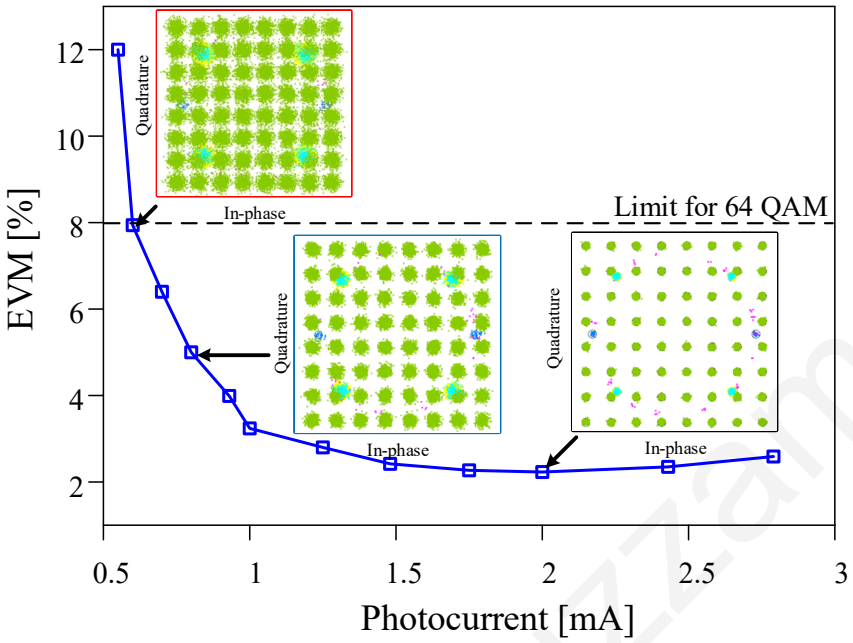

Fig. 5.17. EVM vs photocurrent of the transmission system. The insets are the constellation diagram of a 64 QAM OFDM signal over a 1.3 m wireless transmission distance.

5.5 SOFCG with integral wavelength selection

A simple modification to the SOFCG tropology described in subsection 5.4.1 is illustrated in Fig. 5.18, whereby the WSS is now incorporated within the optoelectronic loop instead of being located after the SOFCG optical output. In this way, rather than all the comb lines being applied to the BPD, the WSS selects two tones corresponding to the RF oscillation frequency of the SOFCG which are then routed to the BPD via the 50:50 coupler and the

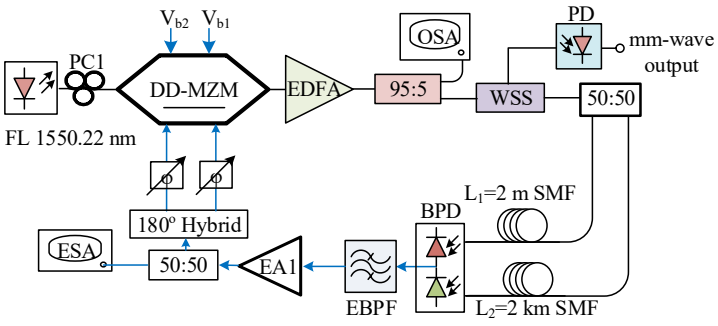

Fig. 5.18. The modified configuration of Fig. 5.7 as an SOFCG where the WSS is included inside the OEO loop.

fibres L_1 and L_2, and a further two tones which are routed to the other output of the WSS in order to generate the desired mm-wave output. Typical phase noise performance is shown in Fig. 5.19, which is comparable to the performance of the SOFCG results shown in Fig. 5.11 and Fig. 5.13.

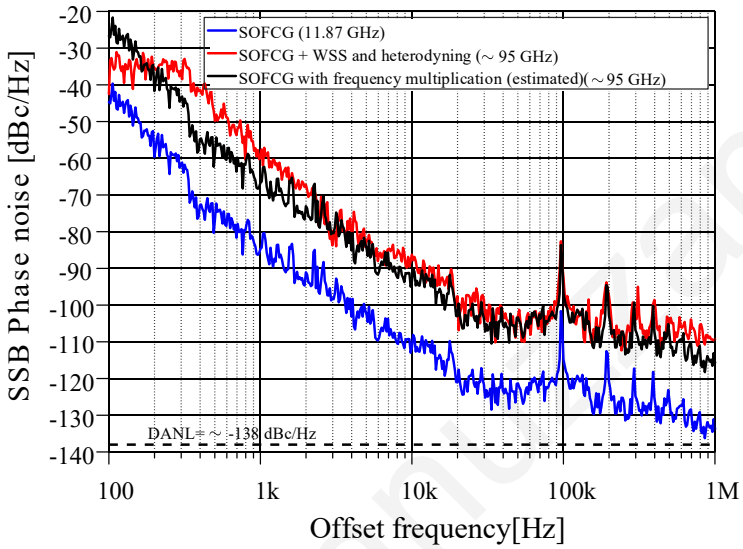

Fig. 5.19. SSB phase noise of the 11.87 GHz oscillation obtained by modified SOFCG (blue line) and of the 95 GHz oscillation obtained from optical heterodyning (red line), along with estimated SSB phase noise (black line) assuming $\times 8$ frequency multiplication of the 11.87 GHz output.

5.6 Conclusion

We have demonstrated a self-oscillating frequency comb generator that combines the advantages of a conventional optical frequency comb with those of an optoelectronic oscillator, namely generation of a stable optical comb allowing mm-wave signals to be synthesized, along with the low phase noise characteristics that are typical of OEOs. The SOFCG provides 23 comb lines with 11.84 GHz spacing that can potentially generate mm-waves up to 260 GHz. The phase noise performance of an SOFCG with a loop oscillation frequency of 11.84 GHz was compared and contrasted with that of a conventional microwave synthesizer, and the phase noise performance when used to generate a 94.8 GHz signal either through optical heterodyning or electronic multiplication was also evaluated. The SSB phase noise of the 11.84 GHz oscillation is -110 dBc/Hz at a 10 kHz offset, while for the 94.8 GHz output it is -97 dBc/Hz at a 10 kHz offset.

The SOFCG was then used to implement a W-band radio-over-fibre link, in which an LTE Advanced standard 64 QAM signal was sent over a wireless path of 1.3 m with an EVM as low as 2.35%. Finally, we have indicated how the SOFCG topology may be potentially modified via the inclusion of the wavelength selective switch within the optoelectronic loop of the SOFCG, without adversely affecting phase noise performance..

CHAPTER 6

Tunable OEO and THz Transmission

6.1 Introduction

Since the THz region is positioned between the microwave and infrared, there exist two enabling technologies for mm-wave and THz signal generation, namely electronics and photonics [20, 147]. Apart from diode-based approaches, the multiplication method is also used, whereby the mm-wave signal can be generated from a low-frequency oscillator by frequency multiplication. However, the phase noise of the output signal increases according to the relationship $20\times\log_{10}(N)$, where N is the multiplication factor, meaning a 6 dB increase of phase noise with every doubling of frequency which in turn makes this method unsuitable for generating low phase noise mm-waves. In contrast, photonic-assisted approaches to generate mm-waves and THz waves not only allow the generation of high-quality carriers but also enable distribution to a remote site via optical fibre. Of the photonics-based approaches to microwave and mm-wave signal generation, as stated previously the optoelectronic oscillator (OEO) is particularly attractive because it can generate low phase noise oscillation without any reference RF signal [3]. The OEO oscillation frequency is limited by the RF and electro-optic components used inside the loop, such as the electro-optic modulator and narrow bandpass filter. The highest reported OEO oscillation frequency is 60 GHz with the use of a microwave photonic filter (MWPF) [53]. However, there is interest in wireless links operating in the W-band (75 – 110 GHz) and in the 200 – 300 GHz band, where the atmospheric attenuation is lower than that at 60 GHz [148] as shown in Fig. 6.1. Such frequency

ranges are very challenging for OEO implementations due to the lack of suitable modulators. Although polymer-based modulators work beyond 100 GHz, problems with their long-term stability remain. In contrast, an optical frequency comb generator (OFCG) can produce highly phase correlated optical tones over a wide range with a fixed frequency spacing [149] and by filtering two lines of the appropriate frequency spacing, with subsequent heterodyning in a photodiode, it is possible to generate pure mm-wave and THz signals above 100 GHz [22]. It is also possible to implement heterodyning in a simpler fashion using two free-running lasers with the appropriate wavelength spacing, but this approach suffers from phase fluctuations whereas in the optical comb the tones are highly phase correlated. Conventionally, in OFCGs based on external modulators, an external microwave synthesizer is used to provide the seed tone and to determine the frequency spacing. However, it is possible to dispense with the need for an external RF source by driving the OFCG with an OEO instead. The use of an OEO to drive an optical frequency comb (OFC) generator (either directly or via a self-oscillating approach) for subsequent low-phase noise generation of mm-wave and THz signals is a promising concept.

In chapter 5, we experimentally generated a mm-wave signal from a self-oscillating optical frequency comb with a comb spacing of 11.84 GHz that was determined by an electrical bandpass filter [133, 134]. A 95 GHz mm-wave was generated using this method, and a RoF link was implemented to transmit wireless signals modulated with a standard LTE advanced

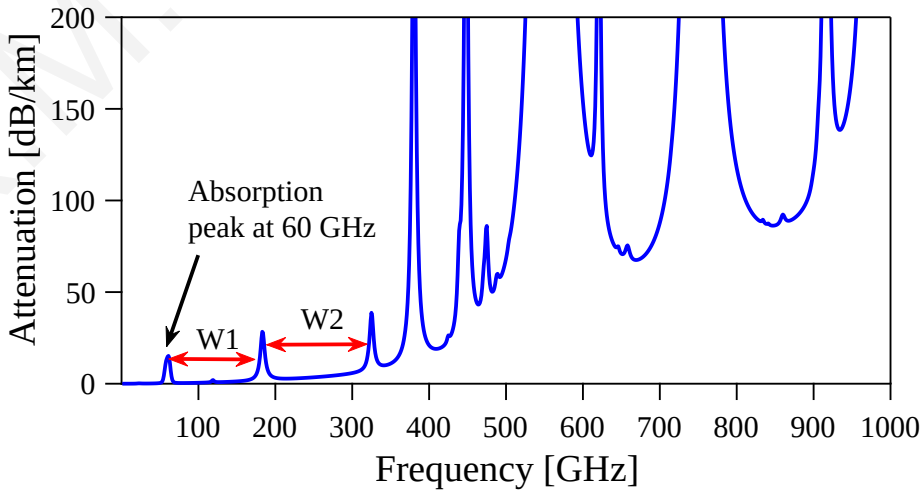

Fig. 6.1. Specific attenuation of the Earth's atmosphere at sea level in the frequency range 1 GHz to 1000 GHz for an air pressure of 1013 hPa, a temperature of 15^0 C and a water vapour density of 7.5 g/m^3.

signal. However, this proposed system still lacks the frequency tunability of the OEO and hence the mm-wave and THz signal frequency can only be tuned by changing the selected lines spacing.

In this chapter, we propose and experimentally demonstrate the photonic generation of mm-wave and THz signals using a tunable OEO driven OFCG and a RoF link at THz band. We use a MWPF-based approach to achieve the OEO frequency tunability (6.58 -18.36 GHz), where a PM-TOBF combination functions as a MWPF [79]. The SSB phase noise is below -103 dBc/Hz throughout the entire tuning range. To analyse the short-term and long-term stability of the OEO, we also measured the Allan deviation, and the frequency and power drifting of the generated RF carrier. The measured Allan deviation is 6.1×10^{-8} at 1 s observation time for 17.33 GHz oscillation frequency. The peak frequency drift is 7 kHz, and power fluctuation is below 0.7 dB over a 30 minute observation duration. The system provides the opportunity to generate a tunable low phase noise THz signal without requiring any reference RF input. The electrical signal from the OEO is used as a driving electrical signal to generate 22 optical comb lines, covering a range of 360 GHz within a 20 dB envelope. By selecting two optical comb lines, and beating them in a uni-traveling carrier photodiode (UTC-PD), we generate THz signals at 101.5 GHz and 242.6 GHz when the OEO oscillation frequencies are 16.92 GHz and 17.33 GHz, respectively. The measured phase noises (after down conversion) of the 101.5 GHz and 242.6 GHz signals are -90 dBc/Hz and -78 dBc/Hz, respectively at 10 kHz offset frequency. A RoF link is subsequently implemented with the OEO-driven OFCG at 242.6 GHz and the results are compared with an electrical local oscillator (LO) driven OFCG. The obtained bit error rate (BER) is below the hard decision forward error correction limit for a wireless distance of 30 cm and a data rate of 24 Gbps modulated with 16 QAM.

We then modify OEO topology by cascading an additional optoelectronic infinite impulse response (IIR) filter section with a view to generating a spur-free RF signal. The OEO with the IIR filter is also applied to a an OFCG to generate THz signals through optical heterodyning.

6.2 Tunable mm-wave and THz signals generation

6.2.1 MWP filter based tunable OEO

A. Operating principle of PM based MWP

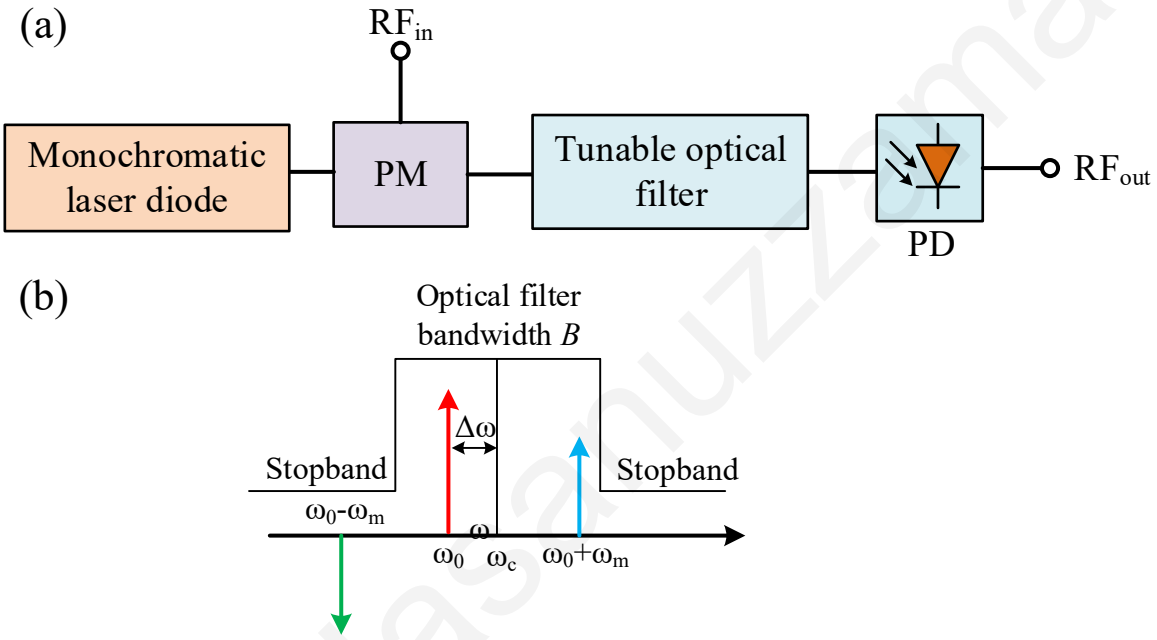

Fig. 6.2. (a) Arrangement of PM based MWP filter (b) operating principle of the MWP filter

The output of a PM can be represented by the following equation in connection to the arrangement of Fig. 6.2:

$$E_{out}(t) = E_0 e^{\omega_0 t}[e^{jASin\omega_m t}]) \tag{6.1}$$

$$E_{out}(t) = J_0(A)E_0 e^{\omega_0 t} + \sum_{n=1}^{\infty} J_n(A)E_0 e^{j(\omega_0+\omega_m)t} + \sum_{n=1}^{\infty}(-1)^n J_n(A)E_0 e^{j(\omega_0-\omega_m)t}. \tag{6.2}$$

If we consider only the first order terms and small signal modulation condition, then:

$$E_{out}(t) = J_0(A)E_0 e^{\omega_0 t} + J_1(A)E_0 e^{j(\omega_0+\omega_m)t} - J_1(A)E_0 e^{j(\omega_0-\omega_m)t} \tag{6.3}$$

where E_0 is the optical field of the source, J_n is the n-th order Bessel function of the first kind, A is the phase modulation index, ω_0 is the angular frequency of the optical carrier, and ω_m is the angular frequency of the RF signal. Therefore, a PM generates optical side-bands with opposite phase around the optical carrier when it is modulated with an external RF source. By placing an optical bandpass filter (with a centre frequency equal to the optical

carrier frequency) after the PM, the anti-phase sidebands are transmitted symmetrically as shown in Fig. 6.3(a). Consequently, after photodetection only a DC current is generated. However, if the centre frequency of the optical carrier (ω_0) is shifted slightly from the centre frequency of the optical filter (ω_c), this results in asymmetrical sideband suppression as shown in Fig.6.3(b). The beating between the remaining unbalanced sideband and the optical carrier will be detected by the photodiode, generating a single sideband RF response, where the centre frequency and bandwidth are determined by the spectral response of the TOBF. The centre frequency in the electrical domain is equal to half the bandwidth of the TOBF (B/2) while the bandwidth is equal to twice the offset between the laser oscillation frequency and TOBF centre frequency ($\Delta\omega = \omega_c - \omega_0$), as shown in Fig. 6.3(b).

By increasing the bandwidth of the TOBF, the centre frequency of the RF filter increases ($f_3 > f_2 > f_1$) (Fig.6.3(c)), while the bandwidth of the RF filter changes with the changes of offset frequency (Fig. 6.3(d)).

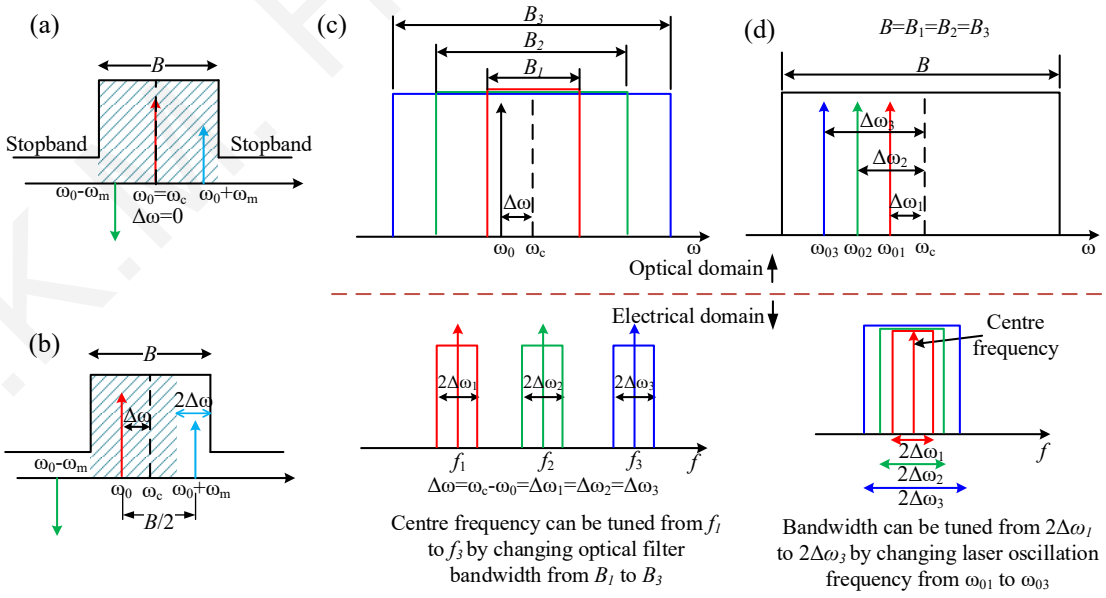

Fig. 6.3. (a) Symmetrically transmitted sidebands (b) Asymmetrically transmitted sidebands (c) Centre frequency tuning by changing the optical bandwidth (B) of the TOBF, and (d) Bandwidth tuning by changing the laser wavelength.

B. Operating principle of optical frequency comb generator

The OFC generator is based on an asymmetrically dual-driven Mach-Zehnder modulator (DD-MZM); the principle of operation is shown in Fig. 6.4. Higher order side modes are generated when a DD-MZM is modulated with a large amplitude RF signal where the spacing between the side modes is determined by the oscillation frequency of the RF signal. The spectral flatness of the generated comb lines depends on a specific phase and amplitude condition as described below [138, 150]. The optical phase shifts introduced by the RF

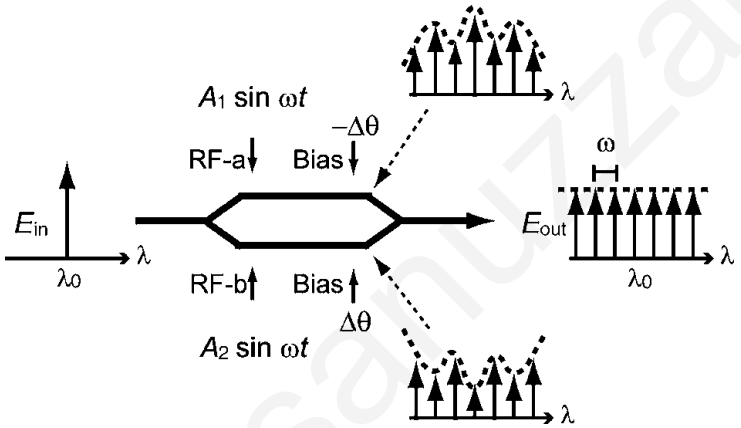

Fig. 6.4. Operating principle of the DD-MZM based optical frequency comb generator. After [138]

signals in the two arms of the DD-MZM are $A_1 \sin\omega_m t$ and $A_2 \sin\omega_m t$ respectively. Therefore, the output electric field of the DD-MZM can be expressed by:

$$E_{out}(t) = \frac{1}{2} E_{in}(t) \sum_{k=-\infty}^{\infty} [J_k(A_1) \exp^{(j\omega_m t+\theta_1)} + J_k(A_2) \exp^{(j\omega_m t+\theta_2)}] \tag{6.4}$$

where J_k denotes the k-th order Bessel function. θ_1 and θ_2 are the phase shifts induced by the DC biasing. The analysis in [138] shows that a maximally flat OFC can be obtained when the driving signals satisfy the following condition:

$$\Delta A \pm \Delta\theta = \frac{\pi}{2} \tag{6.5}$$

where $\Delta A = A_1 - A_2/2$ and $\Delta\theta = \theta_1 - \theta_2/2$.

6.2.2 Experimental set-up of MWPF based THz signal generation

The experimental arrangement of the proposed concept is shown in Fig. 6.5. It consists of three subsections: (i) the optoelectronic oscillator (OEO) section, (ii) the optical frequency

comb generator (OFCG), and (iii) two-tone selection and THz generation section, in which two tones are filtered out, prior to heterodyne detection and transmission over a wireless path.

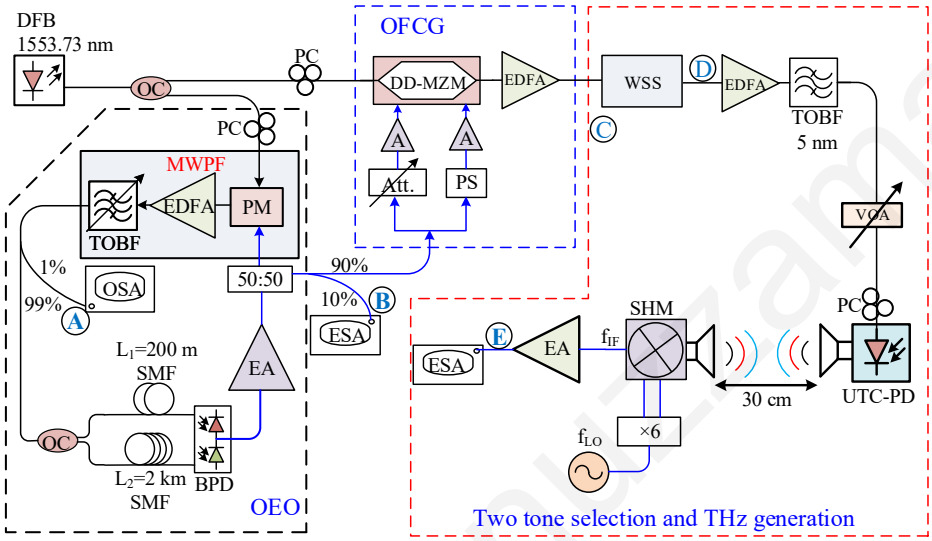

Fig. 6.5. Experimental arrangement of the OEO driven OFCG

A. Tunable OEO

A distributed feedback (DFB) laser with a centre wavelength of 1553.73 nm and a linewidth of 10 kHz acts as an optical source (via a 50:50 optical coupler) for both the OEO and OFCG subsections. The phase modulator (PM) within the OEO loop is used (i) as an electrical-to-optical (E/O) converter, and (ii) as a MWPF, when combined with a tunable optical bandpass filter (TOBF) [79, 151]. In the experimental setup, the TOBF that was used is a Yenista Optics XTM-50 (with a minimum and maximum bandwidth of 6.25 GHz, and 120 GHz, respectively). The OEO is based on a dual-loop balanced detection configuration in which fibre lengths of L_1 = 200 m and L_2 = 2 km, respectively, feed a balanced photodiode (DSC730, with a 3-dB bandwidth of 25 GHz, and a responsivity of 0.60 A/W). E/O and O/E conversion losses in the loop are compensated with two microwave amplifiers in cascade, with the output of this amplifier chain being used to drive both the PM in the OEO loop, and also the DD-MZM (Photonic Systems Inc.) in the optical frequency comb generator.

B. OFC generator

The OFC generator is based on the principle discussed in section 6.2(B) and the experimental set up illustrated in the blue dotted box of Fig. 6.5. The microwave output of the OEO passes through a splitter. One of the output arms of this splitter is then connected to an attenuator (Att.) and the other to a phase shifter (PS). Through suitable adjustment of both of these components, the drive signals for the following DD-MZM have the required amplitudes and phases so as to satisfy the flat spectrum condition in [138]. The resulting optical comb is subsequently amplified optically prior to being connected to the final section in which two tone selection and THz frequency generation take place.

C. Two tone selection and THz generation

A programmable wavelength selective switch (WSS) is employed to select two optical tones from the OFCG output that have a wavelength spacing corresponding to the desired THz frequency, which results from heterodyning in a UTC-PD. The WSS was a Finisar Wave-Shaper (4000S) based on liquid crystal on silicon (LCoS) technology. The optical output of the WSS was then amplified and filtered to remove the amplified spontaneous emission (ASE) noise before photodetection in an unpackaged UTC-PD with an integrated coplanar waveguide (CPW). The output of the photodiode was connected to a 20 dBi horn antenna (WR-5.1) using a coplanar mm-wave probe, with the transmitted THz signal then being received by an identical horn antenna. In order to measure the phase noise of the received THz signal, it was down-converted to a microwave intermediate frequency (IF) within the range of RF components by using a sub-harmonic mixer (SHM). A Rohde &Schwarz synthesizer (SMA100A) was used as a local oscillator (LO), with its output frequency being multiplied ($\times 6$) and mixed with the THz signal in the SHM. The IF signal was then amplified and connected to an electrical spectrum analyser to measure the phase noise performance.

6.2.3 Experimental Results

A. Electrical spectrum generated by OEO section

The PM-TOBF combination functions as a tunable MWP filter as described in Section 6.2; by tuning the bandwidth of the TOBF filter, we were able to generate continuous tunable microwave signals from 6.58 GHz to 18.36 GHz. Typical spectra of the generated RF carriers

(as measured at point Ⓑ in Fig. 6.5) are shown in Fig. 6.6. The tuning range is limited by the bandwidth of the electrical amplifier used in the OEO loop since the bandwidth of the balanced photo-detector and the phase modulator is greater than that of the electrical amplifier. An optical spectrum analyzer with a resolution bandwidth (RBW) of 0.01 nm was used to measure the optical spectrum at the output of the TOBF, which is shown in Fig.6.7

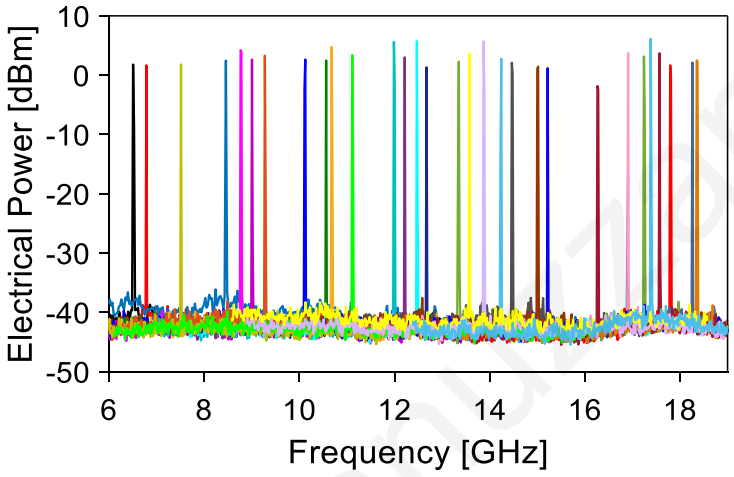

Fig. 6.6. Electrical spectra of the generated microwave signal for different frequencies measured at point Ⓑ in Fig. 6.5.

The electrical spectrum of the generated RF signal at 17.33 GHz is shown in Fig. 6.8 for a span of 5 MHz. Side modes at an offset frequency of 1 MHz from the carrier (corresponding to the short fibre length, L_1=200 m) with more than 65 dB suppression were observed. Side modes at 100 kHz offset corresponding to the long fibre (L_2=2 km) were suppressed due to the dual loop effect [19].

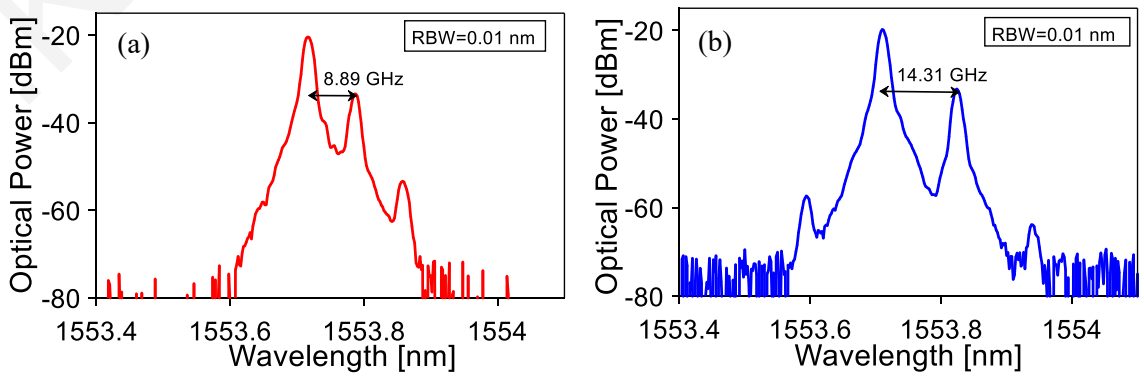

Fig. 6.7. Optical spectra at the output of the TOBF for the oscillating frequency (a) 8.89 GHz, and (b) 14.31 GHz, respectively at point Ⓑ of Fig. 6.5.

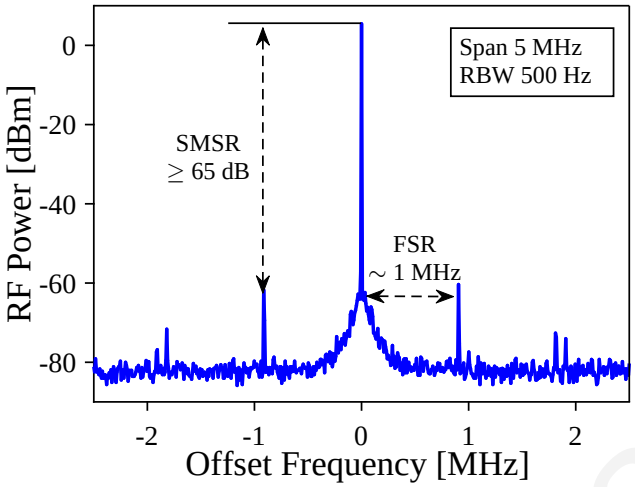

Fig. 6.8. Electrical spectrum of the generated RF signal from OEO at 17.33 GHz signal with span of 5 MHz and RBW of 3 kHz (measured at point Ⓑ of Fig. 6.5)

B. Phase noise and stability

We measured the single side band phase (SSB) noise of the OEO and compared it with an external Rohde & Schwarz signal generator (R&S®SMF100A). At offset frequencies higher than 3 kHz the SSB phase noise of the OEO is better than the signal generator. The measured single side band (SSB) phase noise of the OEO and external generator is -106 dBc/Hz and -102 dBc/Hz respectively at 17.33 GHz oscillation and 10 kHz offset frequency as shown in Fig. 6.9. From the phase noise curve, we also observe side modes at multiples of the 1 MHz offset. The SSB phase noise at 10 kHz offset frequency of the generated electrical signals is shown in Fig. 6.10(a). We then measured the Allan deviation (δ_τ) to determine the short time stability of the OEO. Figure 6.10(b) shows the measured Allan deviation, as calculated using the Allan deviation measurement option of the Rohde & Schwarz spectrum analyzer (R&S®FSU26) with the frequency counter method. The measured Allan deviation for an observation time of 1 second is 6.1×10^{-8} for the oscillation frequency of 17.33 GHz. We also measured the oscillation frequency and electrical output power of the OEO at one second intervals for half an hour using an Agilent spectrum analyzer. Fig. 6.11(a) shows the frequency drift and Fig. 6.11(b) shows the peak power of the signal as a function of time. The peak frequency drift is 7 kHz and the power deviation is less than 0.7 dB during the measurement duration.

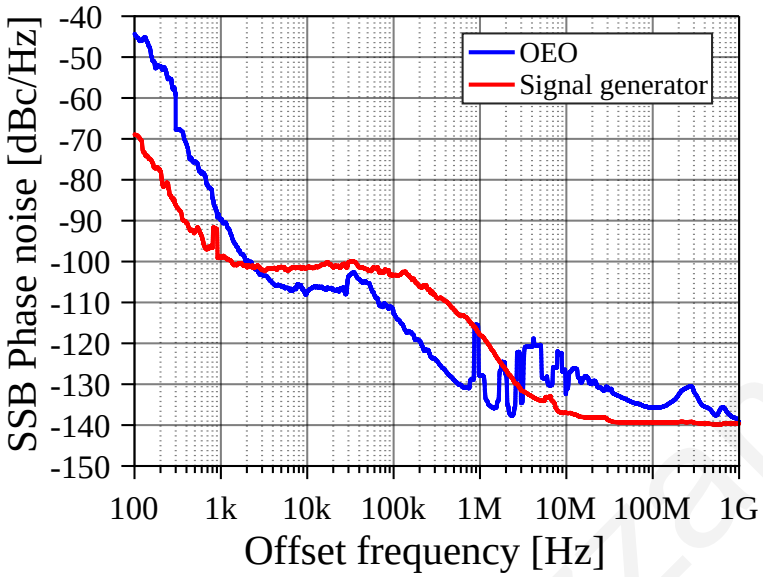

Fig. 6.9. SSB phase noise of the OEO and RF signal generator at 17.33 GHz.

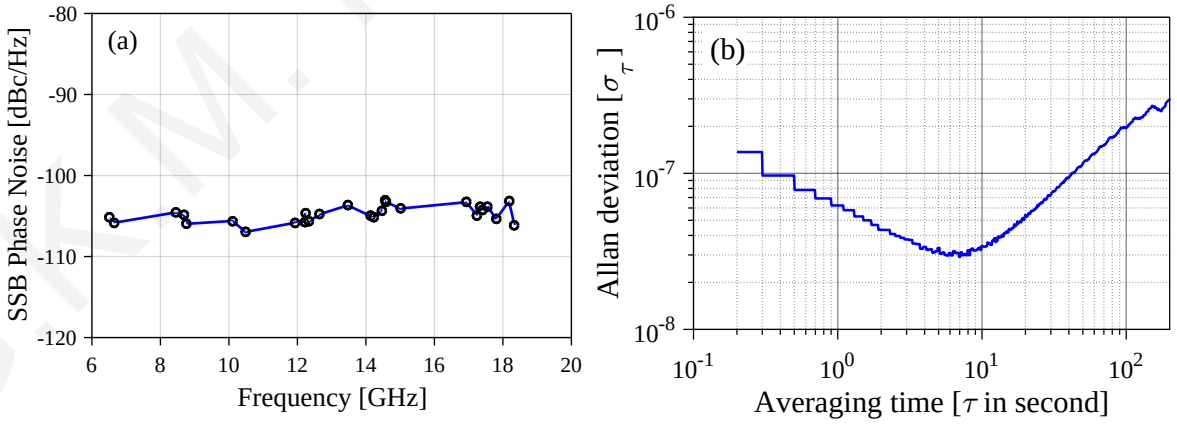

Fig. 6.10. Electrical spectrum of the generated RF signal from OEO at 17.33 GHz signal with span of 5 MHz and RBW of 3 kHz (measured at point Ⓑ of Fig. 6.5).

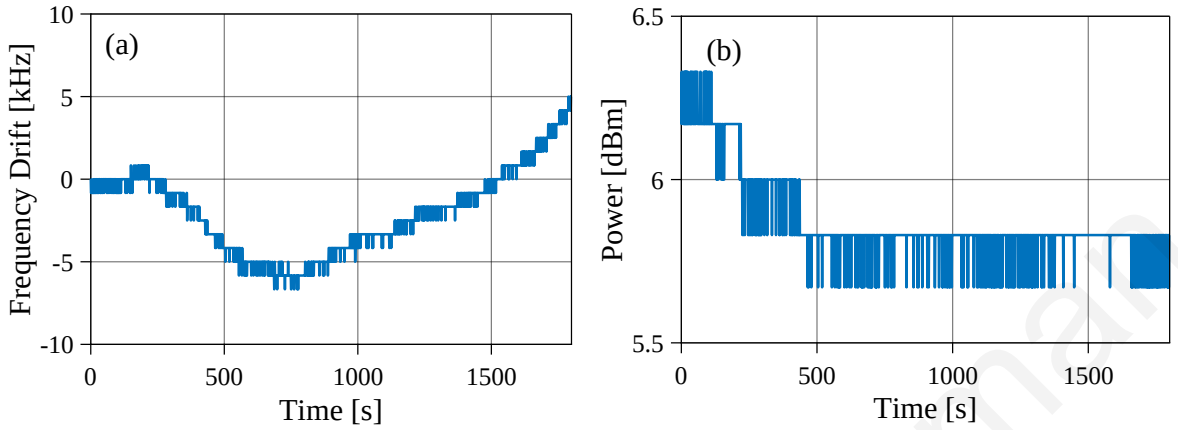

Fig. 6.11. (a) Frequency drift over time, (b) oscillating signal power over time

C. Generated mm-wave and THz wave

It is possible to generate THz signals over a broad frequency range by varying either the OEO oscillation frequency or filtering out two tones from the comb that are separated by an integer multiple of the comb line spacing. The optical comb spectra for three different OEO oscillation frequencies (10.5 GHz, 16.92 GHz, and 17.33 GHz) are shown in Fig. 6.12 (a), (b) & (c), respectively. A spectrum of 22 optical tones with a spacing of 17.33 GHz is observed (Fig. 6.12(c)), covering a bandwidth of 360 GHz within a 20 dB envelope. The number of comb lines that can be generated is limited primarily by the amplitude of the driving signals applied to the RF ports of the DD-MZM of Fig. 6.5. In turn, the amplitude of the RF signals is limited by the gain and saturated output power of the electrical amplifier used in the OFCG section. The optical bandwidth of the optical amplifiers and modulators used is sufficiently wide to support hundreds of comb lines in principle, hence these components are not a limiting factor in this respect. In addition, the remaining components (such as the photodiodes and electrical amplifiers) need only have a bandwidth wide enough to support the comb spacing, which is only a few GHz in our work.

By selecting any two optical comb lines, it is possible in principle to generate THz signals up to 360 GHz through heterodyne detection with a UTC-PD. In this work, we generated an RF signal at 102 GHz, and 242.6 GHz when the OEO oscillation frequency was set to 16.9 GHz, and 17.33 GHz, respectively. Fig. 6.12(d) shows the optical spectra of the two selected optical tones for the latter case. The electrical spectra of the down-converted signals are shown in Fig. 6.13(a) and 6.13(b) for 102 GHz and 242.6 GHz signal, respectively.

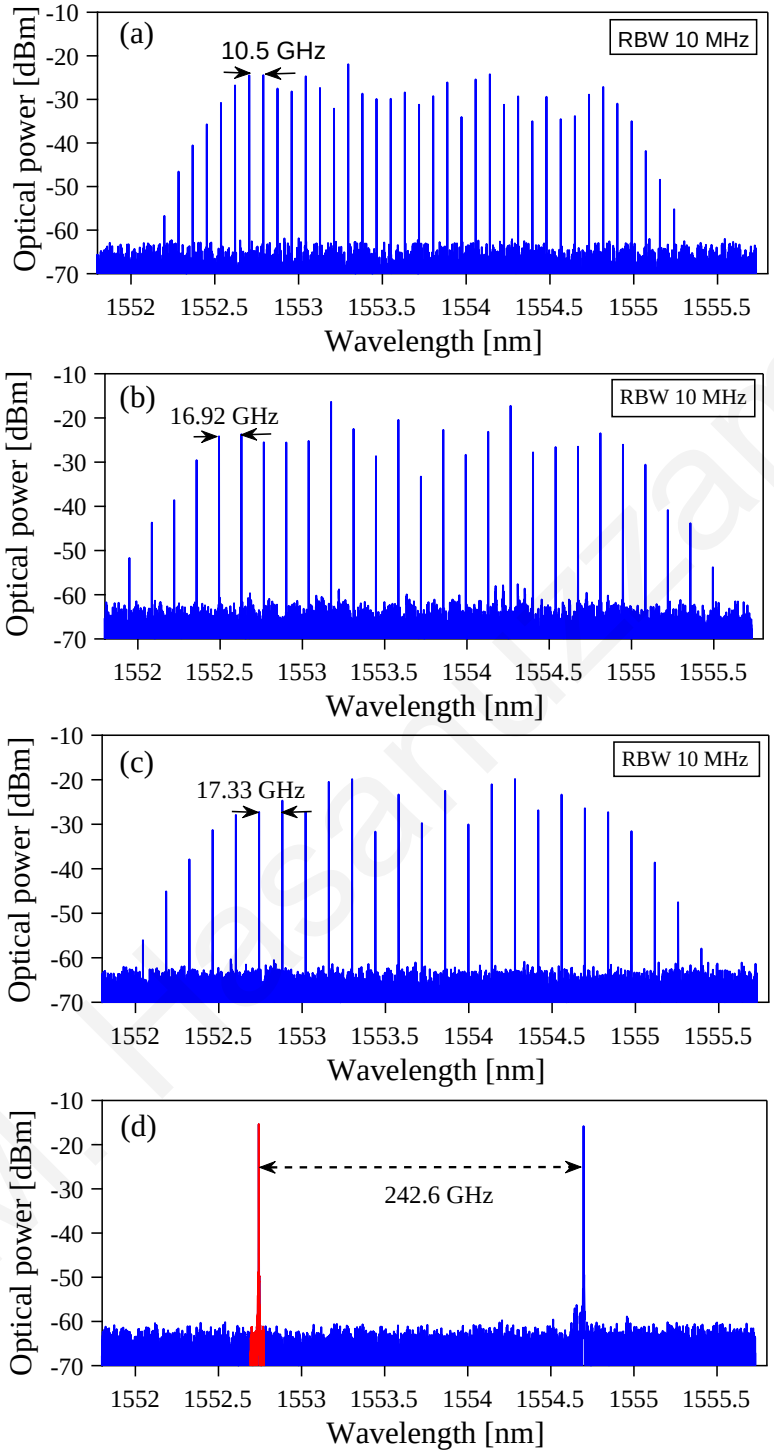

Fig. 6.12. Optical spectra of the generated optical frequency combs with a frequency spacing of (a) 10.5 GHz (b) 16.92 GHz (c) 17.33 GHz at the centre wavelength of 1553.73 nm (measured with an OSA at point Ⓒ in Fig. 6.5 (d) Optical spectrum of the selected comb lines (measured with an OSA at point Ⓓ in Fig. 6.5).

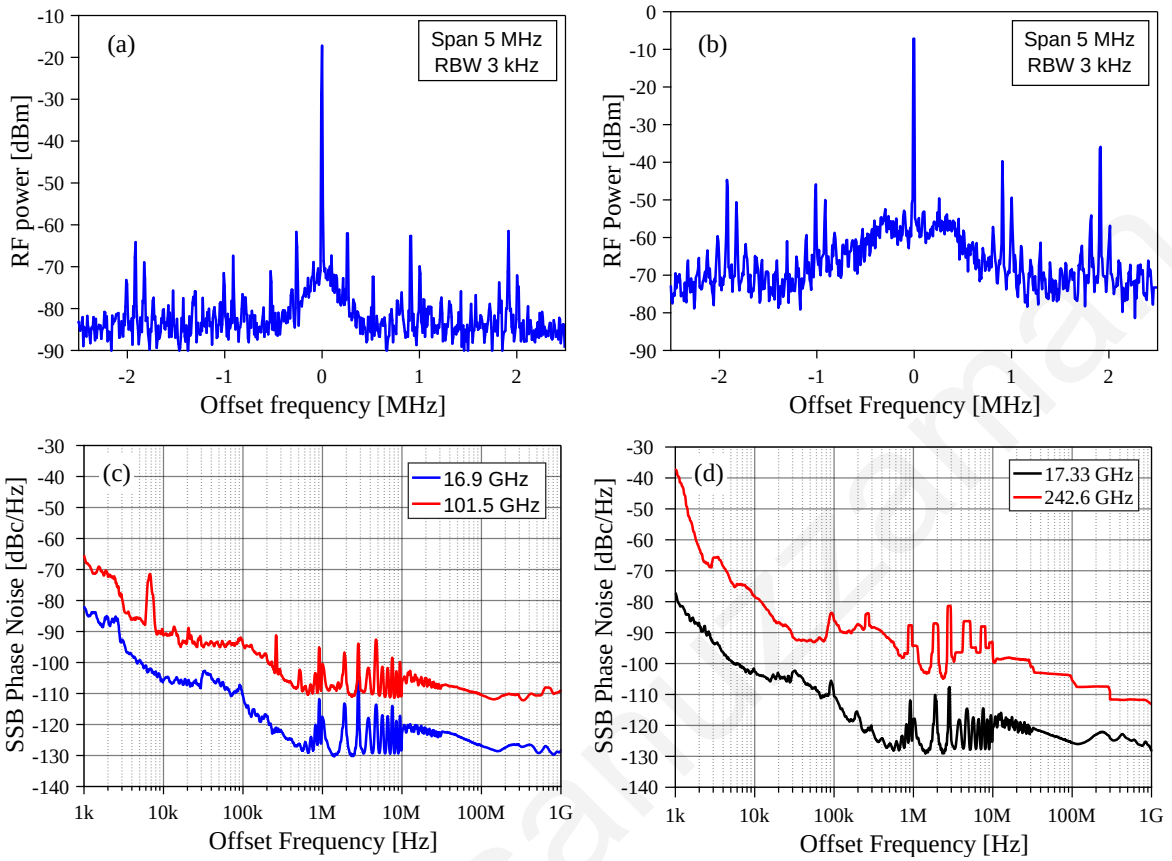

Fig. 6.13. Electrical spectra of the down-converted THz signals (a) 101.5 GHz, and (b) 242.6 GHz. Measured SSB phase noise of the down-converted THz signals (c) 101.5 GHz, and (d) 242.6 GHz (measured at point Ⓔ in Fig.6.5).

We found side modes spaced approximately 1 MHz apart (corresponding to the short length L_1=200m) around the carrier and side modes of 100 kHz spacing (corresponding to the long length L_2=2 km) with relatively low amplitude around the $\sim$ 1 MHz spaced side modes. The SSB phase noise of the down-converted signals was measured and is shown in Fig. 6.13(c) and 6.13(d). The SSB phase noise of the 101.5 GHz and 242.6 GHz signals is -90 dBc/Hz and -78 dBc/Hz respectively at 10 kHz offset frequency; the SSB phase noise is degraded by 15 dB for the 101.5 GHz, and 25 dB for the 242.6 GHz signal from their seed oscillation. This degradation also includes the phase noise addition during the down-conversion process due to the optical and electrical amplifiers. The SSB phase noise degradations are in good agreement with the carrier phase noise generated by the multiplication $20\times \log_{10}N$.

6.3 RoF link based on tunable OEO driven OFCG

6.3.1 Experimental set-up

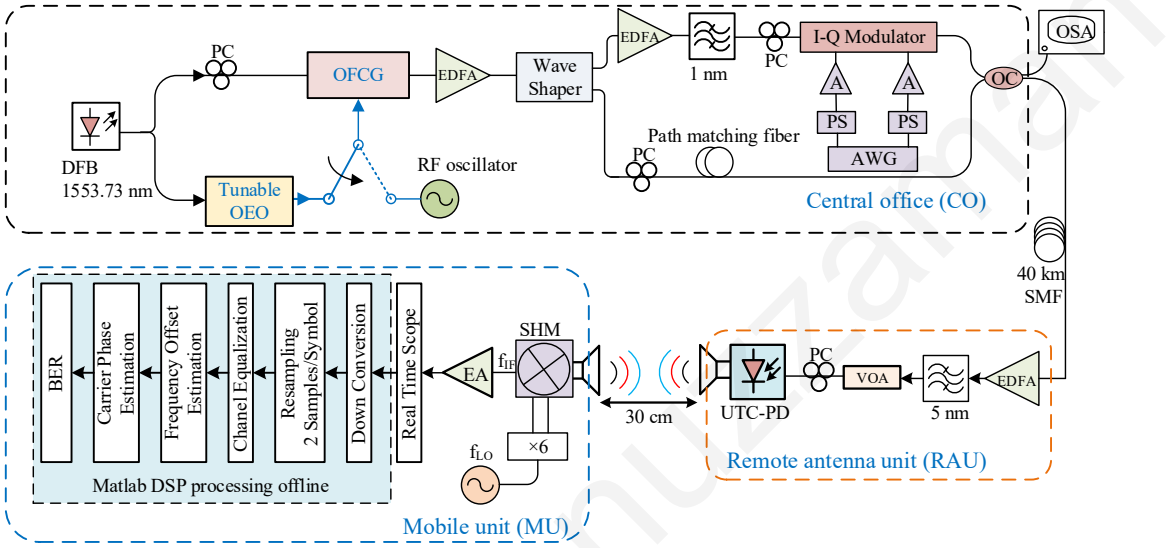

Fig. 6.14. Experimental set-up of the tunable OEO driven OFCG based radio over fibre link

We developed a RoF link at 242.6 GHz using the OEO driven OFCG. Fig. 6.14 shows the experimental arrangement for the RoF link, which uses the OEO and OFCG subsections that were described in section 6.2. To implement the RoF link, the output of the OFCG section was passed through a WSS after optical amplification via an EDFA. The OEO oscillation frequency was set to 17.33 GHz (with the corresponding optical comb as shown in Fig. 6.12 (c)). Two optical tones with a frequency spacing of 242.6 GHz were selected and guided into two different output ports of the WSS; one optical tone was used as a local oscillator (LO) while the other was used for data modulation. This second tone was amplified by an EDFA and passed through a 1 nm optical band pass filter to eliminate the out of band amplified stimulated emission (ASE) noise. The output of the filter was then fed to an I-Q modulator after being polarization controlled. An arbitrary waveform generator (AWG) from Tektronix (AWG7000) with a sampling rate of 50 GSa/s was used to generate $2^{11} - 1$ pseudo random bit pattern (PRBS) I and Q signals. Prior to being connected to the I-Q modulator, the I and Q signals were electrically amplified and phase shifted. During the experiment, we used 10 Gbaud QPSK and 6 Gbaud 16 QAM modulation formats with a square root raised cosine (SRRC) filter of 0.1. The LO tone was passed through a polarization

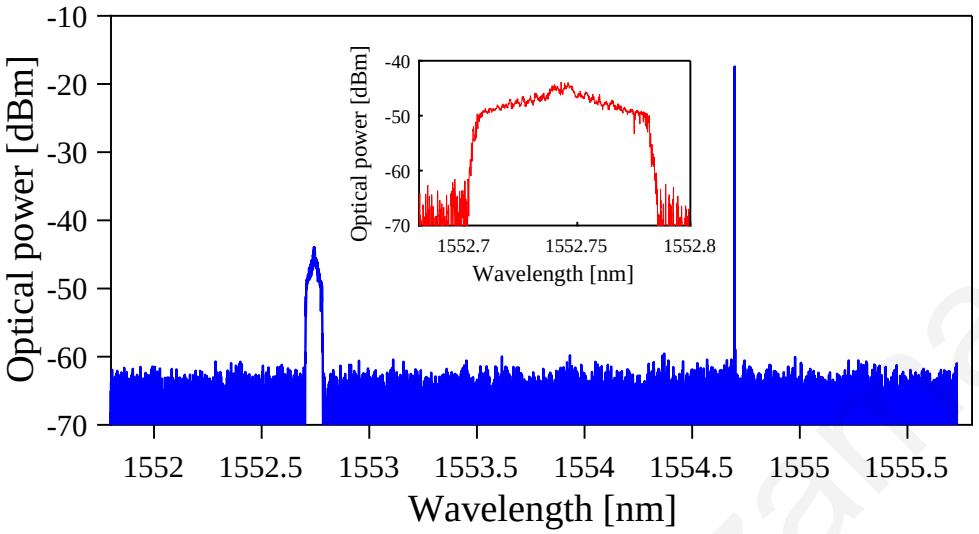

Fig. 6.15. Optical spectrum of the selected two tone for RoF link. The left-hand tone is modulated with 10 Gbaud QPSK. The inset shows the zoom view of data modulation.

controller (PC) to align the polarization state and a short path matching fibre of 39.5 m length was used to compensate for the optical path difference introduced between the two branches (modulator and LO branch) due to the inclusion of an EDFA and optical filter in the modulator branch. An optical attenuator was used in the LO branch to match the optical power between the modulated and LO tone. Then the modulated tone and the LO tone were combined in an optical coupler (OC), one output of which was connected to an optical spectrum analyzer (OSA) while the other was passed through a SMF of 40 km length. The optical spectrum after combining the two tones is shown in Fig. 6.15. Prior to detection by an unpackaged UTC-PD, the optical signal was amplified by an EDFA to compensate the fibre transmission loss, filtered by a 5 nm OBPF to remove out-of-band ASE, controlled by a VOA to evaluate the system performance, and polarization aligned by a PC to reduce polarization dependent loss. The beating product of the LO and modulated tone in a UTC-PD was transmitted over a 30 cm wireless distance with a 20 dBi horn antenna. Another antenna of the same gain and polarization received the transmitted THz signal, which was subsequently down-converted to an IF frequency with the electrical LO-SHM combination as described in section 6.2. The electrical LO signal frequency was selected in such a way as to place the IF signal around 9 GHz, within the bandwidth of the analogue to digital converter (ADC) of the real time oscilloscope (RTO). The IF signal was then amplified and connected to a RTO with 36 GHz bandwidth and sampling rate of 80 GSa/s for further processing;

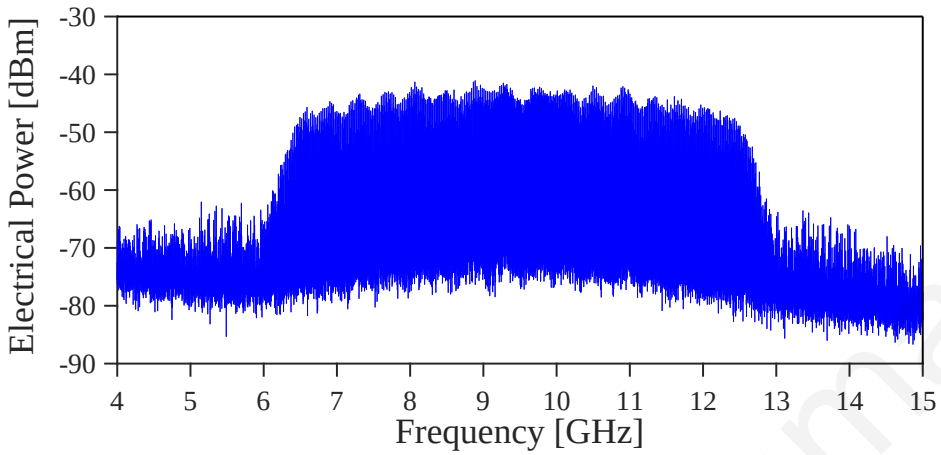

Fig. 6.16. Electrical spectrum using FFT of the received IF signal for 6 Gbaud 16 QAM.

the IF spectrum of the down-converted THz signal obtained by fast Fourier transform (FFT) in the RTO is shown in Fig. 6.16. Due to the non-flat response of the IF amplifier, the IF signal has a slight asymmetry. The digitized signal was then processed with an offline DSP processor in MATLAB to demodulate the QPSK/ QAM signal. The DSP processing includes down conversion, down sampling (2 samples/symbol), channel equalization (blind equalizer algorithm), carrier recovery and phase noise estimation. Finally, the bit error rate (BER) performance was evaluated by varying the input optical power (through a variable optical attenuator, VOA) to the UTC-PD.

6.3.2 Results and discussion

As mentioned earlier, the RoF link was evaluated with two different modulation formats: 10 Gbaud QPSK and 6 Gbaud 16 QAM and two different OFCG driving scenarios: OEO and external RF synthesizer. The BER was measured first when the OFCG was driven by the OEO, then when the OFCG was driven by an external RF synthesizer. Fig. 6.17 shows the measured BER versus received optical power for the four experimental conditions. There is a small power penalty between the OEO driven and external synthesizer driven curve which is due to the effect of phase noise stability. The external RF synthesizer has a superior close to carrier phase noise performance compared to the OEO as shown in Fig. 6.9, and the obtained BER is below the hard decision forward error correction limit of 3.8×10^{-3} for 7% overhead. The obtained data rates are 20 Gbps and 24 Gbps for 10 Gbaud QPSK and 6 Gbaud 16 QAM respectively.

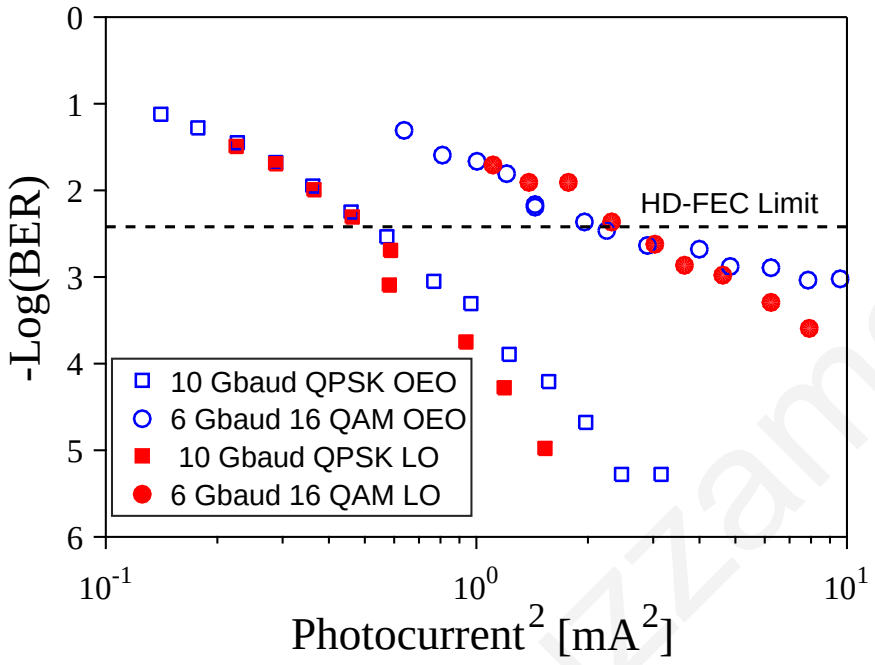

Fig. 6.17. BER as a function of photocurrent

6.4 Side-mode suppressed tunable OEO

Low phase noise, side mode suppressed, and wideband-frequency tunable OEOs as a microwave source are indispensable for several applications, for example in radar to detect slow moving targets. In [83], a side mode suppressed tunable OEO (from 8.5 to 9.5 GHz) is implemented using an EBPF of large bandwidth through the injection locking technique (via an external electrical synthesizer). The injection locking technique realizes both the side mode suppression and tuning function. Although the technique provides spur-free oscillation, the tuning range is limited by the passband of the electrical bandpass filter. In second generation OEOs, the electrical bandpass filter is replaced by a tunable microwave photonic (MWP) filter which effectively eliminates the tunability limitation of the electrical filter. Other key advantages of MWP filters include wideband capability, reconfigurability, and immunity to electromagnetic interference. Two types of MWP filter can be identified according to the number of passbands, namely those with a single passband and those with periodically repeating passbands (implemented either with FIR or IIR transfer functions). Although FIR and IIR filters provide a high Q factor, a single FIR or IIR filter stage is inappropriate for OEO implementations due to its periodic response.

One promising approach to achieve both a high selectivity and Q factor is to cascade a single

passband filter with a periodic spectral response filter (FIR or IIR). Generally, the FIR filter requires a large number of taps to achieve high Q and frequency selectivity, and the system becomes bulky. On the other hand, the IIR filter requires fewer components. An IIR filter can be realized with an all optical approach or optoelectronic approach with the latter providing several benefits over the former, including the elimination of phase-induced intensity noise (PIIN), and avoidance of issues associated with optical coherence. Also, the optoelectronic IIR transfer function can be easily reconfigured from passband to stopband by changing the bias point of the electro-optic modulator.

By cascading a single passband filter and an optoelectronic IIR section, one can suppress the side modes by reducing the passband of the filter. The single passband section determines the centre frequency of oscillation and the IIR section provides the high Q filtering for side mode suppression. Such a topology was used in [62] with an electrical bandpass filter and an optoelectronic IIR section. The OEO provides side mode suppression of 93 dB at an oscillation frequency of 29 GHz. Although the system managed to suppress the side modes, it lacks frequency tunability. In [63], a tunable OEO is reported incorporating a stimulated Brillouin scattering (SBS) based tunable MWP filter and an active recirculating delay lined based IIR filter. The reported OEO provides a side mode suppression of 95 dB and a tuning range of DC to 40 GHz.

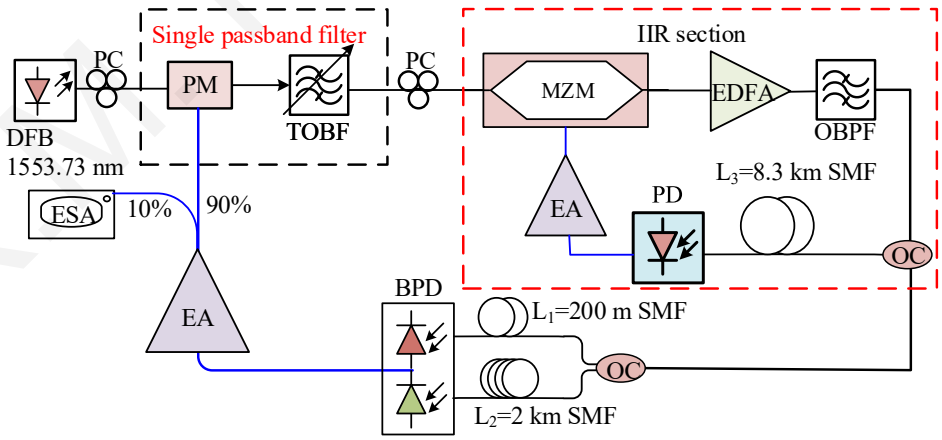

Fig. 6.18. Experimental set-up of the proposed tunable OEO. The black dotted section represents the single passband section and the red dotted section represents the IIR section.

In this section, we experimentally demonstrate a highly side mode suppressed tunable dual-loop OEO by cascading a single passband MWP filter and an optoelectronic IIR section as shown in Fig. 6.18. A phase modulator (PM) and an optical bandpass filter (OBPF)

combination provides the single passband as described in subsection 6.2.1. We obtained the tuning function by changing the bandwidth of the OBPF. We examined the effect of the IIR section by performing experiments with and without it in place. Inclusion of the IIR section suppresses the nearest neighbouring side modes by 125 dB, whereas not including it leads to a suppression of 113 dB. Furthermore, with the inclusion of the IIR section, the close to carrier phase noise is reduced by 20 dB and the Allan deviation is reduced by a factor of ten to 6×10^{-9}. The OEO was then used to drive an optical frequency comb generator (OFCG), and through two-tone selection via a wavelength selective switch (WSS) and subsequent optical heterodyning in a uni-traveling carrier photodiode (UTC-PD), we generated a THz signal at 242.6 GHz. In down-converting the THz signal, we found that the side modes are less pronounced when the IIR section is included in the OEO.

6.4.1 IIR filter

A. Operating principle

A first-order optoelectronic IIR filter is depicted in the red dotted-line box of Fig. 6.19. In essence, the IIR section is an optoelectronic feedback loop with open loop gain less than unity [152–154]. It comprises a Mach-Zehnder modulator (MZM), an erbium doped fiber amplifier (EDFA) with an OBPF, a long fibre of several kilometers, a high-speed photo-detector (PD), and an electrical amplifier. The quality factor (Q) and the rejection ratio of the IIR filter increase with higher open loop efficiency which depends on: the gain of the optical and electrical amplifier; optoelectronic conversion efficiency of the MZM and PD; and the input optical power to the IIR section. The IIR loop is operated in the incoherent regime where the total loop delay (T) is greater than the laser diode coherence time, providing a periodic passband and stopband with a free spectral range (FSR) of $1/T$, where T is the loop time delay provided by the IIR section. The bias point of the MZM can control the position of the passband and stopband; for example, the stopband response may be swapped with the passband by switching the bias point from positive quadrature to negative quadrature [152, 155].

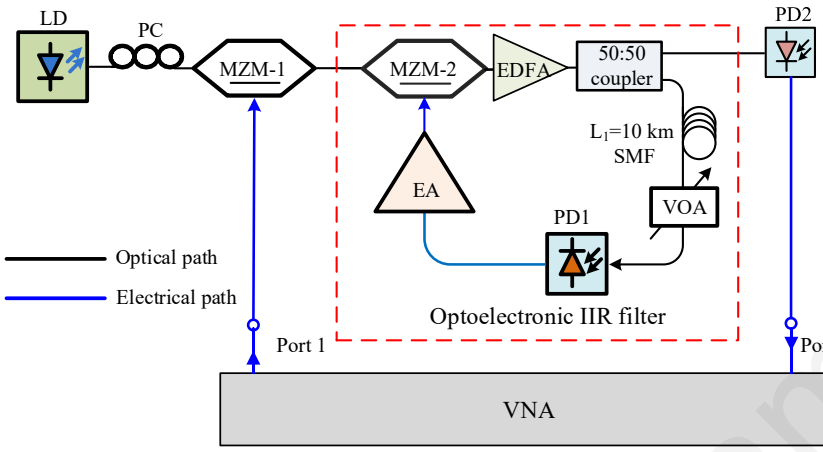

Fig. 6.19. Experimental arrangement for measurement of the frequency response of an optoelectronic IIR filter. VNA: Vector Network Analyser.

B. Analytical model

In the steady-state condition, MZM-1 is modulated by a microwave signal $V_{in} = V_e \cos(\omega_e t)$ of amplitude V_e and modulation frequency ω_e. Under small-signal conditions the output optical power P_{MZM-1} of MZM-1 can be approximated as:

$$P_{MZM-1}(t) = \frac{P_{in}(t)}{2}\left\{1 - \cos\left[\frac{\pi}{2} + m\cos\left(\omega_e t\right)\right]\right\} = \frac{P_{in}(t)}{2}\left[1 + m\cos\left(\omega_e t\right)\right] \tag{6.6}$$

where $P_{in}(t)$ is the laser's optical power and $m = \pi V_e / V_\pi$ is the modulation index. The optical power of P_{MZM-1} is detected at PD1, generating a current,

$$i(t) = \Re G_0 G_{e1} R P_{in} \kappa L_v m \cos\left(\omega_e t\right) \tag{6.7}$$

where $\Re$ is the responsivity of PD1 and G_{e1} the microwave amplifier gain while κ is the coupling coefficient and L_v is the attenuation from the VOA and G_o is the optical gain of the EDFA. Hence the loop efficiency $\eta = \Re G_0 G_{e1} R P_{in} \kappa L_v$ of the O/E IIR filter is characterised by the optical loop losses, optical and electrical gain (this includes the EDFA gain which is coupled into the loop) and R is the conversion efficiency of MZM-2. The photocurrent modulates MZM-2 and after an infinite number of cycles inside the loop (with $\eta < 1$ to

prevent instability) the current reduces to:

$$\begin{aligned} i(t) &= m\Big[\cos\left(\omega_e t\right) + \overbrace{\eta\cos\left(\omega_e(t-T_1)\right)}^{\text{1st-cycle}} + \underbrace{\eta^2\cos\left(\omega_e(t-2T_1)\right)\Big]}_{\text{2nd-cycle}} + \ldots \\ &= \sum_{N=0}^{\infty} m\Big[\eta^N\cos\left(\omega_e(t-NT_1)\right)\Big] \\ &= \frac{m}{2}\frac{\exp(j\omega_e t)}{1-\eta\exp(-j\omega_e T_1)} + \frac{m}{2}\frac{\exp(-j\omega_e t)}{1-\eta\exp(j\omega_e T_1)} \end{aligned} \tag{6.8}$$

The delay $T_1 = nL_1/c$ is the round-trip time of the fibre and is inversely proportional to the FSR. Therefore, the optical output power of MZM-2 becomes:

$$P(t) = \gamma\frac{G_0 P_{in}(t)}{2}\Big[1 + \frac{m}{2}\frac{\exp\left(j\omega_e t\right)}{1-\eta\exp(-j\omega_e T_1)}\Big]. \tag{6.9}$$

The negative frequency components in Eq. 6.9 are not included while the DC components and harmonics of ω_e are filtered by the PD bandwidth.

C. Experimental results

The measured results with the arrangement of Fig. 6.19 are shown in Fig. 6.20(a) and Fig. 6.20(b), respectively, for 8.3 km and 10 km fibre as the delay element. The top figure shows the normalised magnitude response of a passband at the centre with a 19 dB extinction ratio while the bottom figure shows a stopband at the centre with 25 dB extinction ratio.

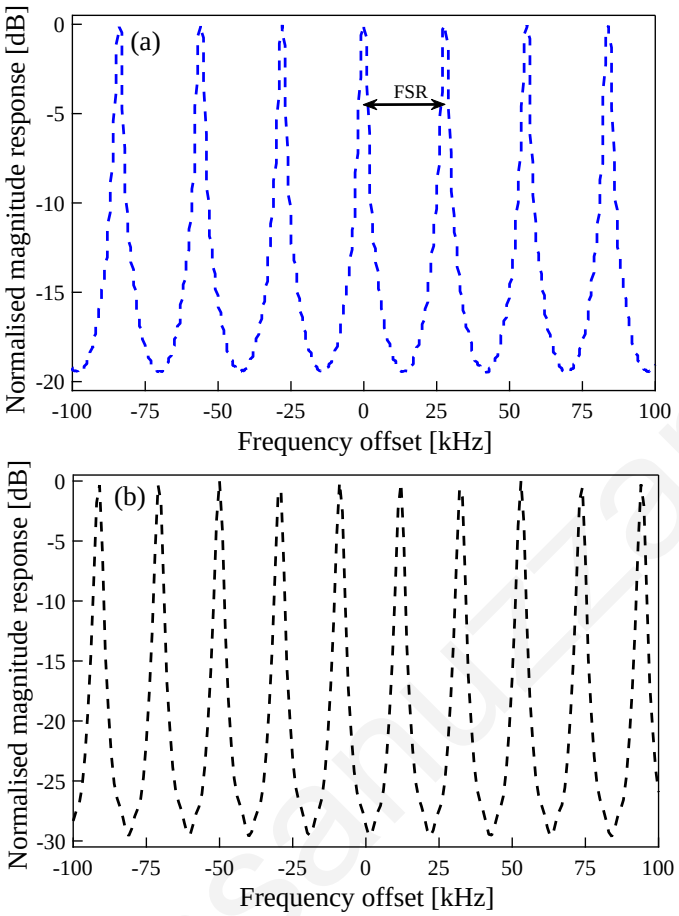

Fig. 6.20. Frequency response of an optoelectronic IIR filter (a) 8.3 km fibre (b) 10 km fibre as a delay element

.

6.4.2 Experimental set-up of the side-mode suppressed tunable OEO

Fig. 6.18 shows the overall experimental arrangement. Light from a distributed feedback laser (DFB) passes through a single passband filter (black dotted portion of Fig. 6.18) composed of a phase modulator (iXblue MPZ-LN-40) and a tunable optical bandpass filter (XTM-50) as described in section 6.2. Apart from being an integral part of the tunable MWPF, the PM also functions as an electrical-to-optical (E/O) converter for the OEO loop [151]. The output of the single passband filter is then connected to the optoelectronic IIR section (red dotted portion of Fig. 6.18), in which an EDFA is used to compensate for the O/E and E/O conversion losses of the IIR loop, and can thus control the loop gain. A 1 nm OBPF was placed immediately after the EDFA to reject the out-of-band amplified spontaneous emission (ASE) noise. The output of the OBPF is split into two paths by a 3 dB

optical coupler, with one output being passed through an 8.3 km single mode fiber (SMF), photodetected in a high-speed photodiode, electrically amplified and finally connected to the RF port of MZM to complete the IIR loop. The other output of the coupler passes through a dual loop OEO section with short (L_1) and long (L_2) loop lengths of 200 m and 2 km, respectively. The optical output of the two fiber spools is fed to a balanced photodetector (DSC730, with a 3-dB bandwidth of 25 GHz, and responsivity of 0.60 A/W), with the photodetected signal being amplified in order to compensate the O/E and E/O conversion losses of the main OEO loop. Finally, a 10:90 electrical coupler is used for spectrum analysis (the 10% output is connected to an electrical spectrum analyzer (ESA)) while the remaining 90% is connected to the RF port of the PM to complete the OEO loop.

6.4.3 Experimental results and discussion

The generated RF signal from the proposed setup is shown in Fig. 6.21. The RF signal can be tuned from 6.5 GHz to 17.8 GHz by tuning the optical bandwidth of the TOBF of Fig. 6.18; the tuning range is limited by the bandwidth of the RF and electro-optic components of the OEO loop. The characteristics of the generated RF signals are described below, for two scenarios, namely the OEO with and without the IIR section. For the latter case, we completely removed the IIR section. However, in both cases we maintained a nearly identical oscillating signal power.

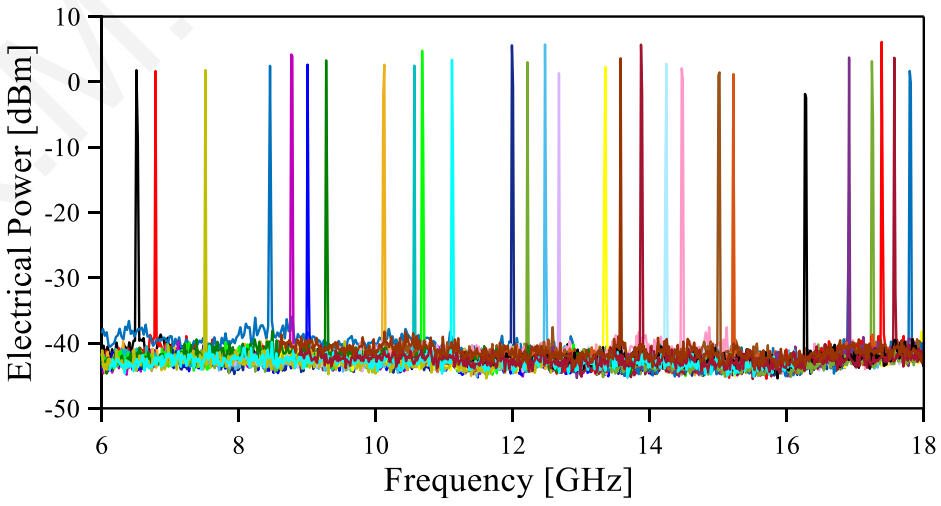

Fig. 6.21. Electrical spectra of the generated microwave signals for the whole tuning range.

A. Side mode suppression and close to carrier phase noise improvement

Fig. 6.22 shows the electrical spectrum of the generated RF signal at the oscillation frequency of 17.33 GHz. The IIR section in the OEO suppresses the side modes by an additional 12 dB as compared to the OEO without the IIR section. This improvement is due to the enhancement of the Q factor of the OEO loop that results from cascading the tunable single passband section with the IIR section. The suppression effect is also discernable in the phase noise plot as shown in Fig. 6.23, where inclusion of the IIR section leads to a 20 dB reduction of the SSB phase noise close to carrier (at an offset frequency of 200 Hz). Again, the postulated reason behind the phase noise improvement is due to the Q factor improvement which is supported by the second term of the Leeson formula for oscillator phase noise [156]:

$$L(f) = 10\log\left[\left(\frac{FKT}{P_{in}}\right)\left(1+\frac{f_0^2}{(2f_mQ_L)^2}\right)\left(1+\frac{f_c}{f_m}\right)\right]. \tag{6.10}$$

Here f_m is the offset frequency, f_0 is the oscillation frequency, f_c is the $1/f$ corner frequency, F is the active device noise figure, and Q_L is the loaded quality factor of the loop. The Q factor of the optoelectronic loop fundamentally determines the close-to-carrier phase noise. The noise floor is determined by the shot noise power of the photo-detector [58]. The noise floor is essentially the same for both arrangements since the parameters that determine the

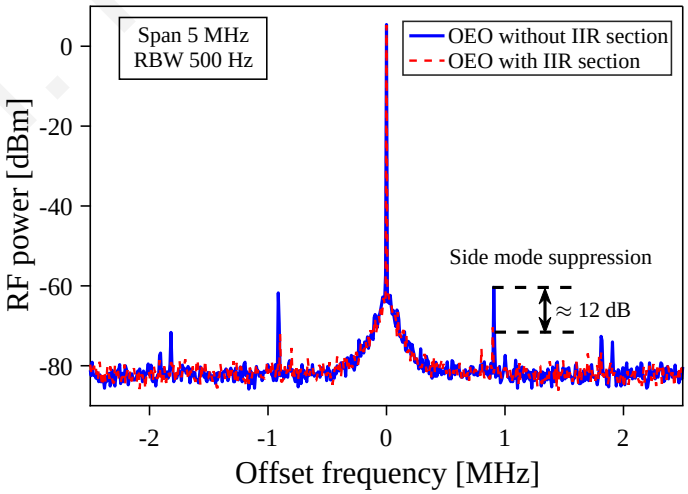

Fig. 6.22. Electrical spectrum of the generated RF signal using the tunable OEO at 17.33 GHz. The blue line represents OEO oscillation without the IIR section while the red dotted line represents oscillation with the IIR section in place. There is a 12 dB improvement in SMSR using the IIR section.

noise floor are identical for the OEO with and without the IIR section.

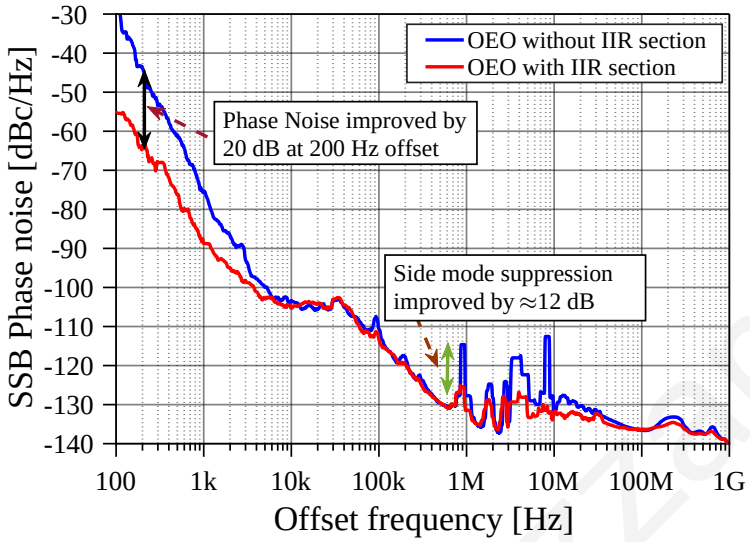

Fig. 6.23. Phase noise of the generated RF signal using the tunable OEO at 17.33 GHz. There is a 12 dB improvement in SMSR using the IIR section and 20 dB improvement of phase noise at 200 Hz offset frequency.

B. Improved Allan deviation

The measured Allan deviation (using the Allan deviation measurement functionality of the Rohde & Schwarz spectrum analyzer (FSU)) at 1 s observation time is 6×10^{-9} for the OEO with the IIR section and 6×10^{-8} for the OEO without the IIR section, as shown in Fig. 6.24. The improvement of short-term stability is due to the relatively high Q factor introduced by cascading the two microwave photonic filters.

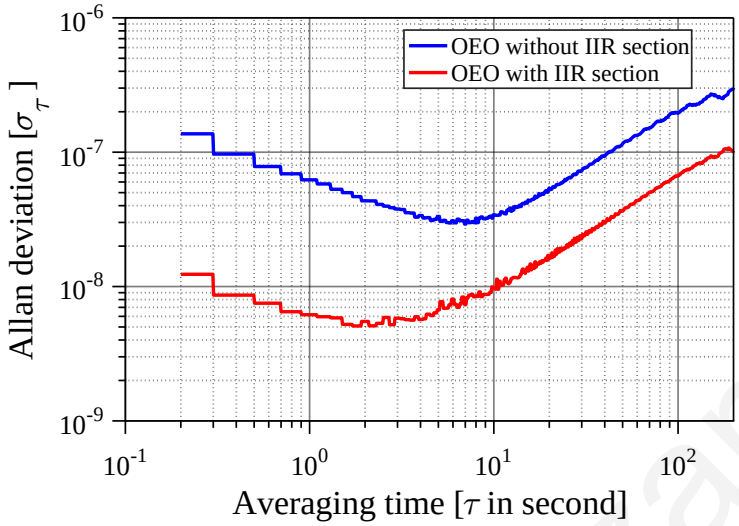

Fig. 6.24. Allan deviation of the generated RF signal at 17.33 GHz.

C. Side mode suppressed THz signal generation

Finally, we generated a THz signal by using the OEO as an RF source for an optical frequency comb generator (OFCG) via two-tone selection and optical heterodyning techniques as shown in Fig. 6.25. The optical frequency comb as shown in Fig. 6.26 was generated by driving the two RF ports of a dual drive Mach Zehnder modulator (DD-MZM) with RF signals of different amplitudes and phases. The comb generation technique described in section 6.2 is used here. We selected two comb lines (using a wavelength selective switch (WSS)) and generated a THz signal of 242.6 GHz though beating in a unitravelling carrier photodiode (UTC-PD). Before heterodyning in a UTC-PD, the selected two tones from the WSS were amplified with an EDFA, filtered by a 5 nm optical bandpass filter and then controlled by a variable optical attenuator (VOA). The UTC-PD is an unpackaged device which was connected to a horn antenna (20 dBi) using a coplanar mm-wave probe. Another identical horn antenna was used to receive the transmitted THz signal over a 30 cm wireless path. The

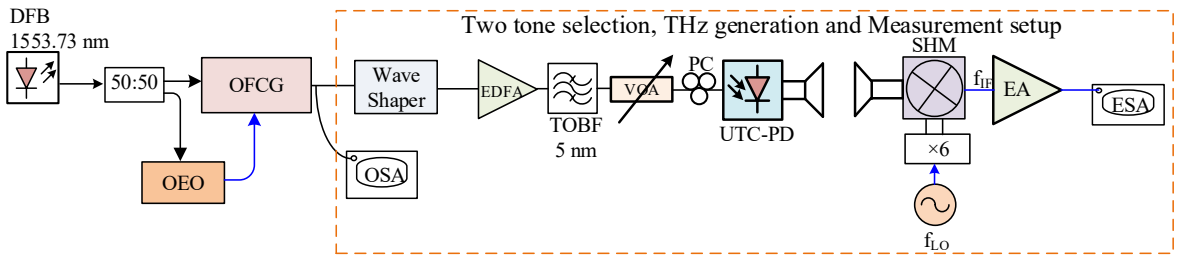

Fig. 6.25. Experimental set-up for THz generation

received THz signal was then down-converted by mixing it in a sub-harmonic mixer (SHM) with the signal generated from an external local oscillator (LO). Prior to connecting it to the SHM, the LO signal was passed through an electrical multiplier with a multiplication factor of six. The SHM mixes the second harmonics of the electrical multiplier's output with the received THz signal. The mixer output was adjusted at an intermediate frequency (IF) within the operating range of the microwave components and instruments by varying the LO frequency. Fig. 6.27 depicts the electrical spectrum of the down-converted signal, and it is seen that the side modes in the THz signal are suppressed when the IIR section is included in the driving OEO.

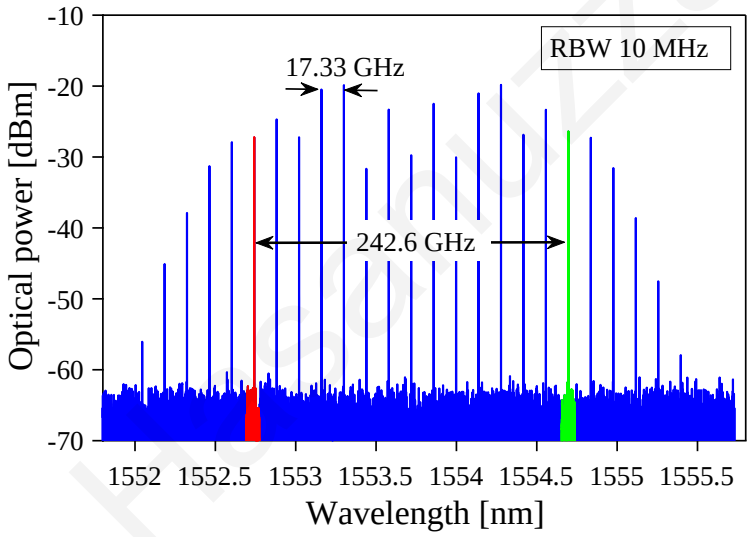

Fig. 6.26. Experimental set-up for THz generation

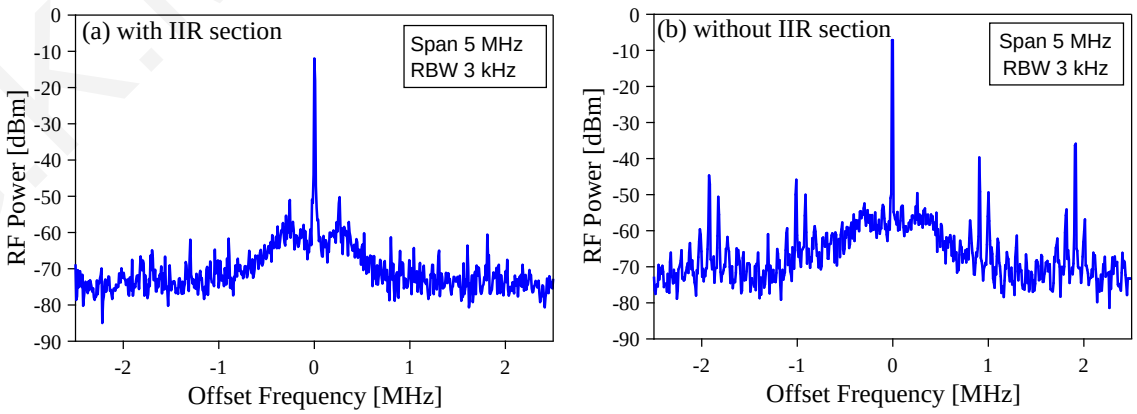

Fig. 6.27. Electrical spectrum of the down-converted 242.6 GHz signal, (a) with the IIR section (b) without the IIR section.

6.5 Conclusion

A low phase noise THz generation technique in which a tunable OEO is used to drive an OFC generator was demonstrated. With the OEO oscillation frequency set to 17.33 GHz, a THz signal at 242.6 GHz with a phase noise level of -78 dBc/Hz at 10 kHz offset was generated. This was then used to implement a RoF link which was evaluated for transmission of 10 Gbaud QPSK and 6 Gbaud 16 QAM over 40 km of SMF and a wireless distance of 30 cm.

We then modified the OEO structure by cascading an optoelectronic IIR filter section with the phase modulator based single passband section to improve the Q factor with a view to reducing the close to carrier phase noise, and suppressing the side modes. The experimental results show that the OEO with the IIR section improves the side mode suppression by 12 dB, the close to carrier phase noise by 20 dB and the Allan deviation by a factor of ten. Inclusion of the IIR section also enhances side mode suppression when the OEO is used to drive an OFCG for THz signal generation.

Through tuning the OEO oscillation frequency, the demonstrated system can generate a tunable THz signal. Hence it can be potentially applied in multi-carrier or multi-band radio over fibre links with a reconfigurable THz carrier frequency. The signal stability of the generated THz signal depends on the OEO stability. The following points could be considered for further improvement.

- Although the SSB phase noise of our OEO is comparable to other reported designs, the SSB phase noise of the system could be improved by using a long fibre. In addition, the long-term stability of the set-up could be improved by thermal stabilization, since the refractive index of the fibre depends on temperature, variation of which results in frequency drift of the OEO oscillation. This oscillation frequency drift could be controlled by using a temperature stabilized box or by phase locking with an external reference.
- Recently, hollow core photonic band gap (HC-PBG) fibers have been considered in OEO implementations to enhance long term stability, and improve the temperature stability by a factor of more than 15, as compared to standard single mode fibre [157–160].

CHAPTER 7

Conclusions and Future Work

7.1 Introduction

With the background and motivation of this work having been covered in chapters 1, 2 and 3, the preceding three chapters have discussed in detail the original contributions of this thesis in the broad theme of photonically-enabled technology for the generation and guidance of signals covering the mm-wave and THz regions of the electromagnetic spectrum, with the primary context being the FiWiN5G project, of which this project was a constituent part. FiWiN5G was primarily concerned with the application of photonics to the development of devices, subsystems and systems for 5G applications. Given that a major thrust of 5G is the exploitation of the mm-wave region (in order to confer a sufficiently high bandwidth) and that there is also considerable work looking beyond 5G, for which the THz region will be explored, the work focused on both the W-band and also 240 GHz for radio-over-fibre. In brief, the key contributions of the thesis are:

- the design of hollow core anti-resonant (HC-AR) fibres for THz wave guidance;
- the demonstration of a low-phase noise self-oscillating optical frequency comb generator (SOFCG) operating in the W-band;
- and the implementation of an optoelectronic oscillator (OEO) driven optical frequency comb generator (OFCG) for low phase noise mm-wave and THz signal generation.

The last two contributions provided the key elements for the realization of high data rate

radio-over fibre systems at W band and 242.6 GHz, which transmitted over wireless distances of 1.3 m and 30 cm respectively. Although these transmission distances are modest, it should be borne in mind that many projected applications for mm-wave and THz communications are destined for indoor applications and even for data centre interconnects. This chapter will provide an overview of the above work and evaluate its importance to the future deployment of mm-wave and THz communications.

7.2 Summary of key contributions of the thesis

Although the primary focus of FiWiN5G was communications, both the mm-wave and THz band have other significant applications in areas such as radar, sensing, astronomy and material characterisation. Hence much of the work presented earlier has potential applications in these areas; for example, the W-band system could be readily modified to operate as a W-band radar for applications such as foreign-object detection. Irrespective of the particular application, the key theme of the research was the guidance and generation of mm-wave and THz signals. For the latter, many systems operate in free space due to the low attenuation of dry air, but fibres that are capable of supporting THz transmission are of increasing importance for situations in which it is required to focus THz signals to smaller spot sizes. Hence chapter 4 considered the design of low-loss THz fibres based on hollow-core anti-resonant concepts.

In terms of signal generation, two key parameters are phase noise and frequency. For the former, optoelectronic oscillators are undisputed as providing far superior performance compared to electronics-based approaches, hence much of the research effort was directed to this area. However, the vast majority of optoelectronic oscillators have been reported in the X-band, and it would be desirable to extend their operation to at least the mm-wave spectrum whilst continuing to take advantage of the low phase noise afforded by high-Q optical elements. In this respect, optical frequency comb generators when combined with optical heterodyning offer the prospect of generating not only mm-wave, but also THz, signals. However, Mach-Zehnder modulator based combs generally require an external RF synthesizer, which somewhat negates the advantage of going to a photonics-based approach. Hence we developed a novel self-oscillating comb, whose topology derives from the OEO principle and also demonstrates good phase noise performance. A further advantage that

pertains to the comb approach is the potential to develop a radio-over-fibre system in which the wavelength selective switch can be configured to support multiple carrier frequencies simultaneously (e.g. 30 GHz, 60 GHz and 90 GHz) for multiband applications. Nevertheless, the SOFCG reported in Chapter 5 lacks frequency tunability, which is potentially also an important factor in future reconfigurable systems. Hence Chapter 6 described an OEO-driven OFCG in which frequency tunability with high side mode suppression was achieved with cascaded microwave photonic filter sections, with this then being applied to a 242 GHz radio-over-fibre demonstration.

7.2.1 Low loss THz fibres

In Chapter 4, two polymer based hollow core anti-resonant fibre structures have been numerically investigated with the state-of-the-art finite element package COMSOL at an operating frequency 1 THz. The first design is a modified version of a HC-AR fibre where additional nested tubes are inserted inside the resonant elements. These anti-resonant elements are non-touching, resulting in a hollow core nested anti-resonant node-less fibre (HC-NANF). A six-element based HC-NANF design is predicted to provide low loss THz guidance (with a transmission loss of 0.05 dB/m at 1 THz, a 0.4 THz wide low-loss transmission window and a 0.6 THz flat dispersion window). This proposed design is the first demonstration of a HC-NANF fibre in the THz band and it provides the lowest material absorption loss amongst the state-of-the-art fibres operating at 1 THz (as compared in Table 4.2). Therefore, the HC-NANF is a strong potential candidate for long-haul THz guided transmission. Although the HC-NANF offers low transmission loss, it cannot guarantee single mode guidance due to strong confinement of both the fundamental mode and higher order modes (HOMs). Hence a second design was proposed, in which a regular HC-AR fibre is considered to obtain single mode guidance by maintaining the shape factor *d/D* of the fibre, where *d* is the inner diameter of the anti-resonant tubes and *D* is the core diameter. At $d/D = 0.69$, the core guided higher order modes are phase matched with the anti-resonant tube guided modes. As a result, the HOMs exhibits higher transmission loss than the fundamental mode and the fibre effectively operates under single mode guidance. The HC-AR fibre provides relatively higher transmission loss than the HC-NANF fibre, but it maintains a high HOM extinction ratio. A key point to note is that both the designs proposed in this thesis are amenable to fabrication; only 13

capillaries are required for the HC-NANF while seven capillaries are required for the HC-AR fibre including the outer jacket. This contrasts well with other reported fibres, such as hollow core photonic bandgap fibres and porous core fibres, which have significantly more complex cross sections with the order of 50 air holes.

7.2.2 Self-oscillating optical frequency comb

In chapter 5, the experimental results of an external modulation based self-oscillating optical frequency comb (SOFCG) were described. Twenty-three optical comb lines were generated using a single dual-drive Mach-Zehnder modulator with a frequency spacing of 11.84 GHz defined by an electrical band pass filter in the optoelectronic loop. Selecting two comb lines and heterodyning in a photo-diode, a mm-wave signal at 94.8 GHz was experimentally generated and indeed signals up to 260 GHz can potentially be generated if a suitably high bandwidth photo-diode is used.

The key advantage of the SOFCG topology is that it dispenses with the external RF oscillator that is normally used in Mach-Zehnder modulator implementations of OFCGs. This is achieved by using an optoelectronic oscillator loop topology, and in essence the SOFCG can be regarded as an OEO, in which use is made of dual-loop topologies to provide a high optical Q while maintaining side mode suppression. As with the OEO, the SOFCG provides a dual output, i.e. a direct microwave signal and an optical signal. In the OEO, this direct microwave output signal results through photodetection of a microwave modulated signal (typically a double sideband spectrum in the case of intensity modulator based devices), whereas in the SOFCG the modulator output is an optical comb, and photodetection of the comb spacing results in the RF signal that both drives the dual-drive Mach-Zehnder modulator and can be used as a direct output. Moreover, the SOFCG is found to outperform a conventional OFCG that is driven by an RF synthesizer, with a single sideband phase noise that is 27 dB better at an offset of 10 kHz, which augurs well for application to highly demanding applications such as Doppler radar or phase-modulated radio-over-fibre systems. A comprehensive parametric study showed that this approach will also outperform an OEO which employs electronic multiplication to reach the W-band.

Subsequently, a W-band radio-over-fibre (RoF) link was implemented with a 64 QAM LTE-Advanced signal transmitted over a 1.3 m wireless distance, with an error vector mag-

nitude (EVM) less the EVM limit. This implementation is the first experimental demonstration of an SOFCG for a RoF link at W-band (specifically 94 GHz), which has strong potential application to front hauling in 5G systems and beyond-5G systems. In addition to front hauling, the SOFCG topology may be applied to multiband and multi-carrier RoF links as described earlier.

7.2.3 THz radio-over-fibre system based on OEO-driven optical comb

Since the SOFCG of Chapter 5 consists of an electrical band pass filter of fixed centre frequency, the system suffers from a lack of frequency tunability. This limitation may be overcome through using a conventional OEO topology to directly drive the dual drive Mach-Zehnder modulator of an OFCG, as described in Chapter 6. By decoupling the OEO from the OFCG, one essentially uses separate modulators in these two subsystems, thus allowing the OEO to be implemented with a phase modulator instead of an intensity modulator. This provides a significant advantage, in that when a phase modulator is combined with a tunable optical bandpass filter, it can act both as a phase modulator and also as a tunable microwave photonic filter. The phase modulator (PM) based MWP filter was tuned to generate microwave oscillations from 6.58 to 18.36 GHz, with this microwave output then being applied to the OFCG stage. Signals at 101.5 GHz and 242.6 GHz were generated through two tone selection and optical heterodyning in a uni-travelling carrier photodiode (UTC-PD). This tunable THz generation technique is an attractive alternative to other techniques in that it is implemented with commercial off-the-shelf telecommunications industry components. Further, a RoF link at 242.6 GHz with 6 Gbaud 16 QAM modulation was implemented that results in a throughput of 24 Gbps. The obtained bit error rate was below the forward error correction (FEC) limit. The demonstrated RoF link can be deployed as a fixed-wireless link in situations where high capacity is required on a temporary basis, such as a major sporting event, or as a wireless bridge in the event of a pre-existing fibre link being damaged through a natural disaster. One of the issues with the first iteration of the OEO-driven OFCG was the inability of the PM based single passband MWP filter to select a single (spur free) oscillating mode, resulting in side modes of the microwave drive signal from the being translated into the synthesised THz signal that was down converted from the wireless path. To suppress the spurious modes and reduce the close to carrier phase noise, we cascaded an optoelectronic

infinite impulse response (IIR) filter with the existing PM based single band pass filter in the OEO loop. Cascading of these two microwave photonic filters enhances the OEO loop Q factor and thus helps to suppress the side modes by additional 12 dB, subsequently reducing the close to carrier phase noise by an additional 20 dB in the generated microwave signal.

7.3 Future work

The core experimental results of this thesis mainly focused on the implementation of the OEO topology along with the OFCG to generate optical frequency combs and then the subsequent application of these to low phase noise mm-wave and THz signal generation and radio over fibre links. Although an OEO-driven OFCG is able to generate low phase noise mm-wave signals, the phase noise is degraded in the multiplication process during up-conversion. To avoid the multiplication penalty, direct generation of W-band signals via an OEO topology is considered highly desirable. In addition, the discrete arrangement of the components to realise the above microwave photonic systems (i.e. the SOFCG and the OEO-driven OFCG and associated RoF systems) is appropriate for proof-of-concept systems. However, practical deployments of 5G systems are likely to require nanocells, picocells and even femtocells, which implies a need for mass production of large numbers of remote antenna units (RAU). Although the work presented here is mostly focused on equipment that would be located at a central office (for which cost is less of an issue), it is still the case that reduction of SWaP (size, weight and power requirements) is critical to the future success of 5G. Hence there is significant interest in integrated microwave photonics. Moreover, electrical connection to the RAU is crucial. Multi-core fibre (MCF) in conjunction with power-over-fibre (PoF) and zero-biased uni-travelling carrier photodiode technology can solve this. The details of this proposed concept are discussed in the next section, along with suggestions for integrated photonic implementations of the work in Chapters 5 and 6, and the development of mm-wave OEOs.

7.3.1 Multicore fibre Based mm-wave Generation, Radio over-fibre and Power-over-fibre

A number of technologies have been considered in order to meet the demand for high wireless and wireline data rates with low latency. These include mm-wave radio-over-fibre (RoF),

distributed antenna systems (DAS) in micro- or nanocell architectures, and spatial division multiplexing (SDM) using multicore fibre (MCF) [161]. In both RoF and DAS micro- and nanocell access networks, a key need is to have remote antenna units (RAU) of small footprint, low complexity, low cost and low power consumption. For the latter requirement, zero-biased uni-travelling carrier photodiodes (UTC-PD) and the delivery of power-over-fibre (PoF) help to eliminate the use of electrical supply lines and also lead to simpler RAU architectures.

PoF is an emerging technology where electrical power is transmitted over fibre to from a remote location with the aid of photonic power converters (PPC) and high power laser diodes [162]. More recently, PoF technology was demonstrated in a MCF-based RoF link to bias the microwave components of a RAU in a microcell architecture. In [163] an optical link feeding 60W along with bidirectional radio over fibre was demonstrated. Generation of spectrally pure microwave and mm-wave carrier signals is also a key aspect of high-speed data links since higher phase noise introduces jitter and results in a high error vector magnitude (EVM). Optoelectronic oscillators (OEO) can provide low phase noise microwave and mm-wave oscillation [3]. Recently MCF has been proposed for implementing a multi-loop OEO topology in [164] and experimentally demonstrated in [165] with a phase noise of -85 dBc/Hz at a 10-kHz offset from a 4.494 GHz carrier. We want to extend the above concepts by proposing the use of a single MCF to implement three key functions, namely: (i) an OEO for low phase noise mm-wave generation (ii) an RoF link for providing high capacity low latency access network and (iii) PoF for biasing the RAU.

The proposed architecture for the simultaneous generation of a microwave carrier, its subsequent implementation in a RoF link and the use of PoF for this link is shown in Fig. 7.1. More details on the use of MCF are discussed in Appendix A.

Here a 9-core MCF is used to illustrate the concept for a single microcell; six of these cores are used to implement a dual-loop OEO, two are allocated to PoF and the final core is employed for the RoF link. The number of cores depends on the number of cells according to the relation $6+3M$, where M is the number of microcells. Referring to Fig. 7.1, the optical signal from a fibre laser (FL) is fed to a dual drive Mach-Zehnder modulator (DD-MZM), which functions both as an optical frequency comb generator (OFCG) for optical multi-tone generation and an E/O converter for the OEO loop. After being amplified by

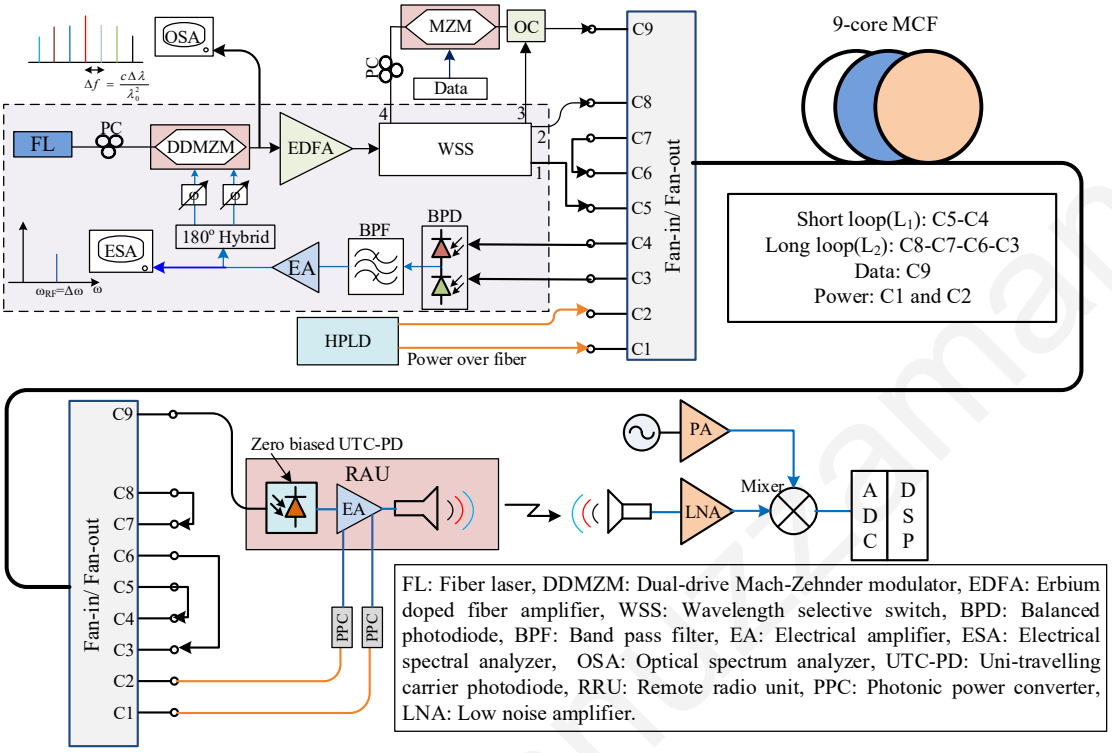

Fig. 7.1. Schematic structure of multicore fibre based microwave and millimeter wave generation, radio over fibre link and power over fibre link. The optical and electrical paths are indicated by black and blue lines respectively. The orange lines indicate the power over fibre link.

an erbium doped fibre amplifier (EDFA), the optical comb passes through a programmable wavelength selective switch (WSS) where four comb lines are selected and then diverted to four different output ports. Of these, two tones (port-1 and port-2 of the WSS) are used for the dual-loop OEO loop, in which the short loop (L_1) comprises two cores (core-4 and core-5) while the long loop (L_2) is formed from four cores (cores 3, 6, 7, and 8). In order to implement the short loop (L_1) the output from core-5 is connected to core-4 in the lower fan-in/fan-out module. For the long loop, the output from core-8 is connected to core-7, the output from core-7 is connected to core-6 and finally the output from core-6 is connected to core-3. The outputs from core-3 and core-4 are then connected to the two input ports of a balanced photodetector (BPD). The photodetected signal is then amplified and filtered by an electrical amplifier and bandpass filter respectively. Prior to connecting to the DD-MZM for completing the optoelectronic loop, the electrical signal is divided into two by an 180-degree hybrid. Two electrical phase shifters are placed after the 180-degree hybrid to obtain the

flat comb condition described in [166]. Through appropriate biasing and phase condition the optoelectronic loop can be configured to act as a self-oscillating comb generator as described in chapter 5 [133].

The other two tones selected by the WSS (at port 3 and port 4) are used for mm-wave generation (via heterodyning at the RAU) and data modulation as shown in Fig. 7.1. A MZM is used for data modulation, and an optical coupler (OC) is then used to combine the modulated tone with the other CW tone. Then the combined signal is propagated through core-9 of the MCF and heterodyne detected in a zero-biased UTC-PD. The photodetected mm-wave signal is then amplified before wireless propagation via the antenna. The amplifier in the remote radio unit is biased through the photonic power converted signal which is transmitted to the RAU using core-1 and core-2 of the MCF as illustrated in Fig. 7.1. A second identical antenna of the same polarization is used to receive the transmitted signal mm-wave signal. Subsequently, the received signal is amplified by a low noise amplifier, down-converted by a mixer and analysed with a digital signal processor (DSP).

7.3.2 W band Optoelectronic oscillator

W band (75-110 GHz) has several exciting applications including radar, fixed wireless connectivity and for supporting advanced mobile communication such as 5G and beyond-5G [13]. For example, the frequency range of 75-110 GHz has recently been used for detecting small objects from a distance for detection of debris on airport runways [13]. A low phase noise mm-wave signal is indispensable for such applications, and photonic generation of mm-waves has several advantages over electronic approaches. As described in chapter 1 a simple way of generating mm-waves and THz waves is to heterodyne two free running lasers that have a wavelength difference corresponding to the desired frequency spacing, but in this approach the stability of the generated signal may fail to meet the fluctuation tolerance of the ITU regulation [30]. In contrast, optical frequency comb generators (OFCG) overcome this problem due to their highly phase correlated optical tones with a fixed frequency spacing [23]. By appropriate selection of comb lines, it is possible to generate mm-wave and THz signals as illustrated in Chapter 5 and 6, and this approach can eliminate frequency and phase fluctuations. However, the phase noise increases with $20\times\log N$, where N is the multiplication factor [167], and it desirable to avoid this multiplication penalty.

On the other hand, optoelectronic oscillators (OEO) are able to generate ultra-low phase noise microwave and mm-wave signals. The highest reported OEO oscillation frequency is up to 60 GHz [53, 69] and commercially available OEOs operate up to 34-36 GHz [168], hence results at W-band have not been reported yet. In a classical OEO, generally, an electrical bandpass filter is used to define the oscillation frequency. However, an electrical bandpass filter is unable to select a single oscillation mode as its bandpass is much broader than the free spectral range (FSR) of the long-cavity OEO. For example, a 2 km fibre as a cavity provides FSR of 100 kHz, and a bandpass filter at W band with such a narrow passband is unrealizable. Moreover, wide range tunability of several GHz is also hard to implement. In second generation OEOs, the electrical bandpass filter has been replaced by tunable microwave photonic filters (MWPF), which eliminates the high-frequency operation and tunability limitation of the electrical counterpart [53].

We postulate that W-band signals can be generated directly from an OEO in order to exploit the inherit low phase noise capability offered by an OEO, without any subsequent frequency multiplication in either the optical or electrical domain, and without the need for a reference RF signal as required in an OFCG. Such a system will able to therefore mitigate the problems associated with conventional approaches such a phase noise and signal instability in the free-running laser approach and phase noise degradation in the multiplication technique. To implement the concept, the OEO architecture described in section 6.4 can be considered (by replacing the components such as the photodiode, modulator and electrical amplifiers with those operating at W band) where a single passband MWP filter is cascaded with an optoelectronic IIR filter.

7.3.3 Integrated self-oscillating optical frequency comb generator

Integrated microwave photonics (IMWP) is an emerging area of current research of microwave photonics aiming to reduce the size, weight, and power consumption (SWaP) and cost of the communication system, amongst others. IMWP has already applied to realise MWP functions such as MWP filters [169], photonic generation of mm-wave [170] and photonic beamforming [171]. Recently, two integrated OEOs were reported, with one implemented on a silicon Photonic platform [172] and the other on an InP platform [173]. A schematic diagram of the integrated OEO on the InP platform is shown in Fig. 7.2. An

integrated OFCG has also been developed at UCL as shown in Fig. 7.3. We believe that it is possible to extend the above work to develop an integrated self-oscillating optical frequency comb generator by combining the OEO and OFCG to generate low phase noise mm-waves and THz signals.

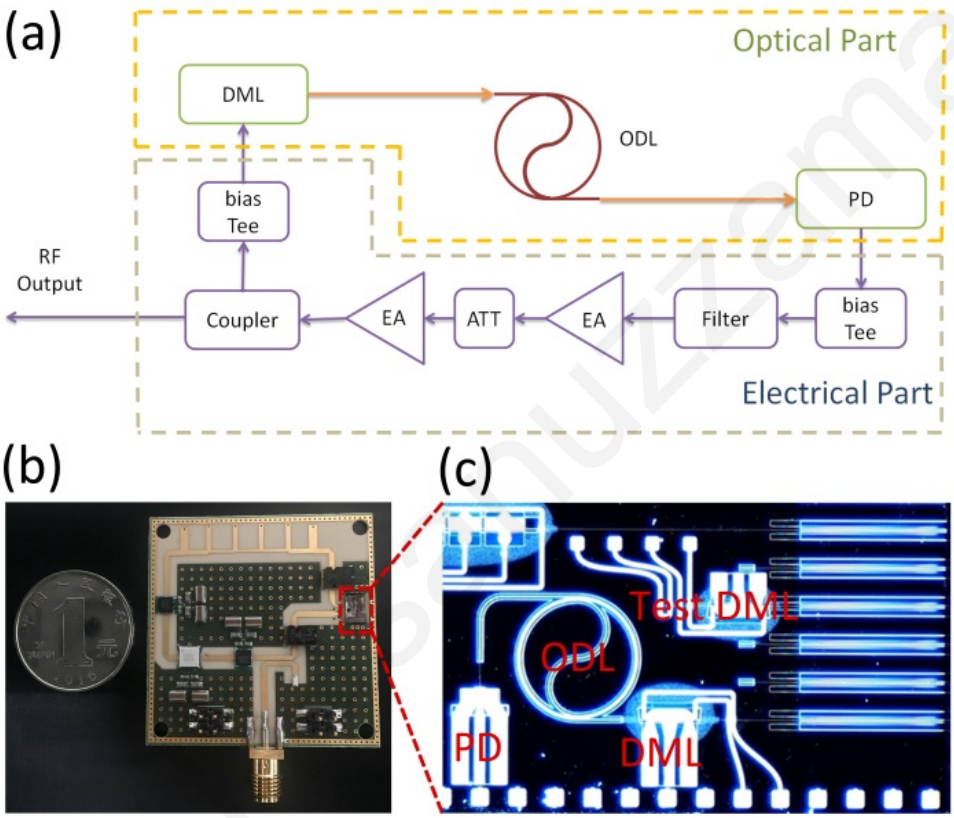

Fig. 7.2. Schamtic diagram of the reported integrated OEO. (b) Photograph of the integrated OEO (c) Optical part of the integrated OEO in InP platform. DML: directly modulated laser, ODL: optical delay line, PD: photo detector, EA: electrical amplifier, ATT:attenuator. After [173].

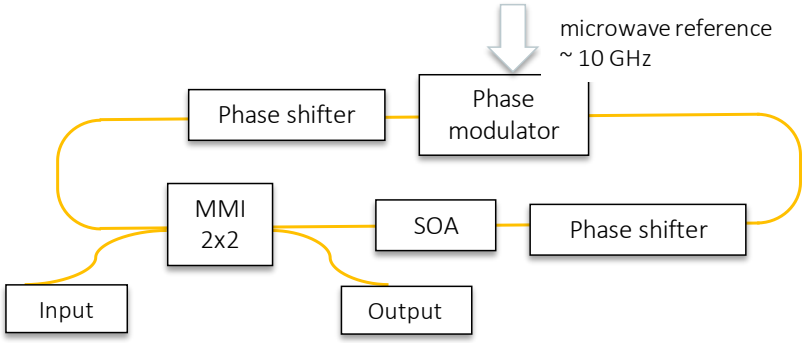

(a)

(b)

Fig. 7.3. (a) Schematic of the re-circulating loop OFCG (b) Fabricated OFCG PIC photograph. Dimensions 2 x 6 mm. Courtesy: Prof. Cyril Renaud, Department of Electronic and Electrical Engineering, University College London.

Appendices

APPENDIX A

Pre-emphasis Techniques for Multi-core Fibre Links

A.1 Introduction

As single-core single-mode fibre (SC-SMF) approaches its fundamental limit of 100 Tbps due to limitations from amplifier bandwidth, nonlinear noise and fibre fuse phenomena [161], multicore fibres (MCFs) offer scaling of transmission capacity through space division multiplexing (SDM) as indicated in Fig. A.1. Apart from data communications, MCF technology is also being considered for microwave photonics applications such as multi-cavity opto-electronic oscillators [164] and signal processing [174], since it offers identical mechanical and environmental conditions for all parallel cores. Figure A.2 shows some application of MCF in the microwave photonics field. As described in chapter 7, we aim to apply MCF to photonic generation of mm-waves for a radio-over-fibre demonstration in future work.

In this appendix, we report preliminary work on MCF links carried out during a secondment at DTU (Denmark). Specifically, a 2 km long 7-core MCF is characterized and a FPGA-based real-time multicore fibre based transmissions link is experimentally demonstrated. By means of adaptive pre-emphasis, deterministic distortions due to the limited bandwidth of the link are compensated. Experimental results show that a 2.5 Gbps non-return-to-zero on-off-keying (NRZ-OOK) modulated signal in each core can be transmitted with a BER level below the FEC limit, enabling post-FEC error-free transmission.

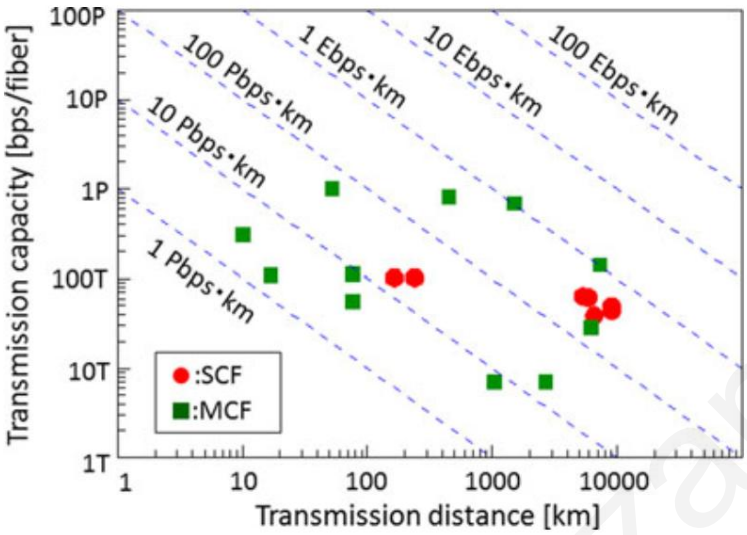

Fig. A.1. Recently reported transmission capacity and transmission distance by using single-mode single-core fibres and single-mode multicore fibres. After [161].

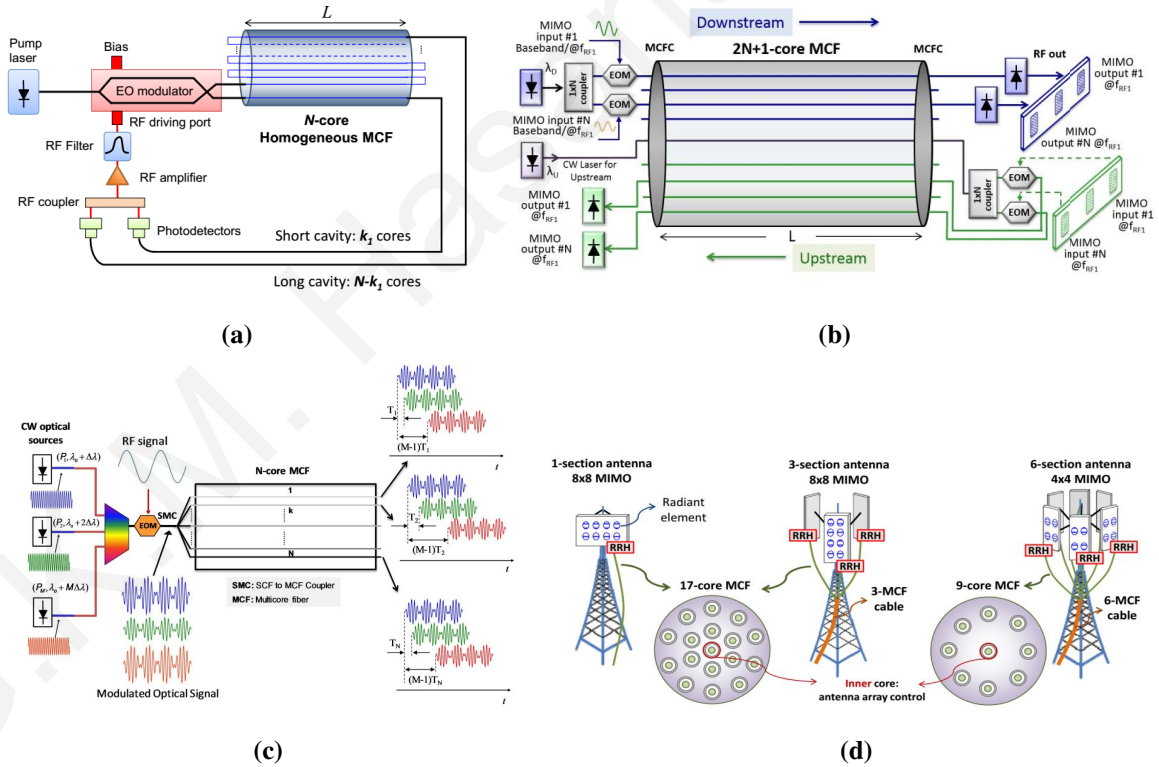

Fig. A.2. Application of MCF (a) Multi cavity Optoelectronic oscillator. After [164]. (b) Reconfigurable Radio Access Networks Using Multicore fibres. After [175]. (c) Microwave signal processing using MCF. After [176]. (d) Digital RoF distribution schemes over MCF for sectorized antennas with spatial MIMO. After [177].

A.2 Multi-core fibre in SDM

Several experimental results have been reported regarding the implementation of SDM in systems with MCFs, including 109 Tbps in a 7-core fibre [178],112 Tbps in a 7-core fibre [179], 305 Tbps in a 19-core fibre [180], and 1.02 Pbps in a 12-core fibre [181]. Furthermore, MCFs have also been implemented in fibre-wireless links such as a full duplex, 802.11ac-complient, 3×3 Multiple-Input Multiple-Output (MIMO) system using 7-core fibre [182], and Centralized Radio Access Networks (C-RANs) [175]. However, crosstalk between neighbouring cores is a fundamental limitation of MCFs in SDM applications. Crosstalk fundamentally arises due to power coupling between the adjacent cores during signal propagation and can be determined from the structural parameters of MCFs. Imperfect splices and multicore erbium doped fibre amplifiers also affect crosstalk. There are basically two known approaches for crosstalk reduction: (i) the first is to reduce the coupling coefficient between the cores in a homogeneous MCF, as in trench-assisted or hole-assisted MCFs [161]; (ii) the second approach is to introduce an intrinsic index difference between the adjacent cores, resulting in heterogeneous core MCFs. In addition to modified MCFs, offline digital signal processing (DSP) techniques and MIMO equalization [179], have been used to reduce the impact of crosstalk in strongly coupled 3-core MCFs. However, DSP introduces additional latency in the system which is undesirable in applications such as 5G networks [183].

A.3 Characterization of the Multi-Core Fibre

We characterized the crosstalk level and insertion loss of a 2 km seven core MCF shown in Fig. A.3. To measure the pairwise crosstalk and insertion loss of the MCF fibre, we launched optical power from a laser diode to each one of the cores in turn and measured the output of each core with a high sensitivity optical power meter, thus obtaining a 7×7 coupling matrix as shown in Table A.1. Figure A.4(a) shows the measured pair-wise power coupling between all seven cores. The total crosstalk per core is shown in Fig. A.4(b). The central core (core 0) exhibits the highest crosstalk as expected and other outer cores (1,2,4,6) have roughly equal crosstalk where core 3 and core 5 are much lower and higher than the other outer cores, respectively.

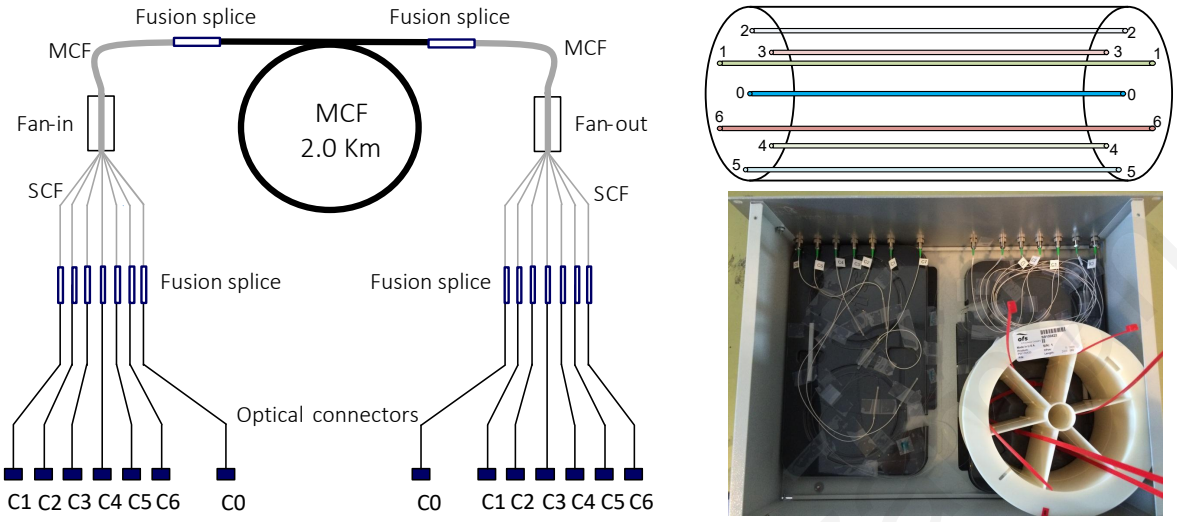

Fig. A.3. Connectorized 2 km MCF fibre spool with seven standard input and output SMF fibre patch-cords (FC/APC)

Table A.1: Multicore fibre coupling matrix

XT [dB]		Output						
		C0	C1	C2	C3	C4	C5	C6
Input	C0		-38.35	-41.4	-46.05	-36.8	-39	-40
	C1	-49.33		-39.99	-43.71	-48.39	-39.39	-45.67
	C2	-34.97	-54.86		-44.16	-63.99	-54.47	-52.46
	C3	-39.71	-56.17	-42.95		-44.48	-47.19	-60.47
	C4	-37.14	-51.43	-50.02	-45.5		-62	-42.49
	C5	-44.01	-37.49	-52.31	-46.68	-54.6		-39.01
	C6	-40.31	-58.23	-58.02	-47.06	-41.46	-34.66	
Total XT		-32.03	-34.66	-36.18	-37.56	-34.76	-32.17	-35.01
IL [dB]		2.08	5.59	4.59	3.75	3.05	4.72	4.32

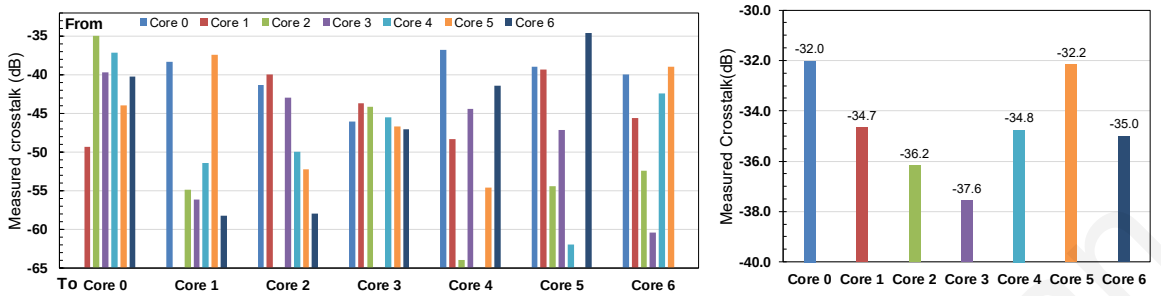

(a) **(b)**

Fig. A.4. (a) Measured pairwise crosstalk between cores (b) Measured total crosstalk per core.

A.4 Pre-emphasis

Pre-emphasis is a signal processing method which increases the amplitude of high frequency bands and decreases the amplitudes of lower bands to improve the quality of the signal in data transmission. Its function is to compensate the distortion conferred by the transmission medium to the transmitted signal. Correct use of the pre-emphasis mechanism results in less signal distortion at the receiver and consequently reduces the number of bit errors. The function of pre-emphasis is briefly illustrated in Fig. A.5

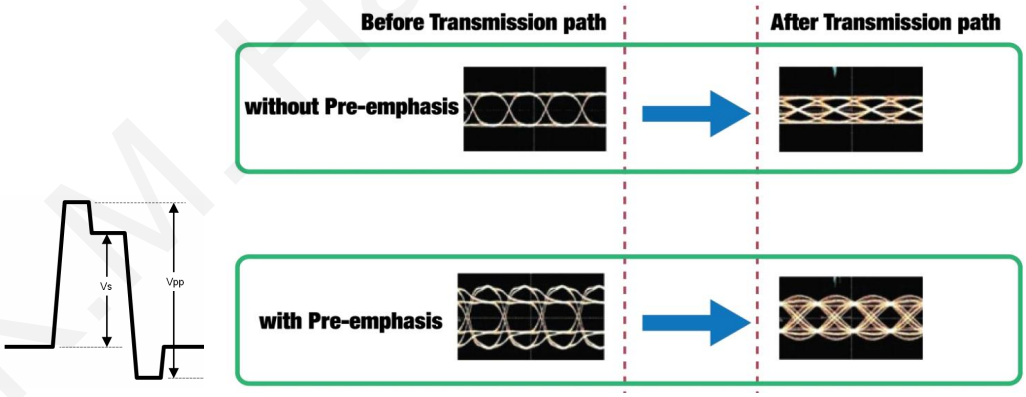

Fig. A.5. Pre-emphasis principle. After [184].

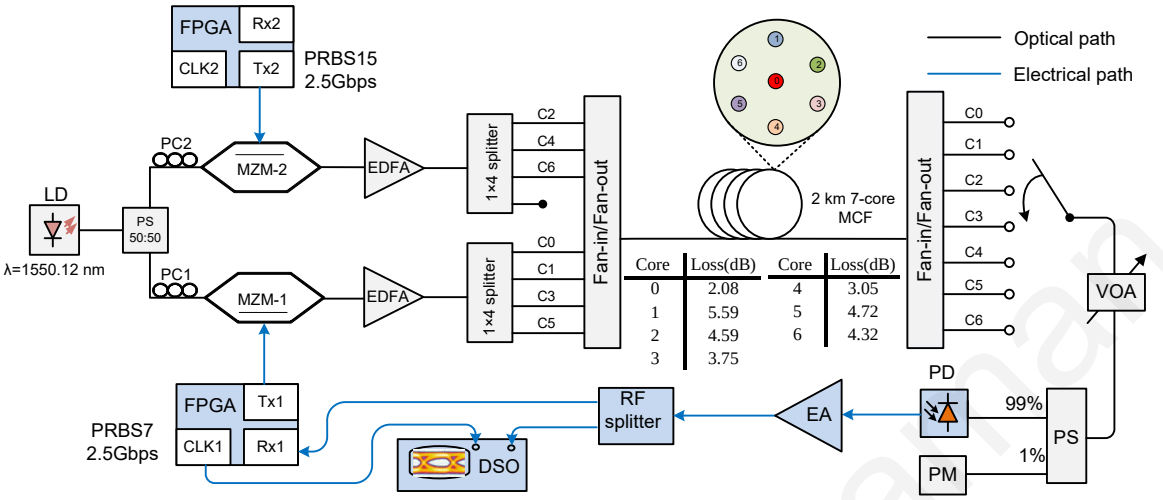

Fig. A.6. Experimental setup for BER and eye diagrams measurements.

LD: laser diode, PS: power splitter, PC: polarization controller, MZM: Mach-Zehnder modulator, FPGA: field-programmable gate array, PRBS: pseudo-random binary sequence, EDFA: erbium-doped fibre amplifier, C: core, MCF: multicore optical fibre, VOA: variable optical attenuator, PM: optical power meter, PD: photodiode, EA: electrical amplifier, DSO: digital storage oscilloscope.

A.5 Experimental Setup

Figure A.6 shows the experimental setup for BER measurements and signal quality characterization, which includes a 2 km long seven-core MCF with four transmission channels (cores 0,1,3,5) and three interfering channels (cores 2,4,6). The output of the laser source is divided by a 50:50 power splitter to the input of two quadrature biased Mach-Zehnder modulators (MZMs): MZM-1 (bias point 1.2 V) and MZM-2 (bias point 4.6 V). Polarization controllers (PC1, PC2) are placed before the MZMs to reduce polarization dependent loss. An Altera Stratix V FPGA module that contains seven transceiver channels is used to generate data streams and estimate the BER. MZM-1 and MZM-2 are modulated by 2.5 Gbps OOK signals generated from the FPGA module transmitters with PRBS 7 and PRBS 15 bit patterns, respectively. The modulated output from the MZMs is split by a 1×4 power splitter after being amplified by erbium-doped fibre amplifiers (EDFAs). The 1×4 splitter's outputs are connected to the inputs of the MCF's cores via a fan-in module. One of the MCF's outputs is connected to photodetector through a variable optical attenuator (VOA) for BER measurements. The signal into adjacent outer cores is decorrelated by transmitting PRBS 7 in cores 0,1,3,5 and PRBS 15 in 2,4 and 6. The detected electrical signal is then amplified

by a 26 dB broadband RF amplifier and divided into two paths; one is connected to a digital storage oscilloscope (DSO) to display the eye diagram and the second is connected to the receiver part of the FPGA for BER estimation. During the experiments, the optical power of each core was kept nearly equal.

A.6 Results and Discussion

The obtained BER of core-0 in response to received optical power at photodiode (PD) is shown in Fig.A.7 in two different scenarios, with and without signal pre-emphasis for mitigation of signal distortions. Applying the FPGA pre-emphasis option we can reduce the effect of distortions in each core and the BER is far below the level of the forward error correction (FEC) limit as shown in Fig.A.7 and A.8. The measured optical output power of core 0 after 2 km MCF transmission varied from -12.55 to -4.35 dBm, where the 2.5 Gbps NRZ-OOK signal's BER without equalization was from 1.4×10^{-2} to 8.7×10^{-7}, but with equalization it varied from 2.6×10^{-4} to 5.1×10^{-7}, as shown in Fig.A.7. Eye diagrams of the received signal without any signal equalization and with FPGA equalization are shown in Fig. A.9.

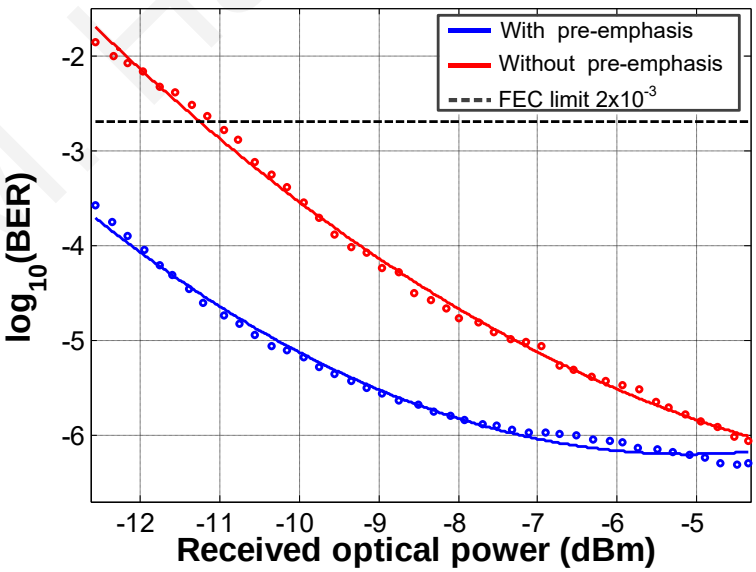

Fig. A.7. Comparison of measured BER versus received optical power of a 2.5 Gbps NRZ-OOK signal with and without FPGA equalization enabled for central core 0 and outer cores 1, 3 and 5. Eye pattern of the received 2.5 Gbps signal.

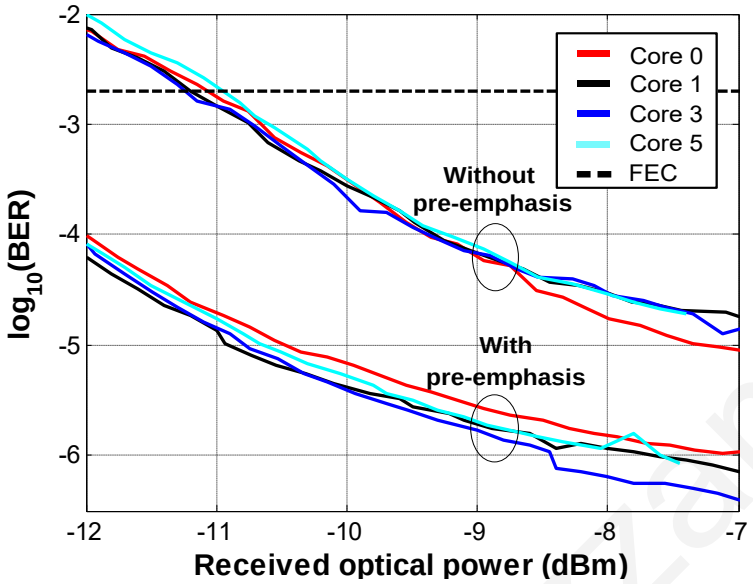

Fig. A.8. Comparison of measured BER versus received optical power of a 2.5 Gbps NRZ-OOK signal with and without FPGA equalization enabled (a) for central MCF core (core 0).

Results show that by using FPGA pre-emphasis functions we minimized crosstalk and decreased the BER value of received signals for each of seven MCF cores. Hence FPGA-based real-time multicore fibre technology is a viable future solution for high speed and high capacity communications.

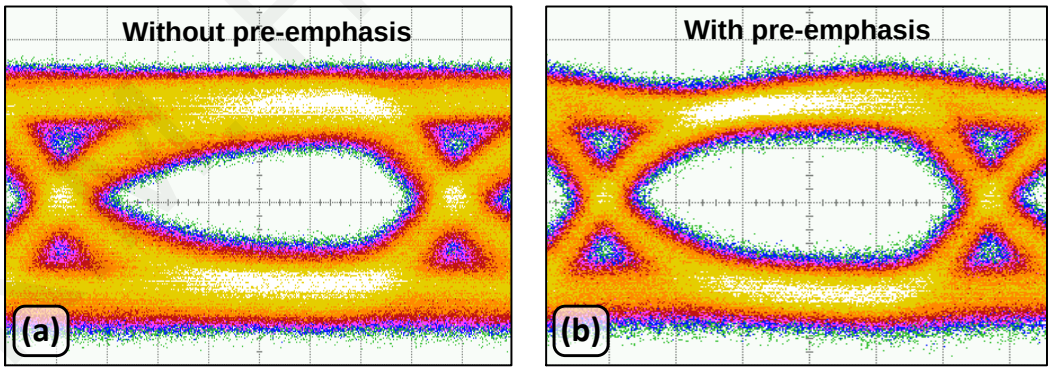

Fig. A.9. Eye pattern of the received 2.5 Gbps signal (a) without equalization and (b) with FPGA equalization for central MCF core 0.

References

[1] J. Capmany and D. Novak, "Microwave photonics combines two worlds," *Nature Photonics*, vol. 1, pp. 319–330, Jun. 2007.

[2] J. P. Yao, "Microwave Photonics," *Journal of Lightwave Technology*, vol. 27, no. 3, pp. 314–335, 2009.

[3] X. S. Yao and L. Maleki, "Optoelectronic microwave oscillator," *Journal of the Optical Society of America B*, vol. 13, pp. 1725–1734, Aug 1996.

[4] M. Bolea, J. Mora, B. Ortega, and J. Capmany, "Photonic arbitrary waveform generation applicable to multiband UWB communications," *Optics Express*, vol. 18, no. 25, p. 26259, 2010.

[5] J. Beas, G. Castanon, I. Aldaya, A. Aragon-Zavala, and G. Campuzano, "Millimeter-wave frequency radio over fiber systems: A survey," *IEEE Communications Surveys Tutorials*, vol. 15, pp. 1593–1619, Fourth Quarter 2013.

[6] V. Ferrero and S. Camatel, "Optical phase locking techniques: an overview and a novel method based on single side sub-carrier modulation," *Opt. Express*, vol. 16, pp. 818–828, Jan 2008.

[7] J. Yao, "A Tutorial on Microwave Photonics," *Photonics society newsletter*, vol. 26, pp. 1–12, Jun 2012.

[8] H. Shahoei and J. Yao, "Delay Lines," *Wiley Encyclopedia of Electrical and Electronics Engineering*, pp. 1–15, Dec. 2014.

[9] N. Sarkhosh, H. Emami, L. Bui, and A. Mitchell, "Reduced cost photonic instantaneous frequency measurement system," *IEEE Photonics Technology Letters*, vol. 20, pp. 1521–1523, Sep. 2008.

[10] A. Kanno, P. T. Dat, N. Sekine, I. Hosako, T. Kawanishi, Y. Yoshida, and K. Kitayama, "High-speed coherent transmission using advanced photonics in terahertz bands," *IEICE Transactions on Electronics*, vol. E98.C, pp. 1071–1080, Dec. 2015.

[11] A. Kanno, P. T. Dat, N. Sekine, I. Hosako, N. Yamamoto, Y. Yoshida, K. Kitayama, and T. Kawanishi, "Seamless fiber-wireless bridge in the millimeter- and terahertz-wave bands," *Journal of Lightwave Technology*, vol. 34, pp. 4794–4801, Oct 2016.

[12] A. Kanno, P. T. Dat, T. Kuri, I. Hosako, T. Kawanishi, Y. Yoshida, Y. Yasumura, and K. Kitayama, "Coherent radio-over-fiber and millimeter-wave radio seamless transmission system for resilient access networks," *IEEE Photonics Journal*, vol. 4, pp. 2196–2204, Nov. 2012.

[13] A. Kanno, P. T. Dat, N. Yamamoto, and T. Kawanishi, "Millimeter-wave radio-over-fiber network for linear cell systems," *Journal of Lightwave Technology*, vol. 36, pp. 533–540, Jan. 2017.

[14] *Millimeter- and terahertz-wave over fiber technologies for high-speed communication and non-telecom applications*, vol. 10128, 2017.

[15] Cisco, "VNI Global Fixed and Mobile Internet Traffic Forecasts," 2019.

[16] ITU-R, "Recommendation ITU-R M.2083-0 - IMT Vision-Framework and overall objectives of the future development of IMT for 2020 and b eyond M Series Mobile, radiodetermination, amateur and related satellite services," Tech. Rep. M Series, 2015.

[17] 3GPP, "Technical Specification Group Services and System Aspects; Network architecture (Release 15)," Tech. Rep. TS 23.002 V13.4.0, 3gpp, 2019.

[18] N.-n. Chen, J. Liang, and L.-y. Ren, "High-birefringence, low-loss porous fiber for single-mode terahertz-wave guidance," *Appl. Opt.*, vol. 52, no. 21, pp. 5297–5302, 2013.

[19] T. Nagatsuma, "Terahertz technologies: Present and future," *IEICE Electronics Express*, vol. 8, pp. 1127–1142, Jul. 2011.

[20] J. A. Nanzer, P. T. Callahan, M. L. Dennis, and T. R. C. Jr, "Photonic Signal Generation for Millimeter- Wave Communications," *Johns Hopkins APL Technical Digest (Applied Physics Laboratory)*, vol. 30, no. 4, pp. 299–308, 2012.

[21] J. Yao, "A Tutorial on Microwave Photonics," *Photonics society newsletter*, vol. 24, no. April, pp. 4–12, 2012.

[22] S. Koenig, D. Lopez-Diaz, J. Antes, F. Boes, R. Henneberger, A. Leuther, A. Tessmann, R. Schmogrow, D. Hillerkuss, R. Palmer, T. Zwick, C. Koos, W. Freude, O. Ambacher, J. Leuthold, and I. Kallfass, "Wireless sub-THz communication system with high data rate," *Nature Photonics*, vol. 7, pp. 977–981, Dec. 2013.

[23] H. Shams, T. Shao, M. J. Fice, P. M. Anandarajah, C. C. Renaud, F. Van Dijk, L. P. Barry, and A. J. Seeds, "100 Gb/s multicarrier THz wireless transmission system with high frequency stability based on a gain-switched laser comb source," *IEEE Photonics Journal*, vol. 7, pp. 1–11, Jun. 2015.

[24] J. K. Hmood, S. D. Emami, K. A. Noordin, H. Ahmad, S. W. Harun, and H. M. H. Shalaby, "Optical frequency comb generation based on chirping of Mach-Zehnder Modulators," *Optics Communications*, vol. 344, pp. 139–146, Jan. 2015.

[25] T. Kawanishi, T. Sakamoto, and A. Kanno, "Sub-THz radio-over-fiber signal generation using external modulation," *EICE Electronics Express*, vol. 12, pp. 1–12, Jul. 2015.

[26] D. Hillerkuss, T. Schellinger, M. Jordan, C. Weimann, F. Parmigiani, B. Resan, K. Weingarten, S. Ben-Ezra, B. Nebendahl, C. Koos, W. Freude, and J. Leuthold, "High-quality optical frequency comb by spectral slicing of spectra broadened by SPM," *IEEE Photonics Journal*, vol. 5, Oct. 2013.

[27] J. Dai, X. Xu, Z. Wu, Y. Dai, F. Yin, Y. Zhou, J. Li, and K. Xu, "Self-oscillating optical frequency comb generator based on an optoelectronic oscillator employing cascaded modulators," *Optics Express*, vol. 23, p. 30014, Oct. 2015.

[28] A. Kanno, P. T. Dat, T. Kuri, I. Hosako, T. Kawanishi, Y. Yoshida, and K. Kitayama, "Evaluation of frequency fluctuation in fiber-wireless link with direct IQ down-converter," in *European Conference on Optical Communication, ECOC*, (France), pp. 6–8, 2014.

[29] ITU, "ITU-R M.2003 Multiple Gigabit Wireless Systems in frequencies around 60 GHz," tech. rep., 2012.

[30] Rec. ITU-R SM.1045-1, "Frequency tolerance of transmitters."

[31] M. Fice, E. Rouvalis, F. Van Dijk, A. Accard, F. Lelarge, C. Renaud, G. Carpintero, and A. Seeds, "146-GHz millimeter-wave radio-over-fiber photonic wireless transmission system.," *Optics Express*, vol. 20, pp. 1769–1774, Jan. 2012.

[32] S. E. Alavi, M. R. K. Soltanian, I. S. Amiri, M. Khalily, A. S. M. Supa'at, and H. Ahmad, "Towards 5G: A Photonic Based Millimeter Wave Signal Generation for Applying in 5G Access Fronthaul," *Scientific Reports*, vol. 6, no. 1, pp. 1–11, 2016.

[33] D. Eliyahu, D. Seidel, and L. Maleki, "RF amplitude and phase-noise reduction of an optical link and an opto-electronic oscillator," *IEEE Transactions on Microwave Theory and Techniques*, vol. 56, pp. 449–456, Feb. 2008.

[34] H. Shams, M. J. Fice, K. Balakier, C. C. Renaud, F. van Dijk, and A. J. Seeds, "Photonic generation for multichannel THz wireless communication.," *Optics express*, vol. 22, pp. 23465–23472, Sep. 2014.

[35] H. Shams, M. J. Fice, K. Balakier, C. C. Renaud, A. J. Seeds, and F. van Dijk, "Multichannel 200ghz 40gb/s wireless communication system using photonic signal generation," in *Microwave Photonics (MWP) and the 2014 9th Asia-Pacific Microwave Photonics Conference (APMP) 2014 International Topical Meeting on*, pp. 366–369, Oct. 2014.

[36] X. Li, J. Yu, J. Zhang, Z. Dong, F. Li, and N. Chi, "A 400G optical wireless integration delivery system.," *Optics express*, vol. 21, pp. 18812–9, Aug. 2013.

[37] J. Yu, X. Li, and N. Chi, "Faster than fiber: over 100-Gb/s signal delivery in fiber wireless integration system," *Optics Express*, vol. 21, pp. 22885–22904, Sep. 2013.

[38] F. Li, Z. Cao, X. Li, Z. Dong, and L. Chen, "Fiber-wireless transmission system of PDM-MIMO-OFDM at 100 GHz frequency," *Journal of Lightwave Technology*, vol. 31, pp. 2394–2399, Jul. 2013.

[39] A. Hirata, T. Kosugi, H. Takahashi, J. Takeuchi, H. Togo, M. Yaita, N. Kukutsu, K. Aihara, K. Murata, Y. Sato, T. Nagatsuma, and Y. Kado, "120-GHz-band wireless link technologies for outdoor 10-Gbit/s data transmission," *IEEE Transactions on Microwave Theory and Techniques*, vol. 60, pp. 881–895, Mar. 2012.

[40] H. Packard, "Phase Noise measurement Seminar," tech. rep., Hewlett Packard, New Jersey, 1985.

[41] E. Rubiola, *Phase noise and frequency stability in oscillators*, vol. 9780521886. Cambridge: Cambridge University Press, 2008.

[42] M. S. Jankov, *Phase Noise in Microwave Oscillators and Amplifiers*. PhD thesis, 2010.

[43] T. L. Breault, "The Effects of Crystal Oscillator Phase Noise on Radar Systems," tech. rep.

[44] A. Georgiadis, "Gain, phase imbalance, and phase noise effects on error vector magnitude," *IEEE Transactions on Vehicular Technology*, vol. 53, pp. 443–449, Mar. 2004.

[45] W. Kester, "Converting Oscillator Phase Noise to Time Jitter MT-008," tech. rep.

[46] I. F. Akyildiz, J. M. Jornet, and C. Han, "Terahertz band: Next frontier for wireless communications," *Physical Communication*, vol. 12, pp. 16–32, Feb. 2014.

[47] T. Schneider, A. Wiatrek, S. Preussler, M. Grigat, and R. P. Braun, "Link budget analysis for terahertz fixed wireless links," *IEEE Transactions on Terahertz Science and Technology*, vol. 2, pp. 250–256, Mar. 2012.

[48] Recommendation ITU-R P.838-3, "Specific attenuation model for rain," tech. rep., 2005.

[49] Recommendation ITU-R P.840-6, "Attenuation due to clouds and fog," tech. rep., 2013.

[50] J. M. Jornet and I. F. Akyildiz, "Channel modeling and capacity analysis for electromagnetic wireless nanonetworks in the terahertz band," *IEEE Transactions on Wireless Communications*, vol. 10, pp. 3211–3221, Oct. 2011.

[51] Recommendation ITU-R P.676-11, "Attenuation by atmospheric gases," tech. rep., 2013.

[52] T. Bánky, B. Horváth, and T. Berceli, "Optimum configuration of multiloop optoelectronic oscillators," *Journal of the Optical Society of America B*, vol. 23, pp. 1371–1380, Jul. 2006.

[53] H. Peng, C. Zhang, X. Xie, T. Sun, P. Guo, X. Zhu, L. Zhu, W. Hu, and Z. Chen, "Tunable DC-60 GHz RF generation utilizing a dual-loop optoelectronic oscillator based on stimulated brillouin scattering," *Journal of Lightwave Technology*, vol. 33, pp. 2707–2715, Jul. 2015.

[54] X. Zou, X. Liu, W. Li, P. Li, W. Pan, L. Yan, and L. Shao, "Optoelectronic oscillators (OEOs) to sensing, measurement, and detection," *IEEE Journal of Quantum Electronics*, vol. 52, pp. 1–16, Jan. 2016.

[55] Y. Wang, J. Zhang, and J. Yao, "An optoelectronic oscillator for high sensitivity temperature sensing," *IEEE Photonics Technology Letters*, vol. 28, pp. 1458–1461, Jul. 2016.

[56] H. Yu, M. Chen, H. Gao, C. Lei, H. Zhang, S. Yang, H. Chen, and S. Xie, "Simple photonic-assisted radio frequency down-converter based on optoelectronic oscillator," *Photonics Research*, vol. 2, pp. 1458–1461, Aug. 2014.

[57] L. Maleki, "The optoelectronic oscillator," *Nature Photonics*, vol. 5, pp. 728–730, Dec. 2011.

[58] L. Maleki, "The opto-electronic oscillator (oeo): Review and recent progress," in *2012 European Frequency and Time Forum*, pp. 497–500, Apr. 2012.

[59] "Low phase noise and spurious level in multi-loop opto-electronic oscillators," pp. 405–410, May 2003.

[60] X. Yao, L. Maleki, and G. Lutes, "Dual-loop opto-electronic oscillator," *Proceedings of the 1998 IEEE International Frequency Control Symposium (Cat. No.98CH36165)*, pp. 545–549, 1998.

[61] I. Ozdur, M. Akbulut, N. Hoghooghi, D. Mandridis, M. U. Piracha, and P. J. Delfyett, "Optoelectronic loop design with 1000 finesse Fabry – Perot etalon," *Optics Letters*, vol. 35, no. 6, pp. 799–801, 2010.

[62] A. Liu, J. Liu, J. Dai, Y. Dai, F. Yin, J. Li, Y. Zhou, T. Zhang, and K. Xu, "Spurious Suppression in Millimeter-Wave OEO with a High-Q Optoelectronic Filter," *IEEE Photonics Technology Letters*, vol. 29, no. 19, pp. 1671–1674, 2017.

[63] H. Tang, Y. Yu, Z. Wang, L. Xu, and X. Zhang, "Wideband tunable optoelectronic

oscillator based on a microwave photonic filter with an ultra- narrow passband," *Optics Letters*, vol. 43, pp. 2328–2331, May 2018.

[64] L. Bogataj, M. Vidmar, and B. Batagelj, "Opto-electronic oscillator with quality multiplier," *IEEE Transactions on Microwave Theory and Techniques*, vol. 64, no. 2, pp. 663–668, 2016.

[65] W. Zhou and G. Blasche, "Injection-Locked Dual Opto-Electronic Oscillator With Ultra-Low Phase Noise and Ultra-Low Spurious Level," *IEEE Transactions on Microwave Theory and Techniques*, vol. 53, no. 3, pp. 929–933, 2005.

[66] O. Okusaga, E. J. Adles, E. C. Levy, W. Zhou, G. M. Carter, C. R. Menyuk, and M. Horowitz, "Spurious mode reduction in dual injection-locked optoelectronic oscillators," *Optics Express*, vol. 19, no. 7, p. 5839, 2011.

[67] Y. Jiang, H. Li, Z. Zhou, S. Wang, L. Hu, G. Bai, and J. Xu, "Frequency Locked Single-Mode Optoelectronic Oscillator by Using Low Frequency RF Signal Injection," *IEEE Photonics Technology Letters*, vol. 25, no. 4, pp. 382–384, 2013.

[68] J. Yang, Y. Jin-long, W. Yao-tian, Z. Li-tai, and Y. En-ze, "An Optical Domain Combined Dual-Loop Optoelectronic Oscillator," vol. 19, no. 11, pp. 807–809, 2007.

[69] M. Bagnell, J. Davila-Rodriguez, and P. J. Delfyett, "Millimeter-wave generation in an optoelectronic oscillator using an ultrahigh finesse etalon as a photonic filter," *Journal of Lightwave Technology*, vol. 32, no. 6, pp. 1063–1067, 2014.

[70] A. Docherty, C. R. Menyuk, J. P. Cahill, A. Docherty, C. R. Menyuk, J. P. Cahill, O. Okusaga, and W. Zhou, "Rayleigh-Scattering-Induced RIN and Amplitude-to-Phase Conversion as a Source of Length-Dependent Phase Noise in OEOs Amplitude-to-Phase Conversion as a Source of Length-Dependent Phase Noise in OEOs," *IEEE Photonics Journal*, vol. 5, no. 2, p. 5500514, 2013.

[71] K. Volyanskiy, Y. K. Chembo, L. Larger, and E. Rubiola, "Contribution of laser frequency and power fluctuations to the microwave phase noise of optoelectronic oscillators," *Journal of Lightwave Technology*, vol. 28, no. 18, pp. 2730–2735, 2010.

[72] K. Volyanskiy, Y. K. Chembo, L. Larger, and E. Rubiola, "Contribution of laser frequency and power fluctuations to the microwave phase noise of optoelectronic oscil-

lators," *Journal of Lightwave Technology*, vol. 28, no. 18, pp. 2730–2735, 2010.

[73] O. Okusaga, J. P. Cahill, A. Docherty, C. R. Menyuk, W. Zhou, and G. M. Carter, "Suppression of Rayleigh-scattering-induced noise in OEOs," *Optics Express*, vol. 21, no. 19, p. 22255, 2013.

[74] D. Eliyahu, W. Liang, E. Dale, A. A. Savchenkov, V. S. Ilchenko, A. B. Matsko, D. Seidel, and L. Maleki, "Resonant widely tunable opto-electronic oscillator," *IEEE Photonics Technology Letters*, vol. 25, no. 15, pp. 1535–1538, 2013.

[75] B. Pan, D. Lu, L. Zhang, and L. Zhao, "A Widely Tunable Optoelectronic Oscillator Based on Directly Modulated Dual-Mode Laser," *IEEE Photonics Journal*, vol. 7, no. 6, 2015.

[76] W. Li and J. Yao, "An optically tunable optoelectronic oscillator," *Journal of Lightwave Technology*, vol. 28, pp. 2640–2645, Sep. 2010.

[77] X. Li, Z. Dong, J. Yu, N. Chi, Y. Shao, and G.-K. Chang, "Fiber-wireless transmission system of 108 Gb/sdata over 80 km fiber and 2×2multiple-input multiple-output wireless links at 100 GHz W-band frequency.," *Optics Letters*, vol. 37, no. 24, pp. 5106–5108, 2012.

[78] X. Xie, C. Zhang, T. Sun, P. Guo, X. Zhu, L. Zhu, W. Hu, and Z. Chen, "Wideband tunable optoelectronic oscillator based on a phase modulator and a tunable optical filter.," *Optics letters*, vol. 38, no. 5, pp. 655–7, 2013.

[79] X. Xie, T. Sun, Huanfa Peng, C. Zhang, P. Guo, L. Zhu, W. Hu, and Z. Chen, "Widely tunable dual-loop optoelectronic oscillator," in *2014 Conference on Lasers and Electro-Optics (CLEO) - Laser Science to Photonic Applications*, pp. 1–2, June 2014.

[80] H. Peng, C. Zhang, P. Guo, X. Xie, T. Sun, X. Zhu, F. Chen, L. Zhu, W. Hu, and Z. Chen, "Tunable dc-40 ghz rf generation with high side-mode suppression utilizing a dual loop brillouin optoelectronic oscillator," in *Optical Fiber Communication Conference*, p. M3E.5, Optical Society of America, 2015.

[81] L. Zhuang, C. G. H. Roeloffzen, M. Hoekman, K.-J. Boller, and A. J. Lowery, "Programmable photonic signal processor chip for radiofrequency applications," *Optica*,

vol. 2, no. 10, p. 854, 2015.

[82] M. O. M. Erklein, B. I. S. Tiller, I. R. V. K. Abakova, U. D. S. M. Utugala, K. V. U. Hu, S. T. J. M. Adden, B. E. J. E. Ggleton, and R. A. S. Lavík, "Widely tunable , low phase noise microwave source based on a photonic chip," *Optics letters*, vol. 41, no. 20, 2016.

[83] M. Fleyer, A. Sherman, M. Horowitz, and M. Namer, "Wideband-frequency tunable optoelectronic oscillator based on injection locking to an electronic oscillator," *Optics Letters*, vol. 41, no. 9, p. 1993, 2016.

[84] B. Yang, X. Jin, Y. Chen, J. Zhou, X. Zhang, S. Zheng, and H. Chi, "A tunable optoelectronic oscillator based on a dispersion-induced microwave photonic filter," *IEEE Photonics Technology Letters*, vol. 25, no. 10, pp. 921–924, 2013.

[85] C. Li, Y. Wang, W. Wang, Z. Xu, B. Zhao, H. Wang, and D. Tang, "Widely tunable optoelectronic oscillator using a dispersion-induced single bandpass MPF," *IEEE Photonics Technology Letters*, vol. 30, no. 1, pp. 7–10, 2018.

[86] V. Torres-Company and A. M. Weiner, "Optical frequency comb technology for ultra-broadband radio-frequency photonics," *Laser and Photonics Reviews*, vol. 8, no. 3, pp. 368–393, 2014.

[87] S. T. Cundiff and J. Ye, "Colloquium: Femtosecond optical frequency combs," *Rev. Mod. Phys.*, vol. 75, pp. 325–342, Mar 2003.

[88] "RP Photonics Encyclopedia - mode locking, active, passive, modelocking, ultrashort pulses, pulse generation, instabilities."

[89] R. Zhou, P. Anandarajah, S. Latkowski, L. P. Barry, J. O'Carroll, and R. Phelan, "40nm wavelength tunable gain-switched optical comb source," *Optics Express*, vol. 19, no. 26, p. B415, 2011.

[90] P. M. Anandarajah, K. Shi, A. Kaszubowska, R. Phelan, L. P. Barry, A. D. Ellis, P. Perry, D. Reid, B. Kelly, A. D. Ellis, R. J. Manning, and I. D. Phillips, "Phase shift keyed systems based on a gain switched laser transmitter," *Optics Express*, vol. 6, no. 6, p. 13, 2004.

[91] P. M. Anandarajah, R. Maher, Y. Q. Xu, S. Latkowski, J. O'Carroll, S. G. Murdoch,

R. Phelan, J. O'Gorman, and L. P. Barry, "Generation of coherent multicarrier signals by gain switching of discrete mode lasers," *IEEE Photonics Journal*, vol. 3, no. 1, pp. 112–122, 2011.

[92] G. A. Sefler and K. Kitayama, "Frequency comb generation by four-wave mixing and the role of fiber dispersion," *Journal of Lightwave Technology*, vol. 16, no. 9, pp. 1596–1605, 1998.

[93] L. Shang, Y. Li, L. Ma, and J. Chen, "A flexible and ultra-flat optical frequency comb generator using a parallel Mach–Zehnder modulator with a single DC bias," *Optics Communications*, vol. 356, pp. 70–73, 2015.

[94] A. Kanno and T. Kawanishi, "Phase noise analysis of an optical frequency comb using single side-band suppressed carrier modulation in an amplified optical fiber loop," *IEICE Electronics Express*, vol. 9, no. 18, pp. 1473–1478, 2012.

[95] T. Kawanishi, T. Sakamoto, S. Shinada, and M. Izutsu, "Optical frequency comb generator using optical fiber loops with single-sideband modulation," *IEICE Electronics Express*, vol. 1, no. 8, pp. 217–221, 2004.

[96] G. H. Smith, "Overcoming chromatic-dispersion effects in fiber-wireless systems incorporating external modulators," *IEEE Transactions on Microwave Theory and Techniques*, vol. 45, no. 8 PART 2, pp. 1410–1415, 1997.

[97] S. F. Kaijage, Z. Ouyang, and X. Jin, "Porous-core photonic crystal fiber for low loss terahertz wave guiding," *IEEE Photonics Technology Letters*, vol. 25, no. 15, pp. 1454–1457, 2013.

[98] S. Atakaramians, S. Afshar V., M. Nagel, H. K. Rasmussen, O. Bang, T. M. Monro, and D. Abbott, "Direct probing of evanescent field for characterization of porous terahertz fibers," *Applied Physics Letters*, vol. 98, no. 12, pp. 1–4, 2011.

[99] K. Nielsen, H. K. Rasmussen, P. U. Jepsen, and O. Bang, "Porous-core honeycomb bandgap THz fiber," *Optics Letters*, vol. 36, no. 5, p. 666, 2011.

[100] J. Anthony, R. Leonhardt, S. G. Leon-Saval, and A. Argyros, "THz propagation in kagome hollow-core microstructured fibers," *Optics Express*, vol. 19, no. 19, p. 18470, 2011.

[101] M. Uthman, B. M. A. Rahman, N. Kejalakshmy, A. Agrawal, and K. T. V. Grattan, "Design and characterization of low-loss porous-core photonic crystal fiber," *IEEE Photonics Journal*, vol. 4, no. 6, pp. 2315–2325, 2012.

[102] L. Vincetti, "Numerical analysis of plastic hollow core microstructured fiber for Terahertz applications," *Optical Fiber Technology*, vol. 15, no. 4, pp. 398–401, 2009.

[103] K. Nielsen, H. K. Rasmussen, A. J. Adam, P. C. Planken, O. Bang, and P. U. Jepsen, "Bendable, low-loss Topas fibers for the terahertz frequency range," *Optics Express*, vol. 17, no. 10, p. 8592, 2009.

[104] A. Hassani, A. Dupuis, and M. Skorobogatiy, "Low loss porous terahertz fibers containing multiple subwavelength holes," *Applied Physics Letters*, vol. 92, no. 7, 2008.

[105] G. K. M. Hasanuzzaman, M. Selim Habib, S. M. Abdur Razzak, M. A. Hossain, and Y. Namihira, "Low Loss Single-Mode Porous-Core Kagome Photonic Crystal Fiber for THz Wave Guidance," *Journal of Lightwave Technology*, vol. 33, pp. 4027–4031, Oct. 2015.

[106] M. I. Hasan, S. M. A. Razzak, G. K. M. Hasanuzzaman, and M. S. Habib, "Ultra-low material loss and dispersion flattened fiber for THz transmission," *IEEE Photonics Technology Letters*, vol. 26, no. 23, pp. 2372–2375, 2014.

[107] J.-Y. Lu, C.-P. Yu, H.-C. Chang, H.-W. Chen, Y.-T. Li, C.-L. Pan, and C.-K. Sun, "Terahertz air-core microstructure fiber," *Applied Physics Letters*, vol. 92, no. 6, p. 064105, 2008.

[108] C. Markos, J. C. Travers, A. Abdolvand, B. J. Eggleton, and O. Bang, "Hybrid photonic-crystal fiber," *Reviews of Modern Physics*, vol. 89, p. 045003, Nov. 2017.

[109] R. F. Cregan, B. J. Mangan, J. C. Knight, T. A. Birks, P. S. J. Russell, P. J. Roberts, and D. C. Allan, "Single-mode photonic band gap guidance of light in air," *Science*, vol. 285, pp. 1537–1539, Sep. 1999.

[110] M. G. Couny, F. Benabid, F. Roberts, P.R. Light, P. S. Raymer, "Generation and photonic guidance of multi-octave optical-frequency combs," *Science*, vol. 318, no. 5853, pp. 1118–1121, 2007.

[111] L. Vincetti, "Single-mode propagation in triangular tube lattice hollow-core terahertz

fibers," *Optics Communications*, vol. 283, no. 6, pp. 979–984, 2010.

[112] L. Vincetti, "Hollow Core Photonic Band Gap Fibre For THz Applications," *Microwave and Optical Technology Letters*, vol. 51, no. 7, pp. 1711–1714, 2009.

[113] J. Anthony, R. Leonhardt, A. Argyros, and M. C. J. Large, "Characterization of a microstructured Zeonex terahertz fiber," *Journal of the Optical Society of America B*, vol. 28, no. 5, pp. 1013–1018, 2011.

[114] R. Islam, M. S. Habib, G. K. Hasanuzzaman, S. Rana, M. A. Sadath, and C. Markos, "A Novel Low-Loss Diamond-Core Porous Fiber for Polarization Maintaining Terahertz Transmission," *IEEE Photonics Technology Letters*, vol. 28, pp. 1537–1540, Jul. 2016.

[115] H. Bao, K. Nielsen, O. Bang, and P. U. Jepsen, "Dielectric tube waveguides with absorptive cladding for broadband, low-dispersion and low loss THz guiding," *Scientific Reports*, vol. 5, no. 1, p. 7620, 2015.

[116] J. Liang, L. Ren, N. Chen, and C. Zhou, "Broadband, low-loss, dispersion flattened porous-core photonic bandgap fiber for terahertz (THz)-wave propagation," *Optics Communications*, vol. 295, pp. 257–261, May 2013.

[117] F. Benabid and P. J. Roberts, "Linear and nonlinear optical properties of hollow core photonic crystal fiber," *Journal of Modern Optics*, vol. 58, no. 2, pp. 87–124, 2011.

[118] F. Poletti, "Nested antiresonant nodeless hollow core fiber," *Optics Express*, vol. 22, no. 20, p. 23807, 2014.

[119] M. S. Habib, O. Bang, and M. Bache, "Low-loss hollow-core silica fibers with adjacent nested anti-resonant tubes," *Optics Express*, vol. 23, no. 13, p. 17394, 2015.

[120] W. Belardi and J. C. Knight, "Hollow antiresonant fibers with reduced attenuation," *Optics Letters*, vol. 39, no. 7, p. 1853, 2014.

[121] L. Vincetti, V. Setti, and M. Zoboli, "Terahertz tube lattice fibers with octagonal symmetry," *IEEE Photonics Technology Letters*, vol. 22, no. 13, pp. 972–974, 2010.

[122] M. S. Habib, O. Bang, and M. Bache, "Low-loss single-mode hollow-core fiber with anisotropic anti-resonant elements," *Optics Express*, vol. 24, no. 8, p. 8429, 2016.

[123] A. Van Newkirk, J. E. Antonio-Lopez, J. Anderson, R. Alvarez-Aguirre, Z. S. Eznaveh, G. Lopez-Galmiche, R. Amezcua-Correa, and A. Schülzgen, "Modal analysis of antiresonant hollow core fibers using Sˆ2 imaging," *Optics Letters*, vol. 41, p. 3277, jul 2016.

[124] M. H. Frosz, P. Roth, M. C. Günendi, and P. S. Russell, "Analytical formulation for the bend loss in single-ring hollow-core photonic crystal fibers," *Photonics Research*, vol. 5, no. 2, p. 88, 2017.

[125] P. Uebel, M. C. Günendi, M. H. Frosz, G. Ahmed, N. N. Edavalath, J.-M. Ménard, and P. S. Russell, "Broadband robustly single-mode hollow-core PCF by resonant filtering of higher-order modes," *Optics Letters*, vol. 41, no. 9, p. 1961, 2016.

[126] F. C. Meng, B. W. Liu, Y. F. Li, C. Y. Wang, and M. L. Hu, "Low Loss Hollow-Core Antiresonant Fiber with Nested Elliptical Cladding Elements," *IEEE Photonics Journal*, vol. 9, no. 1, p. 7100211, 2017.

[127] G. K. Hasanuzzaman, S. Iezekiel, C. Markos, and M. S. Habib, "Hollow-core fiber with nested anti-resonant tubes for low-loss THz guidance," *Optics Communications*, vol. 426, pp. 477–482, May 2018.

[128] H. Bao, K. Nielsen, H. K. Rasmussen, P. U. Jepsen, and O. Bang, "Fabrication and characterization of porous-core honeycomb bandgap THz fibers.," *Optics express*, vol. 20, no. 28, pp. 29507–17, 2012.

[129] E. A. Marcatili and R. A. Schmeltzer, "Hollow Metallic and Dielectric Waveguides for Long Distance Optical Transmission and Lasers," *Bell System Technical Journal*, vol. 43, pp. 1783–1809, Jul. 1964.

[130] M. I. Hasan, N. Akhmediev, and W. Chang, "Positive and negative curvatures nested in an antiresonant hollow-core fiber," *Optics Letters*, vol. 42, p. 703, Feb. 2017.

[131] M. Wang and J. Yao, "Tunable optical frequency comb generation based on an optoelectronic oscillator," *IEEE Photonics Technology Letters*, vol. 25, no. 21, pp. 2035–2038, 2013.

[132] G. K. M. Hasanuzzaman and S. Iezekiel, "Self-oscillating optical comb generator based on optoelectronic oscillator," in *SPIE 10103, Terahertz, RF, Millimeter, and*

Submillimeter-Wave Technology and Applications X, vol. 10103, p. 1010320, International Society for Optics and Photonics, Feb. 2017.

[133] G. Hasanuzzaman, A. Kanno, P. T. Dat, and S. Iezekiel, "W-band radio-over-fiber link based on self-oscillating optical frequency comb generator," in *Optical Fiber Communication Conference*, (San Diego, California United States), p. paper W1F.6, 2018.

[134] G. K. Hasanuzzaman, A. Kanno, P. T. Dat, and S. Iezekiel, "Self-oscillating optical frequency comb: Application to low phase noise millimeter wave generation and radio-over-fiber link," *Journal of Lightwave Technology*, vol. 36, no. 19, pp. 4535–4542, 2018.

[135] A. Kanno, G. Hasanuzzaman, N. Yamamoto, and S. Iezekiel, "Optical frequency comb applied optoelectronic oscillator for millimeter-wave signal generation and its application," in *SPIE Defense and Security, Passive and Active Millimeter-Wave Imaging XXI*, vol. 10634, pp. paper 10634–13, SPIE, May 2018.

[136] T. Sakamoto, T. Kawanishi, and M. Izutsu, "Optoelectronic oscillator using a LiNbO3 phase modulator for self-oscillating frequency comb generation.," *Optics letters*, vol. 31, pp. 811–3, Mar. 2006.

[137] M. E. Belkin, A. V. Loparev, Y. Semenova, G. Farrell, and A. S. Sigov, "Tunable RF-band optoelectronic oscillator and optoelectronic computer-added design model for its simulation," *Microwave and Optical Technology Letters*, vol. 53, pp. 2474–2477, Nov. 2011.

[138] T. Sakamoto, T. Kawanishi, and M. Izutsu, "Asymptotic formalism for ultraflat optical frequency comb generation using a Mach-Zehnder modulator.," *Optics letters*, vol. 32, no. 11, pp. 1515–1517, 2007.

[139] J. Hu, Y. Gu, W. Tan, W. Zhu, L. Wang, and M. Zhao, "Microwave photonic link with improved phase noise using a balanced detection scheme," *Optics Communications*, vol. 370, pp. 1–5, 2016.

[140] C. Jiang, W. Zou, H. Zhang, and J. Chen, "Improvement of phase noise in a widely tunable optoelectronic oscillator based on balanced detection," in *2015 Opto-*

Electronics and Communications Conference, OECC 2015, pp. 1–3, IEEE, Jun. 2015.

[141] X. S. Yao and L. Maleki, "Multiloop optoelectronic oscillator," *IEEE Journal of Quantum Electronics*, vol. 36, no. 1, pp. 79–84, 2000.

[142] T. Asakura, T. Kamiya, F. Krausz, B. Monemar, H. Venghaus, H. Weber, and H. Weinfurter, *High-Order Modulation For Optical Fiber*. Berlin: Springer, 2009.

[143] R. März, *Integrated optics : design and modeling*. Boston: Artech House, 1994.

[144] T. Sakamoto, T. Kawanishi, and M. Izutsu, "Optoelectronic oscillator using a LiNbO 3 phase modulator for self-oscillating frequency comb generation," vol. 31, no. 6, pp. 811–813, 2006.

[145] C. Wang and J. Yao, "Fiber Bragg gratings for microwave photonics subsystems.," *Optics express*, vol. 21, no. 19, pp. 22868–84, 2013.

[146] 3GPP TS36.104 V10.9.0 Releasee 10, "Evolved Universal Terrestrial Radio Access (E-UTRA);Base Station (BS) radio transmission and reception," 2013.

[147] A. J. Seeds, "TeraHertz photonics for communications," *Journal of Lightwave Technology*, vol. 33, no. 3, pp. 579–587, 2014.

[148] G. Ducournau, P. Szriftgiser, F. Pavanello, E. Peytavit, M. Zaknoune, D. Bacquet, A. Beck, T. Akalin, J. F. Lampin, and J. F. Lampin, "THz Communications using Photonics and Electronic Devices: the Race to Data-Rate," *Journal of Infrared, Millimeter, and Terahertz Waves*, vol. 36, no. 2, pp. 198–220, 2015.

[149] H. Shams, K. Balakier, M. Fice, L. Ponnampalam, C. Graham, C. Renaud, A. Seeds, and F. Van Dijk, "Coherent frequency tuneable thz wireless signal generation using an optical phase lock loop system," in *2017 International Topical Meeting on Microwave Photonics*, vol. 2017-Decem, pp. 2–5, 2017.

[150] T. Sakamoto, T. Kawanishi, M. Izutsu, and C. Technology, "Optical Frequency Comb Generation Using Asymmetrically Dual-Driven Mach-Zehnder Modulator," *Technology*, vol. 3, pp. 743–744, 2005.

[151] T. Chen, X. Yi, L. Li, and R. Minasian, "Single passband microwave photonic filter with wideband tunability and adjustable bandwidth.," *Optics letters*, vol. 37, no. 22, pp. 4699–701, 2012.

[152] L. Cheng and S. Aditya, "A novel photonic microwave filter with infinite impulse response," *IEEE Photonics Technology Letters*, vol. 19, no. 19, pp. 1439–1441, 2007.

[153] G. Ning, L. H. Cheng, S. Aditya, P. Shum, and J. Q. Zhou, "Infinite impulse response microwave photonic filter using a dual drive modulator with an optoelectronic feedback loop," *Journal of Modern Optics*, vol. 55, no. 14, pp. 2293–2299, 2008.

[154] G. Ning, L. Cheng, S. Aditya, J. Zhou, and P. Shum, "General analyses of infinite impulse microwave photonic filters with an intensity modulator in an opto-electronic feedback loop," *Applied Physics B: Lasers and Optics*, vol. 92, no. 4, pp. 609–614, 2008.

[155] L. Zhou, X. Zhang, and E. Xu, "Q value analysis of microwave photonic filters," *Frontiers of Optoelectronics in China*, vol. 2, no. 3, pp. 269–278, 2009.

[156] T. H. Lee and A. Hajimiri, "Oscillator phase noise: A tutorial," *IEEE Journal of Solid-State Circuits*, vol. 35, no. 3, pp. 326–335, 2000.

[157] F. Deborgies, H.-W. Li, M. Kaba, Y. Quiquempois, G. Bouwmans, D. Decoster, J.-P. Vilcot, J. Chazelas, and A. Daryoush, "Improving thermal stability of opto-electronic oscillators," *IEEE Microwave Magazine*, vol. 7, no. 4, pp. 38–47, 2006.

[158] G. Beck, L. Bigot, G. Bouwmans, A. Kudlinski, J. P. Vilcot, and M. Douay, "Benefits of photonic bandgap fibers for the thermal stabilization of optoelectronic oscillators," *IEEE Photonics Journal*, vol. 4, no. 3, pp. 789–794, 2012.

[159] U. S. Mutugala, J. Kim, T. D. Bradley, N. V. Wheeler, S. R. Sandoghchi, J. R. Hayes, E. Numkam Fokoua, F. Poletti, M. N. Petrovich, D. J. Richardson, and R. Slavík, "Optoelectronic oscillator incorporating hollow-core photonic bandgap fiber," *Optics Letters*, vol. 42, no. 13, pp. 2647–2650, 2017.

[160] U. S. Mutugala, E. R. Numkam Fokoua, Y. Chen, T. Bradley, S. R. Sandoghchi, G. T. Jasion, R. Curtis, M. N. Petrovich, F. Poletti, D. J. Richardson, and R. Slavík, "Hollow-core fibres for temperature-insensitive fibre optics and its demonstration in an Optoelectronic oscillator," *Scientific Reports*, vol. 8, no. 1, pp. 1–6, 2018.

[161] K. Saitoh and S. Matsuo, "Multicore fiber technology," *Journal of Lightwave Technology*, vol. 34, no. 1, pp. 55–66, 2016.

[162] T. Umezawa, K. Kashima, A. Kanno, A. Matsumoto, K. Akahane, N. Yamamoto, and T. Kawanishi, "100-GHz Fiber-Fed Optical-To-Radio Converter for Radio-And Power-Over-Fiber Transmission," *IEEE Journal on Selected Topics in Quantum Electronics*, vol. 23, no. 3, 2017.

[163] M. Matsuura, H. Furugori, and J. Sato, "60 W power-over-fiber feed using double-clad fibers for radio-over-fiber systems with optically powered remote antenna units," *Optics Letters*, vol. 40, no. 23, pp. 5598–5601, 2015.

[164] S. García and I. Gasulla, "Multi-cavity optoelectronic oscillators using multicore fibers.," *Optics express*, vol. 23, no. 3, pp. 2403–15, 2015.

[165] S. García and I. Gasulla, "Experimental demonstration of multi-cavity optoelectronic oscillation over a multicore fiber," *Optics Express*, vol. 25, no. 20, pp. 23663–23668, 2017.

[166] T. Sakamoto, T. Kawanishi, and M. Izutsu, "Optoelectronic oscillator employing reciprocating optical modulator for millimetre-wave generation," *Electronics Letters*, vol. 43, no. 19, pp. 1031–1033, 2007.

[167] L. Ponnampalam, M. Fice, H. Shams, C. Renaud, and A. Seeds, "Optical comb for generation of a continuously tunable coherent THz signal from 1225 GHz to >27 THz," *Optics Letters*, vol. 43, no. 11, p. 2507, 2018.

[168] OEWaves, "Micro-OEO | OEwaves."

[169] J. S. Fandiño, P. Muñoz, D. Doménech, and J. Capmany, "A monolithic integrated photonic microwave filter," *Nature Photonics*, vol. 11, no. 2, pp. 124–129, 2016.

[170] G. Carpintero, K. Balakier, Z. Yang, R. C. Guzm??n, A. Corradi, A. Jimenez, G. Kervella, M. J. Fice, M. Lamponi, M. Chitoui, F. Van Dijk, C. C. Renaud, A. Wonfor, E. A. J. M. Bente, R. V. Penty, I. H. White, and A. J. Seeds, "Microwave photonic integrated circuits for millimeter-wave wireless communications," *Journal of Lightwave Technology*, vol. 32, no. 20, pp. 3495–3501, 2014.

[171] D. Marpaung, C. Roeloffzen, R. Heideman, A. Leinse, S. Sales, and J. Capmany, "Integrated microwave photonics," *Laser & Photonics Reviews*, vol. 7, no. 4, pp. 506–538, 2013.

[172] W. Zhang and J. Yao, "Silicon photonic integrated optoelectronic oscillator for frequency-tunable microwave generation," *Journal of Lightwave Technology*, vol. 36, pp. 4655–4663, Oct. 2018.

[173] J. Tang, T. Hao, W. Li, D. Domenech, R. B. nos, P. M. noz, N. Zhu, J. Capmany, and M. Li, "Integrated optoelectronic oscillator," *Optics Express*, vol. 26, pp. 12257–12265, Apr 2018.

[174] I. Gasulla, J. Lloret, J. Sancho, S. Sales, and J. Capmany, "Recent breakthroughs in microwave photonics," *IEEE Photonics Journal*, vol. 3, no. 2, pp. 311–315, 2011.

[175] J. M. Galve, I. Gasulla, S. Sales, and J. Capmany, "Reconfigurable radio access networks using multicore fibers," *IEEE Journal of Quantum Electronics*, vol. 52, no. 1, 2016.

[176] I. Gasulla and J. Capmany, "Microwave photonics applications of multicore fibers," *IEEE Photonics Journal*, vol. 4, no. 3, pp. 877–888, 2012.

[177] I. Gasulla and J. Perez, "Multicore fiber opportunities for Centralized Radio Access Networks," in *International Conference on Transparent Optical Networks*, pp. 6–9, 2014.

[178] J. Sakaguchi, Y. Awaji, N. Wada, A. Kanno, T. Kawanishi, T. Hayashi, T. Taru, T. Kobayashi, and M. Watanabe, "109-tb/s (7x97x172-gb/s sdm/wdm/pdm) qpsk transmission through 16.8-km homogeneous multi-core fiber," in *Optical Fiber Communication Conference/National Fiber Optic Engineers Conference 2011*, p. PDPB6, Optical Society of America, 2011.

[179] S. Randel, M. Magarini, R. Ryf, R.-J. Essiambre, a. H. Gnauck, P. J. Winzer, T. Hayashi, T. Taru, and T. Sasaki, "MIMO-based signal processing of spatially multiplexed 112-Gb/s PDM-QPSK signals using strongly-coupled 3-core fiber," *2011 37th European Conference and Exhibition on Optical Communication*, pp. 1–3, 2011.

[180] J. Sakaguchi, B. J. Puttnam, W. Klaus, Y. Awaji, N. Wada, A. Kanno, T. Kawanishi, K. Imamura, H. Inaba, K. Mukasa, R. Sugizaki, T. Kobayashi, and M. Watanabe, "19-core fiber transmission of 19x100x172-Gb/s SDM-WDM-PDM-QPSK signals at 305Tb/s," *National Fiber Optic Engineers Conference*, p. PDP5C.1, 2012.

[181] H. Takara, A. Sano, T. Kobayashi, H. Kubota, H. Kawakami, A. Matsuura, Y. Miyamoto, Y. Abe, H. Ono, K. Shikama, Y. Goto, K. Tsujikawa, Y. Sasaki, I. Ishida, K. Takenaga, S. Matsuo, K. Saitoh, M. Koshiba, and T. Morioka, "1.01-pb/s (12 sdm/222 wdm/456 gb/s) crosstalk-managed transmission with 91.4-b/s/hz aggregate spectral efficiency," in *European Conference and Exhibition on Optical Communication*, p. Th.3.C.1, Optical Society of America, 2012.

[182] Y. Fan, J. Li, Y. Lei, M. Tang, F. Yin, Y. Dai, and K. Xu, "Full-duplex transmission of ieee 802.11ac-compliant mimo wlan signals over a 2-km 7-core fiber," *Chin. Opt. Lett.*, vol. 15, p. 010011, Jan 2017.

[183] V. Bobrovs, S. Spolitis, and G. Ivanovs, "Latency causes and reduction in optical metro networks," in *Proceedings of SPIE*, vol. 9008, p. 90080C, International Society for Optics and Photonics, Dec. 2013.

[184] R. S. Serrano, "Flexible fpga based platform for variable rate signal generation flexible fpga based platform for variable rate signal generation," Master's thesis, Technical University of Denmark, 2013.